

The copyright of this thesis vests in the author. No quotation from it or information derived from it is to be published without full acknowledgement of the source. The thesis is to be used for private study or non-commercial research purposes only.

Published by the University of Cape Town (UCT) in terms of the non-exclusive license granted to UCT by the author.

THE PERFORMANCE OF STRUCTURED COBALT CATALYSTS IN FISCHER-TROPSCH SYNTHESIS

Youqi Zhuang

BSc. Chemical Engineering, University of Cape Town, South Africa

Thesis presented to University of Cape Town
in fulfilment of the requirements
for the degree of

Doctor of Philosophy

Centre for Catalysis Research
Department of Chemical Engineering
University of Cape Town

November 2009

ACKNOWLEDGEMENTS

This work would not be possible without the guidance and the encouragements from Prof. Eric van Steen. His patience, enthusiasm in finding the source of problems, and always giving clear and simple explanations, are my life-long lessons.

Special thanks to my co-supervisor Prof. Michael Claeys for many inspirational discussions and advices.

Thanks to Prof. Klaus Möller who introduced me to the Scilab programming software, and supported me in coding the mathematical model.

I am very thankful to receive technical supports from the following people:

Marc Wüst - the IT guru

Helen Divey and Suzana Vasic - the analytical experts

Walter Böhringer - the 'German dictionary' (and the living encyclopaedia of food)

Miranda Waldron and Mohamed Jaffer - from the Electron Microscopy Unit

Herman, Joe, Peter - the three musketeers in the Workshop

Thanks to all the Chemical Engineering 5th floor dwellers (Lucrécio, Cathrin, Pete, Jako, Jurie, Nico, Nicola just to mention a few) for providing a stimulating and fun environment in which to learn and grow.

This journey would be more difficult without all the research work of the mentioned authors in the references. The pathway of an explorer is indeed the foundation of a trail.

The financial support from NRF, THRIP and Sasol is greatly appreciated.

I am indebted to my wife for her love and her smile.

I am thankful to my grandma, dad, mom, and my in-laws, who prepared and helped me for this journey.

I am grateful for; all the people around me, this opportunity to know more about myself, and to be closer to The One.

This work is dedicated in loving memory of my grandfather and grandmother.

SYNOPSIS

Cobalt is the preferred catalyst metal for the production of clean burning, high cetane number diesel fuel from synthesis gas using the Fischer-Tropsch synthesis. Hence, increasing C5+ selectivity of cobalt catalysts is one of the hot topics in Fischer-Tropsch synthesis. Internal mass transport limitation may affect C5+ selectivity. It was concluded that mild transport limitation is required for maximum C5+ selectivity. Mild transport limitation also increases the catalyst activity, since the reported Fischer-Tropsch rate of reaction has a negative dependency on CO partial pressure. The metal distribution within catalyst pellets may modify product selectivity by changing the local metal density and the diffusion path length. However, current catalyst preparation methods limit metal distribution in transition metal catalysts.

The aim of this study is to explore a possible catalyst synthesis route for egg-shell, egg-yolk and egg-white type of cobalt catalyst pellets. The establishment of the non-uniform cobalt catalyst synthesis method will provide an observational evaluation technique for the investigation of the effect of intra-pellet metal distribution on the activity and product selectivity of the Fischer-Tropsch synthesis.

The non-uniform catalyst synthesis method utilises the hydrophobic nature of the silica pellet. Egg-shell, egg-yolk and egg-white type of cobalt catalyst with sharp metal enriched boundary were synthesized. The intra-pellet cobalt distribution, metal particle size, metal loading, metal surface area and catalyst reducibility were characterised. The performance of these non-uniform catalysts was tested in a modified slurry type reactor. Catalyst pellets were kept in mesh-wire baskets which were mounted inside a slurry reactor, and tested in the absence of external mass transport limitation. The Fischer-Tropsch activity was recorded and modelled using a reaction-diffusion pellet inside a continuous stirred tank reactor model. The product selectivity were analysed with an offline GC.

The Fischer-Tropsch activity is strongly dependent on the intra-pellet metal distribution. The egg-shell type of catalyst outperforms the uniform, egg-yolk and egg-white type of catalyst, in terms of activity, under the influence of internal mass transport limitation. The intra-pellet distribution alters the reactant concentration in the pellet as well as intra-pellet H₂/CO ratio. The reaction-diffusion path length was identified to be a suitable parameter for product selectivity. An increase in the reaction-diffusion path results in an increase in α -olefins re-adsorption, a decrease in olefin content and an increase branched product compounds. Secondary chain growth is not favoured under internal mass transport limitation.

TABLE OF CONTENTS

LIST OF FIGURES.....	12
LIST OF TABLES.....	18
LIST OF SYMBOLS.....	20
1 INTRODUCTION.....	29
2 LITERATURE REVIEW	33
2.1 Fischer-Tropsch Synthesis	33
2.2 General Overview of Reactors	34
2.2.1 Fixed-bed Reactor.....	34
2.2.2 Fluidised-bed Reactor.....	35
2.2.3 Slurry-bed Reactor	37
2.3 Catalysts for the Fischer-Tropsch Synthesis.....	38
2.3.1 Metal Type.....	38
2.3.2 Promoters.....	39
2.4 Preparation of Catalysts	40
2.5 Intrinsic Activity of the Fischer-Tropsch Synthesis.....	42
2.6 Mechanism of the Fischer-Tropsch Synthesis.....	44
2.6.1 Alkyl Mechanism	44
2.6.2 Alkenyl Mechanism	46
2.6.3 Enol Mechanism.....	47
2.6.4 CO-Insertion Mechanism.....	48
2.7 Fischer-Tropsch Product Distribution	49
2.8 Fischer-Tropsch Product Selectivity.....	51
2.8.1 Effect of Temperature	51
2.8.2 Effect of Pressure	51
2.8.3 Effect of Gas Composition	52
2.8.4 Effect of Catalyst Metal Particle Size.....	54
2.8.5 Effect of Catalyst Pore Size	54
2.8.6 Effect of Catalyst Pellet Size.....	55
2.8.7 Effect of Catalyst Structure	57
2.9 Structured Catalysts	58
2.9.1 Type of Structured Catalysts	58
2.9.2 Influence of Catalyst Structure on Product Selectivity	58
2.10 Synthesis of Structured Catalysts	60
2.10.1 Diffusion-Adsorption	60
2.10.2 Deposition-Precipitation	61
2.10.3 Granulation.....	61

2.10.4	Imbibition.....	61
2.11	Catalysts Deactivation.....	62
2.11.1	Poisoning.....	62
2.11.2	Fouling.....	62
2.11.3	Sintering	62
2.11.4	Gas-Solid and Solid-Solid Interactions	63
3	SCOPE OF THIS STUDY.....	65
4	EXPERIMENTAL METHODOLOGY	67
4.1	Catalyst Preparation.....	67
4.1.1	Preparation of Uniform Catalysts.....	67
4.1.2	Preparation of Egg-shell Type of Catalysts	68
4.1.3	Preparation of Egg-yolk Type of Catalysts	69
4.1.4	Preparation of Egg-white Type of Catalysts	70
4.2	Catalyst Characterisation	71
4.2.1	Atomic Absorption Spectroscopy (AAS)	71
4.2.2	Optical Microscopy	71
4.2.3	Scanning Electron Microscopy (SEM).....	71
4.2.4	Transmission Electron Microscopy (TEM)	72
4.2.5	X-Ray Diffraction Spectroscopy (XRD)	72
4.2.6	Physisorption	72
4.2.7	Chemisorption.....	73
4.2.8	Temperature Programmed Reduction and Oxidation (TPR-TPO).....	74
4.3	Fischer-Tropsch Synthesis Test.....	76
4.3.1	Modified Slurry Reactor Set-up.....	76
4.3.2	Post-run Catalyst Characterization.....	79
4.4	Analytical Procedures	80
4.4.1	On-line Analysis of Inorganic Gases and Methane	80
4.4.2	Sampling of Volatile Organic Gases	80
4.4.3	Analysis of Volatile Organic Gases.....	80
4.5	Data Analysis	81
5	RESULTS AND DISCUSSION.....	83
5.1	Characterisation of Structured Cobalt Catalysts.....	83
5.1.1	Intra-pellet Cobalt Distribution in Uniform Catalyst	83
5.1.2	Intra-pellet Cobalt Distribution of Egg-shell Type of Catalysts	85
5.1.3	Intra-pellet Cobalt Distribution of Egg-yolk Type of Catalysts	91
5.1.4	Intra-pellet Cobalt Distribution of Egg-white Type of Catalysts	93
5.1.5	Cobalt Loading	95

5.1.6	Catalyst Surface Area and Pore Size	96
5.1.7	Cobalt Oxide Phase of Calcined Catalysts.....	97
5.1.8	Cobalt Oxide Crystallite and Cluster Sizes.....	98
5.1.9	Reducibility of Structured Catalysts	99
5.2	Fischer-Tropsch Activity of Structured Catalysts.....	106
5.2.1	External Mass Transport Tests in Slurry Phase Set-up.....	106
5.2.2	Catalyst Deactivation	108
5.2.3	Internal Mass Transport in Slurry Phase Set-up.....	111
5.3	Product Selectivity of Structured Catalysts.....	125
5.3.1	Secondary Reactions of Ethene.....	126
5.3.2	Product Selectivity in the C5 Fraction.....	130
5.3.3	Methane Selectivity and C5+ Selectivity.....	138
5.3.4	C3-C8 Chain Growth Probability	145
5.3.5	C5 Oxygenate Content.....	146
6	SUMMARY AND CONCLUSIONS	149
7	RECOMMENDATIONS FOR FUTURE WORK	153
8	REFERENCES.....	155
APPENDIX A		169
1.	GTL & CTL Potential Index.....	169
APPENDIX B		171
1.	AAS Acid Digestion Procedure.....	171
2.	SEM Sample Preparation	172
3.	TEM Image Analysis Procedure	173
4.	XRD Procedure and Calculations	174
5.	BET and BJH Model Calculations	175
6.	Chemisorption Particle Diameter Derivation	177
7.	TPR-TPO Calibrations and Calculations.....	178
8.	TCD Trace	180
9.	FID Operating Conditions and Peak Identification	181
APPENDIX C		185
1.	Scilab Code for Surface Wetting.....	185
2.	Wetting Calculations.....	186
3.	Synthesis Gas Properties at Reaction Conditions	187
3.1.	Density	187
3.2.	Viscosity	187
3.3.	Diffusivity	187
4.	External Mass Transport Limitation Polymath Code	189

4.1. Gas-phase mass transport in Fixed-bed reactor.....	189
4.2. Liquid-phase mass transport in Fixed-bed reactor	189
5. Dimensionless Reaction-Diffusion Model Derivation	190
6. Scilab Code for Derived Reaction Model	194
6.1. Uniform Pellets	194
6.2. Egg-shell Type Pellets	196
6.3. Egg-yolk Type Pellets	198
6.4. Egg-white Type Pellets	200
APPENDIX D	203
1. Fixed-bed Reactor Set-up.....	203
2. Wall Effect in Fixed-bed Set-up.....	205
3. External Mass Transport Limitations in Fixed-bed Set-up	207

University of Cape Town

LIST OF FIGURES

FIGURE 1.1:	DISTRIBUTION OF PROVEN CRUDE OIL RESERVE AS AT 1 JANURARY 2008 [%] (LEFT) ; PERCENTAGE OF CRUDE OIL CONSUMPTION FROM OIL IMPORTS (RIGHT), (CIA, 2008).....	29
FIGURE 1.2:	NOMINAL CRUDE OIL PRICE FOR THE PAST 15 YEARS [US\$/BARREL], (IMF, 2008)	30
FIGURE 1.3:	GEOGRAPHICAL LOCATION OF COMMERCIAL GTL PLANTS REPRESENTED BY ITS COMPANY LOGO ON GTL POTENTIAL INDEX MAP (EXISTING PLANT IN BOLD, FUTURE PLANT IN TIMID, PLANNED PLANT IN ITALIC), PLANT SIZE IN [BPD], (WERGY, 2005)	31
FIGURE 1.4:	GEOGRAPHICAL LOCATION OF COMMERCIAL CTL PLANTS REPRESENTED BY ITS COMPANY LOGO ON CTL POTENTIAL INDEX MAP (EXISTING PLANT IN BOLD, PLANNED PLANT IN ITALIC), PLANT SIZE IN [BPD] (* BERGIUS-PIER PROCESS), (WERGY, 2005)	31
FIGURE 1.5:	OVERVIEW OF LIQUEFACTION PROCESS VIA FISCHER-TROPSCH SYNTHESIS..	32
FIGURE 2.1:	SCHEMATIC REPRESENTATION OF AN INDUSTRIAL FIXED-BED REACTOR.....	34
FIGURE 2.2:	SCHEMATIC REPRESENTATION OF AN INDUSTRIAL CIRCULATING FLUIDISED-BED REACTOR.....	35
FIGURE 2.3:	SCHEMATIC REPRESENTATION OF AN INDUSTRIAL FLUIDISED-BED REACTOR.	36
FIGURE 2.4:	SCHEMATIC REPRESENTATION OF AN INDUSTRIAL SLURRY REACTOR.....	37
FIGURE 2.5:	SCHEMATIC REPRESENTATION OF THE ALKYL MECHANISM	45
FIGURE 2.6:	SCHEMATIC REPRESENTATION OF THE ALKENYL MECHANISM.....	46
FIGURE 2.7:	SCHEMATIC REPRESENTATION OF THE ENOL MECHANISM	47
FIGURE 2.8:	SCHEMATIC REPRESENTATION OF THE CO INSERTION MECHANISM	48
FIGURE 2.9:	COMPARISON BETWEEN ANDERSON-SCHULTZ-FLORY PRODUCT DISTRIBUTION AND EXPERIMENTAL PRODUCT DISTRIBUTION FOR A CHAIN GROWTH PROBABILITY OF 0.7	50
FIGURE 2.10:	EFFECT OF THE STRUCTURAL PARAMETER ON C5+ PRODUCT SELECTIVITY (ADOPTED FROM IGLESIA <i>ET AL.</i> 1997A, [○] DISPERSION/SUPPORT EFFECT, [●] EGG-SHELL THICKNESS EFFECT, [▲] PELLET SIZE VARIATION)	57
FIGURE 2.11:	CROSS-SECTIONAL VIEW OF DIFFERENT TYPE OF STRUCTURED CATALYST	58
FIGURE 4.1:	AN EXAMPLE SHOWING DETERMINATION OF MONOLAYER FROM CHEMISORPTION ISOTHERM (CATALYST U1).....	73
FIGURE 4.2:	EXAMPLE OF TPR SPECTRUM OF REDUCED CATALYST (U1C) PRIOR TPO ANALYSIS.....	75
FIGURE 4.3:	EXAMPLE OF TPO SPECTRUM OF CATALYST (U1C) AFTER TPR ANALYSIS	75
FIGURE 4.4:	FLOW DIAGRAM OF THE SLURRY REACTOR SET-UP USED IN THIS STUDY	77

FIGURE 4.5:	SCHEMATIC REPRESENTATION OF THE MODIFIED SLURRY REACTOR SHOWING MESH-WIRED BASKETS	77
FIGURE 4.6:	EXAMPLE OF SEQUENTIAL CHANGE OF REACTION CONDITION FOR FISCHER-TROPSCH SYNTHESIS TESTS (Y1).....	78
FIGURE 4.7:	SOXHLET EXTRACTION SET-UP USED FOR WAX EXTRACTION OF SPENT CATALYSTS	79
FIGURE 5.1:	BACK-SCATTED SEM OF CATALYST PELLET U1 IMAGE (A) EDX PROCESSED IMAGE SHOWING COBALT ENRICHED REGION (B) OUTLINE SHOWING COBALT BOUNDARY (C)	83
FIGURE 5.2:	BACK-SCATTED SEM IMAGE OF CATALYST WITHOUT INTERMEDIATE CALCINATION (A) EDX PROCESSED IMAGE SHOWING COBALT DISTRIBUTION VARIATION (B) BACK-SCATTED SEM IMAGE OF CATALYST U2 WITH INTERMEDIATE CALCINATION (C) EDX PROCESSED IMAGE SHOWING UNIFORM COBALT DISTRIBUTION IN CATALYST U2 (D).....	84
FIGURE 5.3:	OPTICAL MICROSCOPY IMAGES OF EGG-SHELL TYPE OF CATALYSTS	85
FIGURE 5.4:	EXAMPLE OF BACK-SCATTED SEM IMAGES OF EGG-SHELL CATALYST (S6) (A) EDX PROCESSED IMAGE HIGHLIGHTING COBALT RICH REGION (B) OUTLINED IMAGE SHOWING COBALT ENRICHED BOUNDARY (C)	86
FIGURE 5.5:	PROPOSED POSSIBLE WETTING SCENARIOS IN THE PORES.....	86
FIGURE 5.6:	ILLUSTRATION OF THREE-PHASE EQUILIBRIUM DESCRIBED BY YOUNG'S EQUATION.....	88
FIGURE 5.7:	PREFERENCE OF WETTING SCENARIO I OVER SCENARIO II IN TERMS OF GIBB'S SURFACE ENERGY FOR PORE DIAMETER AND PORE LENGTH OF 16NM.....	88
FIGURE 5.8:	COBALT FREE SILICA CORE SIZE OF EGG-SHELL TYPE OF CATALYSTS AS FUNCTION OF ORGANICS FILLED IN THE PORE.....	90
FIGURE 5.9:	OPTICAL MICROSCOPY IMAGES OF EGG-YOLK TYPE OF CATALYSTS.....	91
FIGURE 5.10:	BACK-SCATTED SEM IMAGE OF Y4 PELLET (A) EDX PROCESSED IMAGE SHOWING CONCENTRATED COBALT CORE (B) OUTLINE IMAGE SHOWING THE COBALT ENRICHED BOUNDARY (C)	91
FIGURE 5.11:	COBALT ENRICHED CORE SIZE OF EGG-YOLK TYPE OF CATALYSTS AS FUNCTION OF ORGANICS FILLED IN THE PORE.	92
FIGURE 5.12:	OPTICAL MICROSCOPY IMAGES OF EGG-WHITE TYPE OF CATALYSTS	93
FIGURE 5.13:	BACK-SCATTED SEM IMAGE OF W3 PELLET (A) EDX PROCESSED SEM IMAGE SHOWING CONCENTRATED COBALT RING (B) OUTLINE IMAGE SHOWING THE COBALT ENRICHED BOUNDARY (C)	94
FIGURE 5.14:	COBALT FREE YOLK SIZE AND COBALT ENRICHED WHITE SIZE ACHIEVED IN EGG-WHITE TYPE OF CATALYSTS	94

FIGURE 5.15:	XRD SPECTRUM OF PURE SILICA SUPPORT AND CALCINED STRUCTURED COBALT ON SILICA CATALYST	97
FIGURE 5.16:	AN EXAMPLE OF TEM IMAGES SHOWING COBALT CLUSTERS IN CATALYSTS (S2)	98
FIGURE 5.17:	TPR SPECTRUM OF CALCINED UNIFORM POWDER (U1C) AND PELLET (U1) CATALYSTS.....	100
FIGURE 5.18:	TPR SPECTRUM OF REDUCED UNIFORM POWDER CATALYST (U1C).....	101
FIGURE 5.19:	TPR SPECTRUM OF REDUCED UNIFORM CATALYSTS (U1C, U1, U2)	102
FIGURE 5.20:	TPR SPECTRUMS OF REDUCED EGG-SHELL TYPE OF CATALYSTS	102
FIGURE 5.21:	TPR SPECTRUMS OF REDUCED EGG-YOLK TYPE OF CATALYSTS	104
FIGURE 5.22:	TPR SPECTRUMS OF REDUCED EGG-WHITE TYPE OF CATALYSTS	105
FIGURE 5.23:	EFFECT OF STIRRING SPEED ON CO CONSUMPTION AND CH ₄ SELECTIVITY OF CATALYST U1C AT 240°C AND 14.1ml/MIN/G _{CATALYST} (STP)	106
FIGURE 5.24:	EFFECT OF STIRRING SPEED ON CO CONSUMPTION AND CH ₄ SELECTIVITY OF CATALYST U1 (220°C AND 13.8ml/MIN/G _{CATALYST} (STP)).....	107
FIGURE 5.25:	DEACTIVATION OF THE UNIFORM POWDER CATALYST U1C AS A FUNCTION OF TIME ON STREAM	108
FIGURE 5.26:	DIFFERENTIAL VOLUME ELEMENT CONSIDERED.....	112
FIGURE 5.27:	COMPARISON OF EFFECTIVENESS FACTOR AS FUNCTION OF THIELE MODULUS (LEFT: DERIVED IN THIS STUDY; RIGHT: IGLESIA ET AL. (1995)).....	115
FIGURE 5.28:	MODELLED INTRA-PELLET REACTANT CONCENTRATION PROFILE OF AN EGG-SHELL TYPE OF CATALYST ($R_c/R_p=0.9$; $D_{PELLET}=2.5\text{MM}$).....	116
FIGURE 5.29:	MODEL PREDICTED EFFECTIVENESS FACTOR OF EGG-SHELL TYPE OF CATALYSTS PELLETS WITH 10% COBALT LOADING UNDER REACTION TEMPERATURE OF 220°C.....	117
FIGURE 5.30:	MODELLED INTRA-PELLET REACTANT CONCENTRATION PROFILE OF AN EGG-YOLK TYPE OF CATALYST ($R_c/R_p=0.5$; $D_{PELLET}=2.5\text{MM}$)	118
FIGURE 5.31:	MODEL PREDICTED EFFECTIVENESS FACTOR OF EGG-YOLK TYPE OF CATALYSTS PELLETS WITH 10% COBALT LOADING UNDER REACTION TEMPERATURE OF 220°C	119
FIGURE 5.32:	MODELLED INTRA-PELLET COBALT DENSITY OF AN EGG-WHITE TYPE OF CATALYST ($R_c/R_p=0.5$; $R_w/R_p=0.75$; $D_{PELLET}=2.5\text{MM}$)	120
FIGURE 5.33:	MODELLED INTRA-PELLET REACTANT CONCENTRATION PROFILE IN AN EGG-WHITE TYPE OF CATALYST ($R_c/R_p=0.5$; $R_w/R_p=0.75$; $D_{PELLET}=2.5\text{MM}$).....	120
FIGURE 5.34:	COMPARISON OF MODEL PREDICTED EFFECTIVENESS FACTOR OF UNIFORM, EGG-SHELL EGG-YOLK TYPE OF CATALYSTS PELLETS WITH 10% COBALT LOADING UNDER REACTION TEMPERATURE OF 220°C	121

FIGURE 5.35:	COMPARISON OF THE OPEN-ENDED CYLINDER EGG-YOLK TYPE OF CATALYST GEOMETRY TO ACTUAL EGG-YOLK TYPE OF CATALYST GEOMETRY	124
FIGURE 5.36:	CROSS-SECTIONAL VIEW OF DIFFERENT TYPE OF STRUCTURED CATALYST SHOWING REACTION-DIFFUSION PATH LENGTH	126
FIGURE 5.37:	C2 OLEFIN CONTENT AS A FUNCTION OF REACTION-DIFFUSION PATH LENGTH AT 220°C	128
FIGURE 5.38:	C2 OLEFIN CONTENT AS A FUNCTION OF REACTION-DIFFUSION PATH LENGTH AT 230°C	128
FIGURE 5.39:	C2 OLEFIN CONTENT AS A FUNCTION OF REACTION-DIFFUSION PATH LENGTH AT 240°C	129
FIGURE 5.40:	C5 OLEFIN CONTENT AS A FUNCTION OF REACTION-DIFFUSION PATH LENGTH AT 220°C	130
FIGURE 5.41:	C5 OLEFIN CONTENT AS A FUNCTION OF REACTION-DIFFUSION PATH LENGTH AT 230°C	131
FIGURE 5.42:	C5 OLEFIN CONTENT AS A FUNCTION OF REACTION-DIFFUSION PATH LENGTH AT 240°C	131
FIGURE 5.43:	C5 α -OLEFIN IN C5 LINEAR OLEFINS AS FUNCTION OF REACTION-DIFFUSION PATH LENGTH AT 220°C	132
FIGURE 5.44:	C5 α -OLEFIN IN C5 LINEAR OLEFINS AS FUNCTION OF REACTION-DIFFUSION PATH LENGTH AT 230°C	132
FIGURE 5.45:	C5 α -OLEFIN IN C5 LINEAR OLEFINS AS FUNCTION OF REACTION-DIFFUSION PATH LENGTH AT 240°C	133
FIGURE 5.46:	C5 α -OLEFIN IN C5 LINEAR OLEFINS AS FUNCTION OF COBALT SURFACE DENSITY AT 220°C	134
FIGURE 5.47:	C5 α -OLEFIN IN C5 LINEAR OLEFINS AS FUNCTION OF COBALT SURFACE DENSITY AT 230°C	134
FIGURE 5.48:	C5 α -OLEFIN IN C5 LINEAR OLEFINS AS FUNCTION OF COBALT SURFACE DENSITY AT 240°C	135
FIGURE 5.49:	C5 BRANCHED TO LINEAR PRODUCT RATIO AS FUNCTION OF REACTION-DIFFUSION PATH LENGTH AT 220°C.....	136
FIGURE 5.50:	C5 BRANCHED TO LINEAR PRODUCT RATIO AS FUNCTION OF REACTION-DIFFUSION PATH LENGTH AT 230°C.....	136
FIGURE 5.51:	C5 BRANCHED TO LINEAR PRODUCT RATIO AS FUNCTION OF REACTION-DIFFUSION PATH LENGTH AT 240°C.....	137
FIGURE 5.52:	METHANE SELECTIVITY AS FUNCTION OF MODEL PREDICTED INTRA-PELLET H_2/CO RATIO AT 220°C.....	139

FIGURE 5.53:	METHANE SELECTIVITY AS FUNCTION OF MODEL PREDICTED INTRA-PELLET H_2/CO RATIO AT 230°C.....	139
FIGURE 5.54:	METHANE SELECTIVITY AS FUNCTION OF MODEL PREDICTED INTRA-PELLET H_2/CO RATIO AT 240°C.....	140
FIGURE 5.55:	METHANE SELECTIVITY AS FUNCTION OF REACTION-DIFFUSION PATH LENGTH AT REACTION TEMPERATURE OF 220°C.....	141
FIGURE 5.56:	C5+ SELECTIVITY AS FUNCTION OF REACTION-DIFFUSION PATH LENGTH AT REACTION TEMPERATURE OF 220°C.....	141
FIGURE 5.57:	METHANE SELECTIVITY AS FUNCTION OF REACTION-DIFFUSION PATH LENGTH AT REACTION TEMPERATURE OF 230°C.....	142
FIGURE 5.58:	C5+ SELECTIVITY AS FUNCTION OF REACTION-DIFFUSION PATH LENGTH AT REACTION TEMPERATURE OF 230°C.....	142
FIGURE 5.59:	METHANE SELECTIVITY AS FUNCTION OF REACTION-DIFFUSION PATH LENGTH AT REACTION TEMPERATURE OF 240°C.....	143
FIGURE 5.60:	C5+ SELECTIVITY AS FUNCTION OF REACTION-DIFFUSION PATH LENGTH AT REACTION TEMPERATURE OF 240°C.....	143
FIGURE 5.61:	C3-C8 CHAIN GROWTH PROBABILITY OF STRUCTURED CATALYST AT REACTION TEMPERATURE OF 220°C.....	145
FIGURE 5.62:	C3-C8 CHAIN GROWTH PROBABILITY OF STRUCTURED CATALYST AT REACTION TEMPERATURE OF 230°C.....	146
FIGURE 5.63:	C3-C8 CHAIN GROWTH PROBABILITY OF STRUCTURED CATALYST AT REACTION TEMPERATURE OF 240°C.....	146
FIGURE A.1:	THEMATIC MAPS OF PROVEN NATURAL GAS (LEFT) AND COAL (RIGHT) RESERVES [10 ⁹ BOE].....	169
FIGURE A.2:	THEMATIC MAPS OF GTL INDEX (LEFT) AND CTL INDEX (RIGHT)	169
FIGURE B.1:	RAW TEM IMAGE OF CATALYST S1 (A) CONTRAST ISOLATED IMAGE SHOWING METAL CLUSTER (B) CONTRAST OUTLINED DEFINING BOUNDARY OF METAL CLUSTER (C).....	173
FIGURE B.2:	SEGMENTED TEM IMAGE OF CATALYST S1 (A) CONTRAST ISOLATED IMAGE SHOWING SEGMENTED METAL PARTICLES (B) CONTRAST OUTLINED DEFINING BOUNDARY OF METAL PARTICLES (C).....	173
FIGURE B.3:	NITROGEN PHYSISORPTION ISOTHERMS (LEFT) AND BET ISOTHERMS (RIGHT) OF PURE SILICA SUPPORT	175
FIGURE B.4:	BJH PORE SIZE DISTRIBUTION OF PURE SILICA SUPPORT	176
FIGURE B.5:	TPR H_2 CALIBRATION (LEFT) AND TPO O_2 CALIBRATION (RIGHT) USING NiO	178
FIGURE B.6:	H_2 AND O_2 CALIBRATION CURVES	178
FIGURE B.7:	EXAMPLE OF A TCD SPECTRUM.....	180

FIGURE B.8:	TEMPERATURE AND PRESSURE PROGRAMS USED FOR THE SEPARATION OF VOC IN FID ANALYSIS.....	181
FIGURE B.9:	EXAMPLE OF PRODUCT DISTRIBUTION (U1C) OBTAINED FROM FID ANALYSIS 181	
FIGURE B.10:	EXAMPLE OF A FID SPECTRUM (U1, 120H07M30S)	182
FIGURE C.1:	OPTICAL IMAGE OF DRY SILICA PELLET (A) N-UNDECANE SOAKED PELLETS WITH SURFACE FREE OF N-UNDECANE (B) PELLET COMPLETELY SOAKED IN N-UNDECANE (C).....	186
FIGURE C.2:	EXPERIMENTALLY DETERMINED AMOUNT OF SOLUTION REQUIRED TO FILL PORE VOLUME.....	186
FIGURE C.3:	DVE OF REACTION-DIFFUSION MODEL.....	190
FIGURE D.1:	FLOW DIAGRAM OF FIXED-BED REACTOR SET-UP.....	203
FIGURE D.2:	SCHEMATIC REPRESENTATION OF PELLET PACKING INSIDE THE FIXED-BED REACTOR.....	206
FIGURE D.3:	FISCHER-TROPSCH PERFORMANCE OF CATALYST PELLET U1 AS A FUNCTION OF THE LINEAR GAS VELOCITY IN A FIXED-BED REACTOR AT 220°C, 20BAR AND 80Ml(STP)/MIN/ G_{CATALYST} WITH H_2/CO RATIO OF 2.	208
FIGURE D.4:	CONCENTRATION PROFILE OF A REACTING SPECIES IN THE VICINITY OF A GAS-CATALYST INTERFACE	209
FIGURE D.5:	CO CONCENTRATION DIFFERENCE BETWEEN BULK AND CATALYST SURFACE AS A FUNCTION OF LINEAR GAS VELOCITY	210
FIGURE D.6:	CONCENTRATION PROFILE OF A REACTING SPECIES IN THE VICINITY OF A GAS-WAX-CATALYST INTERFACE.....	211

LIST OF TABLES

TABLE 2-1:	T_{MELT} , $T_{\text{HÜTTIG}}$ AND T_{TAMMAN} OF TYPICAL FISCHER-TROPSCH CATALYST METALS	63
TABLE 4-1:	AMOUNT OF ORGANIC SOLVENT AND DE-IONIZED WATER USED IN THE SYNTHESIS OF EGG-SHELL TYPE OF CATALYSTS	68
TABLE 4-2:	NUMBER OF IMPREGNATION STEPS USED FOR UNIFORM PRECURSOR AND AMOUNT OF ORGANICS LEFT INSIDE THE PRECURSOR IN THE SYNTHESIS OF EGG-YOLK TYPE OF CATALYST.....	69
TABLE 4-3:	DETAILS OF IMPREGNATION SOLUTION AND ORGANIC SOLVENT USED FOR PREPARATION OF EGG-SHELL TYPE OF PRECURSOR AND AMOUNT OF ORGANIC SOLVENT LEFT INSIDE THE PRECURSOR IN THE SYNTHESIS OF EGG-WHITE TYPE OF CATALYSTS.....	70
TABLE 4-4:	OPERATION CONDITION OF THE COLUMNS USED IN GC.....	80
TABLE 5-1:	COBALT METAL CONTENT OF STRUCTURED CATALYST DETERMINED FROM AAS AND TPR-TPO RESULTS	95
TABLE 5-2:	METAL SURFACE AREA AND CATALYST PORE DIAMETER DETERMINED FROM CO CHEMISORPTION AND N_2 PHYSISORPTION.....	96
TABLE 5-3:	EXPERIMENTALLY DETERMINED COBALT CRYSTALLITE SIZE OF STRUCTURED CATALYSTS.....	98
TABLE 5-4:	DEGREE OF REDUCTION DETERMINED FROM TPR-TPO.....	99
TABLE 5-5:	INITIAL DEACTIVATION OF STRUCTURED CATALYST OPERATING AT 220°C BY COMPARING THE CO CONVERSION AT STEADY-STATE (24HRS ONLINE) AND THE CO CONVERSION AT 4 TIMES THE SPACE TIME	109
TABLE 5-6:	STRUCTURAL PARAMETER OF SYNTHESIZED CATALYST AND THEIR EFFECTIVENESS FACTORS AT VARIOUS REACTION TEMPERATURES.....	111
TABLE 5-7:	SUMMARY OF RATE CONSTANTS OF UNIFORM POWDER CATALYST IN MODIFIED SLURRY REACTOR	114
TABLE 5-8:	RATIO OF DIFFUSIVITY OF H_2 OVER CO IN WAX THAT SATISFIES THE KINETIC MODEL CRITERIA	123
TABLE 5-9:	C5 OXYGENATES IN C5 LINEAR HYDROCARBONS AT VARIOUS REACTION TEMPERATURES.....	147
TABLE B-1:	COMPOSITION OF SPURR'S RESIN USED IN ELECTRON MICROSCOPY.....	172
TABLE B-2:	Co_3O_4 PARTICLE SIZE IN [NM] CALCULATED FROM XRD PATTERN USING DEBYE-SCHERRE EQUATION AT VARIOUS MILLER INDICES.....	174
TABLE B-3:	COMPOUND CODES USED FOR FID PEAK IDENTIFICATION	183
TABLE C-1:	VALUES USED FOR THE ESTIMATION OF GAS VISCOSITY AT 220°C.....	187
TABLE D-1:	ESTIMATED SYNTHESIS GAS PROPERTIES AT REACTION CONDITION.....	209

TABLE D-2: SUMMARY OF RESULTS OF UNIFORM PELLETS (U1) TESTS IN FIXED-BED REACTOR SET-UP	212
--	-----

LIST OF SYMBOLS

Symbol	Description	Units
\bar{A}	Arrhenius constant	[s ⁻¹]
$A_{\text{FID},i}$	FID peak area of compound i	[$\mu\text{V s}$]
$A_{\text{FID,ref}}$	FID peak area of reference compound	[$\mu\text{V s}$]
A_{ij}	Surface area between phase i and j	[cm ²]
A_m	Chemisorption active metal area	[m ² /g _{catalyst}]
A_s	Specific cobalt surface area	[atoms/nm ²]
$A_{\text{TCD},i}$	TCD peak area of compound i	[V s]
$A_{\text{TCD},\text{N}_2}$	TCD peak area of N ₂	[V s]
C_{ads}	Concentration of adsorbed gas	[mol/m ³]
C_{CO}	Concentration of CO	[mmol/cm ³]
$C_{\text{CO},s}$	Concentration of CO at the surface of catalyst pellet	[mmol/cm ³]
C_{H_2}	Concentration of H ₂	[mmol/cm ³]
$C_{\text{H}_2,s}$	Concentration of H ₂ at the surface of catalyst pellet	[mmol/cm ³]
C_T	Molar concentration of liquid phase	[mol/m ³]
$C(0)$	Concentration of inlet gas at time 0	[mol/ ℓ]
$C(t)$	Concentration of exit gas at time t	[mol/ ℓ]
D_{AB}	Mutual diffusivity at infinite dilution of A in B	[m ² /s]
D_{CO}	Diffusivity of CO in wax	[m ² /s][cm ² /s]
D_{eff}	Effective diffusivity	[m ² /s]
D_{H_2}	Diffusivity of H ₂ in wax	[cm ² /s]
d	XRD particle diameter	[nm]
d_{core}	Cobalt free silica core diameter / cobalt enriched silica core diameter	[mm]
d_{pellet}	Pellet diameter	[mm]

Symbol	Description	Units
d_{pore}	Pore diameter	[nm]
$d_{(r)}$	Intra-pellet cobalt distribution function	[-]
d_{volume}	Average volume based metal particle diameter	[nm]
d_{white}	Diameter of the outer cobalt enriched boundary of egg-white type of catalyst	[mm]
d_{wire}	Wire diameter	[mm]
E_a	Activation energy	[mmol/s]
F_{CO}	Flow rate of CO	[mmol/s]
F_s	Chemisorption stoichiometry number	[-]
$f_{\text{TCD},i}$	TCD response factor of the inorganic compound i	[-]
$f_{\text{FID},i}$	FID response factor of compound i	[-]
$f_{\text{FID,ref}}$	FID response factor of the reference compound	[-]
G_s	Gibbs surface free energy	[J]
$G_{s,ij}$	Gibbs surface free energy of phase i and j	[J]
$G_{s,1}$	Gibbs surface free energy of wetting scenario 1	[J]
$G_{s,2}$	Gibbs surface free energy of wetting scenario 2	[J]
$\Delta G_{s,1-2}$	Gibbs surface free energy difference between wetting scenario 1 and 2	[J]
H_{CO}	Henry's constant of CO	[bar]
$-\Delta H_{\text{rxn}, 170^\circ\text{C}}$	Heat of reaction at 170°C	[kJ/mol]
$-\Delta H_{\text{rxn}, 250^\circ\text{C}}$	Heat of reaction at 250°C	[kJ/mol]
K_{ads}	Dimensionless CO adsorption constant	[-]
k	XRD shape factor	[-]
k_{ads}	CO adsorption constant	[cm ³ /mmol]
k_c	Mass transfer coefficient	[m/s]
$k_{(r)}$	Cobalt metal surface based rate constant as function of radius position	$\left[\frac{\text{cm}^6}{\text{s m}^2 \text{ mmol}} \right]$

Symbol	Description	Units
k_0	Intrinsic rate constant	$\left[\frac{\text{cm}^6}{\text{s m}^2 \text{ mmol}} \right]$
L	Pore length	[nm]
L_{CO}^0	Cobalt loading of the catalyst	[%]
l_{pellet}	Pellet length	[cm]
M_A	Molar mass of A	[g/mol]
M_B	Molar mass of B	[g/mol]
M_{catalyst}	Mass of catalyst	[g]
M_{CO}	Molar mass of CO	[g/mol]
M_{Co}	Mass of cobalt	[g]
M_{H_2}	Molar mass of H ₂	[g/mol]
M_{sg}	Molar mass of syngas	[g/mol]
N_A	Avogadro's number	[atoms/mol]
$N_{\text{c},i}$	Number of carbon atoms of compound i	[-]
$N_{\text{c,ref}}$	Number of carbon atoms of reference compound	[-]
N_s	Chemisorption accessible active sites	[-]
$\dot{n}_{\text{CO,in}}$	Inlet molar flow rate of CO	[mmol/min]
$\dot{n}_{\text{CO,out}}$	Outlet molar flow rate of CO	[mmol/min]
\dot{n}_i	Molar flow rate of compound i	[mmol/min]
\dot{n}_{N_2}	Molar flow rate of N ₂	[mmol/min]
\dot{n}_{ref}	Molar flow rate of reference compound	[mmol/min]
P	Pressure	[bar]
P_{CO}	Partial pressure of CO	[bar]
P_g	Probability of chain growth	[-]
P_{H_2}	Partial pressure of H ₂	[bar]

Symbol	Description	Units
P_{H_2O}	Partial pressure of H_2O	[bar]
P_{sat}	Condensation pressure	[bar]
P_{sg}	Syngas pressure	[bar]
P_T	Operating pressure	[bar]
Q	Energy flux	[W/cm ³]
R	Ideal gas constant	[Pa m ³ /mol/K]
Re	Reynolds number	[-]
R^o	Degree of reduction	[%]
R_{CO}^*	Reference rate of CO consumption	[mol m ² /s]
R_{volume}	Rate of reaction per unit volume of catalyst	[mmol/s/cm ³]
$-rate_{CO}$	Rate of CO consumption	[mol/s/g _{catalyst}]
$rate_d$	Rate of desorption	[mol/s]
$rate_g$	Rate of chain growth	[mol/s]
r	Catalyst pellet radius	[cm]
$r_{active,i}$	Radius of the inner boundary of the cobalt enriched region	[mm]
$r_{active,j}$	Radius of the outer boundary of the cobalt enriched region	[mm]
r_c	Radius of cobalt free silica core / cobalt enriched core	[mm]
$r_{olefin,primary}$	Primary olefin formation rate	[mmol/s/g]
$r_{olefin,re-adsorb}$	Olefin re-adsorption rate	[mmol/s/g]
r_p	Radius of pellet	[mm]
$r_{paraffin}$	Paraffin formation rate	[mmol/s/g]
r_{pellet}	Radius of pellet	[m]
r_{pore}	Radius of pore	[m]
r_w	Radius of outer boundary of cobalt enriched region of egg-white type of catalysts	[mm]

Symbol	Description	Units
Sc	Schmidt number	[-]
S _{C5+}	C5+ selectivity	[-]
S _{C,i}	Product selectivity of product i on carbon basis	[-]
S _{CO*}	Unit active cobalt metal surface area per silica support	[m ² /g _{silica}]
S _{BET}	BET surface area	[m ² /g]
Sh	Sherwood number	[-]
T	Temperature	[K]
T _{Hüttig}	Hüttig temperature	[K]
T _{melting}	Melting temperature	[K]
T _{Tamman}	Tamman temperature	[K]
T _s	Temperature at the catalyst surface	[K]
t	Statistical thickness of adsorbed film	[-]
t	Thickness of organic layer	[cm]
t	Time	[s]
U	Liner gas velocity	[cm/s]
V _A	Molar volume of A	[cm ³ /mol]
V _{ads}	Volume of physically adsorbed gas	[mℓ/g]
V _{Co}	Volume of cobalt	[mℓ]
V _{core}	Volume of cobalt free silica core	[mℓ/g _{silica}]
V _{mol}	Molar volume	[mℓ/mol]
V _{mono}	Chemisorbed monolayer	[mℓ/g]
V _{organic}	Volume of organics in the silica pellet	[mℓ/g _{silica}]
V _{pellet}	Pellet volume	[mℓ/g _{silica}]
V _{pore}	Pore volume	[mℓ/g _{silica}]

Symbol	Description	Units
W_{CO}	Mass flux of CO	[mmol/s/cm ²]
X_{CO}	CO conversion	[%]
X_N	Mole fraction of product with N carbon atoms	[-]
$X_{ss,220}$	Steady-state CO conversion at 220°C	[%]
X_w	Fraction of pore volume occupied by water	[-]
X_{4t}	CO conversion at 4 times space time	[%]
Greek symbols		
β	XRD line broadening of full width at half maximum intensity	[radian]
β	Prater number	[-]
χ	Structural parameter	[m ⁻¹]
ε	Characteristic energy of interaction between molecules	[-]
ε	Porosity (fraction of void)	[-]
ε_{AB}	Lennard-Jones parameter	[-]
Φ	Thiele Modulus	[-]
Γ	Dimensionless temperature	[-]
φ_B	Association factor of solvent B	[-]
γ_a	Arrhenius number	[-]
γ_{ij}	Surface tension between phase i and j	[dyn/cm ²]
γ_{ov}	Surface tension between organic and air	[dyn/cm ²]
γ_{so}	Surface tension between silica and organic	[dyn/cm ²]
γ_{sv}	Surface tension between silica and air	[dyn/cm ²]
γ_{sw}	Surface tension between silica and water	[dyn/cm ²]
γ_{wo}	Surface tension between water and organics	[dyn/cm ²]
γ_{wv}	Surface tension between water and air	[dyn/cm ²]

Symbol	Description	Units
η	Effectiveness factor	[-]
η'	Experimentally determined effectiveness factor	[-]
η'_{220}	Experimentally determined effectiveness factor at 220°C	[-]
η'_{230}	Experimentally determined effectiveness factor at 230°C	[-]
η'_{240}	Experimentally determined effectiveness factor at 240°C	[-]
κ	Boltzmann constant	[K ⁻¹]
κ_t	Thermal conductivity	[W/m/K]
λ	XRD X-ray wavelength	[nm]
λ	Dimensionless catalyst radius	[-]
μ	Viscosity	[g/cm/s]
μ_B	Viscosity of B	[g/cm/s]
ρ_{CO}	Density of CO	[g/ml]
ρ_{Co}	Density of cobalt	[g/ml]
ρ_{CO^*}	Average metal surface density of active cobalt	[m ² /cm ³]
ρ_{H_2}	Density of H ₂	[g/ml]
ρ_m	Catalyst metal density	[atoms/m ²]
ρ_{sg}	Density of syngas	[g/ml]
ρ_{silica}	Unit volume of silica support	[ml/g]
ρ_{total}	Total metal density of catalyst	[g/ml]
θ	XRD diffraction angle	[°]
θ_o	Contact angle of organic on silica	[°]
θ_w	Contact angle of water on silica	[°]
σ	Characteristic diameter of gas molecule	[Å]
σ_{AB}	Lennard-Jones parameter	[-]

Symbol	Description	Units
$\sigma_{\text{egg-shell}}$	Metal density function of egg-shell type of catalysts	[-]
$\sigma_{\text{egg-white}}$	Metal density function of egg-white type of catalysts	[-]
$\sigma_{\text{egg-yolk}}$	Metal density function of egg-yolk type of catalysts	[-]
$\sigma_{\text{structure}}$	Structure specific metal density function	[-]
σ_{uniform}	Metal density function of uniform catalysts	[-]
τ	Space time	[s]
τ	Tortuosity	[-]
ν	Kinematic viscosity	[s/cm ²]
ψ	Diffusivity reactive parameter	[m]
ψ_{CO}	Dimensionless CO concentration	[-]
ψ_{H_2}	Dimensionless H ₂ concentration	[-]
Ω_{μ}	Coefficient of viscosity	[-]

1 INTRODUCTION

Mankind is continuously striving for better energy sources and improved conversion processes to sustain growth and bringing higher order to the state of living. Hydrocarbons are currently the main energy source contributing 87.9% towards the global primary energy consumption (BP, 2007). They can be found in the form of coal, natural gas and crude oil. Crude oil contributes 35.8% towards the global primary energy consumption. It has a higher energy density than natural gas ($37000\text{kJ/g}_{\text{crude oil}}$ versus $54\text{kJ/g}_{\text{natural gas}}$ (EIA, 2008)), and is easier to combust than coal, making it the preferred fuel for transport vehicles. However, crude oil reserves are not equally distributed and are concentrated in the Middle East. As a result, the rest of the world relies on oil imports. This dependency can be reduced by processes converting natural gas, coal or other carbon-containing materials into liquid fuels. These technologies would be attractive to countries which are largely dependent on oil imports.

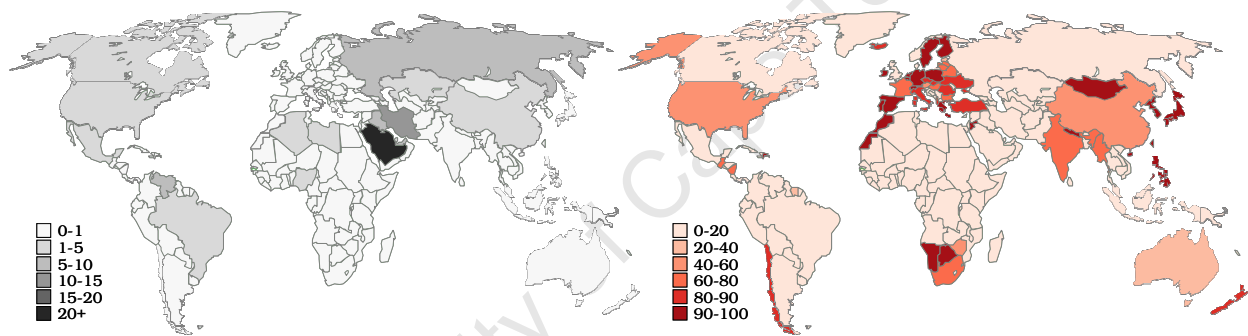


Figure 1.1: Distribution of proven crude oil reserve as at 1 January 2008 [%] (left) ; Percentage of crude oil consumption from oil imports (right), (CIA, 2008)

There are various technologies for the production of liquid fuels, for example

- liquefying natural gas (Cook, 2005)
- hydrogenation of coal - Bergius process (Bergius, 1932)
- carbonization of coal - Karrick process (Karrick, 1942)
- indirect liquefaction of coal, natural gas and biomass via Fischer-Tropsch process
- trans-esterification of vegetable oil or animal fat - biodiesel (Huber *et al.*, 2006)

The Fischer-Tropsch process is the only commercially applied process which is economically viable for the production of high purity liquid fuel on a large scale. The oldest, still operating Fischer-Tropsch plant (Sasol I) using coal as a feedstock was commercialised in South Africa in 1955. It served as a tool for liquid fuel independency for the country, during the economical sanctions of apartheid era (1948-1990) in South Africa. Sasol I demonstrated to the world the economical feasibility of

this process at crude oil price greater than 20\$ per barrel (Rostrup-Nielsen, 1994; Jager, 1998; Vosloo, 2001), during the years of oil crisis (1973-1986). It spurred a tremendous growth in process and catalyst development for the Fischer-Tropsch process. Furthermore, the crude oil price hike (Figure 1.2) during the past decade has encouraged the commercial developments in countries with large natural gas or coal reserves. The unstable crude oil prices are driving more countries to focus on alternative liquid fuels. China, for example, is prepared to invest more than 40 billion US\$ in CTL (Wu, 2006) as part of their national energy strategy. Currently, there are 3 operating commercial GTL plants and 2 under construction (see Figure 1.3) and 2 existing commercially operating CTL plants, viz. Sasol I (Sasolburg, South Africa; and Sasol II-III (Secunda, South Africa)) (see Figure 1.4) worldwide that are based on Fischer-Tropsch synthesis (see Appendix A.1). However, more commercially operating GTL-CTL plants are in the design phase, although the realisation might be retarded in the current economic environment. It can nevertheless be concluded that the Fischer-Tropsch process will play a major role in the production of liquid fuels until the end of the carbon based energy paradigm.

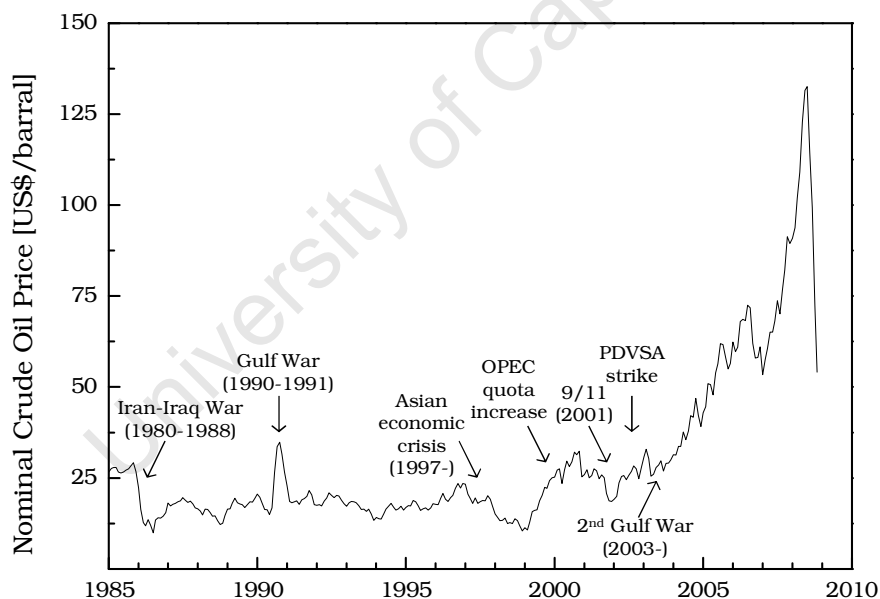


Figure 1.2: Nominal Crude Oil Price for the past 15 years [US\$/barrel], (IMF, 2008)

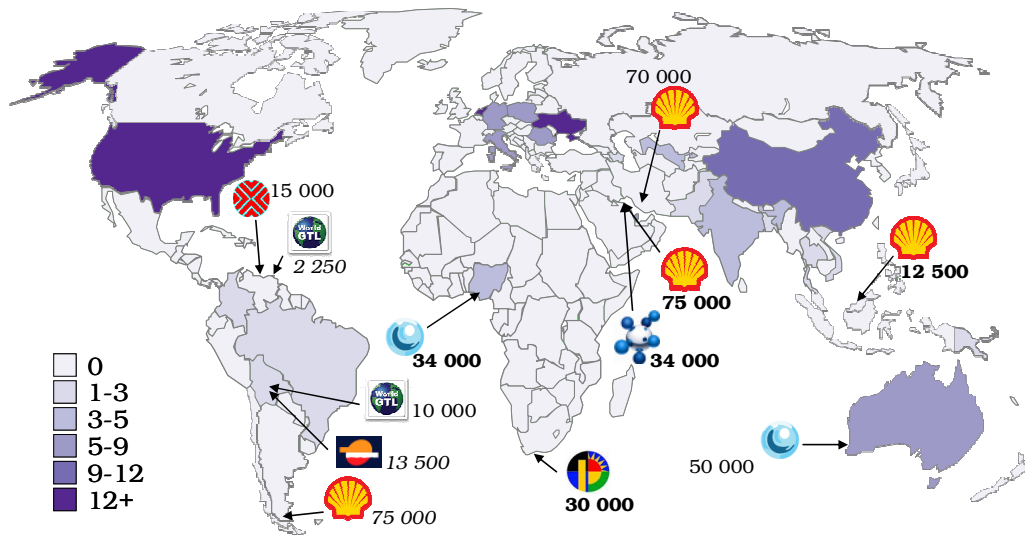


Figure 1.3: Geographical location of commercial GTL plants represented by its company logo on GTL potential index map (existing plant in bold, future plant in timid, planned plant in italic), plant size in [bpd], (WERGY, 2005)

Note: The Shell plant in Qatar and Sasol-Chevron plant in Nigeria are still under construction.

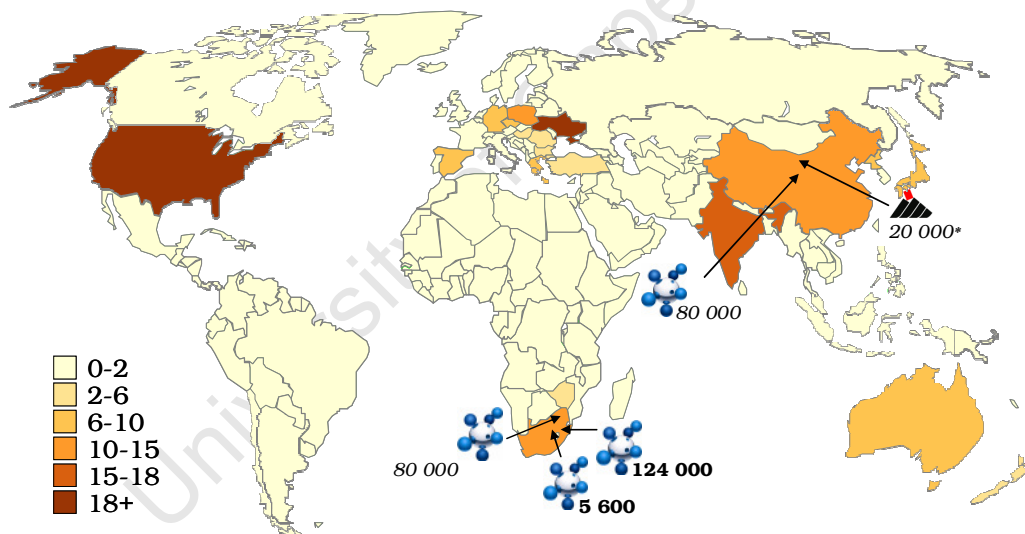


Figure 1.4: Geographical location of commercial CTL plants represented by its company logo on CTL potential index map (existing plant in bold, planned plant in italic), plant size in [bpd] (* Bergius-pier process), (WERGY, 2005)

The Fischer-Tropsch process consists of three major steps (see Figure 1.5), viz. synthesis gas generation, Fischer-Tropsch synthesis, and product work-up and separation (Dry, 2004a). In the synthesis gas production stage, carbon-containing raw materials are converted into a mixture of H_2 and CO (synthesis gas) via partial oxidation, steam reforming or gasification. This mixture of syngas is then converted to a wide range of hydrocarbons in the Fischer-Tropsch synthesis. The product mixture is subsequently converted into fuels (e.g. using hydrocracking for diesel production).

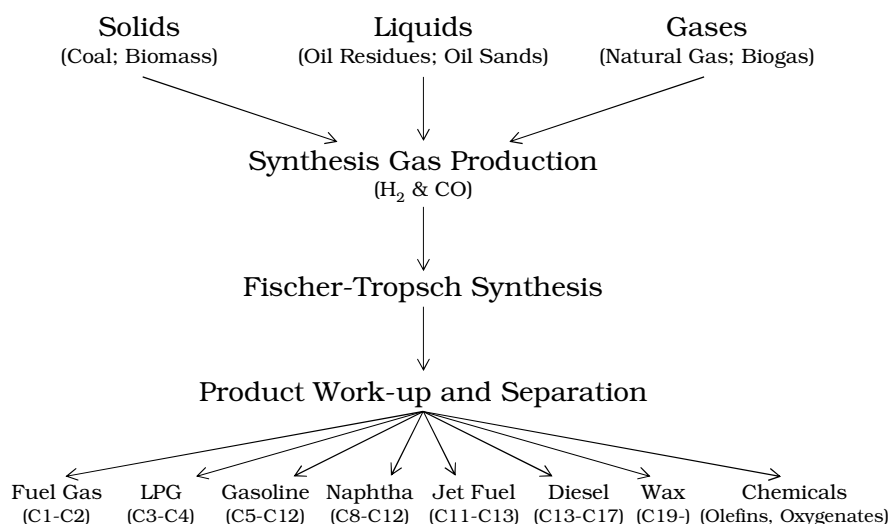


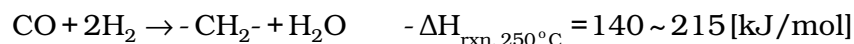
Figure 1.5: Overview of liquefaction process via Fischer-Tropsch synthesis

The Fischer-Tropsch synthesis will always produce a mixture of products ranging from C1 to C100+, due to the polymerization nature of the reaction. At ambient conditions, products with carbon number greater than 5 (C5+) are in liquid phase. Hence the C5+ product selectivity of the Fischer-Tropsch synthesis needs to be maximised to increase the process efficiency in terms of liquefaction. Thus the aim of this thesis is to contribute to the knowledge of tuning the Fischer-Tropsch product selectivity by modifying the structure of the catalyst.

2 LITERATURE REVIEW

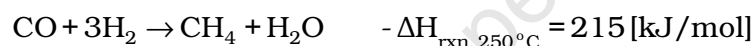
2.1 Fischer-Tropsch Synthesis

The Fischer-Tropsch synthesis is an exothermic polymerisation reaction occurring on a metallic catalyst, which can be represented as



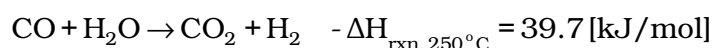
The heat of reaction depends on product distribution obtained (Claeys and van Steen, 2005). The Fischer-Tropsch synthesis yields predominately linear n-paraffins and n-olefins-(1), and smaller amounts of oxygenates such as alcohols and aldehydes. A minor quantity of methyl-branched products is also formed in the Fischer-Tropsch synthesis.

Methanation is thermodynamically the most favoured reaction (Schulz and Cronjé, 1977; Anderson, 1984). The formation of other products is less preferred. The broad product spectrum obtained in the Fischer-Tropsch synthesis shows that the reaction is kinetically controlled.



Hydrogen and carbon monoxide are utilised in the Fischer-Tropsch synthesis in a molar ratio of approximately 2 to 1. Hence the commercial operation which typically includes recycle would require a feed composition to the Fischer-Tropsch synthesis with a H_2/CO ratio equals 2 (Espinoza *et al.*, 2004). Furthermore, an increase in H_2/CO ratio would favour methane formation and increase primary paraffin selectivity (Claeys *et al.*, 2004), hence reducing the selectivity for C5+. A lower H_2/CO feed ratio may favour coke formation and increase primary olefin selectivity.

The water-gas-shift reaction takes place simultaneously on iron-based catalysts, while cobalt-based catalysts show negligible water-gas-shift activity. This allows iron-based catalysts to be used for H_2/CO feed ratio lower than 2 (Govender *et al.*, 2006), such as feed gas originating from coal.



Another reaction that can take place under Fischer-Tropsch conditions is the Boudouard reaction, which causes catalyst deactivation through deposition of carbon.



2.2 General Overview of Reactors

2.2.1 Fixed-bed Reactor

The easiest and by far the most common way to carry out any heterogeneously catalysed reaction (such as the Fischer-Tropsch synthesis) is by passing a fluid over a fixed catalyst bed, a fixed-bed reactor. A typical fixed-bed reactor is filled with catalyst pellets having sizes in the range of 1-3mm (Davis, 2005). The catalyst pellets are packed to minimise the pressure drop over the catalyst bed and the variation of gas flow along the radius of the reactor. Typical pellet shapes are spheres, cylinders, rings, flat disc pellets or crushed material of a certain sieve fraction.

An example of a commercial fixed-bed reactor is the ARGE fixed-bed reactor for Fischer-Tropsch synthesis commissioned at Sasol in 1955 by the Ruhrchemie and Lurgi Company. The reactor consists of 2050 vertical tubes of 2inch×12m, which are filled with pellets of iron-based catalysts (Dry, 1996).

The advantages of using the fixed-bed reactor are

- Ease of operation (Dry, 1996)
- Ease of catalyst-product separation (Espinoza *et al.*, 1999)
- Suitability for operation in the low and high temperature mode (Schulz, 1999)

The disadvantages of fixed-bed reactor are

- High-pressure drop over the reactor
- High temperature gradient (compared to other types of reactors)
- Tediousness of the replacement of spent catalyst (Dry, 1996)

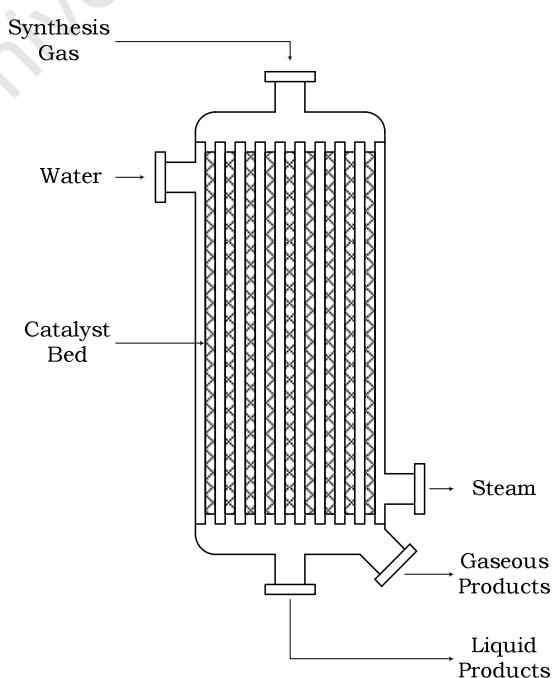


Figure 2.1: Schematic representation of an industrial fixed-bed reactor

2.2.2 Fluidised-bed Reactor

In the fluidized-bed reactor the catalyst particles are suspended by the fluid stream. The weight of the catalyst particle is balanced by the force of the upward stream of gas or liquid. In many respects, the fluidized bed behaves as a liquid. This is an advantageous feature of the fluidised bed reactor, as there is excellent gas-solid contact in the bed, good gas-solid heat and mass transfer, and high bed-wall and bed-internals heat-transfer coefficients (Werther, 2008). There are two types of fluidised-bed reactors used in the Fischer-Tropsch synthesis (Steynberg *et al.*, 1999), namely circulating fluidised-bed reactor and fixed fluidised-bed reactor. In the circulating fluidised-bed, the catalysts particles (40-150 μm) are carried by the high velocity synthesis gas flowing upward the reactor tube (Sie and Krishna, 1999). The catalyst re-enters the hopper with the gas and it is separated by means of cyclones (Steynberg *et al.*, 1999). The heat of reaction is removed from the reactor by cooling coils generating steam. The linear gas velocity in the circulating fluidised-bed is three to four times higher than in fixed fluidised-bed (Dry, 2004b).

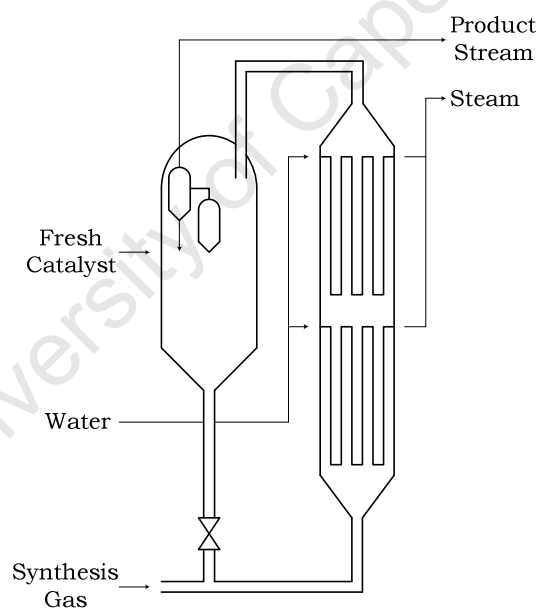


Figure 2.2: Schematic representation of an industrial circulating fluidised-bed reactor

The catalyst in the fixed fluidised-bed reactor is not transported in the system (unlike the circulating fluidised-bed reactor). The high flow rate of the synthesis gas entering the reactor keeps the catalyst particles suspended. Cyclones are used to separate the catalyst fines from the gaseous product stream (Steynberg *et al.*, 1999).

The fixed fluidised-bed reactor has many advantages over the circulating fluidised-bed reactor (Sie and Krishna, 1999)

- Physically smaller with the same production capacity
- Less costly to construct
- Easier to scale-up
- Simpler to operate

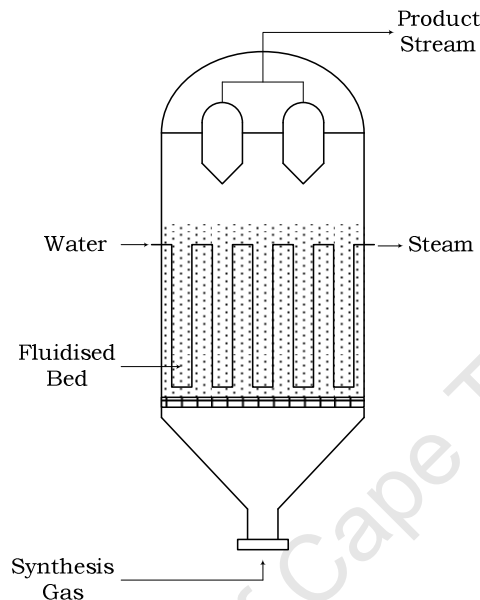


Figure 2.3: Schematic representation of an industrial fluidised-bed reactor

Fluidised bed reactors are only utilised for high temperature mode Fischer-Tropsch synthesis (Steynberg *et al.*, 1999), since the formation of a liquid phase under operation conditions must be avoided to maintain a fluidized bed. The types of operating temperature mode of Fischer-Tropsch synthesis will be discussed further in section 2.8.

2.2.3 Slurry-bed Reactor

An intense and intimate contact between gas phase, liquid phase, and the finely dispersed catalyst particles is achieved in slurry reactors. The catalyst is suspended in the liquid medium by either mechanical or gas induced agitation. A high catalyst loading is used in industrial practice, and the liquid phase is usually an organic liquid (Werther, 2008). The liquid medium can either be an inert medium or the product. Particle size is typically between 50 and 170 μm (Malherbe, 2006). The use of finer catalyst particles with diameters in the range of 2 to 50 μm would allow the particles to be suspended in the liquid phase without re-circulating the liquid flow, but these fine particles are difficult to separate from the liquid products.

Sasol developed a slurry reactor for the Fischer-Tropsch synthesis with iron-based or cobalt-based catalyst, in which fine catalyst powder is suspended in wax. Synthesis gas is distributed at the bottom and rises through the slurry, providing agitation to keep the catalyst in suspension. A special technique for the slurry reactor of catalysts-wax separation was developed for slurry reactor (Davis, 2002). Currently, the slurry-bed reactor operating in the low temperature mode is regarded as the most efficient reactor for the Fischer-Tropsch synthesis (Schulz, 1999).

Some of the advantages of slurry reactors over the fixed-bed reactor are

- Efficient catalyst utilisation (due to the absence of mass transfer limitation)
- Easier control of reaction temperature
- Easier catalyst replacement

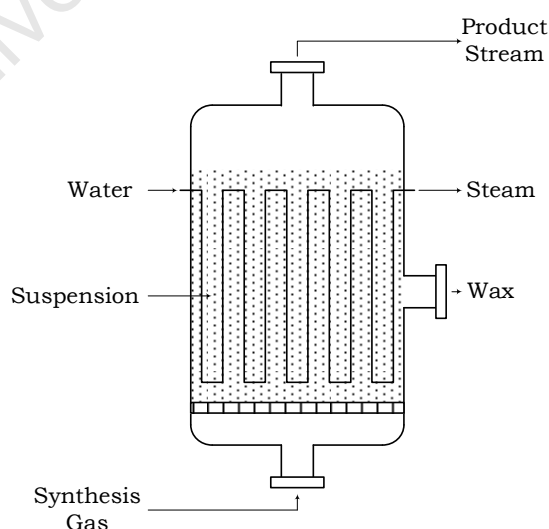


Figure 2.4: Schematic representation of an industrial slurry reactor

2.3 Catalysts for the Fischer-Tropsch Synthesis

2.3.1 Metal Type

All group VIII metals have the ability to catalyse the Fischer-Tropsch synthesis. Amongst them, ruthenium, iron, nickel and cobalt are the most active transition metals (Vannice, 1975b). The ability of these metals to adsorb CO dissociatively makes them suitable for Fischer-Tropsch synthesis (Vannice, 1975a).

Ruthenium is the most active amongst the studied transition metals. The Fischer-Tropsch synthesis can take place over ruthenium at temperature as low as 150°C. However, the high price and the scarce availability limit the use of ruthenium to academic studies.

Fischer-Tropsch synthesis using nickel is highly selective towards methane. Nickel is therefore not commercially applied.

Iron and cobalt are the only metals used for industrial application. Iron is cheaper than cobalt, although the life time of iron catalyst in industrial application is about 8 weeks (Dry, 1981). Iron-based catalyst show water-gas-shift activity and can therefore handle H_2/CO feed ratio less than 2 (Govender *et al.*, 2006), making it the preferred metal for synthesis gas generated from coal. The Fischer-Tropsch product obtained over iron-based catalyst contains larger amounts of olefins and oxygenates, which can be used as chemicals or solvents.

Cobalt-based catalyst are more active than iron-based catalyst (Li *et al.*, 2002) and have a life time of 5 years (Schulz, 1999), but they are more expensive than iron-based catalyst (Dry, 1990). A long catalyst life is required to compensate for the high cost of cobalt. Hence catalyst stability is an important feature in cobalt catalyst design and operation of cobalt-based Fischer-Tropsch reactors. Cobalt does not show any significant activity for the water-gas-shift reaction. It is therefore suitable for hydrogen rich feed such as ones derived from natural gas. The Fischer-Tropsch synthesis over cobalt-based catalysts is not inhibited by water (Yates and Satterfield, 1991) in contrast to the Fischer-Tropsch synthesis over iron-based catalysts (Huff and Satterfield, 1984). Thus, a high conversion per pass can be achieved in the Fischer-Tropsch synthesis over cobalt-based catalysts (van Berge, 1997). Cobalt is also known for its high affinity for olefins (Schulz and Claeys, 1999b), which increases α -olefin re-adsorption on to active site. The re-adsorbed α -olefin may act as a chain growth initiator and grows further, which may result in an enhanced C5+ selectivity.

2.3.2 Promoters

Various types of promoters can be added to the catalyst to enhance its structural integrity, surface area, thermal and chemical stability. However, interaction between support and metal may occur and may reduce the activation of the catalyst precursor (Tauster *et al.*, 1978; Ioannides and Verykios, 1993).

In contrast to the iron-based catalyst, cobalt contains fewer promoters. For example, potassium promotion of cobalt-based catalyst results in a decrease in the Fischer-Tropsch activity (Kazansky *et al.*, 1988; Liu, 1992; Blekkan *et al.*, 1993).

Alumina and silica are examples of structural promoters/support materials. All commercial cobalt catalysts utilise a structural support to maximise its use required due to the high price of cobalt.

Platinum, palladium and ruthenium may be used as reduction promoters. They facilitate the reduction via hydrogen spill-over (Haggin, 1991).

2.4 Preparation of Catalysts

There are two major groups of catalysts, namely unsupported catalyst and supported catalyst. The catalyst preparation methods for unsupported catalysts include fusion, sol-gel, micro-emulsion and precipitation. The catalyst preparation methods for supported catalysts include deposition-precipitation, impregnation, ion-exchange and grafting. Cobalt-based Fischer-Tropsch catalysts are typically prepared using impregnation.

Impregnation method can be classified as wet impregnation (diffusional) and dry impregnation (capillary or incipient wetness). The wet impregnation involves wetting of a pre-shaped support pellet/powder with a solvent prior to impregnation. Usually, the pore volume of the support is filled with the same solvent as the impregnation solution. The precursor salt migrates progressively from the solution into the centre of the support. The driving force at all times is the concentration gradient between the extra-pellet solution and the advancement front of the soluble precursor in the intra-pellet solution. The migration time depends on the diffusivity of the precursor salt in wetting solvent. After the migration is completed, the impregnated support is then dried to remove the moisture in the support, leaving the metal as a metal salt. This catalyst precursor then exposed to elevated temperatures to convert the metal salt into the metal oxides; this process is referred as calcination. The activation of calcined catalyst involves reduction of the metal oxide to the metal.

The difference between the dry impregnation method and wet impregnation is that the pore volume of the support contains only ambient air at the start of the impregnation process. Usually, the amount of impregnation solution used in the dry impregnation method matches the pore volume of the pre-shaped support material. The replacement of the solid-gas interface by a solid-liquid interface generally causes a considerable decrease in the free enthalpy of the system, which causes a release of heat (Che *et al.*, 1997). As soon as the support is placed in contact with the solution, the solution penetrates the pores. Part of the air present in the pore volume will be imprisoned and compressed under the effect of capillary forces. The pressure developed inside the imprisoned gas bubbles depends on the radii of the curve of the liquid-gas menisci. Considerable forces will thus be exerted on the pore walls in contact with these bubbles. The walls that are not strong enough will break down, causing a degradation of the mechanical properties, sometimes even bursting of catalyst pellets.

The dry impregnation method is suitable for controlling metal loading onto the support material, while the pH of the impregnation solution can be varied using the wet

impregnation method. High metal loading with uniform dispersion of metal on support can be achieved with this method (Dry, 1981; Anderson, 1984; Adesina, 1996).

Ion exchange is a process which may occur during impregnation (van Steen *et al.*, 1996). The principle of ion exchange is an electrostatic interaction of the charge of the surface of the support with the ionic species in the solution. Equilibrium will be established between the ions in the solution and the support surface (Che *et al.*, 1997). The position of this equilibrium will be dependent on the nature of the support and on the pH of the impregnation solution.

University of Cape Town

2.5 Intrinsic Activity of the Fischer-Tropsch Synthesis

The kinetics of the Fischer-Tropsch synthesis depends on the catalyst metal and promoters and support. For example, the performance of iron catalysts is very dependent on the extent of alkali promotion. Not only product selectivity is strongly dependent on the amount of alkali promoter present, it also has an effect on the overall rate of the reaction (Dry, 2004a). Various kinetic expressions have been proposed to describe the rate of the Fischer-Tropsch reactions over iron-based catalyst:

$$-\text{rate}_{\text{CO}} = aP_{\text{H}_2}^{0.6}P_{\text{CO}}^{0.4} - b^{0.5}P_{\text{H}_2\text{O}}^{0.5} \quad \text{Anderson and Karn, 1960}$$

$$-\text{rate}_{\text{CO}} = \frac{aP_{\text{CO}}P_{\text{H}_2}}{(P_{\text{CO}} + bP_{\text{H}_2\text{O}})} \quad \text{Dry, 1976}$$

$$-\text{rate}_{\text{CO}} = \frac{aP_{\text{CO}}P_{\text{H}_2}^2}{(P_{\text{CO}}P_{\text{H}_2} + bP_{\text{H}_2\text{O}})} \quad \text{Huff and Satterfield, 1984}$$

$$-\text{rate}_{\text{CO}} = \frac{aP_{\text{CO}}P_{\text{H}_2}}{(P_{\text{CO}} + bP_{\text{H}_2\text{O}} + cP_{\text{CO}_2})} \quad \text{Ledakowicz *et al.*, 1985}$$

The proposed kinetic expressions illustrate the negative effect of water on the rate of the Fischer-Tropsch synthesis over iron-based catalysts. This effect is probably due to the fact that iron is sensitive to oxidation by water vapor. Thus, a higher H_2O partial pressure will lead to a higher occupancy of surface iron sites by oxygen species. This lowers the amount of active sites available for the Fischer-Tropsch synthesis.

Contrary to the kinetic expressions for the Fischer-Tropsch synthesis over iron-based catalysts, water does not seem to inhibit the rate of the Fischer-Tropsch synthesis over cobalt-based catalyst:

$$-\text{rate}_{\text{CO}} = \frac{aP_{\text{H}_2}^2}{P_{\text{CO}}} \quad \text{Brotz, 1949}$$

$$-\text{rate}_{\text{CO}} = \frac{aP_{\text{CO}}P_{\text{H}_2}^2}{(1 + bP_{\text{CO}}P_{\text{H}_2}^2)} \quad \text{Anderson, 1956a}$$

$$-\text{rate}_{\text{CO}} = \frac{aP_{\text{CO}}P_{\text{H}_2}^{0.5}}{(1 + bP_{\text{CO}} + cP_{\text{H}_2}^{0.5})^2} \quad \text{Sarup and Wojciechowski, 1989}$$

$$-\text{rate}_{\text{CO}} = \frac{aP_{\text{CO}}P_{\text{H}_2}}{(1 + bP_{\text{CO}})^2} \quad \text{Yates and Satterfield, 1991}$$

$$-\text{rate}_{\text{CO}} = \frac{a(P_{\text{H}_2}^{3/2}P_{\text{CO}}/P_{\text{H}_2\text{O}})}{(1 + b(P_{\text{H}_2}P_{\text{CO}}/P_{\text{H}_2\text{O}}))^2} \quad \text{van Steen and Schulz, 1999}$$

$$-\text{rate}_{\text{CO}} = \frac{aP_{\text{CO}}P_{\text{H}_2}}{(P_{\text{CO}} + bP_{\text{H}_2\text{O}})} \quad \text{van der Laan and Beenackers, 1999}$$

Metallic cobalt is much more resistant to oxidation than iron. Therefore the metal surface coverage by oxygen/water will be comparatively lower with cobalt than with iron. This might be the reason for the absence of water partial pressure in the reaction expression. The rate expression proposed by Yates and Satterfield (1991) is often cited as a suitable rate expression for cobalt-based Fischer-Tropsch synthesis.

University of Cape Town

2.6 Mechanism of the Fischer-Tropsch Synthesis

Although the mechanism of the Fischer-Tropsch synthesis is still debatable, it is widely accepted that the following key steps are essential for product formation (Claeys *et al.*, 2004).

- (Dissociative) adsorption of reactant gases
- Generation of chain growth monomer
- Generation of chain initiator
- Chain growth through propagation
- Chain growth termination through desorption

The most accepted reaction mechanisms for Fischer-Tropsch synthesis are discussed below. The Fischer-Tropsch synthesis is most likely to occur via various mechanisms operating in parallel.

2.6.1 Alkyl Mechanism

Fischer and Tropsch (1926) proposed the carbide mechanism based on the observation of carbide formation with iron-based catalysts. This mechanism was adapted by many researchers (Ponec and van Barneveld, 1979; Brady and Pettit, 1980; Brady and Pettit, 1981; van Barneveld and Ponec, 1984; Zheng *et al.*, 1988; De Koster and van Santen, 1991; Ciobîcă *et al.*, 2002) to become the widely accepted alkyl mechanism. This mechanism starts with the dissociative chemisorption of CO on the metal surface, from which surface carbon and surface oxygen are formed. The surface oxygen can either be removed as water by reacting with adsorbed surface hydrogen, or be removed as CO₂ by reacting with an adsorbed CO. Surface carbon may undergo sequential hydrogenation to form a surface methyldene (CH), surface methylene (CH₂) and surface methyl (CH₃) species. The surface methylene (CH₂) species is regarded as the monomer in the Fischer-Tropsch synthesis. The surface methyl (CH₃) surface species is regarded as the chain initiator, which can react with surface hydrogen to yield methane or react with a monomer to initiate chain growth. Chain growth termination may occur through β -hydrogen elimination yielding α -olefins or hydrogenation yielding n-paraffins as primary product compounds. This mechanism may describe the primary formation of alcohols through the involvement of surface hydroxyl species (Johnson *et al.*, 1991).

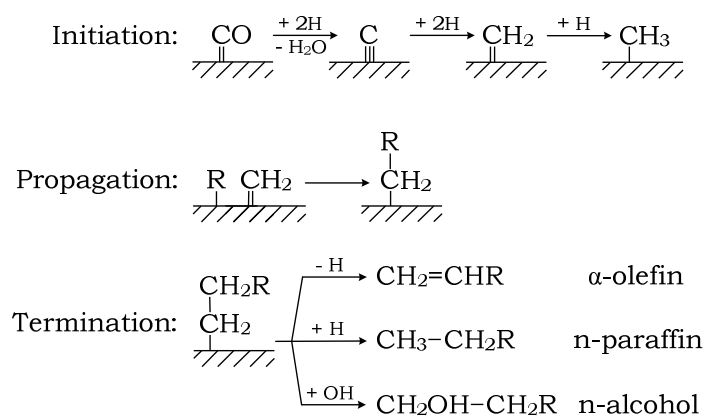


Figure 2.5: Schematic representation of the alkyl mechanism

2.6.2 Alkenyl Mechanism

Maitlis *et al.* (1999) proposed an alternative reaction pathway to describe primary formation of olefins in the Fischer-Tropsch synthesis. The monomer in this mechanism is the same as in the alkyl mechanism, viz. a surface methylene (CH_2) species. The monomer reacts with a surface methyldiene (CH) species forming a C-C bond. This results in the formation of a surface vinyl ($\text{CH}=\text{CH}_2$) species, which is considered to be the chain initiator. Chain propagation is thought to be the reaction of the monomer with the chain initiator yielding a surface allyl species, which isomerises to yield a surface vinyl or alkenyl species. Chain termination may occur via hydrogenation of a surface alkenyl species yielding α -olefins. This mechanism can not explain the primary formation of n-paraffins nor oxygenates.

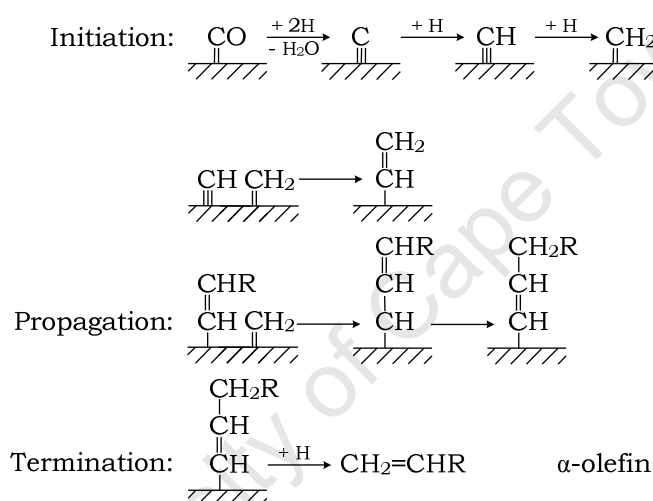


Figure 2.6: Schematic representation of the alkenyl mechanism

2.6.3 Enol Mechanism

Storch *et al.* (1951) proposed the enol mechanism, in which an enol species ($M=CHOH$) plays the role as the chain initiator and the main monomeric species. The generation of the monomer involves the reaction of chemisorbed CO with surface hydrogen. The propagation of chain growth takes place through condensation of two neighbouring enol species. The addition of surface hydrogen to the enol species leads to chain termination as oxygenates or α -olefins. Formation of n-paraffins in this mechanism is described as a secondary reaction by hydrogenation of primarily formed olefins.

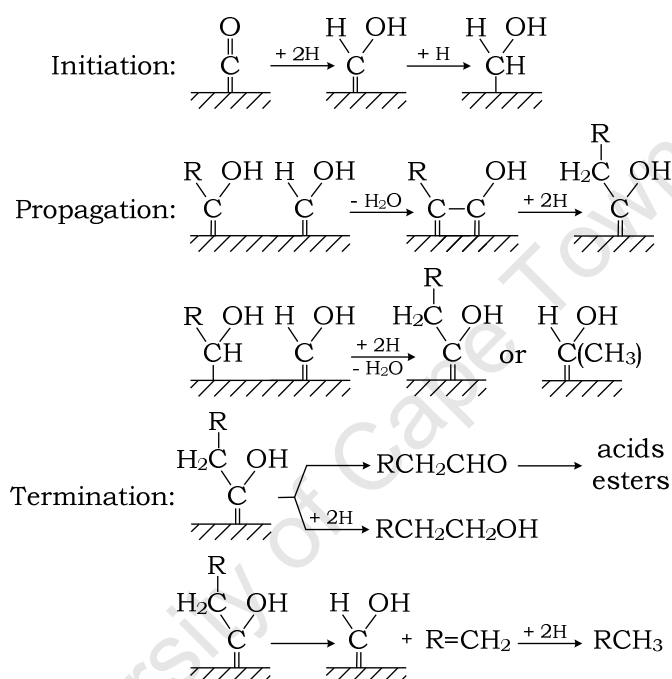


Figure 2.7: Schematic representation of the enol mechanism

2.6.4 CO-Insertion Mechanism

The CO-insertion mechanism was originally proposed by Sternberg and Wender (1959), and subsequently further refined by Pichler and Schulz (1970). This mechanism is often believed to be the main reaction pathway leading to the formation of oxygenates in Fischer-Tropsch synthesis (Hindermann *et al.*, 1993). Chemisorbed CO is considered as the monomeric species, while surface alkyl species is considered as the chain initiator. The propagation of chain growth takes place through CO-insertion in a methyl-alkyl bond leading to a surface acyl species. Hydrogen assisted cleavage of the carbon-oxygen bond leads to longer chain alkyl species. Termination of chain growth may happen in various ways. Desorption of these species as proposed in the alkyl mechanism leads to the formation of α -olefins or n-paraffins. Formation of aldehydes and alcohols may occur by similar desorption pathways of oxygen containing surface species.

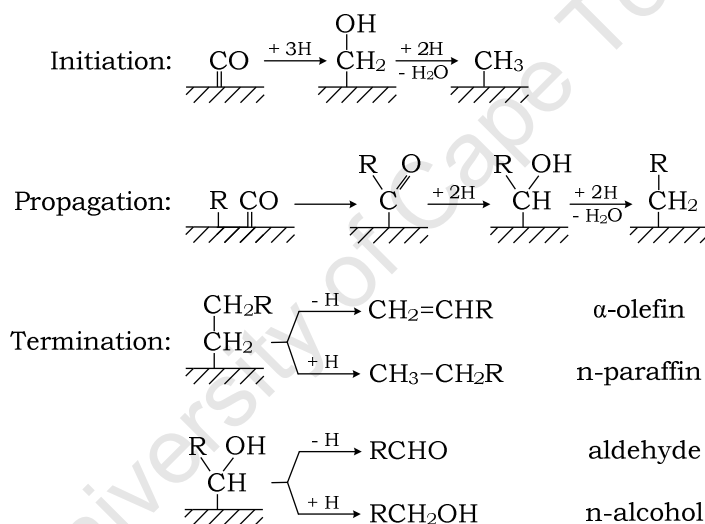


Figure 2.8: Schematic representation of the CO insertion mechanism

2.7 Fischer-Tropsch Product Distribution

The Fischer-Tropsch synthesis is very similar to a polymerisation reaction (Shultz *et al.*, 1962), since the selectivity patterns as a function of the carbon number suggests a strict kinetic basis of surface polymerisation with stepwise addition of C1 monomer species. This ideal polymerisation can be described by considering the formation of a single product (Herington, 1946). The co-adsorption of CO and H₂ on the surface leads to the formation of the monomeric species and a chain initiator, Sp₁. This surface species with a single carbon atom (Sp₁) can either desorb to form a product molecule (Pr₁) with single carbon atom (e.g. methane) or grow further to a surface species with 2 carbon atoms (Sp₂). This surface specie (Sp₂) can either desorb yielding a product molecule (Pr₂) or grow further. This process can be repeated indefinitely yielding surface species with N carbon atoms (Sp_N) and product molecules with N carbon atoms (Pr_N). The probability of chain growth (P_g) can be defined as the rate of desorption over the combined rate of desorption and chain growth.

$$P_g = \frac{\text{rate}_g}{\text{rate}_g + \text{rate}_d}$$

A mass balance around surface species with N carbon atoms (Sp_N) at steady state yields

$$\log(X_N) = N \log(P_g) + \log \frac{(1 - P_g)}{P_g}$$

where X_N is the mole fraction of products with N carbon atoms in the fraction of organic product compounds, and N is the carbon number. This is commonly referred as the Anderson-Schulz-Flory kinetics (Schulz, 1930; Flory, 1936). The polymerisation character of the Fischer-Tropsch synthesis implies that this reaction is not selective towards any product.

The experimentally determined Fischer-Tropsch synthesis product distributions deviate from the theoretical Anderson-Schulz-Flory model. Typically, a higher than expected methane selectivity is observed, which might be caused by methane formation through hydrogenation of CO on different catalytically site (Schulz *et al.*, 1995). A lower than expected selectivity for C₂ is observed. This is thought to originate from the high reactivity of ethene leading to incorporation of ethene into grown chains (Schulz *et al.*, 1999). Other α-olefins may also re-adsorb on the surface of the catalyst and initiate secondary chain growth, in other words acting as a chain growth initiator (Claeys *et al.*, 2004).

Secondary chain growth initiated by re-adsorbed olefins would result in a shift of the Fischer-Tropsch product selectivity towards longer chain hydrocarbons. Thus an

increase in the probability of chain growth with increasing carbon number is often observed (Puskas and Hurlbut, 2003). Hydrogenation of re-adsorbed yielding a paraffin with the same carbon number or double-bond isomerisation to an olefin with an internal double bond will not result in a change of the probability of chain growth. Secondary chain growth of re-adsorbed α -olefins may result in the formation of branched product molecules. However, this reaction is thought to be sterically hindered and suppressed (Schulz and Claeys, 1999b). Jordan and Bell (1987) investigated the co-feeding of 1-butene in the hydrogenation of CO. It was found that the adsorbed α -olefin is likely to act as a chain growth initiator rather to be inserted into a growing chain. They concluded that the efficiency of the olefin in producing chain growth initiator decreases with increase in carbon number (i.e. $C_2H_4 > C_3H_6 > C_4H_8$). However, the likelihood for re-adsorption is believed to increase with increasing carbon number due to an increase in the solubility (Schulz and Claeys, 1999a) and/or a decrease in diffusivity (Iglesia *et al.*, 1993) of olefins with increasing carbon number.

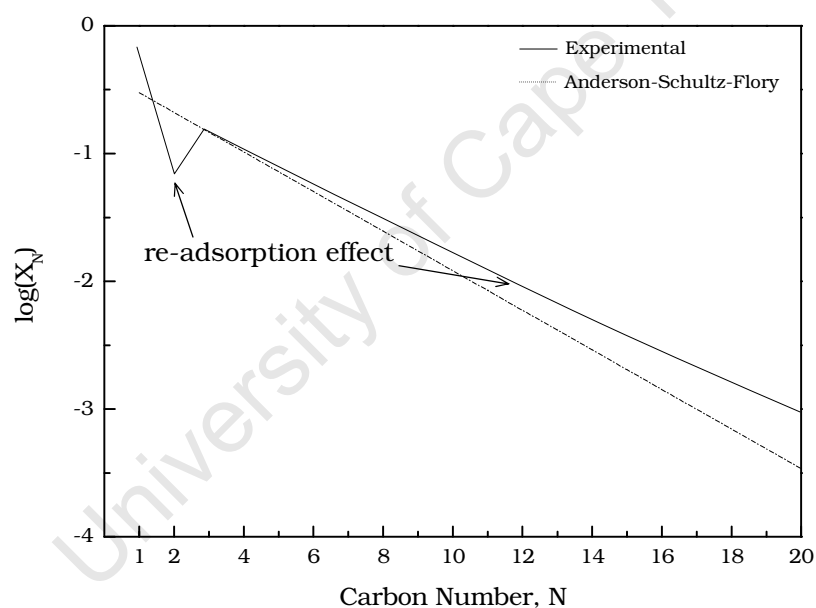


Figure 2.9: Comparison between Anderson-Schultz-Flory product distribution and experimental product distribution for a chain growth probability of 0.7

2.8 Fischer-Tropsch Product Selectivity

2.8.1 Effect of Temperature

An increase in reaction temperature results in a shift in product selectivity towards lower carbon number products and to more hydrogenated products, irrespective of catalyst metal (Dry, 2002). Therefore the Fischer-Tropsch synthesis can be classified into two operation mode in terms of reaction temperature. The low temperature mode (220°C-250°C) minimise overall gaseous product selectivity and maximise high carbon number products. These high carbon number products are hydrocracked to medium carbon number liquid products (Dry, 1996). The drawback of this operation mode is that the main product will be in diesel range fraction (Eilers *et al.*, 1990; Sie *et al.*, 1991). Fixed-bed and slurry reactor are typically used for this mode of operation (Espinoza *et al.*, 1999). However, liquid product formed inside the pores of the catalyst pellet in the fixed-bed reactor may promote catalyst sintering (Dry, 2004b).

The high temperature mode (320°C-350°C) is aimed at the production of gasoline, light olefins and oxygen containing chemicals. Fluidized-bed reactor is typically used for this operation mode (Steynberg *et al.*, 1999).

An increase in the reaction temperature from 170°C to 210°C for cobalt catalysts decreases the olefin content due to secondary hydrogenation (Schulz and Claeys, 1999b). The relative rate of branched product in C5 fraction seems to pass through a minimum in cobalt based catalysts (Claeys *et al.*, 2004). In iron catalysts, the degree of branching increases and the amount of secondary products formed such as ketones and aromatics also increases with increasing reaction temperature (Dry, 2004b).

2.8.2 Effect of Pressure

The typical operating pressure of Fischer-Tropsch synthesis is between 15 to 40bar (Dry, 2004b). Drastic changes in product selectivity can be affected by increasing the operating pressure for cobalt-based catalysts (van Berge, 1997). An increase in operating pressure would increase the monomer concentration on the catalyst surface and would therefore increase reaction rate, irrespective of the reaction mechanism. An increase in reaction pressure increases the formation of oxygenates (Dry, 1990).

2.8.3 Effect of Gas Composition

The partial pressure of the kinetically relevant compounds such as reactants (CO and H₂), intermediate products (α -olefins), and the main products (water) near the active site will affect the activity and selectivity of the Fischer-Tropsch synthesis. The relative importance of the partial pressure of these compounds is related to the adsorption strength of these compounds on the active site. CO chemisorption is generally much stronger than H₂ chemisorption (Toyoshima and Somorjai, 1979 ; Snel, 1987).

It is arguable that a higher CO partial pressure will result in a higher catalyst surface coverage of monomers, irrespective of what the chemical composition of these monomer is (Dry, 2004b). A higher coverage with monomers will result in a higher chain growth probability. However, when the catalyst surface is only covered with CO, no chain growth will take place. Thus, the catalytic activity is expected to pass a maximum with an increasing partial pressure of CO (van Steen and Schulz, 1999).

The probability of chain termination by hydrogenation is expected to increase with an increase in H₂ partial pressure. Therefore a higher H₂/CO ratio increases the product selectivity towards methane, lower carbon number hydrocarbons and paraffin products as observed by Vannice (1975a).

Water as one of the main products of Fischer-Tropsch synthesis competes with CO and H₂ for vacant sites on the catalyst surface. Water may decrease the carbon surface coverage as observed by Claeys and van Steen (2002). Therefore, increasing the H₂O partial pressure may lead to an increase in the Fischer-Tropsch activity due to an increase in the number of vacant sites (Kim, 1989; Claeys and van Steen, 2002). A decrease in methane selectivity and an increase in C₅+ selectivity over cobalt-based catalyst (Kim, 1989; Krishnamoorthy *et al.*, 2002) and a ruthenium-based catalyst (Claeys and van Steen, 2002) with increasing water partial pressure have been observed. On the other hand, Schulz *et al.* (1997) observed no change in the methane selectivity with an increase in water partial pressure over a cobalt-based catalyst. Furthermore, the selectivity for olefins and especially α -olefins increases with increasing water partial pressure (Kim, 1989; Claeys and van Steen, 2002; Krishnamoorthy *et al.*, 2002). This is attributed to the inhibition of the secondary hydrogenation of primarily formed α -olefins by water (Iglesia *et al.*, 1993).

The influence of the partial pressure of the intermediate product (α -olefins) on Fischer-Tropsch product selectivity is typically investigated by co-feeding to the reactor. Schulz and Claeys (1999b) performed Fischer-Tropsch synthesis with a cobalt catalyst in a

slurry reactor and co-fed 1-octene into the reactor. They observed an increase in the double-bond isomerisation of 1-octene to 2-octene. The product selectivity towards isomerisation for the added 1-octene increases with increasing CO partial pressure (Schulz and Claeys, 1999b). Therefore, CO inhibits olefin hydrogenation (Iglesia *et al.*, 1993; Schulz and Claeys, 1999b). Furthermore, the co-feeding of α -olefins had almost no influence on methane selectivity (Schulz and Claeys, 1999b). Thus, the hydrogenolysis of olefins leading to methane is negligible in Fischer-Tropsch synthesis. Schulz and Claeys (1999b) found that 75% of the co-fed 1-octene was hydrogenated, 15% was isomerized and only 10% was re-incorporated. Therefore hydrogenation seems to be the dominant reaction of re-adsorbed α -olefins. However, a decrease in methane selectivity was observed upon co-feeding ethene (Kim and Hills, 1985; Iglesia and Madon, 1987; Schulz and Claeys, 1999b), and a concurrent increase in the C5+ selectivity. Therefore, re-adsorption of reactive α -olefins and re-initiation in the chain growth process may lead to a decrease in methane selectivity and an increase in the C5+ selectivity.

2.8.4 Effect of Catalyst Metal Particle Size

The Fischer-Tropsch synthesis is structure sensitive (Bezemer *et al.*, 2006; Iglesia *et al.*, 1992) and the activity and product selectivity are dependent on the metal crystallite size in the catalyst for metal cobalt crystallite sizes less than 5-6nm. The structure sensitivity might be ascribed to the arrangement of the surface atoms for crystallites smaller than 5nm (van Hardeveld and Hartog, 1969) originating from a combination of electronic and structural effect. Alternatively, the structure sensitivity might originate from a phase transition of small metal particles at particular H_2/H_2O ratios in the Fischer-Tropsch synthesis (van Steen *et al.*, 2005). It should be realised that the crystallite size dependency of the Fischer-Tropsch synthesis has been observed with iron (Mabaso, 2005), cobalt (Bezemer *et al.*, 2006) and ruthenium (Welker, 2007). The product selectivity towards methane and lower carbon number product compounds increases generally with decreasing metal crystallite size. Furthermore, an increase in paraffin product selectivity was obtained with smaller metal crystallites (Bezemer *et al.*, 2006). There is a minimum metal crystallite size above which the Fischer-Tropsch synthesis becomes structure insensitive (e.g. 6nm for cobalt according to Bezemer *et al.*, 2006). Iglesia *et al.* (1992) studied cobalt and ruthenium catalysts with metal particles ranging from 2.2 to 14.8nm, and found that C5+ selectivity is favoured when Fischer-Tropsch synthesis becomes structure insensitive. This was ascribed to a possibility of a rate limiting step that does not depend on local surface structure.

2.8.5 Effect of Catalyst Pore Size

The catalyst pore size is believed to have an effect on intra-pellet reactant and product diffusion, thus affecting internal mass transport of reactant and product compounds. Espinoza *et al.* (1998) stated that the pore size for a cobalt catalyst should be at least 12nm for optimum wax selectivity. Saib *et al.* (2002) investigated the C5+ and methane selectivity over a series of Co/SiO₂ catalysts. They found the C5+ selectivity pass through a maximum while methane selectivity passed through a minimum respectively at a pore size of 10nm for cobalt catalyst supported on silica.

2.8.6 Effect of Catalyst Pellet Size

The catalyst pellet size has an influence on the internal mass transport of reactant and products. When internal mass transport is limited, the concentration of the reactants will be higher at the pore mouth of the catalyst pellet and lower towards the middle of the catalyst pellet. The product selectivity in the Fischer-Tropsch synthesis is strongly affected by the reaction conditions near the active site. Therefore, the Fischer-Tropsch product selectivity can be altered, if the reaction takes place under internal mass transport limitation (Iglesia *et al.*, 1993). When Fischer-Tropsch is performed in slurry reactor or the catalyst pores are filled with liquid product and the reaction is close to isothermal. Thus, the observed rate of the Fischer-Tropsch synthesis is expected to decrease, if internal mass transport limitation is present.

The significance of internal mass transport of reactant and products was confirmed by de Deugd *et al.* (2003) and Kapteijn *et al.* (2005) using monolithic catalyst. Monolithic cobalt catalysts were prepared by wash coating cordierite monoliths with cobalt on γ -alumina powder, the thickness of coating was varied. It was found that methane selectivity and C5+ selectivity were affected when the thickness of the coating is larger than 50 μm .

Comparing the two reactant of Fischer-Tropsch synthesis (CO and H_2), diffusion of H_2 is faster than CO for all diffusion regimes. Thus, diffusion limited reactants arrival at an active site which is deep inside the catalyst pores will lead to a higher local H_2/CO ratio. The high intra-pellet H_2/CO ratio will lead to the primary formation of shorter hydrocarbons and thus a decrease in C5+ selectivity.

Diffusion limited removal of intermediate products (α -olefins) increases their chance of re-adsorption (Iglesia *et al.*, 1993). This may lead to olefin re-incorporation, thus increasing C5+ selectivity (Iglesia, 1997a). This may also lead to secondary hydrogenation of olefins resulting in higher paraffin product selectivity (Schulz and Claeys, 1999b). However, diffusion limited removal of H_2O may increase the H_2O partial pressure in the catalyst pores, and thus resulting in an increase in olefin product selectivity (Iglesia *et al.*, 1993).

The severity of internal mass transport limitation is typically described by using the Thiele modulus (Φ), which is a dimensionless parameter derived from the mass balance of the reactant species under the influence of diffusion. The Thiele modulus is an indication of the ratio of reaction rate over the diffusion rate. Iglesia *et al.* (1995) proposed to split the Thiele modulus into two components. The diffusivity reactive

parameter (ψ) describes the properties of the reaction conditions, and structural parameter (χ) which describes the properties of the catalyst pellet.

$$\Phi^2 = \psi \times \chi = \left(\frac{2H_{CO}R_{CO}^*}{C_T P_T D_{CO}} \right) \times \left(\frac{r_{pellet}^2 \epsilon \rho_m}{r_{pore}} \right)$$

The diffusivity reactive parameter (ψ) depends on the solubility of CO (H_{CO}), the reactivity of CO (R_{CO}^*), the total reactant concentration (C_T), the operating pressure (P_T), and the CO diffusivity (D_{CO}). The structural parameter (χ) depends on the pellet radius (r_{pellet}), the catalyst porosity (ϵ), the catalyst metal density (ρ_m), and the pore radius (r_{pore}).

The influence of the structural parameter (χ) on Fischer-Tropsch product selectivity was investigated by Iglesia *et al.* (1995, 1997a, and 1997b). The structural parameter was varied by changing catalyst pellet size. At low χ values, the C5+ selectivity is low with corresponding high methane selectivity. The C5+ selectivity increases with increasing value for the structural parameter (χ). This was attributed to increased product removal limitations resulting in higher intra-pellet α -olefin concentrations and longer intra-pellet residence times. This would increase the probability of α -olefin re-adsorption, which increases the probability of further chain growth of the re-adsorbed olefin to longer chain products. Thus, this will lead to an increase in the C5+ product selectivity. At higher values of structural parameter (χ), the C5+ product selectivity decreases and correspondingly the methane selectivity increases. This can be explained by severe CO transport limitation leading to high average H_2/CO ratio inside the catalyst pellet. This high H_2/CO ratio increases the probability of chain termination (Dry, 2004a), thus increasing the product selectivity of low carbon number products. A maximum C5+ product selectivity and minimum methane selectivity was observed at intermediate values of the structural parameter (χ). This has been attributed to a limitation in olefin removal while the intra-pellet H_2/CO ratio is not severely altered (see Figure 2.10).

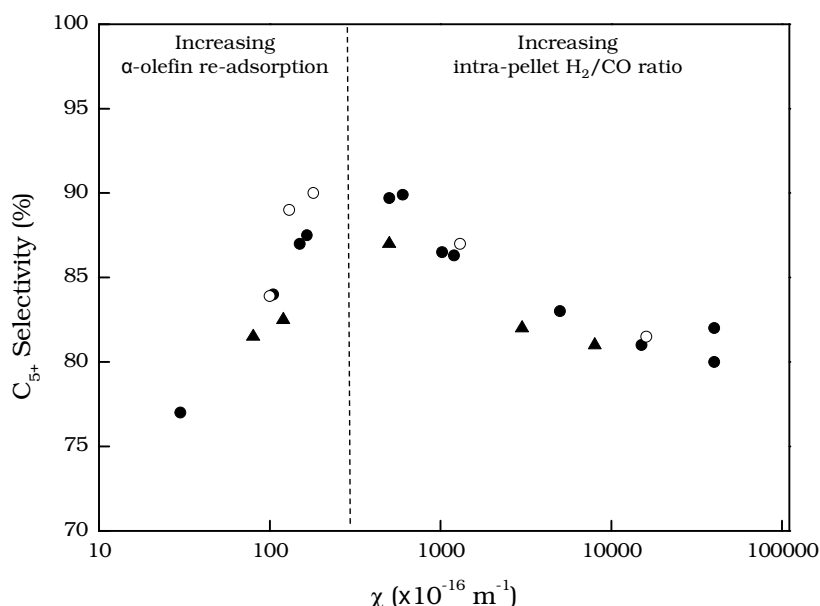


Figure 2.10: Effect of the structural parameter on C₅₊ product selectivity (adopted from Iglesia *et al.* 1997a, [○] dispersion/support effect, [●] egg-shell thickness effect, [▲] pellet size variation)

However, the product selectivity towards paraffin, branched hydrocarbons and internal olefins was not investigated to support this explanation by Iglesia *et al.* (1995; 1997a and 1997b). According to Schulz and Claeys (1999b), most of the re-adsorbed α -olefins would be hydrogenated (75%). Even with slight increase in internal mass transport, the increased intra-pellet H₂/CO ratio would increase the probability of hydrogenation of re-adsorbed α -olefins. Therefore, an investigation of Fischer-Tropsch product selectivity under internal mass transport limitation is needed.

2.8.7 Effect of Catalyst Structure

The size of a catalyst pellet is not the only parameter by which the internal mass transport limitation can be changed. Iglesia *et al.* (1995) synthesized one type of cobalt-based structured catalyst, viz. the egg-shell type, for the Fischer-Tropsch synthesis. The structured catalyst is discussed in more detail in the following section (Section 2.9). By using structured catalysts, the effect of internal mass transport limitations can be tailored for a fixed pellet size. Iglesia *et al.* (1995) observed that the performance of egg-shell type of catalyst was superior to that of the uniform catalyst pellets in terms of C₅₊ selectivity. Other types of structured cobalt-based catalysts (egg-yolk type and egg-white type) have never been utilized for Fischer-Tropsch synthesis.

2.9 Structured Catalysts

2.9.1 Type of Structured Catalysts

Structured catalysts are catalyst with active ingredient structured in a specific way within the catalyst pellet. The catalytically active ingredients can be distributed in different ways leading to four major types of distributions. Cross sectional view of four types of structured catalysts are shown in Figure 2.11. The shaded parts represent the active ingredient deposited on parts of the support. In uniform catalysts, the catalytically active ingredient is distributed uniformly the pellet. The catalytically active ingredients are concentrated towards the outer surface of the pellet in egg-shell type of catalysts. Egg-yolk type of catalysts are characterised by the active ingredients concentrated in the core of the catalyst pellet, while egg-white type of catalysts by a ring containing the catalytically active ingredient.

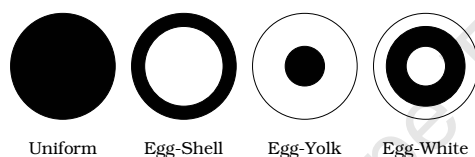


Figure 2.11: Cross-sectional view of different type of structured catalyst

2.9.2 Influence of Catalyst Structure on Product Selectivity

The superiority of non-uniform catalysts was demonstrated by Mars and Gorgels (1964), Michalko (1966) and Kasaoka and Sakata (1968). Kasaoka and Sakata (1968) solved the effect of non-uniform catalyst on reaction and diffusion rate gradients numerically in an infinite slab for a first order reaction with dimensionless parameters. They derived analytical expressions for the effectiveness factor for an isothermal, first order reaction with various catalyst activity distributions. They showed that egg-shell type has a higher effectiveness factors.

Pellets with larger catalyst activity in the interior than on the surface (egg-yolk type) may have a higher effectiveness factors if the reaction have a negative order for the reactant, e.g. the bimolecular Langmuir-Hinshelwood kinetics (Villadsen, 1976; Becker and Wei, 1977a).

Structured catalyst may also be applied in order to minimise catalyst deactivation. Michalko (1966) used egg-white type of $\text{Pt}/\text{Al}_2\text{O}_3$ catalyst and found they exhibited better long-term stability than surface-impregnated (uniform and egg-shell type) pellets. They attributed the improved long time performance of the egg-white catalyst to a reduced loss in the active metal due to attrition. Thus, catalyst pellets with an

outer protective layer of support (egg-yolk type and egg-white type) are beneficial in applications where attrition due to abrasion or vibration occurs, since initially only the inert and inexpensive support is worn off and the precious active materials are retained.

Catalyst deactivation of structured catalyst has been studied by a number of investigators (DeLancey, 1973; Becker and Wei, 1977b; Hegedus and McCabe, 1984). If deactivation occurs by sintering, it is minimized by decreasing the local catalyst concentration, i.e., uniform catalyst offers the best resistance to sintering (Komiya and Muraki, 1990).

Shadman-Yazdi and Petersen (1972) and Corbett and Luss (1974) studied an irreversible isothermal first order consecutive reaction system ($A \rightarrow B \rightarrow C$) for a variety of catalytically active site distributions. The selectivity for the formation of species C is enhanced by distributing the catalytic active ingredient in such a way that activity increases towards the centre of the pellet (egg-yolk type). The selectivity for species B is significantly higher when the catalytic active ingredient is distributed close to the surface of the catalyst pellet (egg-shell type).

Using the analogy derived from Shadman-Yazdi and Petersen (1972), the catalyst metal distribution can be used to optimise the internal mass transport limitation in Fischer-Tropsch catalyst to maximise C5+ product selectivity as suggested by Iglesia *et al.* (1995). The Fischer-Tropsch synthesis can be viewed as a consecutive reaction. CO and H₂ (A) reacts to form α -olefins (B), which re-adsorb on the catalyst surface and initiate further chain growth, leading to the formation of higher carbon number products (C). The egg-shell type of catalyst would decrease the extent of internal mass transport limitation. Hence, the residence time of species B is decreased, and an increase in the product selectivity towards species B should be obtained. More severe internal mass transport limitation would be obtained by using egg-yolk type of catalyst. This would result in an increase in the residence time of species B. Thus, an increase in product selectivity towards species C would be obtained.

2.10 Synthesis of Structured Catalysts

2.10.1 Diffusion-Adsorption

The conventional synthesis method for non-uniform catalysts is through a multi-component impregnation technique. This method is based on an intermediate interaction between the catalyst precursor and support such that the catalyst precursor can adsorb on the support, but can desorb when another competing adsorbing species is introduced. Depending on the interaction between the competitive adsorption and diffusion of the various species in the porous support, a variety of non-uniform distribution of the catalytic active components can be obtained. It is common to first establish the distribution of the adsorbed catalyst precursor during conventional impregnation process. An egg-shell type of catalyst is formed, if the adsorption rate of the catalyst precursor is faster than convective flow of impregnation solution (dry impregnation) or faster than diffusion rate of catalyst precursor in the porous support (wet impregnation) (Maatman and Prater, 1957; Lee and Aris, 1985). The pH and the ionic strength of the impregnation solution have an indirect but significant effect on adsorption characteristics of the precursor. By altering the pH in the direction which favours adsorption of the impregnation species, sharper egg-shell type distributions can be obtained (Goula *et al.*, 1992). Egg-shell, egg-yolk, and egg-white type of catalyst can be synthesized using multi-component co-impregnation technique. Hepburn *et al.* (1989) prepared Rh/ γ -Al₂O₃ egg-white type of catalysts using hydrofluoric acid, hydrochloric acid, citric acid, and their sodium salts as co-impregnants. It was shown that rhodium can be driven toward the centre of the catalyst pellet more effectively by using co-impregnants with a low degree of dissociation in aqueous solution. In co-impregnation, impregnation time and competitor concentration are the two key parameters for controlling the intra-pellet metal distribution. It is observed that by increasing impregnation time, the catalyst layer of an egg-white type of catalyst is pushed deeper inward, yielding egg-yolk type distribution. At long impregnation times, these subsurface cores can be washed out by back diffusion, producing uniform distribution with lower local loading (Shyr and Ernst, 1980; Papageorgiou *et al.*, 1996). The effect of increasing competitor concentration is similar to that of increasing impregnation time: the catalyst layer is pushed deeper inside the pellet (Papageorgiou *et al.*, 1996). However, by introducing an acid will change the pH during impregnation step.

The reducibility of transition metal catalyst depends on the pH during impregnation step (van Steen *et al.*, 1996), therefore this non-uniform synthesis method will affect the reducibility of the catalyst.

2.10.2 Deposition-Precipitation

The deposition-precipitation involves deposition inside pellets of insoluble compounds, such as hydroxides which are formed by a precipitation reaction. Precipitation can be induced by a change of solution pH. After the pellet support is filled with a solution containing the precursor to the catalytically active ingredient. A pH profile develops inside the pellet, which depends on the initial solution pH and the iso-electric point of the carrier. Since precipitation depends on pH, the distribution of the precipitate reflects the pH gradient. Therefore, by appropriate choice of the impregnation conditions, precipitation may occur in inner (egg-yolk type) or the outer (egg-shell type) region of the pellet. The preparation of the egg-shell type of catalyst using this method may lead to the precipitation of the precursor to the catalytically active ingredient outside the pellets. Therefore this method is especially suited for preparation of egg-yolk distributions (De Jong, 1991).

2.10.3 Granulation

This synthesis method involves premixing catalyst powder with a binder, followed by deposition gradually on moist seeds of catalyst support (typically 0.5-2mm), and finally providing layered spherical particles. This can be achieved by a two-stage fluidized bed (Scheuch *et al.*, 1996). This method can be extended for preparation of egg-white type of catalyst by using the corresponding egg-shell type of catalyst as seed granules and depositing inert powder. Similarly, egg-yolk catalysts could be produced using uniform spherical catalyst particles as seed granules. Egg-shell, egg-yolk and egg-white type of transition metal catalysts were synthesized by van Hardeveld *et al.* (2002). However, this synthesis method is prone to loss of catalyst surface due to attrition under extreme reaction condition.

2.10.4 Imbibition

This method is an extension of the diffusion-adsorption method. In the diffusion-adsorption method, diffusion and adsorption rates are the counteracting parameters that determine the intra-pellet metal distribution of the non-uniform catalyst. Iglesia *et al.* (1995) used viscosity of the impregnation solution as an alternative counteracting parameter to catalyst precursor adsorption rate in synthesising egg-shell type of cobalt catalyst. Egg-shell type of catalyst with sharp boundaries can be synthesised with this method. However, only egg-shell type of catalyst can be synthesised.

2.11 Catalysts Deactivation

Loss of catalyst activity during reaction is one of the major problems in catalysed reaction. Deactivation can be caused under the influence of chemical, physical or thermal interactions. In general most catalyst deactivation is irreversible and must be prevented.

2.11.1 Poisoning

Strong irreversible adsorption of reactant or products on the surface of catalyst metal and hence permanently occupying the active site is defined as poisoning. Sulphur, COS, H₂S, NH₃ and metal carbonyls are the most common contaminants for Fischer-Tropsch catalysts (Bartholomew, 1987; Rostrup-Nielsen, 1991; Bromfield and Coville, 1999). These contaminants are usually found in the raw material, for example coal as Fischer-Tropsch contains a significant amount of sulphur. Sulphur concentration in the parts per billion range can cause a significant loss in activity of the catalyst (Shultz *et al.*, 1962, Dry, 1981, Anderson, 1984, Duvenhage *et al.*, 1994; Bromfield and Coville, 1999)

2.11.2 Fouling

Fouling is defined as the physical deposition of species from liquid phase onto the catalyst surface either mechanically blocking the active site or blocking catalyst pores. In the case of Fischer-Tropsch synthesis, carbon or carbonaceous species can cover up metal crystals or plugging catalyst pores. (Rostrup-Nielsen, 1974; Trimm, 1983; Bartholomew, 1987; Menon, 1990; Bartholomew, 2001)

2.11.3 Sintering

Sintering is the loss of active surface area caused by thermal degradation (Wanke and Flynn, 1975; Ruckenstein and Dadyburjor, 1983; Bartholomew, 2001). At high temperatures, metal particle becomes mobile resulting in an increase in the likelihood for crystal growth. The mobility of metal particle is related to melting temperature of the metal, which can be correlated using Hüttig temperature defined as

$$T_{\text{Hüttig}} = 0.3T_{\text{melting}}$$

Atoms become mobile at temperature higher than Hüttig temperature.

Tamman temperature is the minimum temperature at which atoms from bulk will exhibit mobility.

$$T_{\text{Tamman}} = 0.5T_{\text{melting}}$$

Metal particles exposed to reaction temperature greater than Tamman temperature will show some degree of sintering. The Tamman temperature and Hüttig temperature of typical Fischer-Tropsch catalyst metals is tabulated in Table 2-1. Metal crystal growth can also be encouraged by the presence of water during Fischer-Tropsch synthesis (Dry, 1981; Forzatti and Lietti, 1999; Bartholomew, 2001; Moulijn *et al.*, 2001).

Table 2-1: T_{melt} , $T_{\text{Hüttig}}$ and T_{Tamman} of typical Fischer-Tropsch catalyst metals

Metal	T_{Melting} [°C]	$T_{\text{Hüttig}}$ [°C]	T_{Tamman} [°C]
Ru	2250	568	988
Fe	1538	331	632
Co	1495	316	611
Ni	1453	302	590

2.11.4 Gas-Solid and Solid-Solid Interactions

Gas-solid and solid-solid chemical interactions may also cause catalyst deactivation (Bartholomew, 2001). In the case of gas-solid interaction, loss of metal may occur via the formation of volatile compounds such as metal carbonyls. In the case of solid-solid interaction, loss of metal can occur via the formation of metal oxides. Transformation of iron or iron carbide to inactive magnetite Fe_3O_4 in the presence of CO_2 and H_2O is well-known in the deactivation of iron-based catalysts for the Fischer-Tropsch synthesis (Dry, 1981; Anderson, 1984; Jager and Espinoza, 1995; Dry, 2004b). Although direct oxidation cobalt is not feasible under Fischer-Tropsch conditions (Anderson, 1956b), cobalt oxide may form in the presence of water as a by-product of Fischer-Tropsch synthesis (Iglesia, 1997b). Thermodynamic analysis on the oxidation of small cobalt particles by van Steen *et al.* (2005) confirmed that cobalt particles less than 4nm may oxidize under typical Fischer-Tropsch conditions due to surface energy contribution.

3 SCOPE OF THIS STUDY

The Fischer-Tropsch synthesis can be regarded as a polymerisation reaction occurring on transition metal catalyst. One of the intermediate products, α -olefins may re-adsorb on the catalyst surface and initiate further chain growth; this affects the selectivity of the desired product (C5+ selectivity). Internal mass transport limitation was demonstrated as a parameter that affecting C5+ selectivity. Maximum C5+ product selectivity might be achieved at moderate internal mass transport limitation which has been ascribed to enhanced α -olefins re-adsorption with minimal increase in intra-pellet H_2/CO ratio. However the re-adsorbed α -olefin is more likely to be hydrogenated, therefore a simultaneous increase in re-adsorption of α -olefin and increase in intra-pellet H_2/CO ratio due to increase in internal mass transport limitation may not result in an optimum in C5+ selectivity.

The scope of this study is to investigate the product selectivity (methane, C5+, paraffins, olefins, α -olefins, branched hydrocarbon, and oxygenates) in the absence of external mass transport limitations and under the influence of internal mass transport limitation. The product selectivity will provide insight to the key aspect in internal mass transport limitation which affects intra-pellet reactant and product concentration.

Structured catalyst can be used to vary the extent of internal mass transport limitation without vary the catalyst pellet size. However synthesis of egg-yolk and egg-white type of distribution has never been synthesized using transition metal based catalyst. Therefore, the scope of this study includes the synthesis, characterisation as well as testing of the non-uniform cobalt-based catalyst for Fischer-Tropsch synthesis.

4 EXPERIMENTAL METHODOLOGY

4.1 Catalyst Preparation

Four types of structured catalyst pellets were synthesised by a method developed for the purposes of this study (Zhuang *et al.*, 2006). Catalysts with a uniform distribution of the active metal were denoted with the letter U, egg-shell type of catalysts were denoted with the letter S, egg-yolk type of catalysts were denoted with the letter Y, and egg-white type of catalysts were denoted with the letter W.

4.1.1 Preparation of Uniform Catalysts

The base case of uniform catalyst pellets (U1) was prepared by incipient wetness technique. Cylindrical-shaped silica pellets (Degussa[†], Aerolyst 3038, d_{pellet} : 2.5mm, l_{pellet} : 4.5mm, S_{BET} : 270m²/g, d_{pore} : 16nm) were used as catalyst support. The impregnation solution was made by dissolving 0.485g/g_{silica} Co(NO₃)₂·6H₂O (Aldrich, 98%) in 0.92ml/g_{silica} de-ionized water. The catalyst precursor was aged at room temperature for 20 minutes followed by drying in a ventilated oven at 120°C for 2 hours. Subsequently, the dried precursor was calcined in air using a flow rate of 90ml(STP)/min/g_{silica} in a fluidized bed reactor at 350°C for 16 hours (heating rate: 5°C/min).

Uniform powder catalyst (U1C) was made by crushing the calcined uniform catalyst pellets (U1) to obtain a 100% passing through of a 125µm sieve.

A uniform catalyst (U2) with a higher cobalt loading than catalyst U1 was prepared by repeating the incipient wetness impregnation step once on the calcined catalyst pellet. This precursor was then aged at room temperature for 20 minutes followed by drying in a ventilated oven at 120°C for 2 hours. Subsequently, the dried precursor was calcined in air using a flow rate of 90ml(STP)/min/g_{silica} in a fluidized bed reactor at 350°C for 16 hours (heating rate: 5°C/min).

[†] now Evonik

4.1.2 Preparation of Egg-shell Type of Catalysts

The synthesis procedure of egg-shell type of catalysts consists of two stages, viz. protection of the inner core of the silica support against penetration with the cobalt nitrate solution, and impregnation of outer shell of the silica support. The protection was achieved by soaking the silica support in an organic solvent[†] for 20 minutes to ensure its pores were completely filled. The support soaked with the organic solvent was subsequently heated in an oven at 120°C to evaporate some of the organic solvent in the pores. The silica supports were stirred every 30 seconds during the partial evaporation process to ensure even evaporation. The amount of organic solvent remained in the pellets was determined gravimetrically.

Subsequently, the silica supports which were partially covered with the organic solvent were impregnated using the incipient wetness technique with an aqueous cobalt nitrate solution. The amount of cobalt nitrate in the impregnation solution was fixed at 0.485g/g_{silica}, while the amount of de-ionized water was varied proportional to the amount of partially evaporated organic solvent on the basis of total pore volume of 0.92mℓ/g_{silica} (see Table 4-1).

$$V_{\text{organic solvent}} + V_{\text{water}} = V_{\text{pore}} = 0.92\text{mℓ/g}_{\text{silica}}$$

The catalyst precursor was then aged at room temperature for 20 minutes followed by drying in a ventilated oven at 120°C for 2 hours. Subsequently, the dried precursor was calcined in air using a flow rate of 90mℓ(STP)/min/g_{silica} in a fluidized bed reactor at 350°C for 16 hours (heating rate: 5°C/min).

Table 4-1: Amount of organic solvent and de-ionized water used in the synthesis of egg-shell type of catalysts

Catalyst Code	Organic Solvent [†] [g/g _{silica}]	H ₂ O [mℓ/g _{silica}]
S1	0.584	0.131
S2	0.486	0.263
S3	0.389	0.394
S4	0.292	0.526
S5	0.195	0.657
S6	0.097	0.789

[†] n-undecane (Merck, 99.9%)

4.1.3 Preparation of Egg-yolk Type of Catalysts

The synthesis of egg-yolk type of catalysts consists of three stages, viz. preparation of a uniform precursor; protection of the inner core of the precursor, and leaching of cobalt on the outer shell.

To obtain uniform catalysts with various cobalt loadings, a series of uniform pellets as precursor for the synthesis of egg-yolk type of catalyst was prepared using the multi-step incipient wetness technique as previously described (Section 4.1.1). Impregnation solution used in each impregnation step was made up of $1\text{g/g}_{\text{silica}}$ cobalt nitrate and $0.92\text{ml/g}_{\text{silica}}$ of de-ionized water. The uniform pellet precursors were aged at room temperature for 20 minutes followed by drying in a ventilated oven at 120°C for 2 hours. Subsequently, the dried precursor was calcined in air using a flow rate of $90\text{ml(STP)}/\text{min}/\text{g}_{\text{silica}}$ in a fluidized bed reactor at 350°C for 16 hours (heating rate: $5^{\circ}\text{C}/\text{min}$). The uniform pellet precursors were aged, dried, and calcined after each impregnation step. These uniform pellet precursors were reduced in hydrogen using a flow rate of $90\text{ml(STP)}/\text{min}/\text{g}_{\text{silica}}$ in a fluidized bed reactor at 350°C for 16 hours (heating rate: $5^{\circ}\text{C}/\text{min}$).

The reduced uniform pellet precursor was soaked in the organic solvent for 20 minutes to ensure all catalyst pores were filled. The soaked precursors were then evenly dried in oven to partially evaporate the organic solvent (see Table 4-2). Subsequently, the catalysts, which were partially covered with the organic solvent, were contacted with 200ml of diluted nitric acid (1wt% in de-ionized water) for 30 minutes. The leached precursors were washed 5 times, each time with 100ml of de-ionized water. The pellets were subsequently dried in a ventilated oven at 120°C for 2 hours and calcined in air using a flow rate of $90\text{ml(STP)}/\text{min}/\text{g}_{\text{silica}}$ in a fluidized bed reactor at 350°C for 16 hours (heating rate: $5^{\circ}\text{C}/\text{min}$).

Table 4-2: Number of impregnation steps used for uniform precursor and amount of organics left inside the precursor in the synthesis of egg-yolk type of catalyst

Catalyst Code	Impregnation Steps	Organics [$\text{g/g}_{\text{silica}}$]
Y1	1	0.643^{\dagger}
Y2	1	0.596^{\dagger}
Y3	2	0.165^{\dagger}
Y4	4	0.102^{\dagger}
Y5	1	0.660^{\ddagger}
Y6	1	0.802^{\ddagger}
Y7	2	0.861^{\ddagger}

† n-undecane (Merck, 99.9%)

‡ n-tetradecane (Merck, 99%)

4.1.4 Preparation of Egg-white Type of Catalysts

The synthesis of egg-white type of catalysts involves a procedure identical to the synthesis of egg-yolk type of catalysts; except for the use of egg-shell type of pellet as a precursor rather than a uniform catalyst pellet. Four samples of egg-shell type of pellet precursors with varying egg-shell thickness were prepared using various amounts of organic solvent and impregnation solution as tabulated in Table 4-3.

These precursors were reduced and subsequently soaked in organic solvent for 20 minutes and heated at 120°C to partially evaporate the organic solvent ensuring the metal-free core of the pellet. A part of the metal-containing shell of the pellet remained covered with organic solvent. These pellets were subsequently contacted for 30 minutes with 200ml of diluted nitric acid (1wt% in de-ionized water) at room temperature. The leached pellets were washed 5 times, each time with 100ml of de-ionized water. Catalyst pellets were then dried in a ventilated oven at 120°C for 2 hours, and subsequently calcined in air using a flow rate of 90ml(STP)/min/g_{silica} in a fluidized bed reactor at 350°C for 16 hours (heating rate: 5°C/min).

Table 4-3: Details of impregnation solution and organic solvent used for preparation of egg-shell type of precursor and amount of organic solvent left inside the precursor in the synthesis of egg-white type of catalysts

Catalyst Code	Egg-Shell Precursor		Leaching	
	Organic Solvent ^(a)	Co(NO ₃) ₂ ·6H ₂ O	H ₂ O	Organic Solvent ^(b)
	[g/g _{silica}]	[g/g _{silica}]	[g/g _{silica}]	[g/g _{silica}]
W1	0.466	0.602	0.340	0.597
W2	0.280	0.801	0.499	0.689
W3	0.199	1.000	0.539	0.270
W4	0.107	1.200	0.659	0.203

(a) used in synthesis of egg-shell type of precursor

(b) used to prevent the leaching solution entering the core of the catalyst

4.2 Catalyst Characterisation

4.2.1 Atomic Absorption Spectroscopy (AAS)

The cobalt content of the catalysts was determined by using an Atomic Absorption Spectrophotometer Varian 3.0. Calcined pellet samples were crushed to fine powder in the presence of acetone to minimise loss of silica during crushing. All crushed samples were dried at 120°C overnight to eliminate moisture prior the analysis. Subsequently, the samples were weighted and dissolved in aqua-regia with the addition of hydrofluoric acid and perchloric acid (see Appendix B.1). The aqueous samples were made up to a known volume, and subsequently filtered. The cobalt concentration was measured by using AAS.

4.2.2 Optical Microscopy

Catalyst pellets were cut parallel to their cross-sectional area to examine the metal distribution inside the pellet. Images of 10 pellets per catalyst were taken at 30× magnification under a dissecting microscope (Wild M400) which was attached to a digital camera (Zeiss Axiocam). Images were processed and scaled using Zeiss AxioVision image software. Sample average and standard deviation were estimated from these images.

4.2.3 Scanning Electron Microscopy (SEM)

A scanning electron microscope (LEO† S440 SEM, La:Ka) equipped with a Four Quadrant Back Scatter Detector and an energy dispersive Fissions Kevex X-ray spectrometer (ECXA) operating at 20 kV was used to investigate the macroscopic distribution of cobalt oxide in the calcined catalyst pellets. Catalyst pellets were placed individually in a plastic vial which was then filled with liquid resin. Soaked pellets were left to solidify in an oven at 60°C for 24 hours. Thereafter, the pellets were cut and polished to show its cross-sectional area (see Appendix B.2). Back-scatted images and EDX analysis of 4 pellets per sample were taken, from which the sample average and standard deviation were estimated.

† now Zeiss

4.2.4 Transmission Electron Microscopy (TEM)

The cobalt oxide particle size in the calcined catalysts and in the spent catalysts was determined by using a LEO 912 Transmission Electron Microscope operating at 120 kV. Catalyst pellets were crushed to fine powder and subsequently suspended in methanol. A drop of each sample was transferred onto a carbon coated copper grid. Four digital images of each catalyst sample were taken and analyzed by using IMAGE J (see Appendix B.3). A minimum of 2000 particles and 20 clusters were measured per catalyst sample to determine the average particle size and the cluster size.

4.2.5 X-Ray Diffraction Spectroscopy (XRD)

X-ray diffraction was used to identify the cobalt oxide phase present in the calcined catalyst pellets and to estimated the average crystallite size prior to reduction. The pellets were crushed to fine powder prior to the analysis. Diffraction spectra were obtained by using a Phillips X-Ray Generator with Cu-K α radiation of wavelength 0.154nm. The generator voltage was adjusted to 40kV and the current to 25mA. The spectra were scanned in the 2θ range from 3° to 120° at a rate of 3°/min with a step size of 0.05°. Volume-weighted particle sizes were estimated from the peak width at half height using the Debye-Scherrer equation (See Appendix B.4)

$$d = \frac{k\lambda}{\beta \cos\theta}$$

where d is the particle diameter [nm], k is the shape factor (0.9), λ is the X-ray wavelength [nm], β is the line broadening of full width at half maximum intensity [radian] and θ is the diffraction angle.

4.2.6 Physisorption

Physisorption was performed on a Tristar 3000 Micrometrics analyser on calcined catalyst pellets to determined surface area and pore diameter. The pellet samples were evacuated for at least 8 hours at 250°C before analysis. Nitrogen was used as the adsorbate at its liquefaction temperature (77.35K). The isotherms were obtained at a constant temperature at a range of relative pressures between 0 and 1. Brunauer-Emmet-Teller (BET) method was applied to evaluate the total surface area. Pore volume and average pore diameter of the catalysts were estimated using the Barrett-Joyner-Halenda (BJH) method (see Appendix B.5).

4.2.7 Chemisorption

Static volumetric chemisorption was performed on an ASAP 2020 Micromeritics analyser using CO. Catalyst pellets were reduced in-situ at 350°C for 16 hours with a heating rate of 5°C/min and a hydrogen flow rate of 18ml (STP)/min/ g_{silica} . Samples were evacuated at the reduction temperature for two hours to eliminate any chemisorbed hydrogen, and subsequently cooled down to chemisorption temperature (40°C). The adsorption isotherm was recorded between 50 to 550mbar. Chemisorption results were analysed based on the assumption that strongly physisorption of CO at the analysis temperature is negligible. The volume of the chemisorbed monolayer on the active surface was determined by extending a line tangent to the plateau of the isotherm to the y-axis, as illustrated in Figure 4.1. Assuming a stoichiometry number F_s of 1, the number of accessible active sites (N_s) on the surface was determined

$$N_s = \frac{V_{\text{mono}} N_A F_s}{V_{\text{mol}}}$$

where N_A is Avogadro's number and V_{mol} the molar volume of CO at STP.

The active metal area A_m was calculated from

$$A_m = N_s A_s$$

where A_s is the specific cobalt surface area (15.2 fcc atoms/nm² according to Bergeret and Gallezot, 2008). Average cobalt particle size was determined from active metal area assuming particles to be spherical (see Appendix B.6).

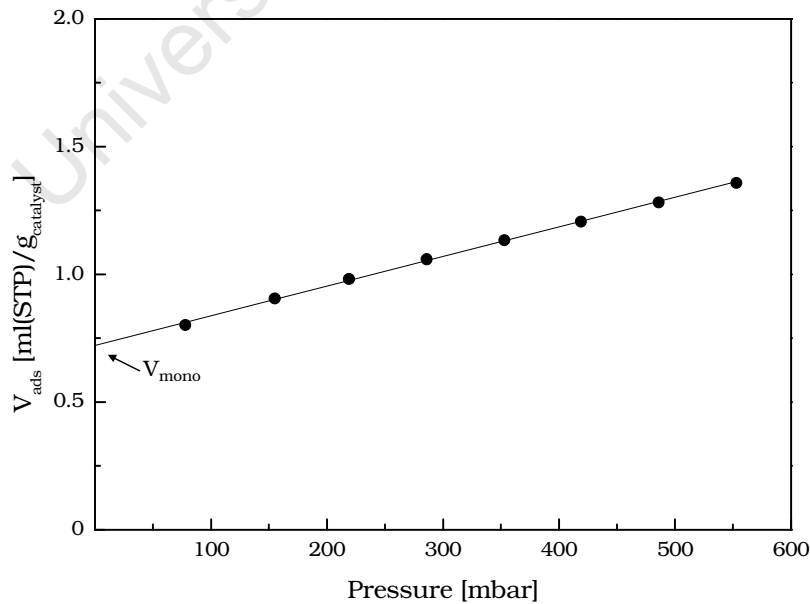
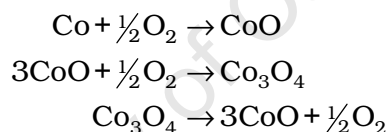


Figure 4.1: An example showing determination of monolayer from chemisorption isotherm (Catalyst U1)

4.2.8 Temperature Programmed Reduction and Oxidation (TPR-TPO)

Temperature programmed reduction and oxidation (TPR-TPO) was used to verify metal loading and to determine the degree of reduction of the catalysts (Sewell, 1996). A Micromeritics AutoChem 2910 (Micromeritics Instrument Corp., USA) with quartz reactor was used for TPO-TPR analysis. Calcined samples were reduced in-situ with hydrogen flow rate of 90ml(STP)/min/g_{silica} at 350°C for 16 hours with heating rate of 5°C/min, and cooled down in argon prior TPR-TPO. TPR of the reduced sample was conducted using 50ml(STP)/min of 5% hydrogen in argon stream. Samples were heated to 1000°C using a linear temperature ramp of 10°C/min with a holding time of 60 minutes. TPO was conducted after TPR using 5.1% oxygen in helium with a flow rate of 50ml(STP)/min using the same temperature program as for the TPR. Hydrogen and oxygen consumption was measured with a thermal conductivity detector (TCD). The instrument was calibrated at regular intervals using standards of pure NiO (see Appendix B.7).

The cobalt loading of the catalyst is calculated base on the assumption that all cobalt are reduced to metallic form after TPR analysis; and the assumed sequential oxidation steps during TPO are



TPO spectrum of all catalysts showed an oxygen consumption peak between 50°C and 700°C, which corresponds to the oxidation of metallic cobalt first to CoO and subsequently to Co₃O₄. TPO spectrum showed an oxygen generation peak between 700°C to 1000°C, which correspond to decomposition of Co₃O₄ to CoO. The cobalt content was calculated by the assumption that all cobalt existed as Co₃O₄ prior to the decomposition at 700°C and they were completely decomposed to CoO at 1000°C. Thus, the amount of cobalt can be determined from the amount of oxygen released during the decomposition of Co₃O₄. The degree of reduction was calculated according to hydrogen consumption peak from TPR analysis by assuming unreduced cobalt exists as Co₃O₄, and all cobalt is reduced after TPR. An example of TPR and TPO spectrum is shown in Figure 4.2 and Figure 4.3 respectively.

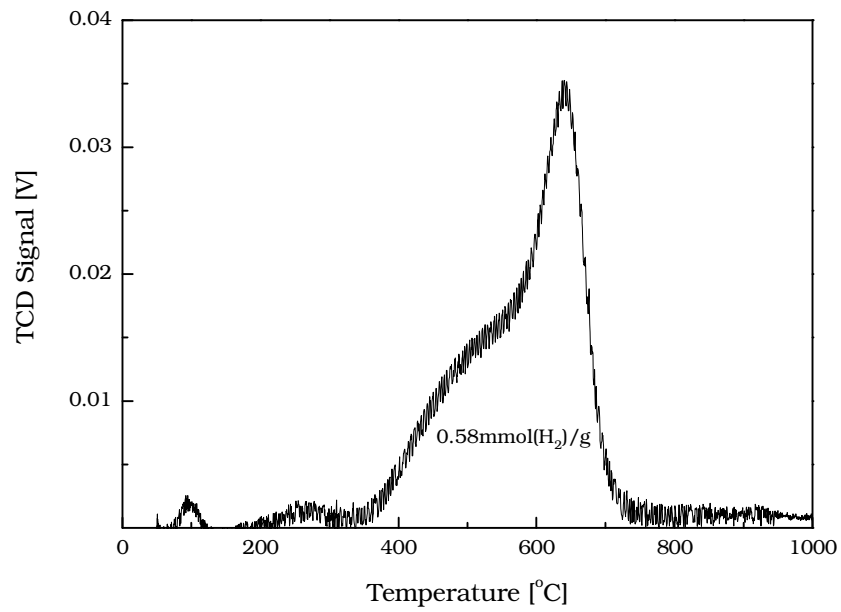


Figure 4.2: Example of TPR spectrum of reduced catalyst (U1C) prior TPO analysis

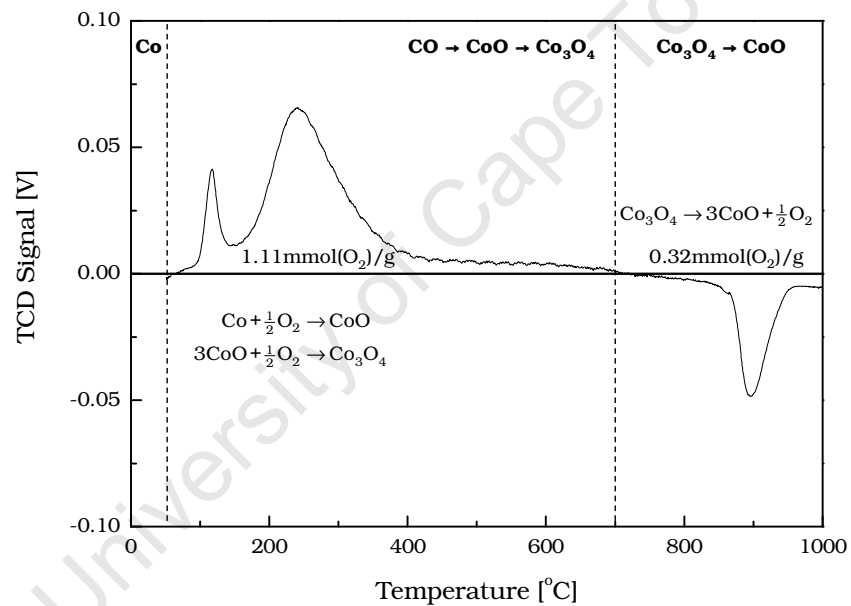


Figure 4.3: Example of TPO spectrum of catalyst (U1C) after TPR analysis

4.3 Fischer-Tropsch Synthesis Test

4.3.1 Modified Slurry Reactor Set-up

Fischer-Tropsch performance of crushed uniform catalyst (U1C) and structured catalyst pellets were tested in a slurry reactor set-up (see Figure 4.4). Similar to the fixed bed reactor set-up, CO (Afrox, 99.97%) and H₂ (Air Liquide, 99.999%) were fed to the reactor at a head pressure of 40bar. Their flow was controlled individually. The streams were mixed before entering the reactor. The composition of the feed gas was determined by leading the gas mixture over the reactor-by-pass through two 3-way valves to the online gas chromatograph equipped with a thermal conductivity detector. A H₂/CO ratio of 2 was ensured before the start of each reaction test. The two 3-way valves were switched to feed gas allowing it to flow through the reactor at the start of the reaction. Argon was added under reaction conditions to the product stream to maintain a reaction pressure of 20bar. A known amount of cyclohexane (0.15%) premixed with N₂ was added to the product effluent stream as an internal standard for quantitative data analysis.

The slurry reactor is a modified 600ml pressure vessel (Parr), with a motor stirrer attached to the lid of the reactor (see Figure 4.5). The gas feed pipe dips down below the tip of the stirrer blade to ensure adequate bubble breaking and dispersing. The catalyst pellets were divided equally over two stainless steel mesh-wire baskets (mesh: Haver & Boecker, aperture: 0.8mm, d_{wire} : 0.315mm, open area: 64%; dimension of baskets: 55×19×6mm) which were mounted on the reactor lid. The mesh-wire baskets were mounted opposite to each other on both sides of the stirrer shaft. A stainless steel inline filter (Swagelok, d_{pore} : 2 μ m) was mounted above the mesh-wire basket to ensure only volatile and liquid products leaves the reactor at reaction temperature. Liquid products were separated from the gas stream in the wax trap operated at 180°C and the water was separated from the gas stream in the cold trap at room temperature. Gas lines from the reactor effluent to the ampoule breaker, in which samples of the effluent were taken, were heated at 180°C to prevent condensation.

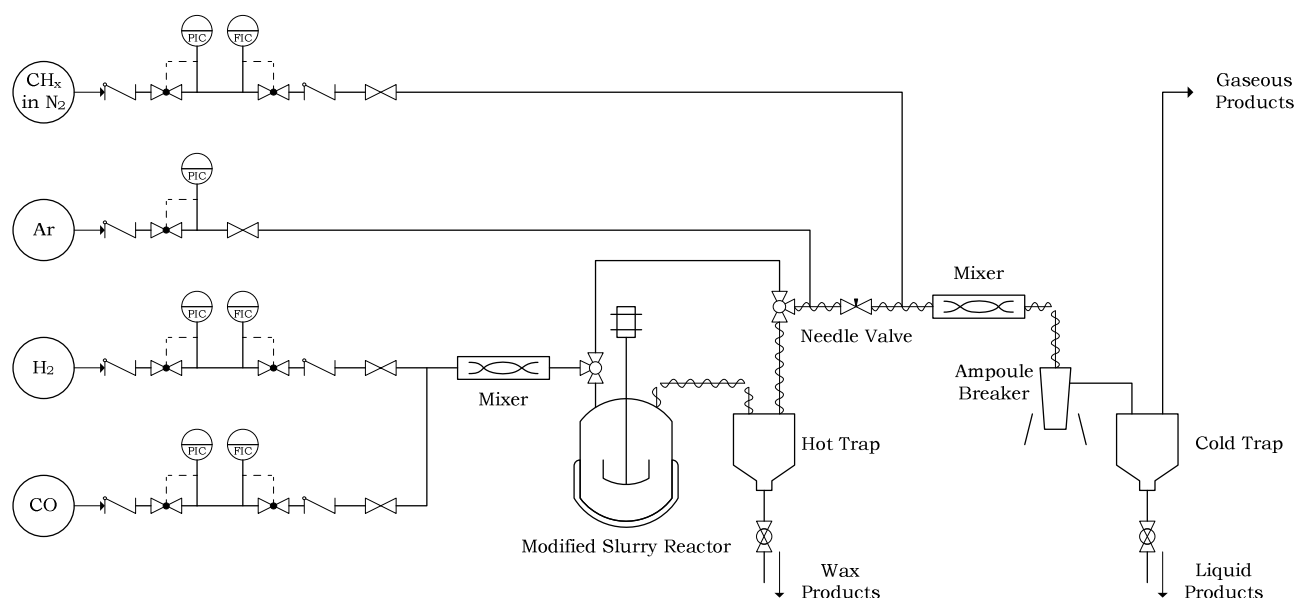


Figure 4.4: Flow diagram of the slurry reactor set-up used in this study

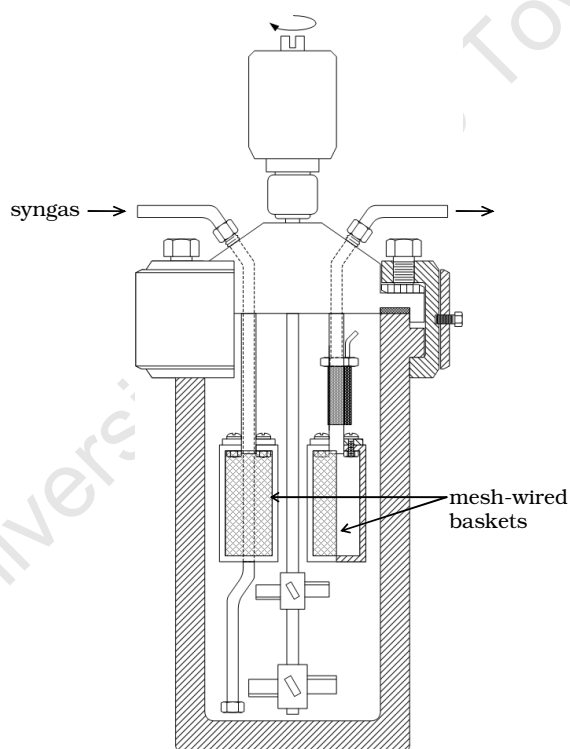


Figure 4.5: Schematic representation of the modified slurry reactor showing mesh-wired baskets

The catalyst (ca. 5g, pellet or powder) was reduced ex-situ in a fluidised bed reactor with the standard reduction condition employed in this study (hydrogen flow rate of 90ml(STP)/min/g_{silica} in a fluidized bed reactor at 350°C for 16 hours with a heating rate of 5°C/min). The crushed uniform catalyst (UC1) was transferred under argon into 60g of wax (Sasol). This mixture of wax and the reduced catalyst was solidified and transferred into the reactor with additional 220g of molten wax. The catalyst

pellets were reduced in the same way and transferred under argon into 30ml of squalene which protects the reduced catalyst pellet from oxidation during the packing of catalyst into the mesh-wire baskets. The reactor was filled with 280g of molten wax for all pellet catalyst experiments to ensure all catalyst pellets were immersed in liquid phase. The existence of vortex on the surface of the liquid was determined by fitting the reactor lid on a transparent plastic beaker with identical dimension to the reactor vessel filled with water. A vortex did not form on the surface of the liquid phase in the reactor even at the highest stirring speed (860rpm) due to large internal fittings in the reactor. The reactor lid with reduced catalyst pellets in mesh-wire baskets was mounted at 160°C to the reactor which is filled with molten wax. Subsequently, the temperature in the reactor was slowly raised up to 220°C and pressurised to 20bar with stirrer operated at 500rpm.

The synthesis gas mixture at flow rate of 13.9ml(STP)/min/g_{catalyst} with a H₂/CO ratio of 2 was introduced into the reactor at the start of the reaction. The reaction temperature as kept at 220°C for the first 48 hours, subsequently the reaction temperature was increased to 230°C. After 24 hours of operation at 230°C, the temperature was decreased to 220°C and held for 12 hours to test for deactivation. Subsequently, temperature was increased to 240°C and held for 48 hours, followed by deactivation test 220°C for the last 12 hours on stream. Samples were taken periodically during the 120 hours of operation. The variation of reaction condition is depicted in Figure 4.6.

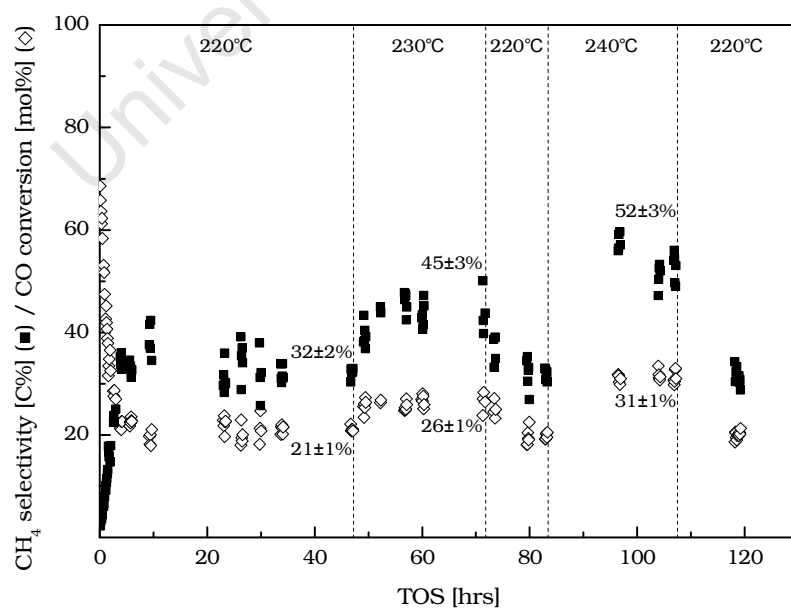


Figure 4.6: Example of sequential change of reaction condition for Fischer-Tropsch synthesis tests (Y1)

4.3.2 Post-run Catalyst Characterization

The spent catalyst pellets were transferred into a Soxhlet extraction set-up (Figure 4.7), in which the wax inside catalyst pores were extracted with xylene under argon for 24 hours. Pellets put in cellulose thimble was placed inside a 1 l soxhlet extractor (Lasec), which was attached to a 1 l two-necked round bottom flask filled with xylene (Merck, mixture of isomers) and a reflux condenser. Xylene was boiled in an oil bath which was kept at 170°C. Argon was fed to the round bottom flask at 50ml(STP)/min in order to prevent the contact of spent catalyst with air. After 24 hours of extraction, pellets were passivated by replacing argon gas feed with CO₂ at a flow rate of 50ml(STP)/min for 30 minutes prior post-reaction analysis under optical microscope and TEM.

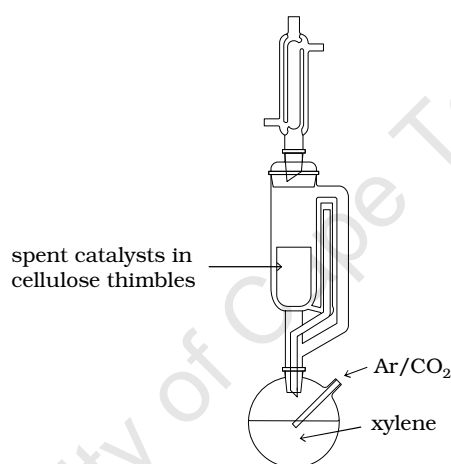


Figure 4.7: Soxhlet extraction set-up used for wax extraction of spent catalysts

4.4 Analytical Procedures

4.4.1 On-line Analysis of Inorganic Gases and Methane

The inorganic gases (Ar, H₂, N₂, CO, CO₂) and methane were analysed on a multi-column Varian CP4900 Micro Gas Chromatograph (GC) equipped with a thermal conductivity detector (TCD). The GC was connected directly to the reactor effluent enabling on-line analysis. Helium was used as the carrier gas with a head pressure of 2bar which was further reduced in different columns. Gases were separated isothermally at 170°C in three columns operating in parallel. An example of TCD spectrum is shown in Appendix B.8.

Table 4-4: Operation condition of the columns used in GC

Column Type	20m 5Å Molsieve	10m Pora Plot Q	10m 5Å Molsieve
Gases separated	Ar, N ₂ , CO, CH ₄	CH ₄ , CO ₂	H ₂ , N ₂
Temperature [°C]	80	60	80
Pressure [bar]	1.5	1.0	1.5

4.4.2 Sampling of Volatile Organic Gases

The gas sampling technique used in this study was developed by Schulz *et al.* (1984). Glass ampoules were prepared by reshaping Pasteur pipettes (Lasec) under an O₂/LPG flame. The capillary of the reshaped pipettes is 120mm in length and has a diameter of about 1.5mm. Reshaped pipettes were evacuated and sealed to obtain an internal volume of approximately 2ml. The capillary end was inserted through an airtight septum into a heated sampling device (ampoule breaker) during sampling as described by Mabaso (2005). Volatile compounds were drawn into the evacuated ampoule when the capillary was broken and was sealed immediately with a butane flame. Samples were stored and analyzed using a Varian 3800 GC equipped with flame ionization detectors (FID).

4.4.3 Analysis of Volatile Organic Gases

The organic product compounds which are volatile at reaction conditions were analyzed on a Varian 3800 GC equipped with FID. The operating conditions of the gas chromatographic and an example of a typical FID chromatogram with peak identification is illustrated in Appendix B.9. Ampoule samples were crushed in a breaking device described by Mabaso (2005). The volatile organic compounds were released in nitrogen and introduced into the injector of the GC. Hydrogen was used as a carrier gas for the separation of the organic products in a 60m OV-1 type capillary column.

4.5 Data Analysis

The quantitative analysis of reaction data was based on known amounts of reference gas mixture (0.15vol% cyclohexane in N₂) which was blended with the exit stream from the reactor. Nitrogen was used as the basis to quantify the flow rates of the inorganic compounds and methane from TCD data. The molar flow rate of compound i is then

$$\dot{n}_i = f_{\text{TCD},i} \left(\frac{A_{\text{TCD},i}}{A_{\text{TCD},\text{N}_2}} \right) \dot{n}_{\text{N}_2}$$

where $f_{\text{TCD},i}$ is the TCD response factor of the inorganic compound i, A_{TCD} the area under the TCD peak, and \dot{n}_{N_2} the molar flow rate of nitrogen. The TCD response factors (f_{TCD}) of all compounds relative to nitrogen were calibrated using a mixture of gas with known composition (24.8% Ar, 14.7% H₂, 15.2% N₂, 15.5% CO, 15.1% CO₂ and 14.7% CH₄). Cyclohexane is not a typical Fischer-Tropsch product, and was therefore used as the basis to quantify the flow rates of the volatile organic products from FID data. The molar flow rate of the volatile organic compound i is then

$$\dot{n}_i = \frac{f_{\text{FID},i}}{f_{\text{FID},\text{ref}}} \frac{A_{\text{FID},i}}{A_{\text{FID},\text{ref}}} \frac{N_{\text{c,ref}}}{N_{\text{c},i}} \dot{n}_{\text{ref}}$$

where A_{FID} is the area under the FID peak, N_{c} is number of carbon atoms, \dot{n}_{ref} is the molar flow rate of cyclohexane, and f_{FID} is the compound specific response factor which was taken from Kaiser (1969). Conversion of CO was calculated from TCD data and is defined as

$$X_{\text{CO}} = \frac{\dot{n}_{\text{CO},\text{in}} - \dot{n}_{\text{CO},\text{out}}}{\dot{n}_{\text{CO},\text{in}}}$$

Selectivity of product j on a carbon basis calculated from FID data is defined as

$$S_{\text{C},i} = \frac{\dot{n}_i}{\dot{n}_{\text{CO},\text{in}} X_{\text{CO}}}$$

C5+ selectivity was calculated by subtracting carbon yield of C4- from amount of CO converted.

$$S_{\text{C5}+} = \frac{\dot{n}_{\text{CO},\text{in}} X_{\text{CO}} - \sum_{i=1}^4 \dot{n}_{\text{C}_i}}{\dot{n}_{\text{CO},\text{in}} X_{\text{CO}}} = 1 - \sum_{i=1}^4 S_{\text{C}_i}$$

5 RESULTS AND DISCUSSION

5.1 Characterisation of Structured Cobalt Catalysts

5.1.1 Intra-pellet Cobalt Distribution in Uniform Catalyst

A SEM-EDX scan was used to determine the intra-pellet cobalt distribution in each type of structured catalyst. Catalysts synthesized by incipient wetness may have intra-pellet cobalt distribution gradient. During the drying process, cobalt nitrate crystallises out via super-saturation. If the rate of cobalt nitrate diffusion in water is faster than the rate of evaporation, the concentration of cobalt nitrate will be uniform throughout the catalyst pore resulting in a uniform distribution of cobalt in the catalyst.

According to the back-scattered SEM image and EDX processed images, the uniform catalyst pellet (U1) synthesized by single-step incipient wetness method has a uniform cobalt distribution along the radius of the support pellet (Figure 5.1). This suggests that drying in a ventilated oven at 120°C is adequate to obtain a uniform cobalt distribution in the catalyst pellet.

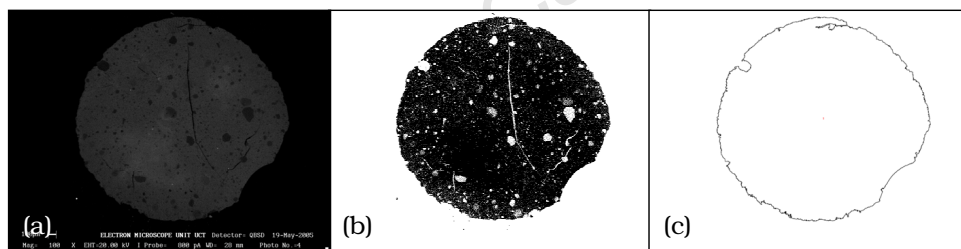


Figure 5.1: Back-scattered SEM of catalyst pellet U1 image (a) EDX processed image showing cobalt enriched region (b) outline showing cobalt boundary (c)

There is a limit in the cobalt loading which can be achieved by the incipient wetness synthesis. The maximum concentration in the impregnation solution is the saturation concentration in the solvent (H_2O). The amount of impregnation solution used in incipient wetness synthesis method is limited by the pore volume of the catalyst. Therefore, there is a limited amount of cobalt nitrate that can be loaded on support per single step of impregnation. In this study, the maximum achieved concentration of cobalt nitrate ($\text{Co}(\text{NO}_3)_2 \cdot 6\text{H}_2\text{O}$) in water, was 1.08g/ml. Hence, pellets with a high cobalt loading can only be synthesised by multiple impregnation steps.

The subsequent impregnation can be done either after drying of the precursor from the previous impregnation step, or after calcination of precursor from the previous impregnation step. The back-scattered SEM image and EDX scan over the catalyst pellet

synthesized by 2-steps impregnation without intermediate calcination showed a cobalt distribution gradient towards the support surface (see Figure 5.2). The cobalt in the catalyst precursor prior calcination is in the form of a nitrate after drying, which only starts to decompose at 150°C (Girardon *et al.*, 2005). During the second impregnation step, crystallised cobalt nitrate in the pores from the first impregnation step, re-dissolves in the newly introduced impregnation solution. This re-dissolution process increases the liquid volume introduced to the pellets in the second impregnation step, resulting an excess of impregnation solution on the surface of the pellet. The saturated impregnation solution in the pores moves towards the pore mouth when the pellet precursor is dried for the second time. Hence a gradient in the cobalt distribution in the catalyst pellets prepared without intermediate calcination was observed.

The back-scattered SEM image and EDX scan over the high loading catalyst pellet (U2) synthesized by the 2-step impregnation with intermediate calcination showed a uniform distribution of cobalt along the pellet radius (see Figure 5.2). During intermediate calcination, cobalt nitrate is converted to insoluble cobalt oxide (Co_3O_4). This prevents the re-dissolution of cobalt nitrate to the impregnation solution introduced during the second impregnation step. This shows that the intra-pellet cobalt distribution gradient can be minimised by calcination of the catalyst precursor after each impregnation step.

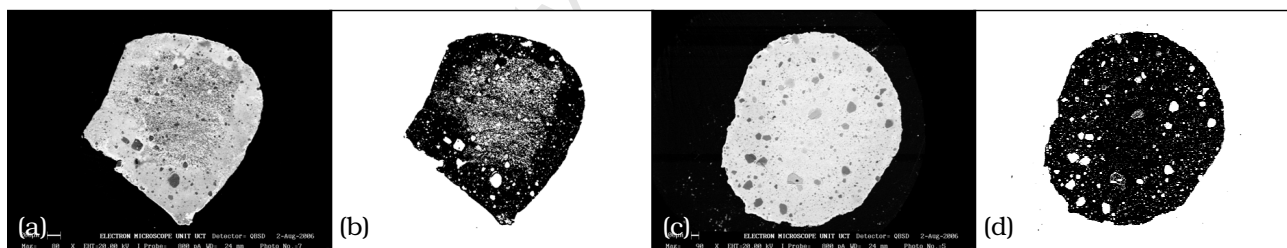


Figure 5.2: Back-scattered SEM image of catalyst without intermediate calcination (a) EDX processed image showing cobalt distribution variation (b) Back-scattered SEM image of catalyst U2 with intermediate calcination (c) EDX processed image showing uniform cobalt distribution in catalyst U2 (d)

5.1.2 Intra-pellet Cobalt Distribution of Egg-shell Type of Catalysts

The optical microscopy images of calcined egg-shell type of catalyst showed a distinct boundary between the cobalt enriched region and cobalt free silica (see Figure 5.3). The back-scattered SEM image and EXD scan on the egg-shell type of catalyst confirms the distinct boundary, and shows the cobalt distribution inside the cobalt enriched region is uniform (see Figure 5.4). Images from optical microscopy and SEM show that the distinct boundary was irregular in shape, which was not expected if the boundary was due to the separation of organic and aqueous phase in the catalyst pores. It should be noted, that SEM images show the presence of cracks in silica pellets going from the pellet surface towards the centre of the pellet. The cobalt enriched shell layer folds along the cracks in the pellet. This suggests that organics used in the synthesis of egg-shell catalyst adequately inhibited impregnation solution from wetting the centre of the pellet, and the variations in cobalt enriched shell thickness and irregular shape of the boundary is due to the cracks in the silica support.

Optical microscopy images were taken of spent catalysts. A distinct boundary between cobalt enriched region and cobalt free silica was still present after exposure to the Fischer-Tropsch synthesis condition for 120 hours (see Figure 5.3).

The average value and the standard deviation of cobalt free silica core size to pellet size ($d_{\text{core}}/d_{\text{pellet}}$) were calculated from optical microscopy and SEM images. The absolute standard deviation is between 0.02 to 0.05, which can be attributed to the degree of even evaporation and cracks inside the various pellets. The average relative core size of calcined catalyst and spent catalyst are within the standard deviation each other, therefore it can be concluded that they are statistically the same. This means the cobalt particle did not move across the boundary of cobalt enriched region and cobalt free silica core.

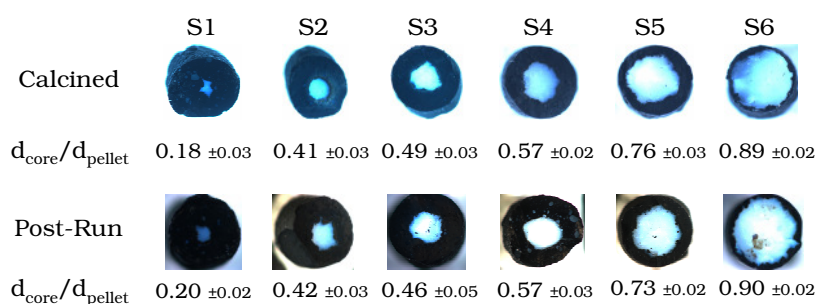


Figure 5.3: Optical microscopy images of egg-shell type of catalysts

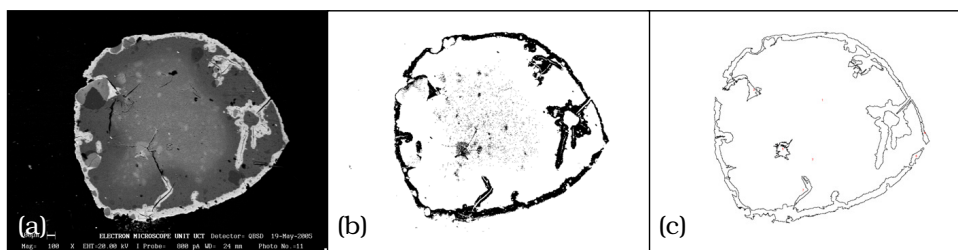


Figure 5.4: Example of Back-Scattered SEM images of egg-shell catalyst (S6) (a) EDX processed image highlighting cobalt rich region (b) Outlined image showing cobalt enriched boundary (c)

The feasibility of the developed synthesis method and the choice of organic solution depend on the surface wetting scenario in the pores. Two surface wetting scenarios can be proposed. In the first scenario, the hydrophobicity of the silica surface is insufficient: the organic solvent does not completely wet the pore surface, and therefore the interface between the organic solvent and aqueous phase is somewhat perpendicular to the walls of the pore. In the second scenario, the surface is very hydrophobic: the organic solvent wets the silica surface completely so that the interface between the organic solvent and aqueous phase are almost parallel to the walls of the pore. The counterpart of these wetting scenarios, where aqueous phase completely wet the surface is not possible due to the hydrophobic nature of the silica surface. The proposed surface wetting scenarios are illustrated in Figure 5.5. Sharp boundary between cobalt enriched region and cobalt free silica support will only exist if the interface between the organic solvent and aqueous is somewhat perpendicular to the walls of the pore. In other words, when wetting scenario I is favoured over wetting scenario II in the pores.

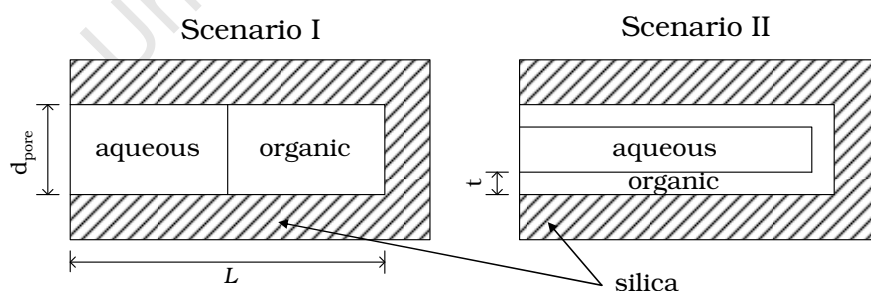


Figure 5.5: Proposed possible wetting scenarios in the pores

The preference of Scenario I over Scenario II was determined by comparing the Gibbs surface free energy (G_s) of each scenario. A sharp boundary will occur, if G_s of Scenario I is less than the G_s of Scenario II. The Gibbs surface free energy (G_s) of the defined systems was determined by taking the sum of $G_{s,ij}$ between the phases exists in the system. $G_{s,phase}$ is defined as

$$G_{s,ij} = \gamma_{ij} A_{ij}$$

where γ_{ij} is the surface tension between phase i and j, and A_{ij} is the surface area between the two phases.

The relationship between the thickness of organic layer (t) and the fraction of pore volume occupied by water (X_w) is

$$X_w = \frac{(d_{\text{pore}} - 2t)^2 (L - t)}{d_{\text{pore}}^2 L}$$

The G_s of Scenario I and Scenario II can then be written as

$$G_{s,1} = \underbrace{\gamma_{wv} \frac{\pi d_{\text{pore}}^2}{4}}_{\text{Area}_{\text{water,air}}} + \underbrace{\gamma_{wo} \frac{\pi d_{\text{pore}}^2}{4}}_{\text{Area}_{\text{water,organic}}} + \underbrace{\gamma_{sw} \pi d_{\text{pore}} L X_w}_{\text{Area}_{\text{water,silica}}} + \underbrace{\gamma_{so} \pi d_{\text{pore}} L (1 - X_w)}_{\text{Area}_{\text{organic,silica}}}$$

$$G_{s,2} = \underbrace{\gamma_{wv} \frac{\pi}{4} (d_{\text{pore}} - 2t)^2}_{\text{Area}_{\text{water,air}}} + \underbrace{\gamma_{ov} \pi \left(\frac{d_{\text{pore}} t}{2} - t^2 \right)}_{\text{Area}_{\text{organic,air}}} + \underbrace{\gamma_{wo} \pi \left((d_{\text{pore}} - 2t)(L - t) + \frac{(d_{\text{pore}} - 2t)^2}{4} \right)}_{\text{Area}_{\text{water,organic}}} + \underbrace{\gamma_{so} \pi \left(d_{\text{pore}} L + \frac{d_{\text{pore}}^2}{4} \right)}_{\text{Area}_{\text{organic,silica}}}$$

The physical properties of n-undecane were approximated with n-hexane. The surface tension of air-water, air-organic and organic-water can be found in literature (Weast, 1983; Overbury *et al.*, 1975). The surface tension of silica-water and silica-hexane was determined by using the three-phase equilibrium defined by Young's equation

$$\gamma_{sw} = \gamma_{sv} + \gamma_{wv} \cos \theta_w$$

$$\gamma_{so} = \gamma_{sv} + \gamma_{ov} \cos \theta_o$$

where γ_{sv} is the surface tension of silica-air (605dyn/cm²; Overbury *et al.*, 1975); γ_{wv} is the surface tension of water-air (71.97dyn/cm²; Weast, 1983); γ_{ov} is the surface tension between n-hexane and air (18.43dyn/cm²; Weast, 1983); θ_w and θ_o is the contact angle of silica-water and silica-hexane respectively. Silica disks (diameter: 15mm, thickness 2mm) with smooth surface were used to determine contact angles, which was made by pressing 2g of crushed silica pellets in a hydraulic press (Specac, Manual 15) with 15ton load. A drop of liquid was placed on top of the silica disk and the contact angle was determined using a goniometer (Ramé-Hart, Model A-100). The contact angle was stable during the measurement of contact angle; measurements were repeated 5 times, each time with a new disk. The measured contact angle of silica-water is 150°±1° and silica-hexane is 6°±1°. The surface tension of silica-water and silica-hexane calculated based on contact angle are 542dyn/cm² and 623dyn/cm² respectively.

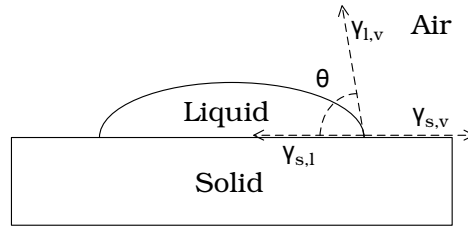


Figure 5.6: Illustration of three-phase equilibrium described by Young's equation

The difference of G_s between Scenario I and Scenario II ($\Delta G_{s,1-2}$) as a function of water fraction was calculated based on the assumption that the pore length is identical to the pore diameter (16nm). $\Delta G_{s,1-2}$ is $-8.3 \times 10^{-17} \text{J}$ at a water fraction of 0.0002 and decreases with increasing water fraction (see Figure 5.7). This suggests that the Scenario I is more stable than Scenario II at these conditions, and this stability increases with an increase in the water to organic ratio in the pores (see Appendix C.1 for Scilab code).

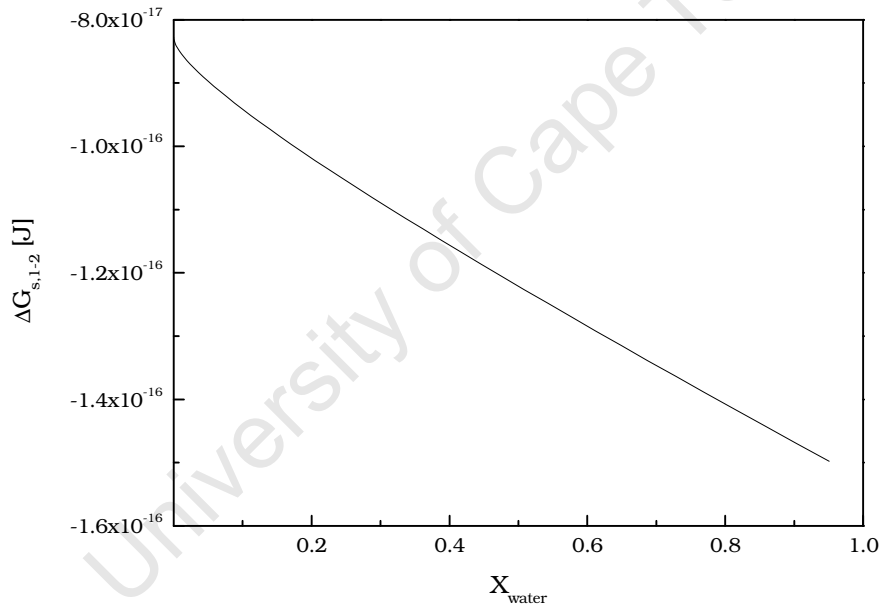


Figure 5.7: Preference of wetting scenario I over scenario II in terms of Gibb's surface energy for pore diameter and pore length of 16nm

The change in the stability of wetting Scenario I ($G_{s,1-2}$) with respect to pore diameter can be described by differentiating $G_{s,1}-G_{s,2}$ with respect to the pore diameter.

$$\frac{d(\Delta G_{s,1-2})}{d(d_{\text{pore}})} = \underbrace{\pi(2t-L)}_{\text{structural}} \gamma_{\text{wo}} - \underbrace{\pi\left(\frac{t}{2}\right)}_{\text{structural}} \gamma_{\text{ov}} + \underbrace{\pi\left(t + \frac{4t^2L}{d_{\text{pore}}^2} - \frac{4t^3}{d_{\text{pore}}^2} - L - \frac{d_{\text{pore}}}{2}\right)}_{\text{structural}} (\gamma_{\text{so}} - \gamma_{\text{sw}})$$

The change of stability with respect to the pore diameter is a function of inter-phase surface tension with its respective structural factor. The structural factor ($\pi(2t-L)$) of inter-phase surface tension between the water and the organic (γ_{wo}) is negative

because the pore length is the dominant factor. The structural factor of $(\gamma_{so} - \gamma_{sw})$ is negative, due to the dominance of the pore length and the pore diameter. This means the derivative of the stability function with respect to the pore diameter will always be negative if γ_{so} is larger than γ_{sw} . Thus, as long as the contact angle between the organic and silica is less than 90° , the preferred wetting scenario (Scenario I) will occur irrespective of the size of the pore diameter.

The derivative of stability function with respect to pore length is

$$\frac{d(\Delta G_{s,1-2})}{dL} = \underbrace{\pi(2t - d_{pore})}_{\text{structural}} \gamma_{wo} + \pi \underbrace{\left(4t - \frac{4t^2}{d_{pore}} - d_{pore} \right)}_{\text{structural}} (\gamma_{so} - \gamma_{sw})$$

Due to the dominance of pore diameter over the thickness of organic phase (t), the derivative of stability function will always be negative if γ_{so} is larger than γ_{sw} . Similar conclusion can be drawn that when contact angle between the organic and silica is less than 90° , the preferred wetting scenario (Scenario I) will always occur irrespective of the pore length. Janssen *et al.* (2006) reviewed the experimentally determined static contact angle between various solutions on silica; they showed that the contact angle of most organic solvent is less than 10° . Therefore, a sharp boundary between cobalt enriched shell and cobalt free silica will always occur irrespective of the size of the pore diameter or pore length. Any organic solvents can adequately cover the inner core of the silica pellet since the contact angle is less than 10° . In this study the choice of *n*-undecane as the organic solvent was based on its boiling point of 194.5°C , which allowed a slow evaporation rate and thus ensuring an even partial evaporation.

Li *et al.* (2008) modified this proposed synthesis method for structured catalyst based on hydrophobicity, by increasing the hydrophobicity of the silica pellet with a surface treatment with trimethyl-chlorosilane. The hydrophobicity of the silica pellet was increased to an extent that the inhibition of impregnation solution can be done by the air trapped inside the pellet during wet impregnation. This further confirms the reasoning for the sharp phase boundary due to the hydrophobic property of silica.

Assuming the porosity of the pellet is uniform throughout the pellet, the size of the cobalt free silica core of the egg-shell type catalyst should be proportional to the fraction of pore volume occupied by organics in the following way

$$\frac{V_{\text{organic}}}{V_{\text{pore}}} = \frac{V_{\text{core}} \epsilon}{V_{\text{pellet}} \epsilon} = \frac{\frac{\pi}{4} d_{\text{core}}^2 (l_{\text{pellet}} - (d_{\text{pellet}} - d_{\text{core}}))}{\frac{\pi}{4} d_{\text{pellet}}^2 l_{\text{pellet}}}$$

The ratio of pellet length to pellet diameter is 1.8, therefore, the above relation can be simplified to

$$\frac{V_{\text{organic}}}{V_{\text{pore}}} = \frac{d_{\text{core}}^2}{1.8d_{\text{pellet}}^2} \left(0.8 + \frac{d_{\text{core}}}{d_{\text{pellet}}} \right)$$

The relative silica core size ($d_{\text{core}}/d_{\text{pellet}}$) of egg-shell type of catalyst was measured by using optical microscopy and SEM images, which were in good agreement. The fraction of pore volume occupied by organics were calculated from the amount of organics left inside the support after partial evaporation relative to the maximum amount of organics that can be filled in the pores (see Appendix C.2 for determination of organic volume required for complete pore filling). The measured relationship between the relative silica core size and the fraction of pore volume occupied by organics is lower than the expected value (see Figure 5.8). This might be attributed to the existence of cracks on the silica support, which increased the apparent cobalt enriched shell thickness and therefore decreased the cobalt free silica core. Another possible explanation is that there is a pore size limit where impregnation solution can not flow through due to capillary pressure, as a result, the impregnation solution would move further into the centre of the pellet, making the observed silica core size less than expected.

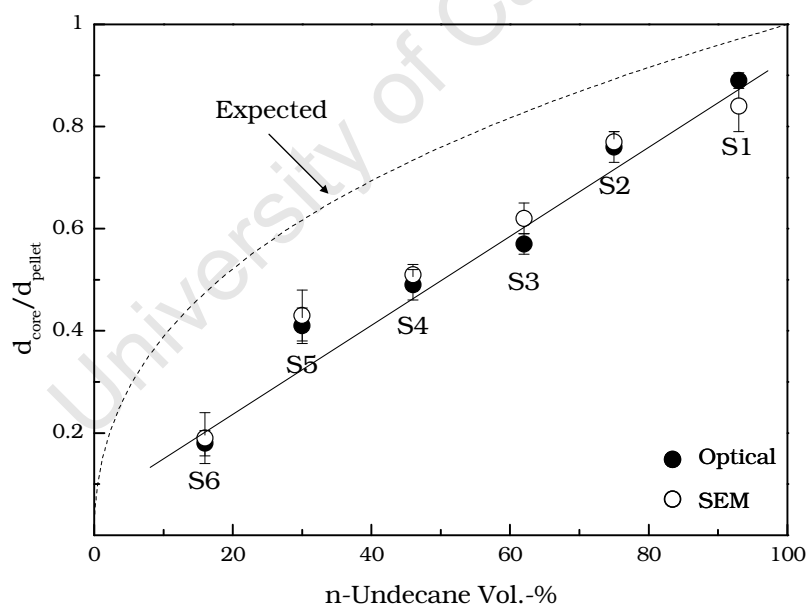


Figure 5.8: Cobalt free silica core size of egg-shell type of catalysts as function of organics filled in the pore.

5.1.3 Intra-pellet Cobalt Distribution of Egg-yolk Type of Catalysts

The optical images of calcined egg-yolk type of catalysts show the existence of a sharp boundary between the apparent cobalt free silica shell and cobalt enriched core (see Figure 5.9). SEM-EDX scan of the calcined catalysts confirms the sharp decrease of cobalt content across the boundary and that the cobalt distribution inside the cobalt enriched core is uniform (see Figure 5.10). This shows that during the leaching stage of egg-yolk type of catalyst synthesis, the organic solvent effectively protected the cobalt metal in the centre of catalyst from contact with the diluted nitric acid. The optical images of spent egg-yolk type of catalysts showed a stable sharp boundary after the exposure to Fischer-Tropsch synthesis conditions for 120 hours. The average value of relative cobalt enriched core size ($d_{\text{core}}/d_{\text{pellet}}$) measured from optical and SEM images of the egg-yolk type of catalysts were within the standard deviation of each other.

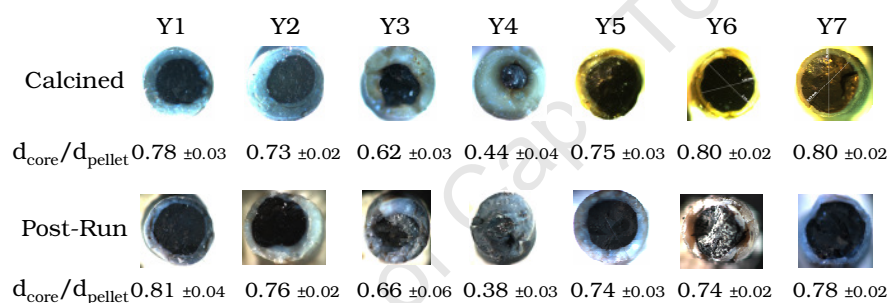


Figure 5.9: Optical microscopy images of egg-yolk type of catalysts

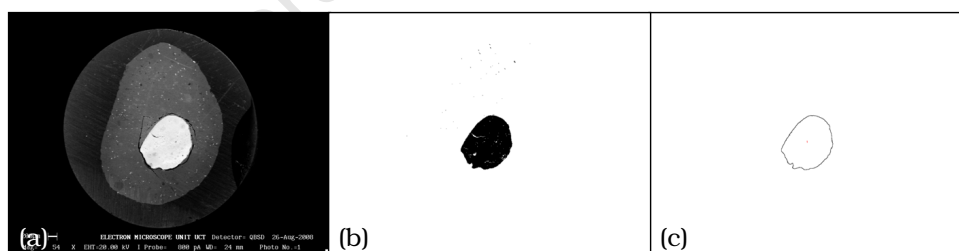


Figure 5.10: Back-Scattered SEM image of Y4 pellet (a) EDX processed image showing concentrated cobalt core (b) Outline image showing the cobalt enriched boundary (c)

During the leaching stage of the synthesis of some of the egg-yolk type of catalysts, catalyst Y1, Y5, Y6 and Y7, the catalyst precursor was brought into contact with diluted acid when the surface of the pellet was still covered by organic solvent (volume of organic solvent used was more than total pore volume). However, their average $d_{\text{core}}/d_{\text{pellet}}$ value of 0.8 falls within standard deviation of each other (see Figure 5.11). This suggests that they have identical relative cobalt enriched core size. It was

observed that the organic solvent on the surface of the pellet was removed as soon as the pellet was introduced into the diluted acid, leaving some of the organic solvent floating on top of the diluted acid. This leads to the suspicion that in this organic, diluted acid and pellet surface system, organic is preferred to be on top of the bulk diluted acid rather than on pellet surface. Some of the organic solvent with in the pores may have been displaced by the diluted acid. As a result, the maximum relative cobalt enriched core size of egg-yolk type of catalyst is limited when the surface of the precursor pellet is covered with organics. However, there is no related information that can be found in literature to support this reasoning.

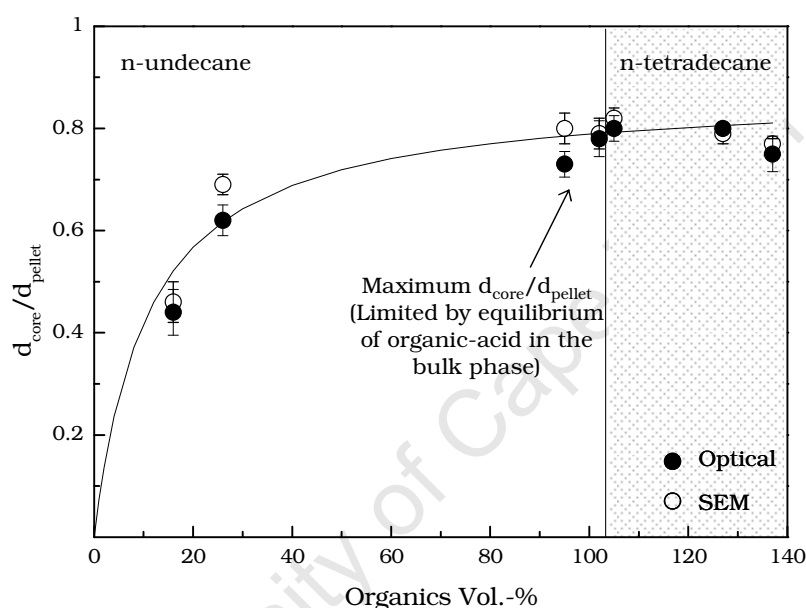


Figure 5.11: Cobalt enriched core size of egg-yolk type of catalysts as function of organics filled in the pore.

5.1.4 Intra-pellet Cobalt Distribution of Egg-white Type of Catalysts

The optical microscopy images of the calcined egg-white type of catalysts show a sharp boundary between the apparent cobalt free silica and inner cobalt enriched ring (see Figure 5.12). The size and the location of the inner cobalt ring of the spent egg-white type of catalysts are statistically the same as those of calcined egg-white type of catalysts. Hence, the egg-white boundary is stable after 120 hours of exposure to the Fischer-Tropsch synthesis conditions (see Figure 5.12). SEM-EDX scan over the calcined egg-white type of catalysts confirms the sharp decrease of cobalt content across the boundaries between cobalt free silica and cobalt enriched region. The distribution of cobalt inside the egg-white boundary is uniform (see Figure 5.13).

The cobalt free core in the egg-white type of catalyst (d_{core}) was formed during the synthesis of egg-shell type of precursor for the synthesis of egg-white type of catalysts. The relationship between the relative size of the cobalt free silica core ($d_{\text{core}}/d_{\text{pellet}}$) and the amount of organic solvent used is identical to those of egg-shell type of catalyst: a linear relationship between the relative silica core size of egg-shell and egg-white type of catalysts with amount of pore volume occupied by organic solvent, is observed. The location of the boundary between the cobalt free silica shell and inner cobalt enriched ring in the egg-white type of catalyst (d_{white}) also displayed a linear relationship with the amount of n-undecane used, as shown in Figure 5.14.

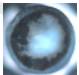
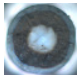
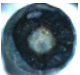

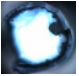



	W1	W2	W3	W4
Calcined				
$d_{\text{white}}/d_{\text{pellet}}$	0.86 ± 0.02	0.78 ± 0.08	0.69 ± 0.04	0.65 ± 0.02
$d_{\text{core}}/d_{\text{pellet}}$	0.63 ± 0.02	0.45 ± 0.06	0.33 ± 0.02	0.23 ± 0.04
Post-Run				
$d_{\text{white}}/d_{\text{pellet}}$	0.83 ± 0.03	0.77 ± 0.03	0.73 ± 0.06	0.67 ± 0.06
$d_{\text{core}}/d_{\text{pellet}}$	0.68 ± 0.02	0.41 ± 0.04	0.35 ± 0.08	0.29 ± 0.04

Figure 5.12: Optical microscopy images of egg-white type of catalysts

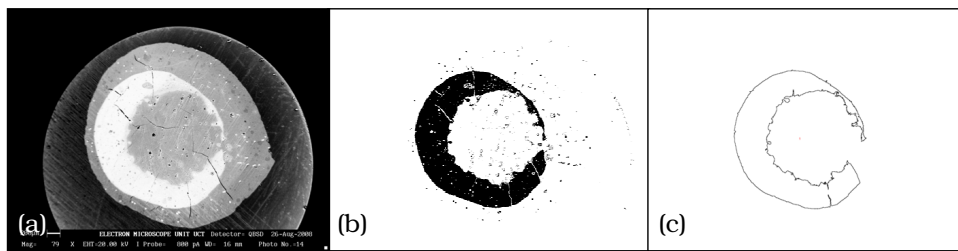


Figure 5.13: Back-Scattered SEM image of W3 pellet (a) EDX processed SEM image showing concentrated cobalt ring (b) Outline image showing the cobalt enriched boundary (c)

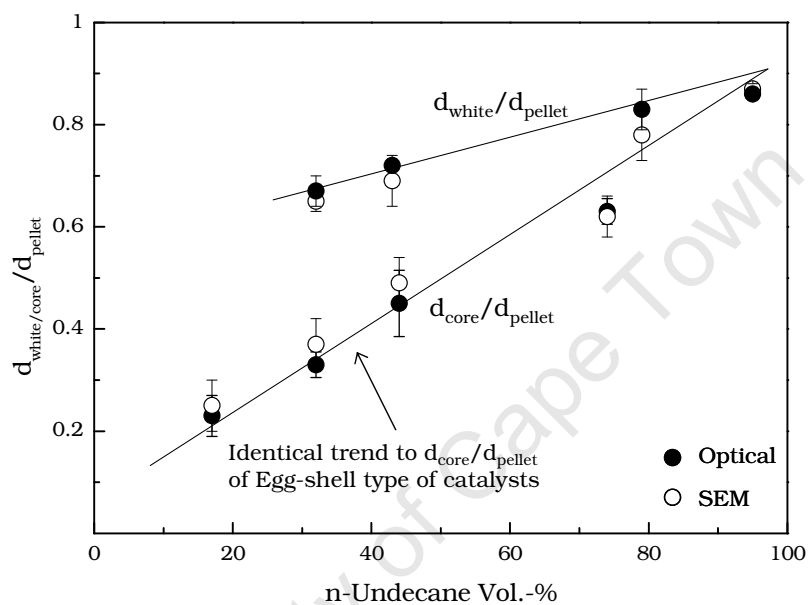


Figure 5.14: Cobalt free yolk size and cobalt enriched white size achieved in egg-white type of catalysts

5.1.5 Cobalt Loading

The cobalt loading of the structured catalysts obtained from AAS and TPR-TPO results is given in Table 5-1. The expected cobalt loading of catalyst synthesised by incipient wetness technique can be calculated from the amount of impregnation solution used per mass of silica, and concentration of cobalt in the impregnation solution. The expected cobalt loading of uniform and egg-shell type of catalyst is 9.1wt.-%. The cobalt loading according to AAS is somewhat lower than the expected value. AAS samples were completely converted to aqueous phase during acid digestion (no residue were found after filter dissolved AAS samples through a filter paper). Therefore, incomplete dissolution of Co_3O_4 is unlikely to be the cause. Cobalt nitrate can absorb moisture in air, thus overestimating the amount of cobalt in the impregnation solution, this can be the reason for lower than expected cobalt loadings. Cobalt loading calculated from TPR-TPO is somewhat higher than the expected value; this can be attributed to poor baseline separation between the oxygen consumption and release peak during TPO. Nevertheless, both results showed that egg-shell type of catalysts with different silica shell thickness and an approximate constant cobalt loading can be synthesised with the developed method. Furthermore, egg-yolk type of catalysts (Y1-Y4) with different cobalt enriched yolk size can be synthesised with an approximate constant cobalt loading. Egg-yolk type of catalysts (Y5-Y7) with constant yolk size with different cobalt loading can also be synthesised. Egg-white type of catalyst (W1-W4) with different inner cobalt enriched ring thickness and approximate constant cobalt loading is achievable. The AAS cobalt loading was used in further calculations.

Table 5-1: Cobalt metal content of structured catalyst determined from AAS and TPR-TPO results

Catalyst Code	$\frac{d_{\text{core}}}{d_{\text{pellet}}}$ †	AAS [wt%]	TPR-TPO [wt%]	Catalyst Code	$\frac{d_{\text{core}}}{d_{\text{pellet}}}$ †	$\frac{d_{\text{white}}}{d_{\text{pellet}}}$ †	AAS [wt%]	TPR-TPO [wt%]
U1	-	8.3	11.8	Y1	0.78	-	8.7	9.9
U2	-	29.0	27.5	Y2	0.73	-	10.0	11.2
S1	0.18	8.2	11.2	Y3	0.62	-	13.7	15.0
S2	0.41	7.9	10.7	Y4	0.44	-	10.8	11.1
S3	0.49	8.1	11.0	Y5	0.77	-	7.8	8.6
S4	0.57	8.0	11.3	Y6	0.79	-	12.5	14.3
S5	0.76	7.9	9.6	Y7	0.80	-	22.0	19.5
S6	0.89	7.7	10.5	W1	0.63	0.86	6.6	7.2
				W2	0.45	0.83	7.0	9.5
				W3	0.33	0.69	7.9	10.5
				W4	0.23	0.67	10.2	11.7

† according to optical microscopy

5.1.6 Catalyst Surface Area and Pore Size

The average pore diameter of structured catalyst was determined by nitrogen physisorption (see Table 5-2). All structured catalysts show negligible deviation much from the pore diameter of the pure silica pellet. This suggests that the integrity of the structure of the silica pellet was not affected by the synthesis method, not even by the acid treatment and hydrogen gas formation during leaching stage of structured catalyst synthesis procedure.

The active metal surface area was calculated according to CO chemisorption. The results show some variation in active metal area. The active metal surface area of the uniform catalyst (U1) is lower than that of the structured catalyst (S1-S6; Y1-Y4; W1-W4), although the cobalt loading was kept approximately constant for all structured catalysts. This may suggest that catalyst pellets experienced mass transport limitation during the reduction process resulting in a decrease in the extent of reduction and hence resulting in a decrease in metal surface, which is discussed further in section 5.1.9.

Table 5-2: Metal surface area and catalyst pore diameter determined from CO chemisorption and N₂ physisorption

Catalyst Code	A _m [m ² /g]	d _{pore} [nm]	Catalyst Code	A _m [m ² /g]	d _{pore} [nm]
U1	1.41	15.23	Y1	1.81	15.52
U2	3.83	15.24	Y2	2.34	14.39
S1	2.25	15.65	Y3	3.92	14.28
S2	1.98	15.79	Y4	2.20	15.36
S3	1.88	15.59	Y5	1.31	18.31
S4	1.70	16.11	Y6	2.01	12.69
S5	2.04	15.96	Y7	3.61	13.80
S6	2.30	15.21	W1	1.47	15.82
Silica	-	15.98	W2	1.12	15.41
			W3	1.65	15.38
			W4	1.99	13.98

5.1.7 Cobalt Oxide Phase of Calcined Catalysts

The XRD spectrum of the structured catalysts (see Figure 5.15) shows the characteristic peaks of the bulk cobalt oxide Co_3O_4 superimposed on characteristic diffraction pattern for silica which decreased with increase in cobalt loading (U2 & Y7).

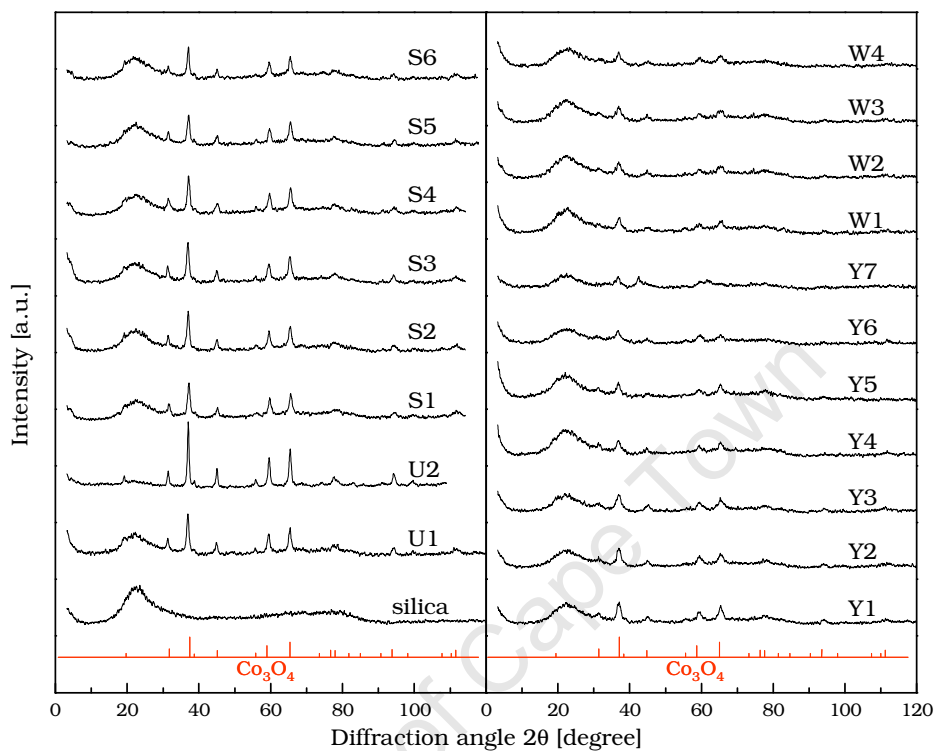


Figure 5.15: XRD spectrum of pure silica support and calcined structured cobalt on silica catalyst

5.1.8 Cobalt Oxide Crystallite and Cluster Sizes

The average cobalt crystallite sizes in the structured catalysts were determined using TEM, XRD and CO-chemisorption (see Table 5-3). The different techniques agree well with each other. Uniform catalysts (U1 and U2) showed an increase in cobalt crystallite size with increase in cobalt loading as previously reported by Iglesia *et al.* (1993) and Ernst *et al.* (1999). Cobalt crystallite size estimation using CO chemisorption shows that all catalyst have cobalt crystallite size are larger than 6nm. The Fischer-Tropsch synthesis becomes structure insensitive above this crystallite diameter according to Bezemer *et al.* (2006).

Table 5-3: Experimentally determined cobalt crystallite size of structured catalysts

Catalyst Code	TEM [nm]	XRD [nm]	Chemisorp [nm]	Catalyst Code	TEM [nm]	XRD [nm]	Chemisorp [nm]
U1	10.9	11.8	9.2	Y1	7.4	6.6	7.0
U2	15.3	17.0	14.9	Y2	7.4	6.5	7.8
S1	11.3	10.8	9.1	Y3	7.7	5.5	6.5
S2	9.4	11.4	11.3	Y4	8.9	6.9	7.1
S3	9.5	10.8	9.5	Y5	7.9	9.3	10.9
S4	9.4	10.3	10.9	Y6	7.6	5.9	10.8
S5	11.7	10.2	10.8	Y7	6.6	5.8	9.3
S6	10.0	13.3	9.3	W1	9.0	7.3	8.0
				W2	8.5	7.1	10.9
				W3	6.9	7.4	8.9
				W4	8.4	7.7	9.2

TEM images show that cobalt crystallites are found in clusters with a size range of 100nm to 120nm. This is commonly observed in supported cobalt catalyst prepared from cobalt nitrate solutions (Feller *et al.*, 1999). No obvious trend was observed in cluster size with cobalt loading (see example in Figure 5.16) and catalyst structure.

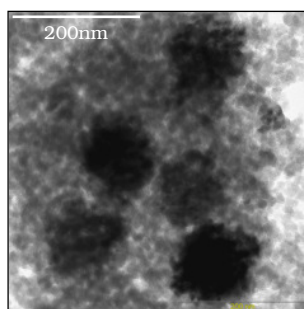


Figure 5.16: An example of TEM images showing cobalt clusters in catalysts (S2)

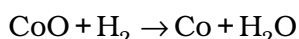
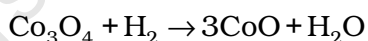
5.1.9 Reducibility of Structured Catalysts

The degree of reduction was calculated from TPR-TPO analysis performed on reduced catalyst which showed variation among the structured catalysts. This suggests that the interaction between the surface cobalt species and silica support is different in structured catalysts (Table 5-4).

Table 5-4: Degree of reduction determined from TPR-TPO

Catalyst Code	R ^{o †} [%]	Catalyst Code	R ^{o †} [%]
U1C	73.0	Y1	63.0
U1	65.9	Y2	50.1
U2	81.4	Y3	57.3
S1	70.3	Y4	62.6
S2	75.6	Y5	38.5
S3	74.8	Y6	32.5
S4	79.7	Y7	42.6
S5	80.2	W1	51.3
S6	79.9	W2	52.2
		W3	48.1
		W4	43.3

The reduction of pure cobalt oxide has been shown to be a two step process (Brown *et al.*, 1982; van't Blik and Prins, 1986; Viswanathan and Gopalakrishnan, 1986). The sequential reduction is described as the conversion of Co₃O₄ to divalent cobalt (CoO) at about 300°C, followed by the reduction of divalent cobalt to metallic cobalt at 400°C (Sexton *et al.*, 1986; Kraum and Baerns, 1999; Borg *et al.*, 2007).



Silica supported catalyst may show reduction peaks at higher temperatures due to the reduction of cobalt (hydro)silicates (van Steen *et al.*, 1996).

To investigate the influence of mass transfer limitation during the reduction, TPR analyses were performed on calcined uniform powder (U1C) and pellet (U1). Both spectrums show a reduction profile with three maxima at 200°C, 300°C and 400°C, tailing off at 900°C. The three maxima correspond to the reduction of undecomposed cobalt nitrate (Kogelbauer *et al.*, 1996), the reduction of Co₃O₄ to CoO, and the reduction of trivalent cobalt to divalent cobalt to metallic cobalt. The hydrogen consumption attributed to the decomposition of cobalt nitrate is less for the catalyst pellet (U1) compared to the crushed catalyst pellet (U1C). Cobalt nitrate can decompose both thermally and under the influence of hydrogen. The thermal nitrate

[†] degree of reduction

decomposition may dominate over the hydrogen assisted decomposition in the catalyst pellet due to mass transfer limitation resulting in a lower observed hydrogen consumption. Furthermore, it can be observed the peak maxima obtained with the catalyst pellet are shifted towards higher temperatures, which might be ascribed to mass transfer limitation during temperature programmed reduction. The amount of hydrogen attributed to the reduction of cobalt hydrosilicate (hydrogen consumption between 600°C-900°C) seems to be unaffected by the size of the catalyst pellets/powder. This implies that the cobalt hydrosilicate are not formed during the reduction process but either during the calcination process or during synthesis of the catalyst. The formation of hydrosilicate during catalyst synthesis can be explained by the electrostatic interaction between the polarised surfaces during adsorption of cobalt-nitrate on silica, which is a function of pH.

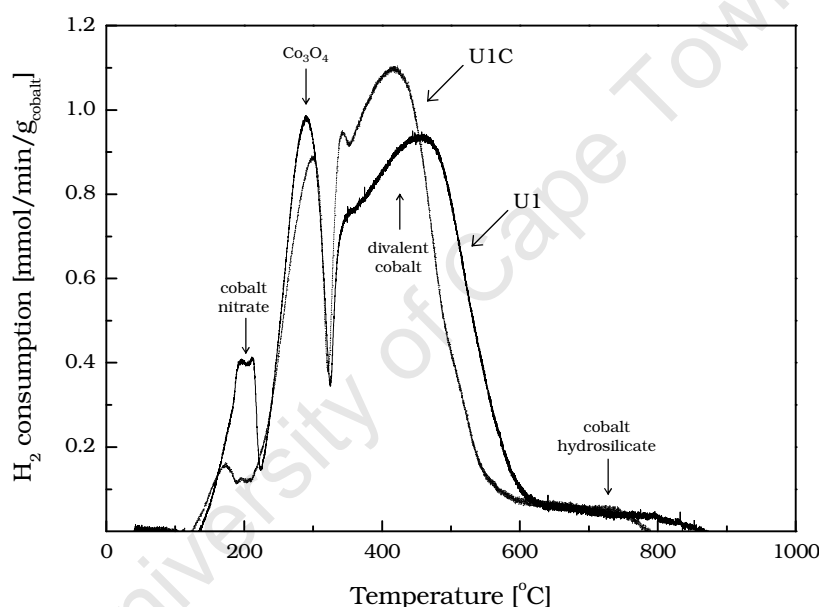


Figure 5.17: TPR spectrum of calcined uniform powder (U1C) and pellet (U1) catalysts

The TPR spectra of reduced catalyst were used to evaluate the degree of reduction. Calcined samples were reduced in-situ in the TPR-TPO unit, with hydrogen flow rate of 90ml(STP)/min/g_{silica} at 350°C for 16 hours with heating rate of 5°C/min, and cooled down in argon prior TPR. The TPR spectrum of reduced uniform catalyst in powder form (U1C) is shown in Figure 5.18 with hydrogen consumption rate [mmol/min] per gram of cobalt. The TPR spectrum shows a broad peak between 400°C to 700°C, which can be attributed to the reduction of at least two species with maxima at ca. 500°C and ca. 650°C. The maxima can be ascribed to the reduction of residual cobalt oxide (CoO) and cobalt hydrosilicates (van Steen *et al.*, 1996).

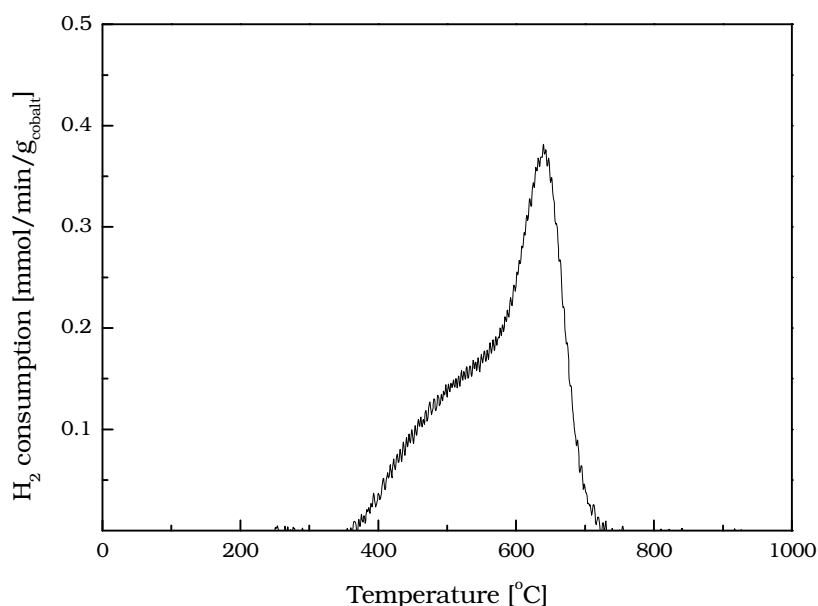


Figure 5.18: TPR spectrum of reduced uniform powder catalyst (U1C)

TPR spectrum of the reduced uniform catalyst in its pellet form (U1) shows broad peak from 400°C to 950°C with two maxima at 500°C and 800°C. The maximum at 800°C can be attributed to the reduction of cobalt silicate (Maruri, 2003). The second maxima of the broad peak shifted from 650°C for the reduced U1C to 800°C. This might be attributed to mass transfer limitations in the reduction process. Water may build-up within the catalyst pore as a result of mass transport limitation which encourages silicate formation (Puskas *et al.*, 2006). These results suggests that the cobalt hydrosilicate formed during reduction of catalyst will convert to stronger bonded cobalt silicate when the reduction is performed under mass transport limitation, since the degree of reduction of uniform pellet (65.9%) is similar to uniform powder (63.9%).

The TPR analysis of the reduced high loading uniform pellets (U2) shows a lower H_2 consumption per cobalt than that of U1 has recorded (see Figure 5.19). This implies a higher degree of reduction for the catalyst with a higher cobalt loading. This is might be attributed to the larger cobalt crystallite in catalyst U2 (14.9nm) than in catalyst U1 (9.2nm). This higher degree of reduction might also be related to the increase in cobalt density, the reduced cobalt crystallites may supply activated hydrogen to non-reduced cobalt crystallites, and thus enhancing the degree of reduction.

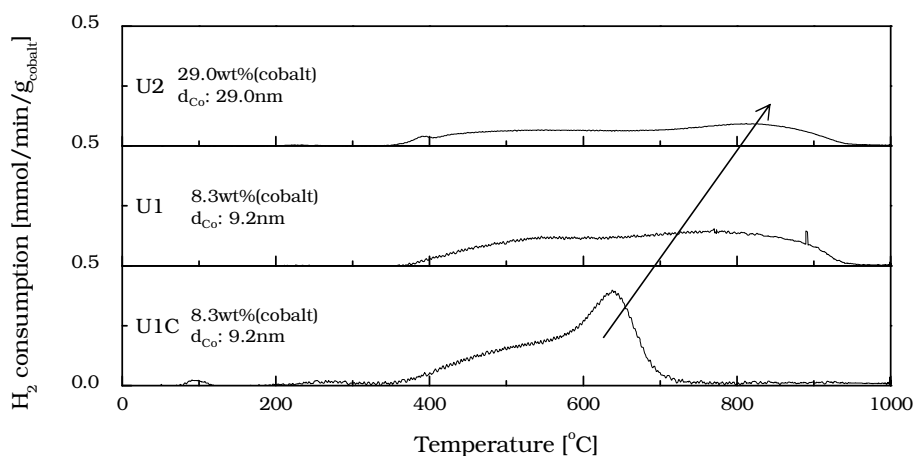


Figure 5.19: TPR spectrum of reduced uniform catalysts (U1C, U1, U2)

The TPR spectrums of reduced egg-shell type of catalysts show a broad peak between 400°C and 950°C, which consists of two maxima at 600°C and ca. 800°C (see Figure 5.20). The second peak maximum shifts towards 900°C as thickness of the cobalt enriched shell of the egg-shell type of catalyst increases. This suggests that internal mass transport limitation during reduction favours the formation of stronger bonded cobalt silicate. It might be concluded that the reduction of uniform and egg-shell type of catalyst is limited by the existence of cobalt silicate formed during reduction.

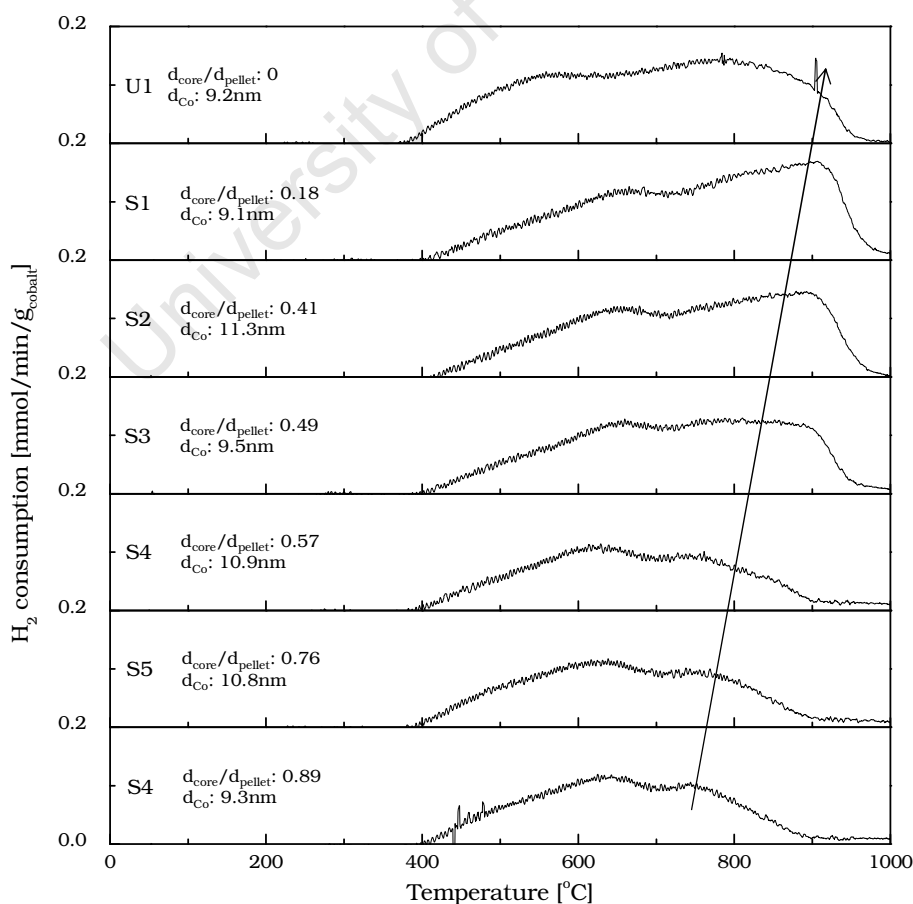


Figure 5.20: TPR spectrums of reduced egg-shell type of catalysts

The TPR spectrums of the reduced egg-yolk type of catalysts with increasing cobalt free silica shell thickness (Y1, Y2, Y3, and Y4) show the same trend as the egg-shell type of catalysts with increasing cobalt enriched shell thickness (see Figure 5.21). This confirms that the formation of stronger bonded cobalt silicate is preferred when mass transport limitation occurs during reduction. However, the degree of reduction of egg-yolk type of catalyst is significantly lower than of the egg-shell type of catalysts (Table 5-4); therefore mass transport limitation during reduction is not the only factor in egg-yolk type of catalyst. The syntheses of egg-yolk type of catalyst involved an acid leach step which didn't occur in the synthesis of egg-shell type of catalysts. In this step most of the cobalt in the outer layer of the pellet was dissolved and washed out of the pores. Some of the cobalt may still be adsorbed on the surface of silica or may have been ion exchanged during the acid leach step. This strongly adsorbed cobalt is most likely to exist as cobalt silicate.

The amount of strongly bonded cobalt silicate per gram of cobalt remains approximately constant for the reduced egg-yolk type of catalysts with identical cobalt free silica shell thickness and increasing cobalt loadings (Y5, Y6, and Y7). The catalysts with a higher loading show a shift in the reduction of some of the strongly bonded cobalt silicate to lower temperatures. This might be attributed to the larger cobalt particles of the high loading catalyst which has low cobalt dispersion. It can be concluded that the reduction of egg-yolk type of catalyst is limited by the formation of cobalt silicate during reduction and possibly during the leaching stage of synthesis.

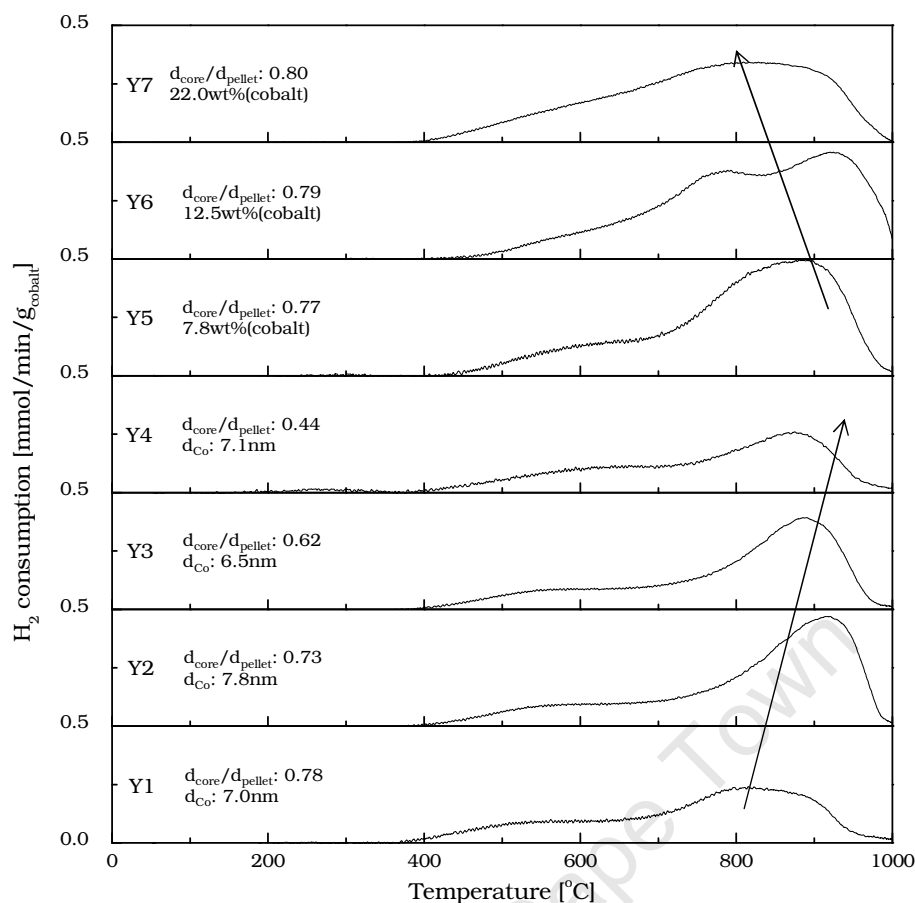


Figure 5.21: TPR spectrums of reduced egg-yolk type of catalysts

The TPR spectrums of the reduced egg-white type of catalysts also show the existence of cobalt silicate (see Figure 5.22). The amount of cobalt silicate increases with decreasing size of the inner cobalt enriched ring of the egg-white type of catalysts. The degree of reduction of egg-white type of catalyst is also significantly lower than the degree of reduction of egg-shell type of catalysts. The synthesis of egg-white type of catalysts involved exposure to diluted nitric acid, which may have resulted in the formation of cobalt silicate.

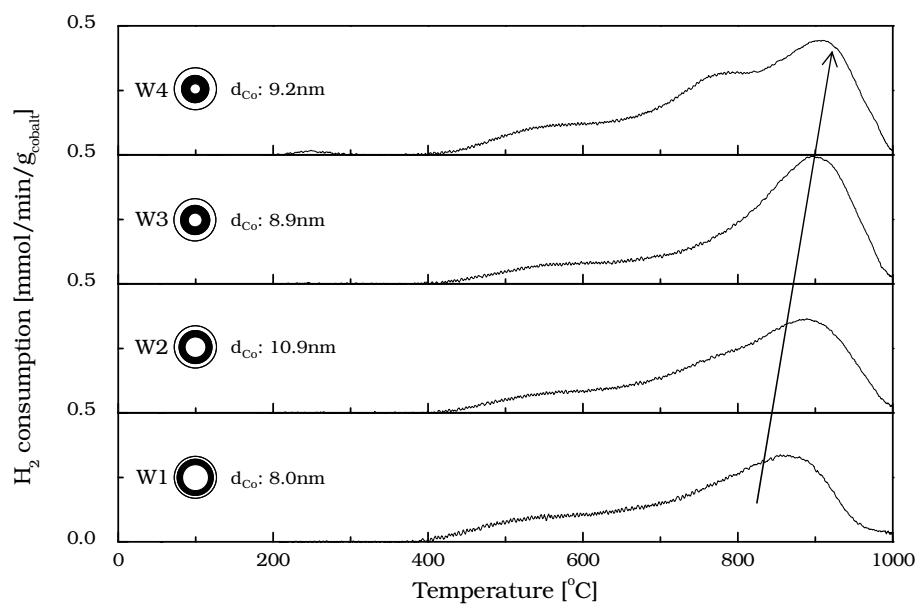


Figure 5.22: TPR spectrums of reduced egg-white type of catalysts

5.2 Fischer-Tropsch Activity of Structured Catalysts

5.2.1 External Mass Transport Tests in Slurry Phase Set-up

To ensure that the observed reaction rate is not limited by the rate of external mass transfer in the slurry reactor, the reduced uniform powder (U1C) was tested at the lowest gas velocity and highest CO consumption rate in this study (22.5ml(STP)/min, 240°C). The stirring speed was incrementally decreased from 860rpm to 280rpm and then re-tested at 860rpm. The CO conversion started from 90% at a stirring speed of 860rpm and decreased to 80% at a stirring speed of 280rpm. However, when the stirring speed was re-adjusted to 860rpm, the CO conversion remained at 80% (see Figure 5.23). Therefore, the initial drop in catalyst activity was due to catalyst deactivation. It can be concluded that there is no change in the CO consumption rate due to the stirring speed between 280rpm to 860rpm. Hence the reaction rate is not limited by external mass transport at a rate of CO consumption rate less than 22.5ml(STP)/min with stirring speeds between 280-860rpm using powdered catalysts.

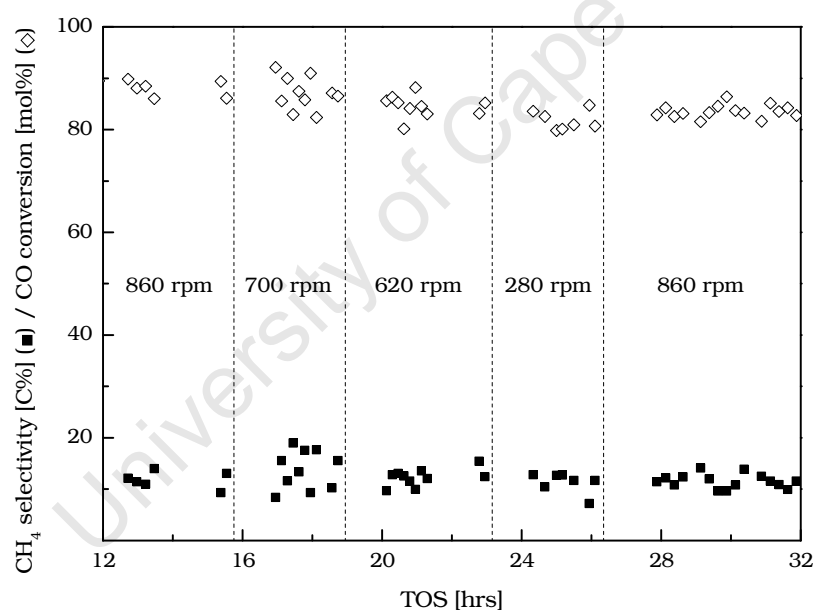


Figure 5.23: Effect of stirring speed on CO consumption and CH₄ selectivity of catalyst U1C at 240°C and 14.1ml/min/g_{catalyst} (STP)

A hypothetical film of wax surrounding the catalyst pellet due to the fixation of catalyst pellet in a mesh-wire basket may act as a mass transport boundary layer and may introduce external mass transport limitations in the testing of catalyst pellets in the slurry reactor. The existence of such an external mass transport boundary layer was tested using the uniform catalyst pellet (U1) by incrementally varying the stirring speed between 148-835rpm. The stirring speed was incrementally decreased from 408rpm to 148rpm and subsequently increased to 835rpm and then returned to

408rpm. When the stirring speed was decreased to below 408rpm, a decrease in the CO conversion and an increase in the CH₄ selectivity was observed. No changes in the CO conversion or in CH₄ selectivity was observed with stirring speeds between 408rpm to 835rpm (see Figure 5.24). Thus, a stirring speed higher than 408rpm can effectively remove this external mass transport boundary layer. Hence, the testing of structured catalyst pellets was performed at stirring speed of 500rpm in the modified slurry reactor.

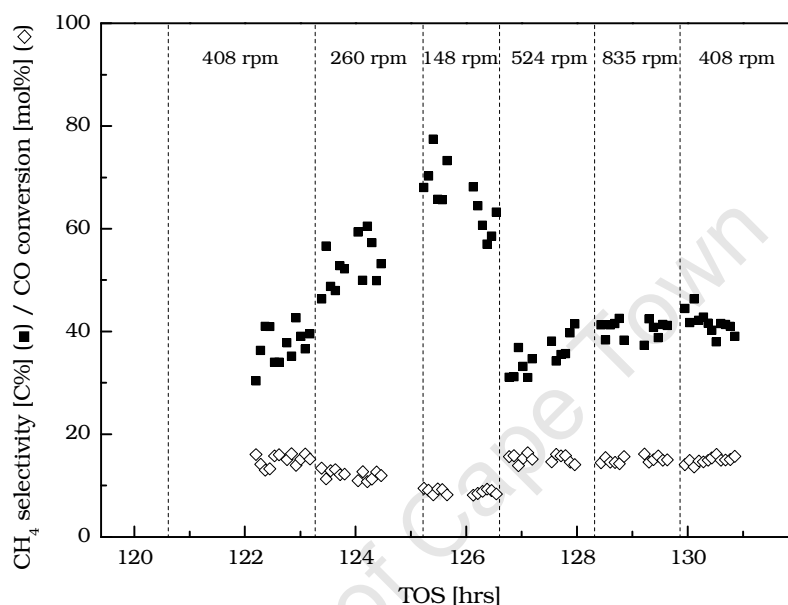


Figure 5.24: Effect of stirring speed on CO consumption and CH₄ selectivity of catalyst U1 (220°C and 13.8mℓ/min/g_{catalyst} (STP))

5.2.2 Catalyst Deactivation

The activity of all catalyst declines with time on stream. It takes approximately 10-15 hours before a constant conversion level is achieved (see Figure 5.25). The catalysts are relatively stable after the initial deactivation. No significant further deactivation was observed up to the end of 120 hours testing period.

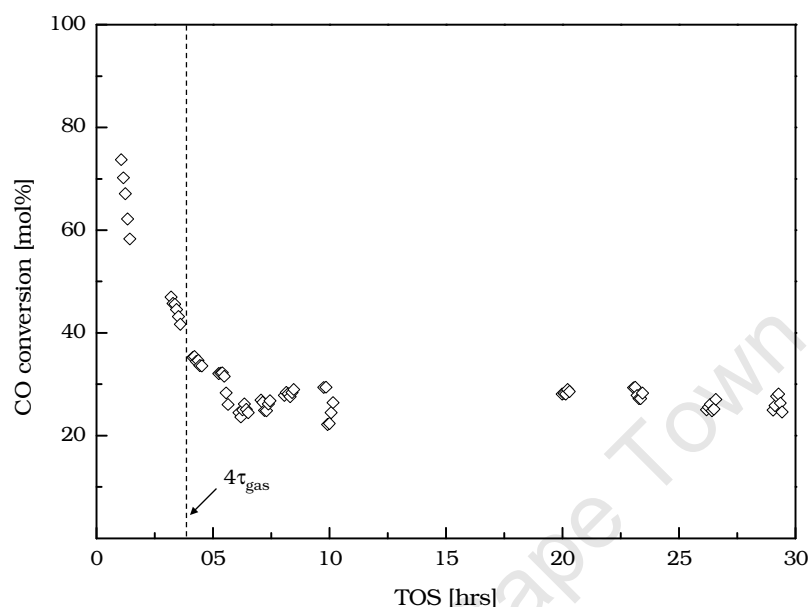


Figure 5.25: Deactivation of the uniform powder catalyst U1C as a function of time on stream

The gases in a slurry reactor are well mixed and, as a result, the extent of catalyst deactivation is difficult to assess. The exit gas concentration in an ideal continuous-stirred tank reactor (Fogler, 1999) can be described as

$$C(t) = C(0)e^{-t/\tau}$$

where $C(t)$ is the concentration of the exit gas, $C(0)$ is the inlet gas concentration, and τ is the space time.

This means that the exit concentration should approach 98.2% of the real steady-state system when t is 4 times greater than space time. The catalyst activity at steady-state was compared to the activity after 4 times the residence time of the gas within the reactor (see Table 5-5), as an indication of the extent of deactivation.

Table 5-5: Initial deactivation of structured catalyst operating at 220°C by comparing the CO conversion at steady-state (24hrs online) and the CO conversion at 4 times the space time

Catalyst	Syngas Feed [†]	M _{catalyst} [g]	X _{4τ} [%]	X _{ss,220} [%]	Activity Loss [‡]
U1C	14.1	5.54	35	26	26
U1	13.8	5.44	37	26	30
U2	55.7	1.85	25	14	46
S1	13.8	5.59	64	48	25
S2	13.8	5.82	57	41	28
S3	13.7	5.94	54	40	26
S4	13.8	5.64	56	34	39
S5	13.8	5.59	63	40	37
S6	13.8	5.83	76	56	26
Y1	15.1	5.02	44	21	52
Y2	17.4	4.91	41	19	54
Y3	23.8	4.62	36	12	67
Y4	18.8	4.90	35	10	71
Y5	13.9	6.02	30	17	43
Y6	13.9	5.90	34	11	68
Y7	13.9	6.18	80	23	71
W1	11.6	5.21	49	27	45
W2	12.2	5.34	30	11	63
W3	13.6	4.87	51	25	51
W4	17.7	4.75	31	10	68

[†] ml/min/g_{catalyst} (STP); [‡] X_{ss,220}/X_{4τ} [%]

The extent of catalyst deactivation estimated in this manner is thus a conservative estimate, since the real extent of catalyst deactivation will be larger. According to the CO conversion data, it can be stated that the catalysts lose at least 25% of their activity between 4 times the residence time of the gas and 24 hours on stream. This extent of catalyst deactivation might be ascribed to an effective reduction in the available metal surface area either due to sintering or coking (Saib *et al.*, 2006; Moodley *et al.*, 2009). The extent of deactivation is slightly affected by the size of the catalyst pellet, since the extent of catalyst deactivation for the catalyst U1 in powder form is less than the decline in activity observed for the same catalyst as a pellet. This implies that mass transport limitation may aggravate the extent of catalyst deactivation. Mass transfer limitations results in an increase in the local concentration of the product compound water. Water is known to enhance sintering (Dry, 1981; Forzatti and Lietti, 1999; Bartholomew, 2001; Moulijn *et al.*, 2001). Hence, it might be speculated that the increase in the local water concentration enhanced the catalyst deactivation. Furthermore, it is clear that the extent of deactivation increases with increasing metal loading (catalyst U2 versus catalyst U1). It might be postulated that

the increase metal density will result in higher likelihood for sintering due to the closer proximity of metal crystallites.

The egg-shell type of catalysts seems to be relatively less affected by catalyst deactivation, with the exception of the egg-shell type of catalysts with a relative diameter of the cobalt-free core between 0.6 and 0.8 (S4 and S5), which lose up to 40% of their activity. The local metal density increases with increasing diameter of the cobalt-free core (or with decreasing shell-thickness), which would result in an increase in the extent of catalyst deactivation. However, the extent of internal mass transport limitation is expected to be reduced with decreasing shell-thickness.

The extent of catalyst deactivation is severe for the egg-yolk type of catalysts and becomes more severe with a decrease in the cobalt-enriched core size in egg-yolk type of catalyst with similar cobalt loading (Y1-Y4). The extent of catalysts deactivation is also more severe in egg-yolk type of catalyst with similar cobalt-enriched core size (Y5-Y7), but with an increase in cobalt loading. This indicates that the local metal density is an important variable in the early-stage catalyst deactivation of cobalt-based catalyst in the Fischer-Tropsch synthesis.

In the case of egg-white type of catalysts, the extent of catalyst deactivation seems to increase with a decrease in unit volume of cobalt-enriched region inside the catalyst pellet at constant cobalt loading, again suggesting that catalyst deactivation is enhanced when cobalt particles are closer to each other.

The difference in the extent of deactivation of the various catalysts needs to be taken into consideration when evaluating the behaviour of the structured catalyst.

5.2.3 Internal Mass Transport in Slurry Phase Set-up

The structural parameter (χ) can be interpreted as the ratio of reactivity against pore radius of catalyst pellet. Therefore, it can be seen as the inherited internal mass transport property of a catalyst pellet. The experimental data of Iglesia *et al.* (1995) showed the C5+ selectivity peaked between structural values of 100-1000 ($\times 10^{-16} \text{ m}^{-1}$). The structural parameter of the tested structured catalyst was determined by incorporating the definition of Iglesia *et al.* (1995) with structure specific metal density function ($\sigma_{\text{structure}}$). The structure parameter ranged from 47 to 1775 ($\times 10^{-16} \text{ m}^{-1}$).

$$\sigma_{\text{uniform}} = 1; \sigma_{\text{egg-shell}} = \frac{r_p^2}{r_p^2 - r_c^2}; \sigma_{\text{egg-yolk}} = \left(\frac{r_p}{r_c}\right)^2; \sigma_{\text{egg-white}} = \frac{r_p^2}{r_w^2 - r_c^2}$$

The experimental effectiveness factor (η') of structure catalyst was estimated by assuming the CO consumption rate of the uniform crushed catalyst (U1C) is the consumption rate in the absence of internal mass transport limitation. These values ranged from 0.22 to 1.18 which indicates the presence of internal mass transport limitation albeit the mixing effect of the modified CSTR was not taken into consideration.

Table 5-6: Structural parameter of synthesized catalyst and their effectiveness factors at various reaction temperatures

Catalyst	χ [$\times 10^{-16} \text{ m}^{-1}$]	η'_{220} [-]	η'_{230} [-]	η'_{240} [-]
U1C	47	1.00	1.00	1.00
U1	296	0.98	0.93	0.83
U2	926	0.69	0.59	0.54
S1	270	1.03	0.95	0.76
S2	302	1.00	0.88	0.80
S3	339	1.02	0.86	0.79
S4	377	0.97	0.92	0.78
S5	595	0.95	0.87	0.75
S6	595	1.18	1.03	0.83
Y1	455	0.61	0.52	0.43
Y2	597	0.57	0.47	0.40
Y3	1134	0.48	0.41	0.33
Y4	1775	0.33	0.25	0.22
Y5	441	0.63	0.58	-
Y6	622	0.27	0.28	-
Y7	1094	0.31	0.25	0.22
W1	613	0.57	0.46	0.40
W2	605	0.42	0.42	0.38
W3	741	0.60	0.49	0.41
W4	820	0.31	-	-

A reaction-diffusion pellet model inside a CSTR model was derived to confirm the observed internal mass transport limitation in structured catalysts. The internal heat transfer limitation in the catalyst pore was neglected. The Prater number, which is defined as the maximum temperature difference in the pores with respect to the pellet surface temperature, was calculated for a heat of reaction of 215kJ/mol (UIC), CO diffusivity of $17.4 \times 10^{-9} \text{ m}^2/\text{s}$ (Erkey *et al.*, 1990), thermal conductivity (κ_t) of 0.2W/m/K (Sasol Fischer-Tropsch wax; Reynhardt, 1985).

$$\beta = \frac{-\Delta H_{\text{rxn}} D_{\text{CO}} C_{\text{CO,S}}}{\kappa_t T_S} = 1.35 \times 10^{-3}$$

This means that at the surface temperature of 493K, the maximum temperature difference in the pores is only 0.7K. The thermal conductivity of silica at 500K is 1.7W/m/K (Liley *et al.*, 2001), therefore the calculated Prater number is the worst case scenario.

The reaction-diffusion model was derived by assuming a steady-state condition inside an open-ended cylinder with a vertical orientation (see Figure 5.26). The CO mass balance is then

$$\overbrace{W_{\text{CO}} \times l_{\text{pellet}} \times 2\pi r|_r}^{\text{Mass In}} - \overbrace{W_{\text{CO}} \times l_{\text{pellet}} \times 2\pi r|_{r+\Delta r}}^{\text{Mass Out}} + \overbrace{R_{\text{volume}} \times l_{\text{pellet}} \times 2\pi r \times \Delta r}^{\text{Generation}} = 0$$

where W_{CO} is mass flux of CO and R_{volume} is rate of reaction per unit volume of catalyst.

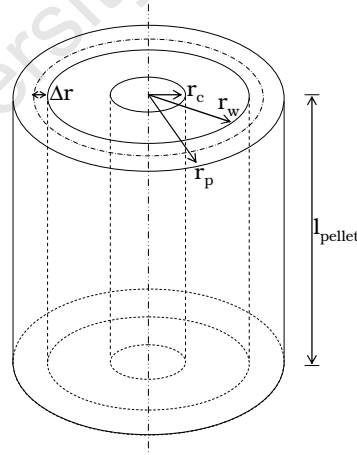


Figure 5.26: Differential volume element considered

By taking the limit of the above equation as Δr approaches 0, realising that the mass flux is concentration driven ($W_{\text{CO}} = -D_{\text{CO}}(dC_{\text{CO}}/dr)$), and using intrinsic reaction rate expression as suggested by Yates and Satterfield (1991) in a metal surface based form; the mass balance is then

$$\frac{d^2 C_{CO}}{dr^2} = -\frac{1}{r} \frac{dC_{CO}}{dr} + \frac{k_{(r)} C_{CO} C_{H_2}}{(1 + k_{ads} C_{CO})^2} \frac{\rho_{co^*} \sigma_{structured}}{D_{CO}}$$

where D_{CO} is diffusivity of CO; $k_{(r)}$ is position dependent, cobalt metal surface based rate constant; ρ_{co^*} is the average metal surface density of active cobalt in $[m^2/cm^3]$ to account for the difference in cobalt loading and reducibility due to internal mass transport limitation during reduction, which is defined as

$$\rho_{co^*} = \frac{S_{co^*}}{V_{pellet}} = \frac{[m_{CO^*}^2]/[g_{catalyst}]}{V_{pellet} [g_{silica}/g_{catalyst}]} = \frac{[m_{CO^*}^2]/[g_{catalyst}]}{\rho_{silica} (1 - L_{co}^o)}$$

where ρ_{silica} is the unit volume of silica support, L_{co}^o is the cobalt loading according to AAS.

The metal density function ($\sigma_{structured}$) is catalyst structure type specific, and defined below. It converts the average metal density of the pellet to the metal density within the cobalt enriched region in each structured catalyst type.

$$\sigma_{uniform} = 1; \sigma_{egg-shell} = \frac{r_p^2}{r_p^2 - r_c^2}; \sigma_{egg-yolk} = \left(\frac{r_p}{r_c}\right)^2; \sigma_{egg-white} = \frac{r_p^2}{r_w^2 - r_c^2}$$

Rate of reaction is only greater than 0 in the cobalt enriched region in structured catalyst. Thus, the rate constant is a function of pellet radius.

The boundary conditions for the mass balance are

$$C_{CO}|_{r=r_p} = C_{CO,S}; \left. \frac{dC_{CO}}{dr} \right|_{r=0} = 0$$

The H_2/CO usage ratio was assumed to be the average experimental value of 2.2 ± 0.2 . The mass balance of H_2 is then

$$\frac{d^2 C_{H_2}}{dr^2} = -\frac{1}{r} \frac{dC_{H_2}}{dr} + 2.2 \frac{k_{(r)} C_{CO} C_{H_2}}{(1 + k_{ads} C_{CO})^2} \frac{\rho_{co^*} \sigma_{structured}}{D_{H_2}}$$

with the following boundary condition

$$C_{H_2}|_{r=r_p} = C_{H_2,S}; \left. \frac{dC_{H_2}}{dr} \right|_{r=0} = 0$$

The intrinsic Fischer-Tropsch rate constant was determined by using the experimental data of uniform powder catalyst (U1C) at steady state. The CO inhibition constant was taken to be the values proposed by Yates and Satterfield ($22.26 MPa^{-1}$ at $220^\circ C$ and $11.61 MPa^{-1}$ at $240^\circ C$).

Table 5-7: Summary of rate constants of uniform powder catalyst in modified slurry reactor

Reaction Temperature	$k_{(r)}$ [$\frac{\text{mmol}}{\text{s m}^2} \frac{\text{cm}^6}{\text{mmol}^2}$]	k_{ads} [cm ³ /mmol]
220°C	127	423
230°C	112	322
240°C	76	221

The rate constant ($k_{(r)}$) decreases with increasing temperature. This implies that the activation energy for the intrinsic Fischer-Tropsch reaction is negative with respect to gas phase carbon monoxide. This has been predicted for stepped CO{101 $\bar{2}$ } and CO{11 $\bar{2}$ 4} surfaces (Ge and Neurock, 2006). It should however be noted that the heat of adsorption in the Yates and Satterfield expression was proposed to be -68kJ/mol, which is lower than the DFT-predicted heat of adsorption for CO. The activation energy of the observed rate of reaction is positive (ca. 64kJ/mol), due to the strong influence of the inhibition term in the Yates and Satterfield equation.

Typically, the activity performance of the pellet can be evaluated by comparing the effectiveness factor which is defined as

$$\begin{aligned}
 \eta &= \frac{\text{overall rate within structured catalyst}}{\text{rate of reaction at catalyst surface (absence of transport limitation)}} \\
 &= \frac{(2\pi r_p l_{\text{pellet}}) D_{\text{CO}} \left. \frac{dC_{\text{CO}}}{dr} \right|_{r=r_p}}{(\pi r_p^2 l_{\text{pellet}} \rho_{\text{co}^*}) \left(k_{(r)} C_{\text{CO},S} C_{\text{H}_2,S} / (1 + k_{\text{ads}} C_{\text{CO},S})^2 \right)} \\
 &= \frac{2D_{\text{CO}} (1 + k_{\text{ads}} C_{\text{CO},S})^2}{r_p \rho_{\text{co}^*} k_{(r)} C_{\text{CO},S} C_{\text{H}_2,S}} \left. \frac{dC_{\text{CO}}}{dr} \right|_{r=r_p}
 \end{aligned}$$

In order to compare the derived reaction-diffusion model with a similar model proposed by Iglesia *et al.* (1995), the mass balances was made dimensionless by introducing the following dimensionless parameters

$$\psi_{\text{CO}} = \frac{C_{\text{CO}}}{C_{\text{CO},S}} ; \psi_{\text{H}_2} = \frac{C_{\text{H}_2}}{C_{\text{H}_2,S}} ; \lambda = \frac{r}{r_p}$$

Substituting the above parameters and introducing Thiele modulus and adsorption constant

$$\begin{aligned}
 \Phi &= r_p \sqrt{\frac{k_{(r)} C_{\text{H}_2,S} \rho_{\text{co}^*} \sigma_{\text{structured}}}{D_{\text{CO}}}} \\
 K_{\text{ads}} &= k_{\text{ads}} C_{\text{CO},S}
 \end{aligned}$$

Dimensionless mass balance for CO and H₂ is now written as (Appendix C.5)

$$\frac{d^2\psi_{CO}}{d\lambda^2} = -\frac{1}{\lambda} \frac{d\psi_{CO}}{d\lambda} + \Phi^2 \frac{\psi_{CO}\psi_{H_2}}{(1+K_{ads}\psi_{CO})^2} \quad \text{BC: } \psi_{CO}|_{\lambda=1} = 1 ; \left. \frac{d\psi_{CO}}{d\lambda} \right|_{\lambda=0} = 0$$

$$\frac{d^2\psi_{H_2}}{d\lambda^2} = -\frac{1}{\lambda} \frac{d\psi_{H_2}}{d\lambda} + 2.2\Phi^2 \frac{D_{CO}}{D_{H_2}} \frac{\psi_{CO}\psi_{H_2}}{(1+K_{ads}\psi_{CO})^2} \quad \text{BC: } \psi_{H_2}|_{\lambda=1} = 1 ; \left. \frac{d\psi_{H_2}}{d\lambda} \right|_{\lambda=0} = 0$$

The effectiveness factor was solved as a function of the Thiele modulus. The observed trend is similar to Iglesia *et al.* (1995). However, the Thiele modulus of the derived reaction diffusion model appears to be larger than those proposed by Iglesia *et al.* (1995) (see Figure 5.27). The main difference between the derived model and model proposed by Iglesia *et al.* (1995) is that a single phase (wax) was assumed to be inside the pores of the catalysts in the slurry phase reactor, where as vapour-liquid equilibrium was assumed by Iglesia *et al.* (1995) for catalyst pellets in a fixed-bed reactor. As a consequence, the diffusion mechanism of the derived model is assumed to be liquid diffusion while Iglesia *et al.* (1995) assumed Knudsen type diffusion (function of pore radius). The Knudsen type diffusion is faster than liquid diffusion for catalyst pellets used here. Thus, the corresponding Thiele modulus of Iglesia *et al.* (1995) is smaller than Thiele modulus in the derived model.

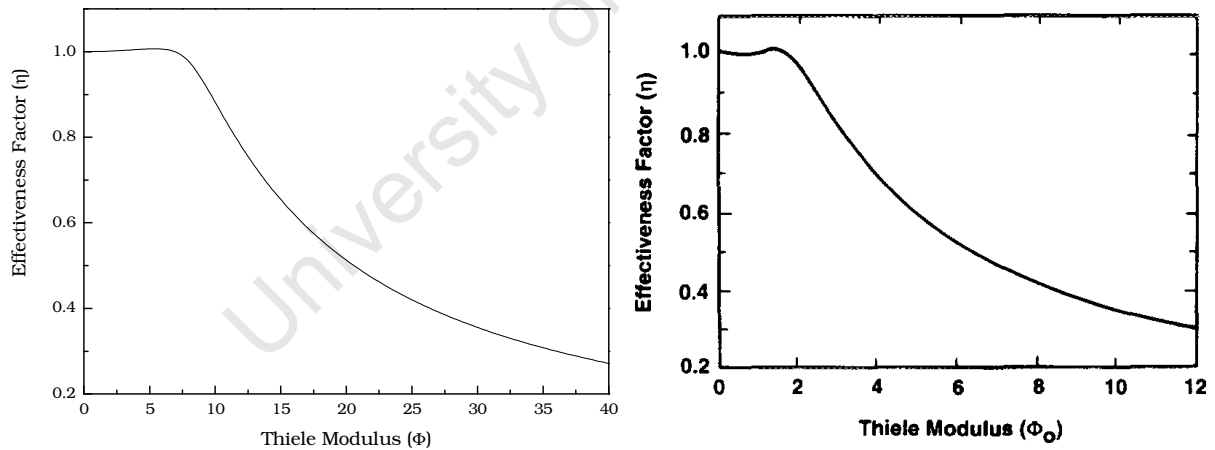


Figure 5.27: Comparison of effectiveness factor as function of Thiele modulus (left: derived in this study; right: Iglesia *et al.* (1995))

Step functions were introduced to describe the various cobalt distributions inside the structured catalysts. In the case of the egg-shell type of catalyst, step function from the boundary of the cobalt-free core to the outer surface of the catalyst was used to describe the boundary of the cobalt-enriched shell. The rate of reaction is set to be zero when the integration falls outside the step function (see Figure 5.28).

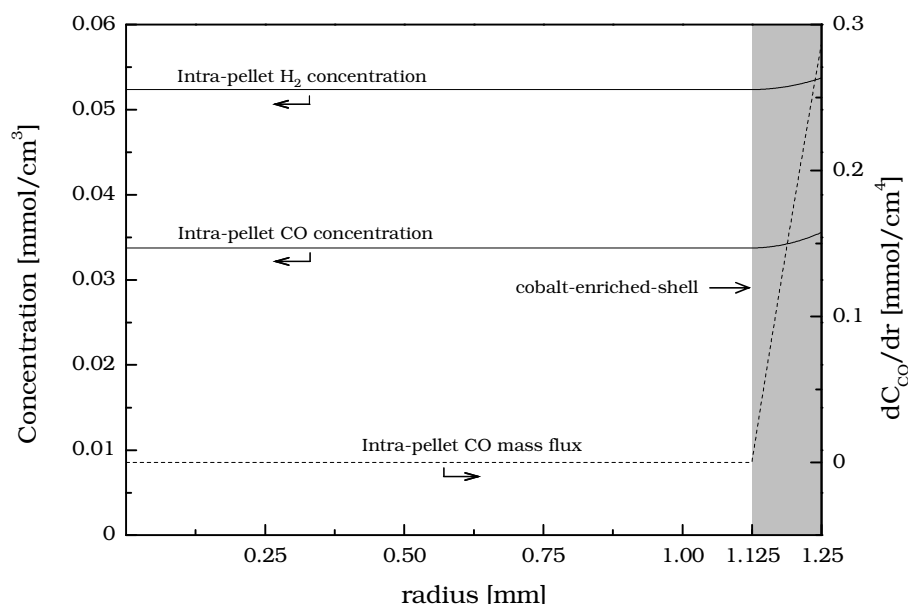


Figure 5.28: Modelled intra-pellet reactant concentration profile of an egg-shell type of catalyst ($r_c/r_p=0.9$; $d_{\text{pellet}}=2.5\text{mm}$)

The effectiveness factor of egg-shell type of catalysts was solved as a function of catalyst pellet size. The behaviour of the egg-shell type of catalyst depends on the severity of internal mass transport limitation. Internal mass transport limitation is severe when effectiveness factor of the uniform pellets drops below 1 due to starvation of reactant. Under such conditions, the severity of mass transport limitations is reduced in egg-shell type of catalysts with equal amount of cobalt loading compared to uniform catalysts by shortening the diffusion-reaction pathway. When internal mass transport limitation is not severe, i.e. no drop in effectiveness factor of uniform catalyst, the egg-shell type of catalyst will behave similar to uniform catalyst (see Figure 5.29).

The experimentally observed ratio of CO consumption rate between the egg-shell type of catalyst and the crushed uniform catalyst indicates slight change of activity (see Table 5-6). This suggests the extent of the internal mass transport limitation in the egg-shell type of catalyst is moderate if not insubstantial. The model supports the experimental observation for catalyst pellet size less than 3mm in diameter.

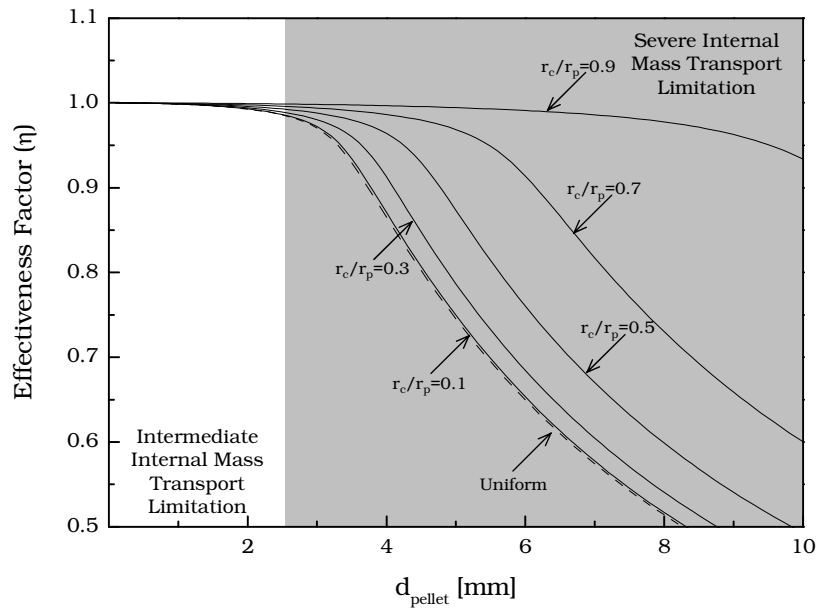


Figure 5.29: Model predicted effectiveness factor of egg-shell type of catalysts pellets with 10% cobalt loading under reaction temperature of 220°C

Intra-pellet reactant concentration profile was solved for egg-yolk type of catalyst by using step function to describe the distribution of cobalt inside the pellet (see Figure 5.30). The egg-yolk type of catalysts behaves contrary to egg-shell type of catalyst. It has cobalt-free-silica-shell as an additional diffusion pathway for the reactant, thus increasing the severity of internal mass transport limitation. Since the diffusivity of H_2 is higher than CO in any diffusion region, an increase in diffusion pathway would increase the intra-pellet H_2/CO ratio. In the region of the cobalt-free shell, the rate of reaction is zero; therefore the rate of CO consumption at the boundary of the cobalt-enriched core is the same as the CO mass flow at the surface of the pellet. The intra-pellet CO mass flux is expected to increase with decreasing radius due to the decreasing unit volume with decreasing radius in a cylindrical geometry. The predicted intra-pellet CO concentration profile agrees with this reasoning.

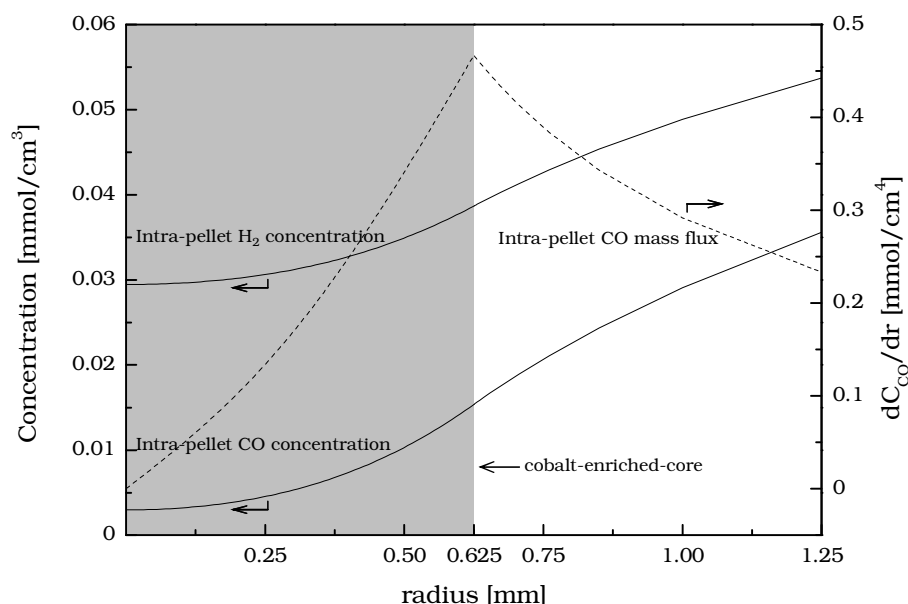


Figure 5.30: Modelled intra-pellet reactant concentration profile of an egg-yolk type of catalyst ($r_c/r_p=0.5$; $d_{\text{pellet}}=2.5\text{mm}$)

Generally, the Fischer-Tropsch rate is inhibited by CO coverage on the metal surface. Therefore an increase in H_2/CO ratio increases the reaction rate. The extra diffusion length of the egg-yolk type of catalyst increases H_2/CO ratio, thus at intermediate internal mass transport limitation, this feature may increase the effectiveness factor. However, at severe internal mass transport limitation, a further increase in H_2/CO ratio would starve the cobalt-enriched core from reactants, and thus lowering the effectiveness factor (see Figure 5.31). According to the model, egg-yolk type of catalyst with pellet diameter of 2.5mm will experience intermediate internal mass transport limitation. Therefore, the effectiveness factor of egg-yolk type of catalysts decreases with decreasing cobalt-enriched core; egg-yolk type of catalyst with thin cobalt-free silica shell may have effectiveness factor greater than 1.

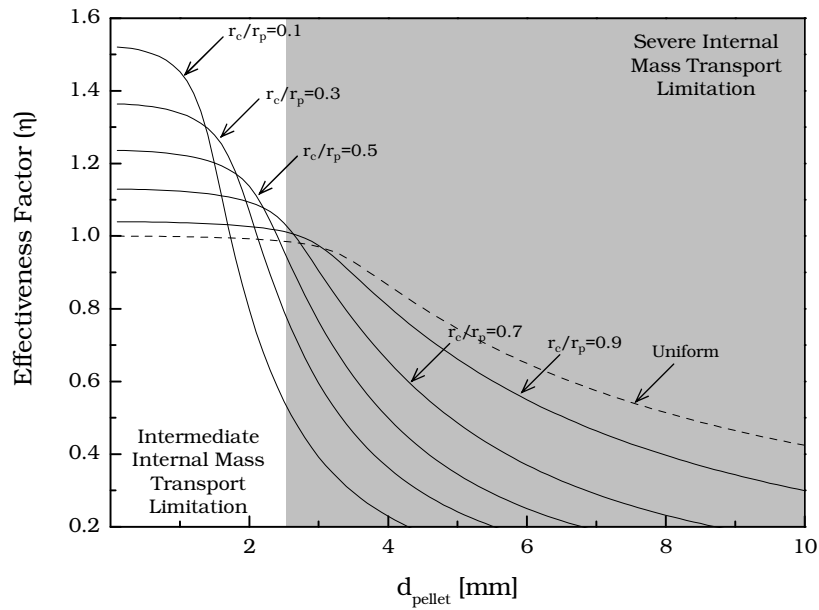


Figure 5.31: Model predicted effectiveness factor of egg-yolk type of catalysts pellets with 10% cobalt loading under reaction temperature of 220°C

The intra-pellet cobalt distribution of egg-white type of catalysts was described using a modified arccot and a modified arctan functions for the easiness of numerical calculation. By locating the mid-point (mid) of the cobalt-enriched ring inside the egg-white type with respect, the distribution of cobalt with respect to pellet radius was defined piece wisely (see Figure 5.32). The intra-pellet CO mass flux modelled using the piecewise distribution function shows sharp turns at the cobalt enriched boundaries. Thus the use of the piecewise function is adequate in describing the intra-pellet cobalt distribution (see Figure 5.33).

$$\text{distribution} = \begin{cases} \frac{1}{\pi} \arctan \left(1000 \frac{r_w - r}{r_p} + \frac{\pi}{2} \right) & |_{r < \text{mid}} \\ \frac{1}{\pi} \text{arccot} \left(1000 \frac{r_c - r}{r_p} + \frac{\pi}{2} \right) & |_{r \geq \text{mid}} \end{cases}$$

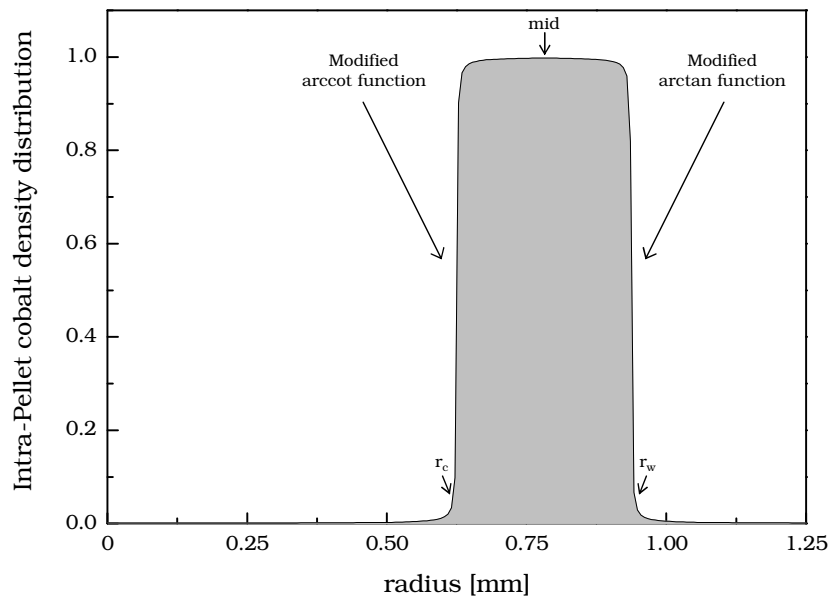


Figure 5.32: Modelled intra-pellet cobalt density of an egg-white type of catalyst ($r_c/r_p=0.5$; $r_w/r_p=0.75$; $d_{\text{pellet}}=2.5\text{mm}$)

The egg-white type of catalyst behaves as a combination of egg-shell and egg-yolk type of catalysts. The cobalt-free silica shell of the egg-white catalysts provides additional diffusion path for the reactant and hence increases the intra-pellet H_2/CO ratio. This feature increases the internal mass transport limitation. The counterpart feature of egg-white catalysts is the cobalt-free silica core, which minimises the starvation of reactants experienced by the cobalt closer to the centre of the pellet. These features allow the egg-white catalyst to alter degree of internal mass transport limitation without severely affecting the intra-pellet H_2/CO ratio (see Figure 5.34).

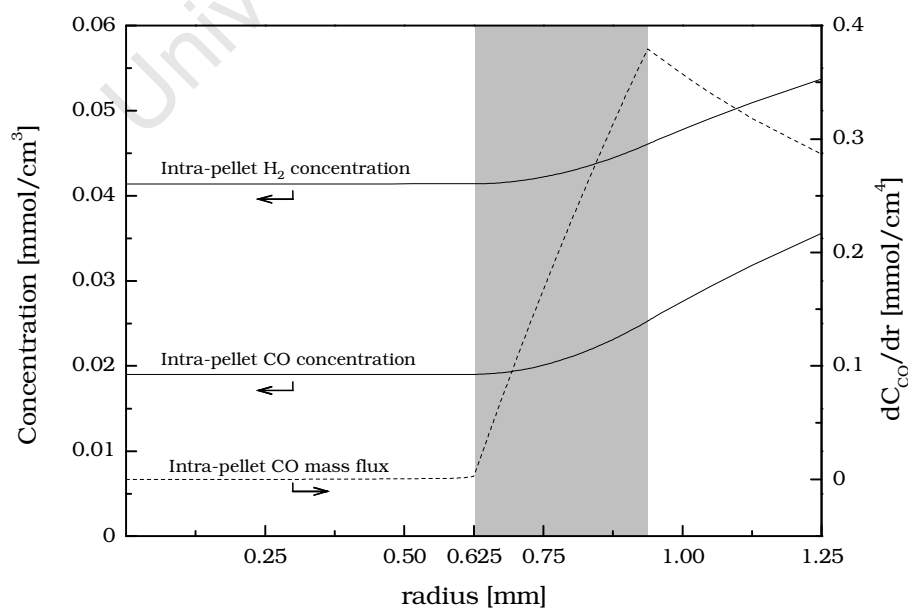


Figure 5.33: Modelled intra-pellet reactant concentration profile in an egg-white type of catalyst ($r_c/r_p=0.5$; $r_w/r_p=0.75$; $d_{\text{pellet}}=2.5\text{mm}$)

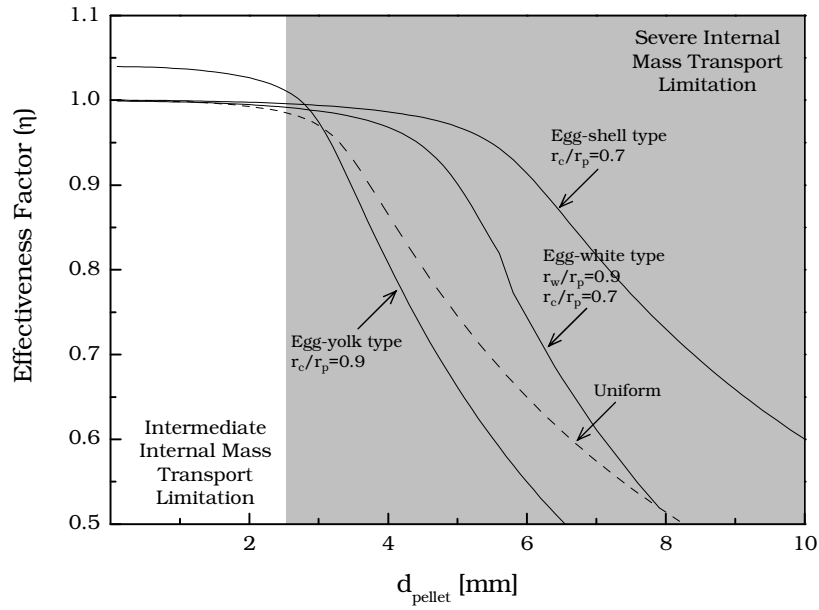


Figure 5.34: Comparison of model predicted effectiveness factor of uniform, egg-shell egg-yolk type of catalysts pellets with 10% cobalt loading under reaction temperature of 220°C

The derived reaction-diffusion pellet model alone can not describe the experimentally determined performance of the structured catalysts, because the Fischer-Tropsch performance test was conducted in a CSTR type reactor, in which the reactant concentration is identical to the exit reactant concentration. The performance of the structured catalyst pellets in a CSTR was modelled by using a calculation loop. This loop calculation is initialised by assuming the reactant concentration is the bulk reactant concentration. The overall conversion of CO is calculated by the following equation

$$X_{CO} = (-rate_{CO} \times M_{catalyst} \times \eta) / F_{CO}$$

where $-rate_{CO}$ is the CO consumption rate in the absence of internal mass transport limitation, $M_{catalyst}$ is the amount of catalyst loaded, and F_{CO} is the flow rate of CO.

The reactant partial pressure in the reactor is then updated based on the calculated CO conversion assuming an average carbon number of 3 in the product. Thus, the partial pressure of CO and H_2 is

$$P_{CO} = \frac{(1 - X_{CO})}{3 - (2.2 - 1/3)X_{CO}} \times P_T$$

$$P_{H_2} = \frac{(2 - 2.2X_{CO})}{3 - (2.2 - 1/3)X_{CO}} \times P_T$$

The variation in the extent of catalyst deactivation was accounted by decrease the metal surface area of the freshly reduced catalysts (metal surface area according to CO

chemisorption) used in the model, relative to the decrease in conversion at steady state compared to conversion at 4 times the space time.

The reactant concentration in the liquid phase was correlated by using the Chou and Chao (1992) correlation. Then a new overall conversion is calculated based on the updated reactant concentration. This calculation loop is terminated when the difference between the newly calculated CO conversion and previously calculated CO conversion is less than 0.1%. The diffusivities of H₂ and CO in wax were used from experimental values over a temperature range of 203°C to 263°C determined by Erkey *et al.* (1990). However, the CSTR model could not predict the experimental conversion within 10% error.

Taking a closer look at the diffusivity experimental data of Erkey *et al.* (1990), the diffusivity of CO is 1.74×10^{-8} m²/s at 231°C. Chang and Wilke (1955) proposed a correlation for dilute, binary mixtures of non-electrolytes in liquids.

$$D_{AB} = \frac{7.4 \times 10^{-8} (\varphi_B M_B)^{1/2} T}{\mu_B V_A^{0.6}}$$

where D_{AB} is the mutual diffusivity at infinite dilution of A in B, φ_B is an association factor of solvent B that accounts for hydrogen bonding (1 for wax), M_B is the molar mass of B, μ_B is viscosity of B at temperature T, and V_A is the molar volume of A.

The molar volume of CO is 32.1 cm³/mol (Prausnitz and Shair, 1961). The viscosity of a middle cut wax produced using cobalt catalyst is 0.555 (Marano and Holder, 1997). According to Chang and Wilke (1955), the CO diffusivity in wax with an average carbon number of 28 at 231°C is 1.71×10^{-8} m²/s. The experimentally determined CO diffusivity (Erkey *et al.*, 1990) is in good agreement with the most widely used Wilke-Chang correlation. However, the diffusivity ratio of H₂ over CO in wax, determined by Erkey *et al.* (1990) is 2.4-2.7 over a temperature range of 203°C to 263°C. The molar volume of H₂ is 28 cm³/mol (Crozier and Yamamoto, 1974), therefore according to the Wilke-Chang correlation, the diffusivity ratio of H₂ over CO in Fischer-Tropsch wax should be about 1.1. This discrepancy might originate from an experimental artefact in the determination of the diffusivity of hydrogen, i.e. the reaction of hydrogen in the used diffusion tube (Erkey *et al.*, 1990).

Due to the lack of reliable experimental data for the diffusivity of H₂ in the Fischer-Tropsch wax, the diffusivity of H₂ in wax was used as the variable parameter in the developed kinetic model. The diffusivity of H₂ in wax was varied until the relative difference between the predicted and the experimental conversion is less than 1%. The

regressed diffusivity ratio of H₂ over CO in wax is 1.15 ± 0.10 at 220°C, 1.31 ± 0.14 at 230°C, and 1.51 ± 0.24 at 240°C (see Table 5-8).

Table 5-8: Ratio of diffusivity of H₂ over CO in wax that satisfies the kinetic model criteria

Catalyst	220°C	230°C	240°C
U1	1.09	1.46	1.99
U2	1.36	1.38	1.67
S1	1.35	1.55	1.60
S2	1.14	1.28	1.35
S3	1.05	1.10	1.16
S4	1.30	1.50	1.80
S5	1.20	1.50	1.60
S6	1.10	1.30	1.50
Y1	1.27	1.34	1.45
Y2	1.19	1.22	1.37
Y3	1.16	1.22	1.25
Y4	1.04	1.11	1.24
Y5	1.10	1.28	-
Y6	1.07	1.34	-
Y7	1.04	1.06	1.36
W1	1.09	1.30	1.57
W2	1.09	1.29	1.89
W3	1.20	1.37	1.43
W4	1.04	-	-

The variation in the H₂ and CO diffusivity ratio from the model correlation may be due to the infinite cylinder catalyst geometry assumption in the model. The actual pellet volume occupied by cobalt in the catalyst is much smaller than the infinite cylinder in the model. This overestimation of reactive volume in the catalyst pellet underestimates the cobalt concentration in the reactive volume and therefore under estimates the severity of internal mass transport limitation in structured (see Figure 5.35).

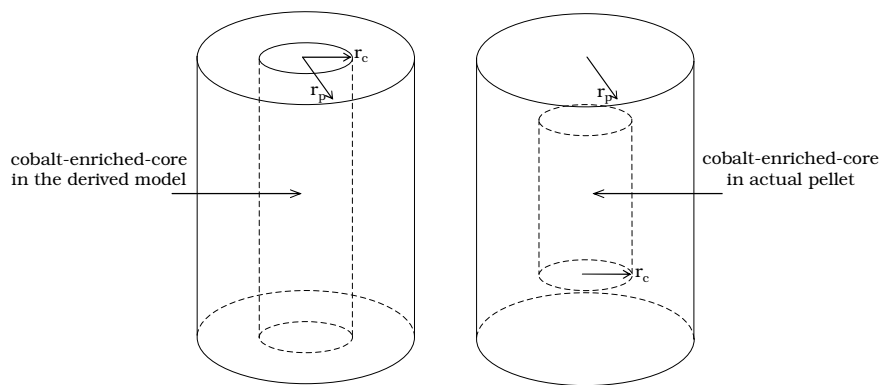


Figure 5.35: Comparison of the open-ended cylinder egg-yolk type of catalyst geometry to actual egg-yolk type of catalyst geometry

It should be noted that this derived kinetic model uses the experimentally measured bulk diffusivity of CO and H₂ in wax (Erkey *et al.*, 1990) in the place of effective diffusivity. The effective diffusivity accounts for the hindrance by the pore walls on bulk diffusivity, which is a function of tortuosity (τ) and void fraction (ϵ_{pellet}) of porous material.

$$D_{\text{eff}} = \frac{\epsilon D_{\text{AB}}}{\tau}$$

Typically, the normal range of tortuosities for silica gel, alumina, and other porous solids is $2 \leq \tau \leq 6$ (Knudsen *et al.*, 2001). This means that the effective diffusivity can be an order of magnitude lower than the bulk diffusivity. The values of tortuosities are usually derived for a known frame of pore structure (e.g. zeolites), or determined experimentally by comparing experimental results with bulk diffusion. In this study, the bulk diffusivity value was decreased step wise until the conversion predicted by the model is exceeds 10% error of the experimental values. Generally, the ratio of the minimum CO diffusivity compare to the literature value is 0.25 at 220°C, 0.4 at 230°C and 0.9 at 240°C. According to the supplier information on the silica support, the pellet void fraction is 0.7. This means, the tortuosity of the pellet is 2.8 (220°C), which is in agreement with literature (Knudsen *et al.*, 2001). The large tortuosities difference at different reaction temperature (1.75 at 230°C, 0.78 at 240°C) could be due to the assumption that the CO adsorption constant in the kinetic expression is constant with respect to temperature.

5.3 Product Selectivity of Structured Catalysts

The Fischer-Tropsch synthesis product is a complex, but regular mixture of organic product compounds. Many selectivity parameters, such as methane selectivity, C5+ selectivity, olefin content, etc. can be used to describe a certain aspects of the product selectivity, and can give insight into the behaviour of the catalyst under reaction conditions. The methane selectivity (in C-%) and the C5+ selectivity are of great industrial importance, since cobalt-based Fischer-Tropsch synthesis is aimed at maximizing the liquid fuel selectivity. These selectivities are linked, and might be influenced by the extent of olefin reincorporation. Hence, the effect of internal mass transport limitation on α -olefins re-adsorption must be explored before looking at the methane and C5+ selectivity of the product.

In literature, the extent of internal mass transport limitation is often presented in terms of the structural parameter (χ) as proposed by Iglesia *et al.* (1995). The structural parameter is a part of the Thiele modulus depending only on the structural properties of the catalysts. In this study, the general definition of the structural parameter would be

$$\Phi^2 = \psi \times \chi = \frac{k_0 C_{H_2, S}}{D_{CO}} \times (r_{\text{pellet}}^2 \rho_{\text{co}} \sigma_{\text{structured}} d_{(r)})$$

$$\chi = r_{\text{pellet}}^2 \rho_{\text{co}} \sigma_{\text{structured}} d_{(r)}$$

where k_0 is the intrinsic rate constant and $d_{(r)}$ is the intra-pellet cobalt distribution function of the structured catalysts. To be able to compare structural parameters of all types of structural parameter, the intra-pellet cobalt distribution ($d_{(r)}$) must be incorporated into the structural parameter. This means that the structural parameter is then a function of position in the pellet. Therefore, it is not possible to describe the extent of the internal mass transport limitation of different types of structured catalysts with a single number. Thus, the Fischer-Tropsch product selectivity is compared among individual types of structured catalysts in terms of reaction-diffusion path length. The reaction-diffusion path length of the structured catalyst is defined as the distance the reactant has to travel within the cobalt-enriched-region of the catalyst pellet.

5.3.1 Secondary Reactions of Ethene

The fraction of C2 hydrocarbons consists only of an olefin, ethene and a paraffin, ethane. Thus, the C2 olefin content in C2 linear hydrocarbons can be used as an indication of the extent of C2 α -olefin re-adsorption leading either to ethane or to re-incorporation of ethene. Under the influence of internal mass transport limitation, the residence time of α -olefin within the pellet increases which might affect the rate of olefin re-adsorption. The distance of the reactive region of structured catalyst from the outer boundary towards the centre of the pellet can be defined as the reaction-diffusion path length, of which its value is proportional to the residence time of the reactant or reactive intermediate product. The residence time of the reactive olefins is expected to increase with increasing length of the diffusion path length. Hence, the olefin content is expected to be a function of reaction-diffusion path length.

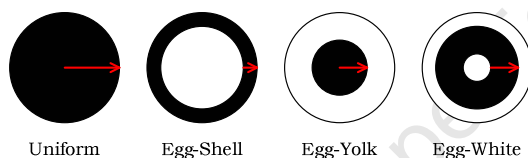


Figure 5.36: Cross-sectional view of different type of structured catalyst showing reaction-diffusion path length

The C2 olefin content as a function of reaction-diffusion path length of structured catalyst pellets with similar cobalt loading is compared with uniform catalyst powder (U1C) (see Figure 5.37). At a reaction temperature of 220°C, a clear decrease in C2 olefin content with increasing reaction-diffusion path length is observed with the egg-shell type of catalysts together with uniform pellet. This might be explained by the increased residence time of the α -olefins with increasing reaction-diffusion path length in the catalyst pellet. As reaction temperature increases, the C2 olefin content of the egg-shell type of catalysts seems to be almost independent of the reaction-diffusion path length (230°C, see Figure 5.38) or passing through a minimum (240°C, see Figure 5.39). The olefin content is given by the rate of primary olefin formation rate minus the rate of olefin re-adsorption over the rate of total product formation.

$$\text{Olefin Content} = \frac{r_{\text{olefin,primary}} - r_{\text{olefin,re-adsorb}}}{(r_{\text{olefin,primary}} - r_{\text{olefin,re-adsorb}}) + r_{\text{paraffin}}} = \frac{1}{1 + \frac{r_{\text{olefin,primary}}/r_{\text{paraffin}} - r_{\text{olefin,re-adsorb}}/r_{\text{paraffin}}}{1}}$$

The olefin content will decrease if $\left(\frac{r_{\text{olefin,primary}}}{r_{\text{paraffin}}} - \frac{r_{\text{olefin,re-adsorb}}}{r_{\text{paraffin}}} \right)$ decreases, i.e. when the rate of primary olefin formation becomes smaller in comparison to the rate of paraffin

formation and/or the difference between the rate of primary olefin formation and rate of olefin re-adsorption is smaller. The ratio of the diffusivity of H_2 to the diffusivity of CO in wax increases with increasing temperature (Chou and Chao, 1992). As a result, the average intra-pellet H_2/CO ratio will increase with an increase in reaction temperature. This may result in a lowering of the rate of primary olefin formation relative to the rate of paraffin formation at higher reaction temperature. The rate of olefin re-adsorption is expected to be dependent on the intra-pellet olefin concentration (Schulz and Claeys, 1999); the olefin concentration is lowered when the primary olefin formation rate is decreased. This means that the difference between the olefin primary formation rate and olefin re-adsorption rate may increase when the olefin concentration is low. This might explain the observed independency of C2 olefin with reaction-diffusion path length at 230°C and passing a minimum at 240°C. Thus, at 220°C, the effect of increased α -olefin residence time is observed, while the effect of diminished olefin formation is observed at higher reaction temperatures.

The C2 olefin content obtained with the egg-yolk type of catalyst is lower than the C2 olefin content obtained with egg-shell type of catalysts at the tested reaction temperature. The C2 olefin content of the egg-yolk catalysts shows a more clear indication of a minimum as a function of reaction-diffusion path length. The additional diffusion path length introduced by the cobalt-free shell of the egg-yolk type of catalysts increases the local intra-pellet H_2/CO ratio. The measured olefin content will decrease when the rate of primary olefin formation becomes smaller in comparison to the rate of paraffin formation and/or the difference between the rate of primary olefin formation and rate of olefin re-adsorption is smaller. The increased local intra-pellet H_2/CO ratio decreases the primary olefin selectivity, and therefore decreases the olefin content. The decreased primary olefin rate formation also lowers the difference between primary olefin formation and rate of olefin re-adsorption. Thus, a minimum in C2 olefin content in the egg-yolk type of catalysts is observed.

The C2 olefin content obtained with egg-white type of catalysts is somewhat between C2 olefin content obtained with the egg-shell and the egg-yolk type of catalysts. The egg-white type of catalyst was ordered with increasing reaction-diffusion path length ($W1 < W2 < W3 < W4$). In this study, the cobalt-enriched region of the egg-white catalyst was made closer to the core of the pellet with increasing reaction-diffusion path length. Thus, the egg-white type of catalyst is physically similar to the egg-yolk type of catalyst as its reaction-diffusion path length increases. Therefore, the C2 olefin content of the egg-yolk type of catalyst is somewhat between the egg-shell and the egg-yolk type of catalyst.

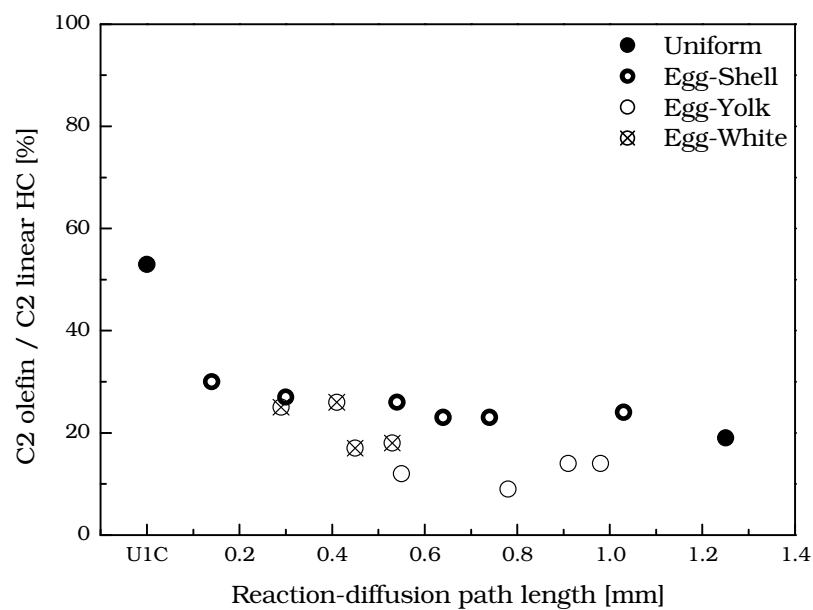


Figure 5.37: C2 olefin content as a function of reaction-diffusion path length at 220°C

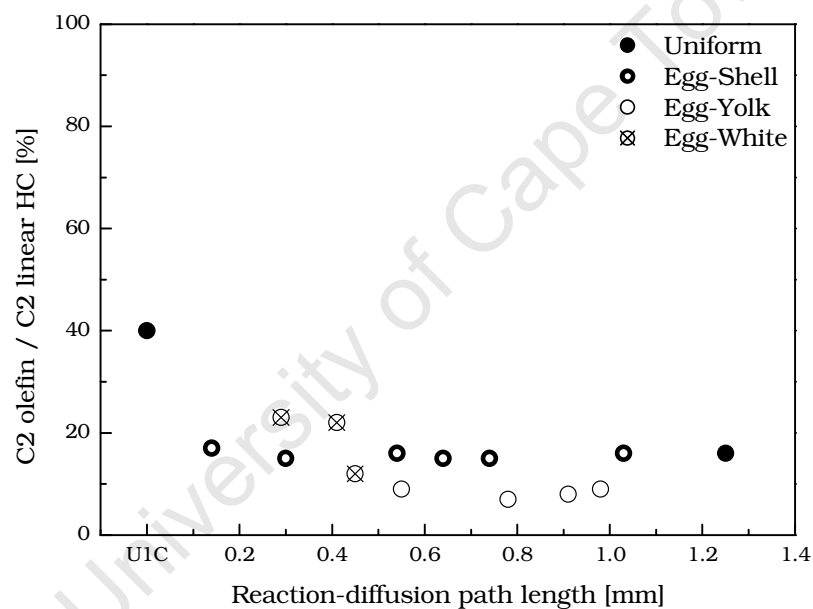


Figure 5.38: C2 olefin content as a function of reaction-diffusion path length at 230°C

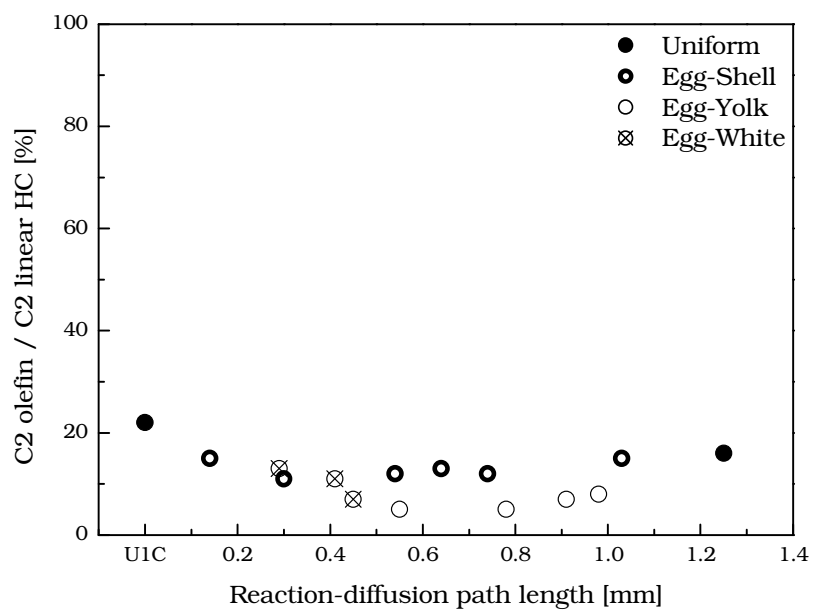


Figure 5.39: C2 olefin content as a function of reaction-diffusion path length at 240°C

5.3.2 Product Selectivity in the C5 Fraction

The olefin content in the fraction of linear C5 hydrocarbons of the structured catalyst shows a distinct decrease with an increase in reaction-diffusion path length at tested reaction temperature (see Figure 5.40-46). This may be explained by the increased average intra-pellet H_2/CO ratio with increasing reaction-diffusion path length. The C5 olefin trend did not change with a change in reaction temperature as was observed with the C2 olefin content over the structured catalysts. The C5 olefin fraction consists of α -olefin and internal olefins (trans-2-pentene and cis-2-pentene), unlike the C2 olefin which only contains the α -olefin. Double-bond isomerisation is a result of secondary olefin re-adsorption (van Steen and Claeys, 2004). It results in an effective decrease in the concentration of the most reactive olefin, viz. 1-pentene (Schulz and Claeys, 1999b) without decreasing the olefin content. When double-bond isomerisation of the re-adsorbed α -olefin is the dominant secondary reaction, the C5 olefin content in C5 linear hydrocarbon can not distinctively represent the extent of olefin re-adsorption.

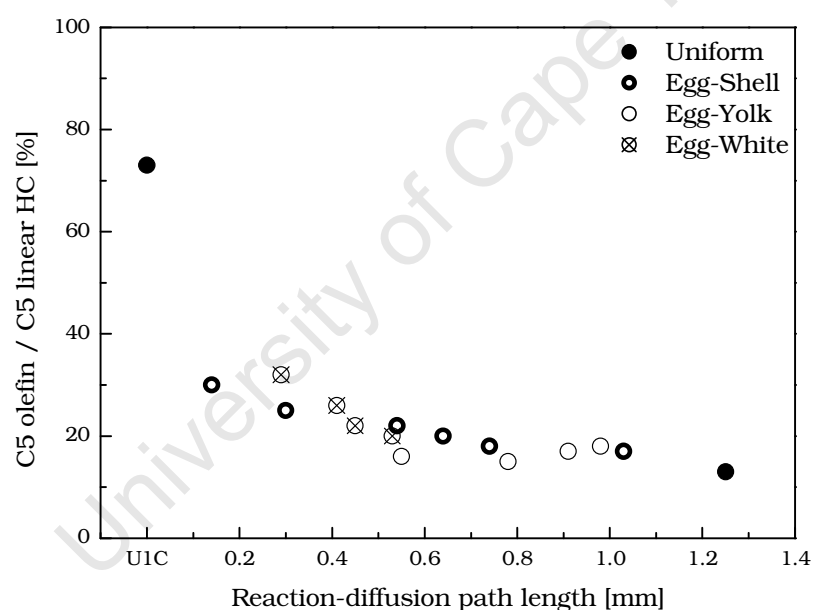


Figure 5.40: C5 olefin content as a function of reaction-diffusion path length at 220°C

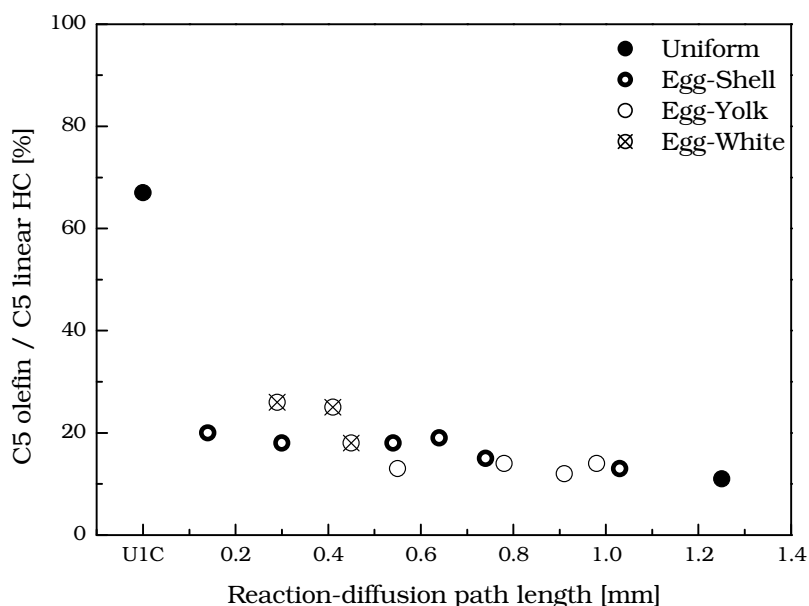


Figure 5.41: C5 olefin content as a function of reaction-diffusion path length at 230°C

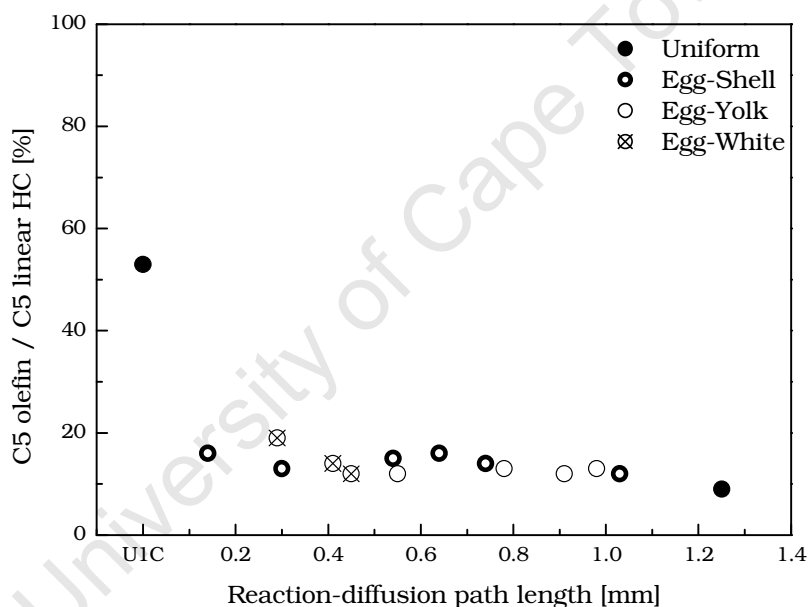


Figure 5.42: C5 olefin content as a function of reaction-diffusion path length at 240°C

The C5 α -olefin content in the fraction of linear C5 olefins is used as an indication of the extent of double-bond isomerisation of re-adsorbed α -olefins. In the absence of internal mass transport limitation, as observed with the uniform powder catalyst (U1C), a minor decline in the C5 α -olefin content in the fraction of linear olefins was observed with increasing reaction temperature (see Figure 5.43-49). This suggests that the double bond isomerisation is not strongly affected by reaction temperature. Generally, the C5 α -olefin content is lower for the catalyst in the pellets form in comparison to catalyst in the powder form. This suggests the reaction-diffusion path length of the structured pellets affects the α -olefin re-adsorption.

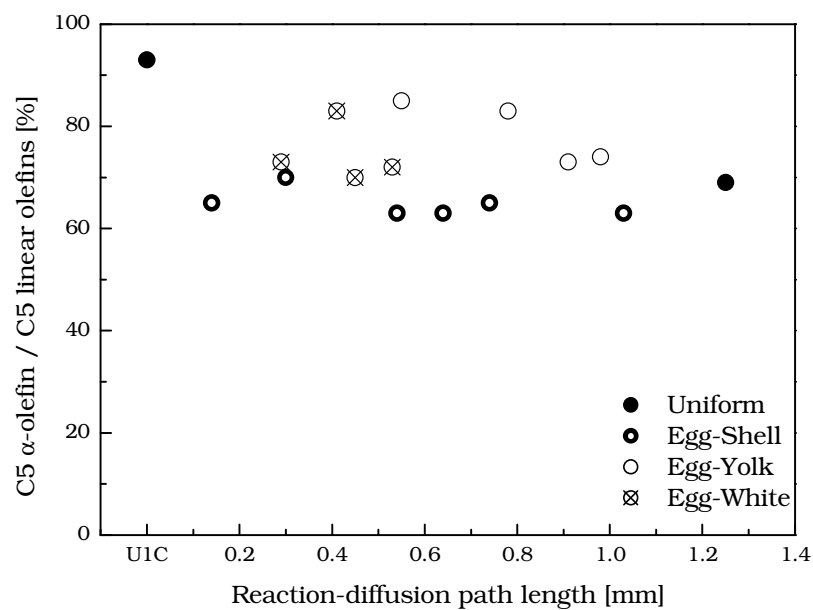


Figure 5.43: C5 α -olefin in C5 linear olefins as function of reaction-diffusion path length at 220°C

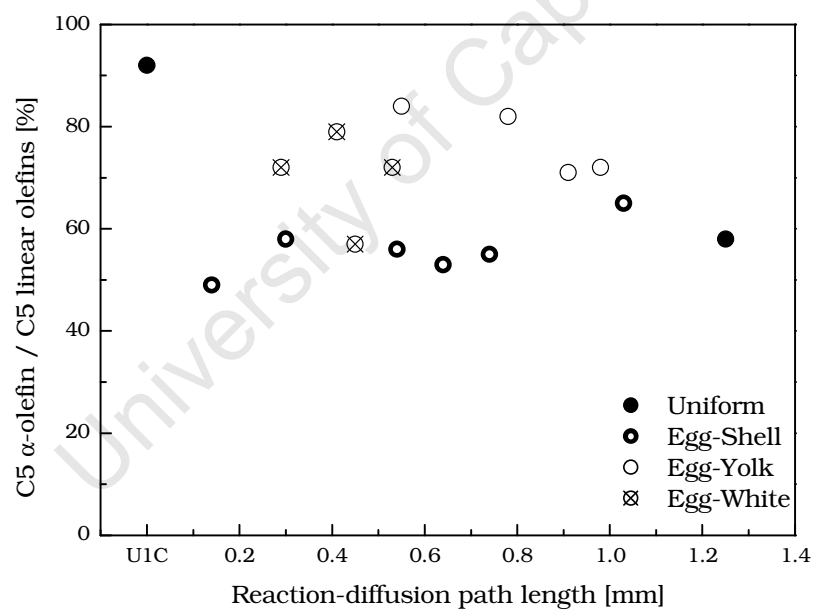


Figure 5.44: C5 α -olefin in C5 linear olefins as function of reaction-diffusion path length at 230°C

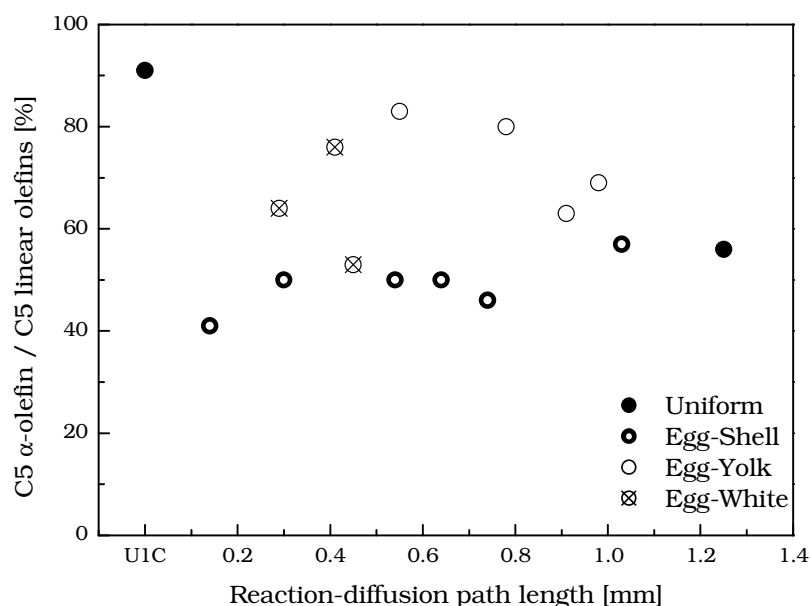
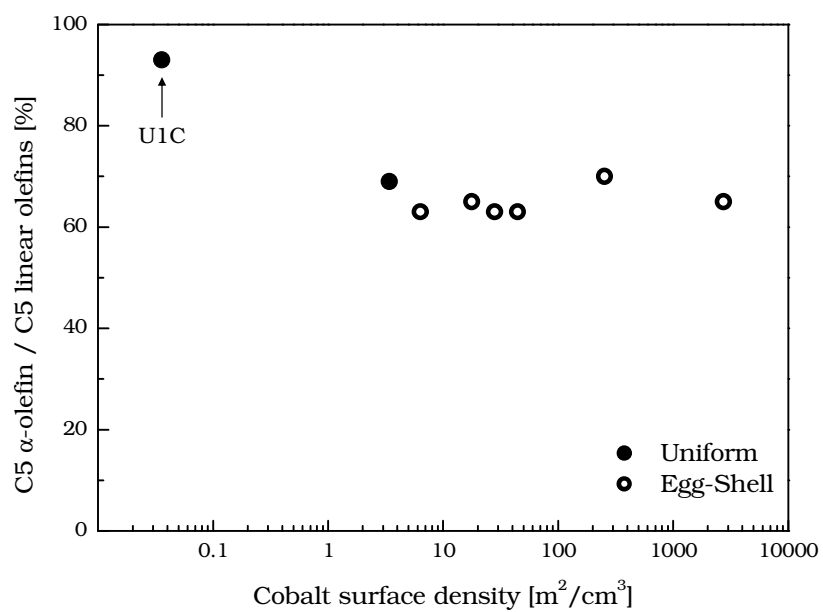
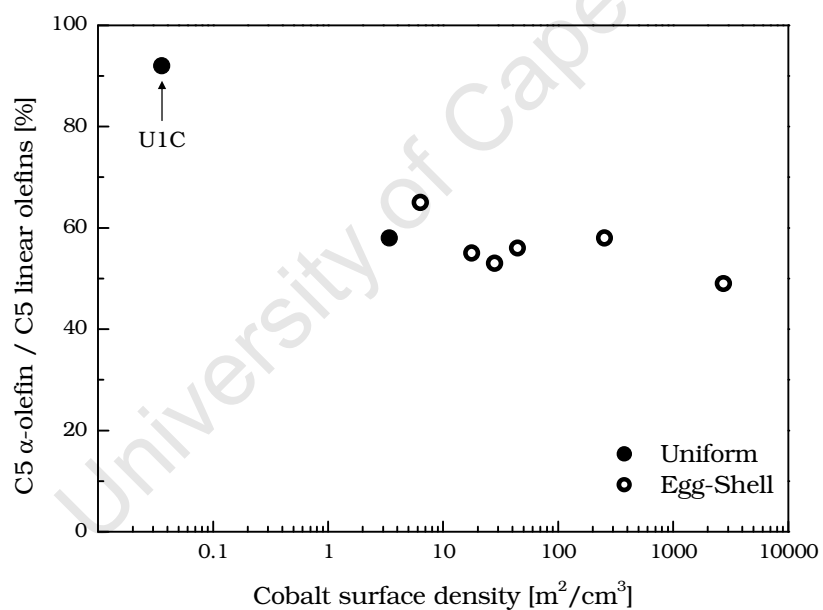


Figure 5.45: C5 α -olefin in C5 linear olefins as function of reaction-diffusion path length at 240°C

The C5 α -olefin content of egg-shell type of catalysts appears to be almost independent and even shows a slight increase with reaction-diffusion path length. Saib *et al.* (2002) showed that the extent of double-bond isomerisation is also a function of the cobalt crystallite density (in their case the cluster size in which cobalt crystallites appears). The density of cobalt crystallites within the egg-shell type of catalysts increases with decreasing reaction-diffusion path length. The cobalt crystallites density is estimated by dividing the cobalt metal surface area according to CO chemisorption by the volume of area of the cobalt enriched region in the structured catalyst (Optic Microscopy). C5 α -olefin in the fraction of linear C5 olefin of the uniform catalyst and egg-shell type of catalyst decreases with increasing estimated cobalt density (see Figure 5.46-52). This means the chance of re-adsorbed α -olefin undergoes double-bond isomerisation is a function of the distance between the cobalt crystallites. Thus, a decrease in reaction-diffusion path length leads to an increase in cobalt crystallite density, and therefore increases double-bond isomerisation.

Figure 5.46: C5 α -olefin in C5 linear olefins as function of cobalt surface density at 220°CFigure 5.47: C5 α -olefin in C5 linear olefins as function of cobalt surface density at 230°C

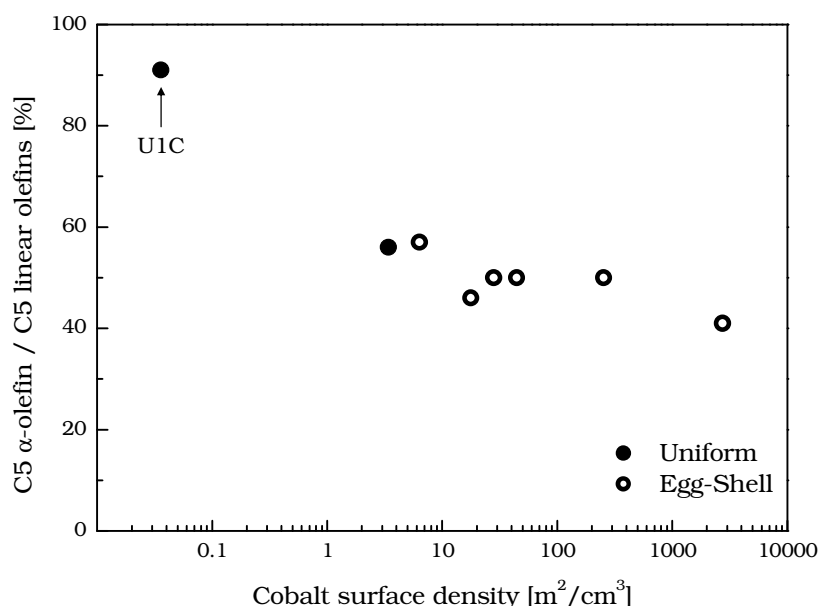


Figure 5.48: C5 α -olefin in C5 linear olefins as function of cobalt surface density at 240°C

The egg-yolk type of catalyst showed a higher C5 α -olefin in linear olefin content, and decreases with increasing reaction-diffusion path length. The cobalt-free shell of the egg-yolk type of catalyst further increases the intra-pellet H_2/CO ratio. Hydrogenation over double-bond isomerisation of the re-adsorbed olefin is likely to be more favoured at higher intra-pellet H_2/CO ratio. When secondary hydrogenation is dominant, the α -olefin in linear olefin content is expected to decrease with increasing reaction-diffusion path length.

The egg-white type of catalyst with lower reaction-diffusion path length seems to behave between egg-shell and egg-yolk type. However, the C5 α -olefin content of the egg-white type of catalyst with higher reaction-diffusion path length (W3 and W4) is lower than the egg-yolk type of catalyst. According to the TPR-TPO results, the cobalt-free shell of the egg-white type of catalysts is likely to contain cobalt silicate due to acid leaching of metal cobalt. Double-bond isomerisation is likely to be enhanced by the presence of cobalt silicate. This could be the reason for the observed decrease in C5 α -olefin or and increase in C5 internal-olefin content in the egg-white type of catalyst with thick cobalt-free shell.

The ratio of branched product to linear hydrocarbons in the C5 fraction is used as an indication of degree of branching. In the absence of internal mass transport limitation, an increase in the formation of branched product compounds relative to the formation of linear product compounds was observed with increasing temperature (U1C) as described in literature (Claeys *et al.*, 2004). The ratio of branched C5 products versus linear C5 products of structured catalyst pellets increases with increasing reaction-

diffusion path length (see Figure 5.49-55). This suggests that branching of re-adsorbed α -olefins is favoured under internal mass transport limitation.

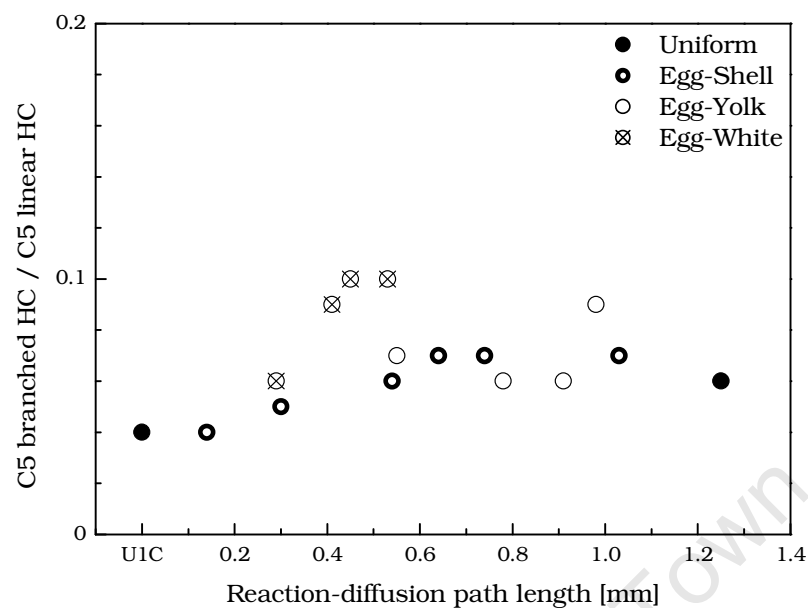


Figure 5.49: C5 branched to linear product ratio as function of reaction-diffusion path length at 220°C

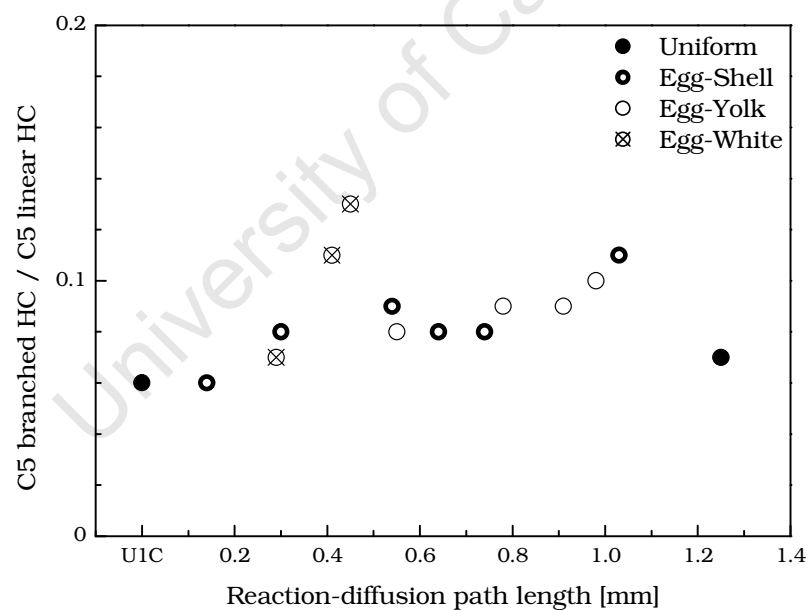


Figure 5.50: C5 branched to linear product ratio as function of reaction-diffusion path length at 230°C

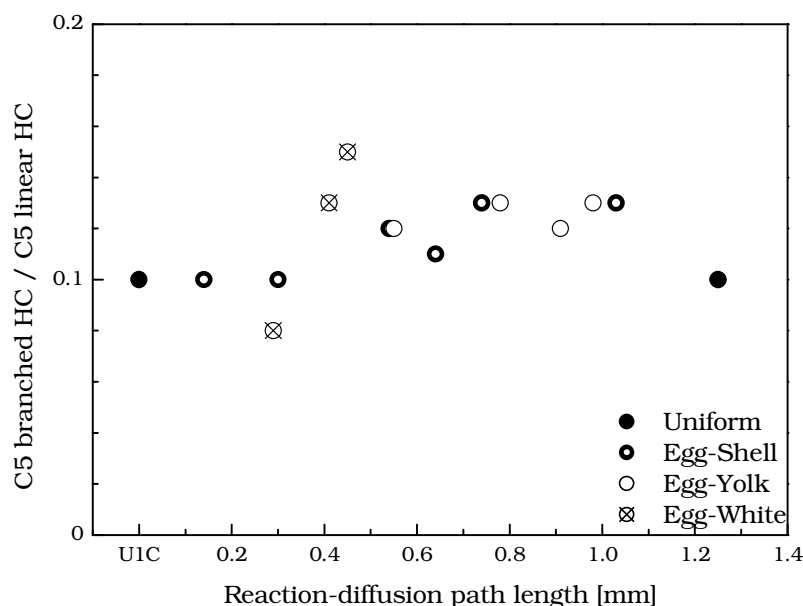


Figure 5.51: C5 branched to linear product ratio as function of reaction-diffusion path length at 240°C

It can be concluded based on the C2 and C5 olefin selectivity, that the re-adsorption of α -olefin is enhanced by internal mass transport limitation. With increasing reaction-diffusion path length, the selectivity for the formation of paraffinic and branched C5-product compounds increases, while the α -olefin and olefin content in the C5 fraction decreases. These results suggest the re-adsorbed α -olefin is likely to be hydrogenated under internal mass transport limitation.

5.3.3 Methane Selectivity and C5+ Selectivity

Methane selectivity (in C-%) can be influenced local H_2/CO ratio. The higher diffusivity of H_2 in Fischer-Tropsch wax compared to the diffusivity of CO in wax (albeit less than reported by Erkey *et al.* (1990)) will affect the intra-pellet H_2/CO ratio and thus affecting product selectivity (Schulz *et al.*, 1994). An average H_2/CO ratio, defined as the ratio of amount of unreacted H_2 over CO over the reactive layer in catalyst pellet, is used to indicate the effect of internal mass transport limitation on local H_2/CO ratio.

$$H_2/CO_{\text{average}} = \frac{\pi r_{\text{pellet}} l_{\text{pellet}} \int_{r_{\text{active},i}}^{r_{\text{active},j}} r \frac{dC_{H_2}}{dr} dr}{\pi r_{\text{pellet}} l_{\text{pellet}} \int_{r_{\text{active},i}}^{r_{\text{active},j}} r \frac{dC_{CO}}{dr} dr} \approx \frac{\sum_{r_{\text{active},i}}^{r_{\text{active},j}} r \times \left. \frac{dC_{H_2}}{dr} \right|_r}{\sum_{r_{\text{active},i}}^{r_{\text{active},j}} r \times \left. \frac{dC_{CO}}{dr} \right|_r}$$

The methane selectivity of structured catalysts is plotted against the predicted average H_2/CO ratio in the structured catalyst pellets (see Figure 5.52-5.58). The trend of methane selectivity verses the predicted average intra-pellet H_2/CO ratio shows that the structural type of the catalyst pellets may affect product selectivity. The methane selectivity in uniform and egg-shell type of catalyst increases with an increase in intra-pellet H_2/CO ratio. The probability of chain termination by hydrogenation is expected to increase with an increase in H_2 partial pressure. Therefore a higher H_2/CO ratio increases the product selectivity towards methane (Vannice, 1975a).

The egg-yolk and egg-white type of catalysts show significantly higher methane selectivity than egg-shell type and uniform catalyst. It should be realised that methane selectivity, and thus also C5+ selectivity, can be influenced by many other factors other than H_2/CO ratio, local partial pressures of the major compounds (H_2 , CO and H_2O), and the extent of the reaction.

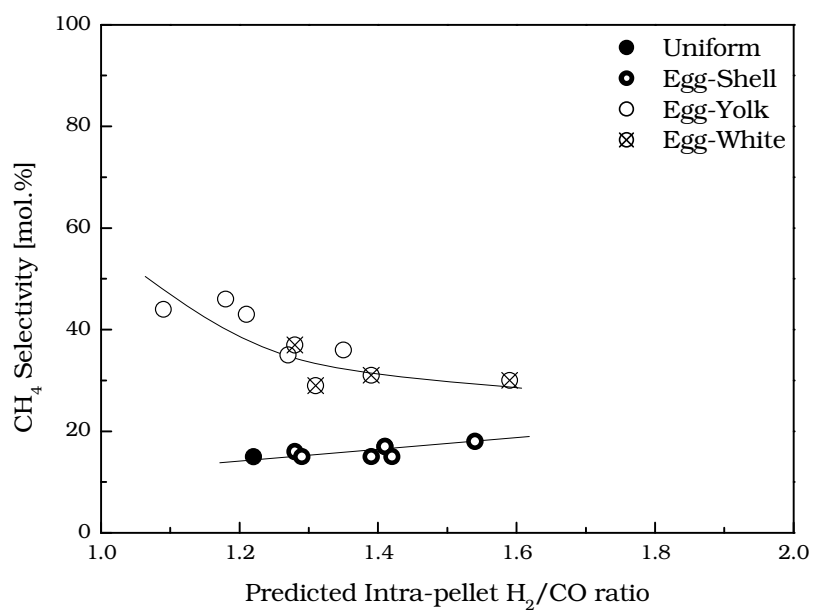


Figure 5.52: Methane selectivity as function of model predicted intra-pellet H_2/CO ratio at 220°C

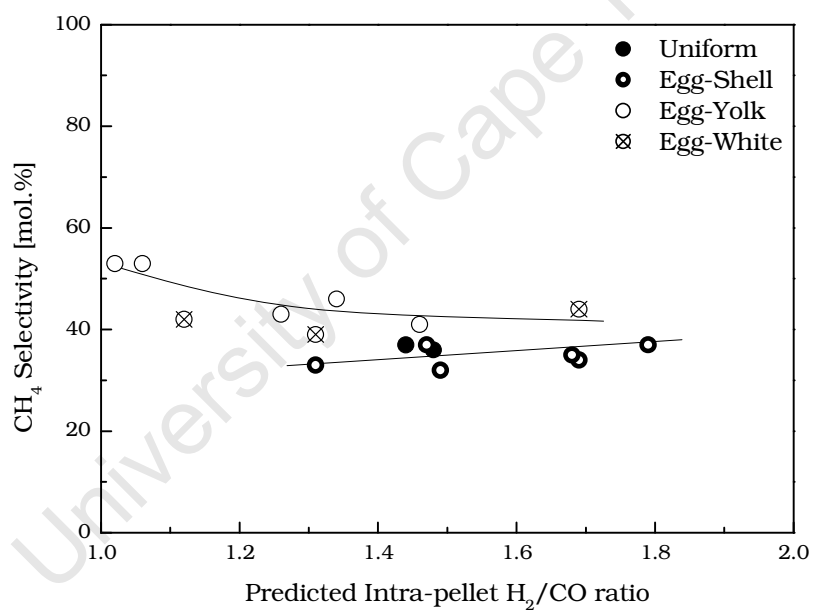


Figure 5.53: Methane selectivity as function of model predicted intra-pellet H_2/CO ratio at 230°C

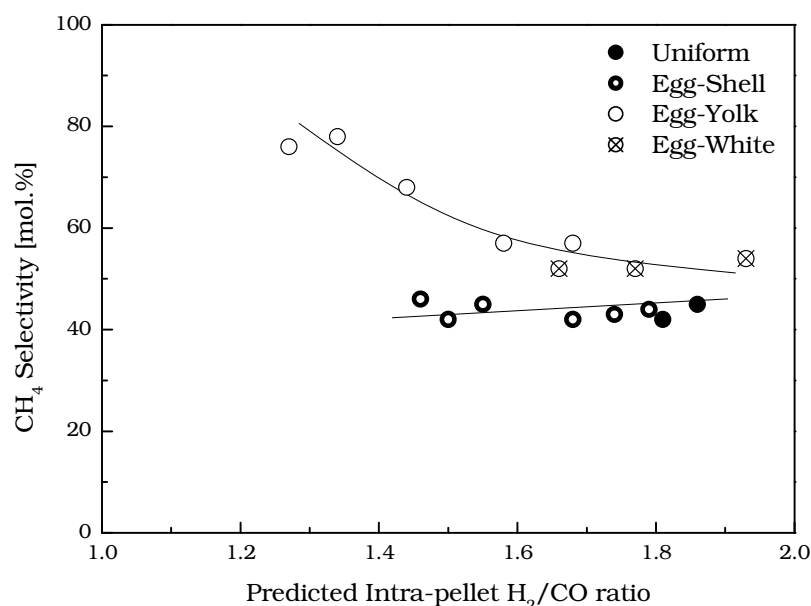


Figure 5.54: Methane selectivity as function of model predicted intra-pellet H_2/CO ratio at $240^\circ C$

The methane selectivity and $C5+$ selectivity of the structured catalysts was compared with respect to reaction-diffusion path length. At reaction temperature of $220^\circ C$, egg-shell type of catalysts shows a slight increase in methane selectivity with an increase in reaction-diffusion path length (see Figure 5.55), and a slight decrease in $C5+$ selectivity with an increase in reaction-diffusion path length (see Figure 5.56). This can be explained by the increased intra-pellet H_2/CO ratio with increasing reaction-diffusion path length, which favours the product selectivity towards methane and short chain products. The methane selectivity of egg-yolk type of catalysts increases with decreasing reaction-diffusion path length, while $C5+$ selectivity decreases with decreasing reaction-diffusion path length. The extent of the reaction (X_{CO}) in the egg-yolk type of catalyst decreases with decreasing reaction-diffusion path length due to the additional diffusion layer. The decreased conversion means that a higher reactant partial pressure and a lower α -olefin partial pressure are expected. The decreasing α -olefin partial pressure would lead to lower secondary chain growth and therefore a lower $C5+$ selectivity. The methane selectivity and the $C5+$ selectivity of the egg-white type of catalyst behave similar to the egg-shell type of catalysts.

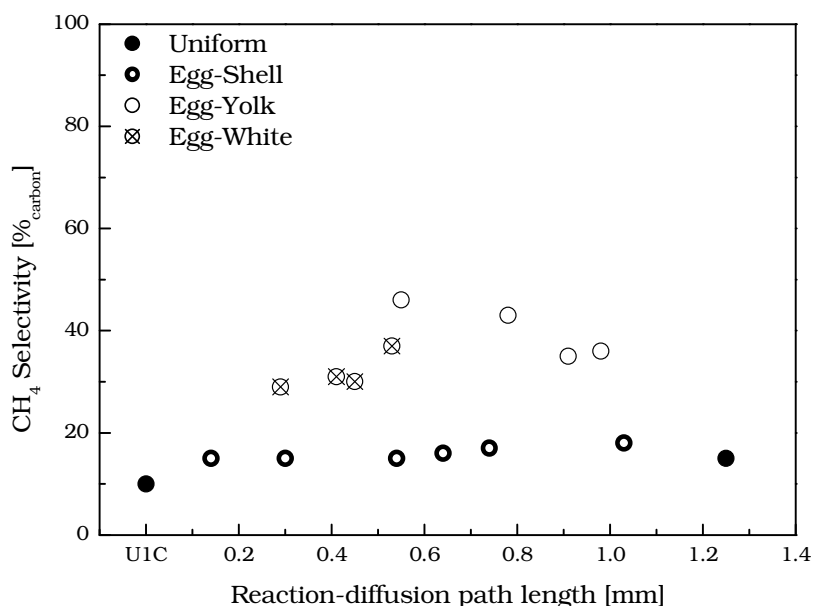


Figure 5.55: Methane selectivity as function of reaction-diffusion path length at reaction temperature of 220°C

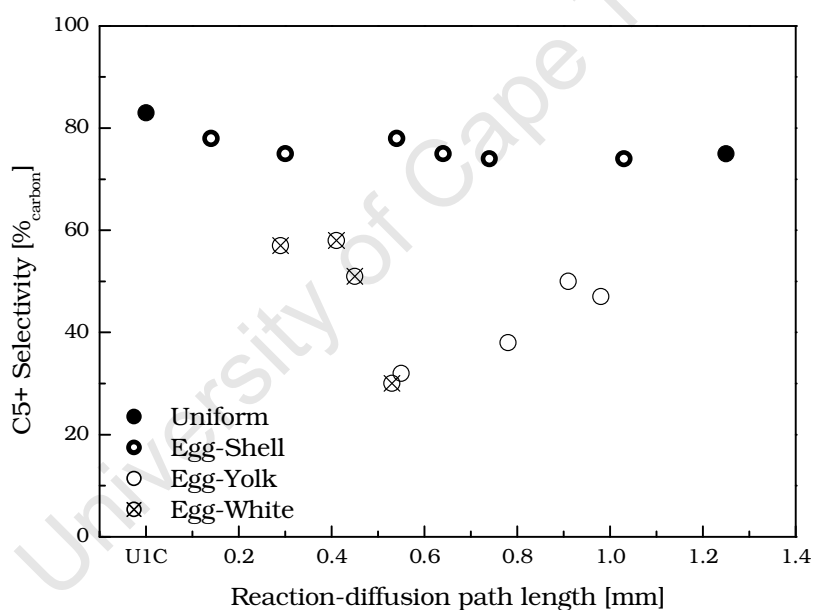


Figure 5.56: C5+ selectivity as function of reaction-diffusion path length at reaction temperature of 220°C

As reaction temperature increases, methane selectivity of egg-shell type of catalysts increases with a decrease in reaction-diffusion path length (see Figure 5.57 and Figure 5.59), while C5+ selectivity decreases with an increase in reaction-diffusion path length (see Figure 5.58 and Figure 5.60). The reaction-diffusion path length is a combination effect of reaction rate and diffusion path length. At a high reaction temperature, in other words a high reaction rate, the metal density becomes the stronger factor than diffusion path length. For constant metal loading, the metal density increase with decreasing reaction-diffusion path length. An increase in local

reaction rate may increase intra-pellet H_2/CO ratio. Thus explains the changes in product selectivity trend.

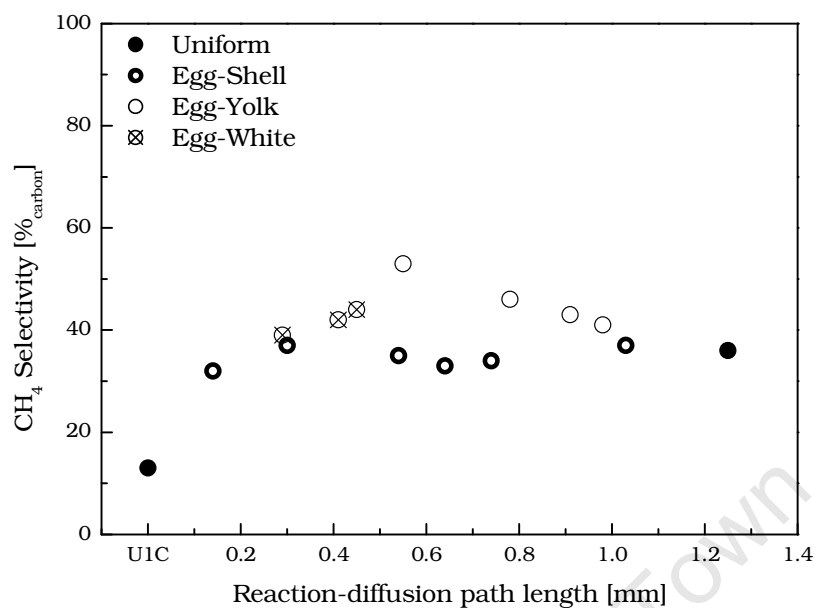


Figure 5.57: Methane selectivity as function of reaction-diffusion path length at reaction temperature of 230°C

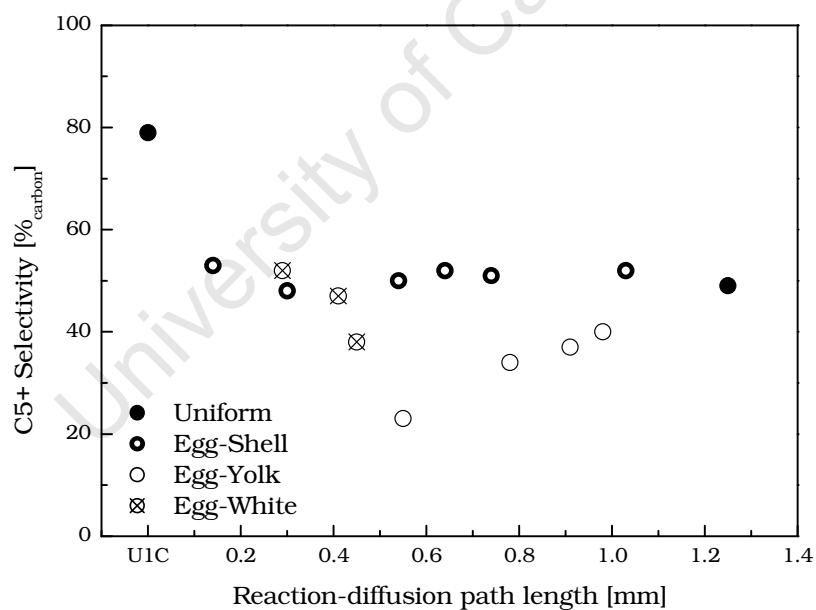


Figure 5.58: C5+ selectivity as function of reaction-diffusion path length at reaction temperature of 230°C

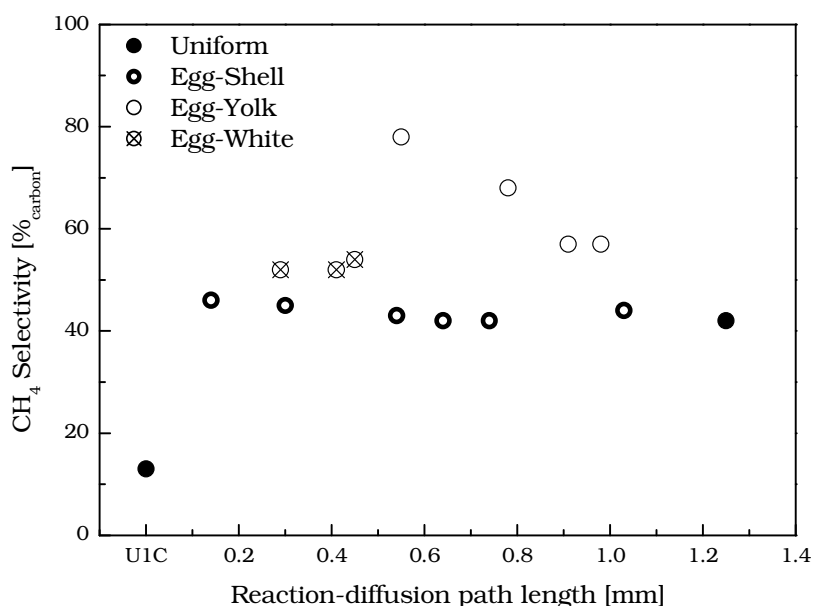


Figure 5.59: Methane selectivity as function of reaction-diffusion path length at reaction temperature of 240°C

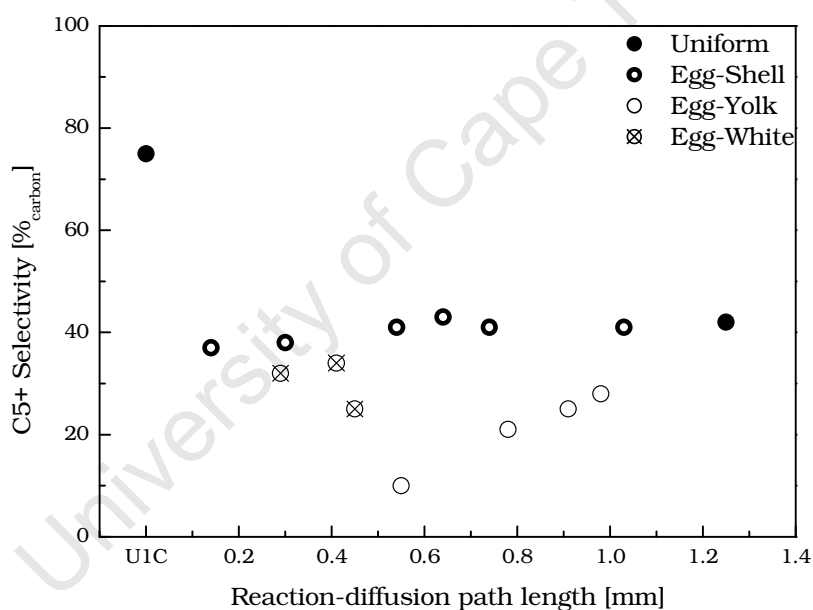


Figure 5.60: C5+ selectivity as function of reaction-diffusion path length at reaction temperature of 240°C

According to Iglesia (1997a), an increase in internal mass transport limitation increases the residence time of α -olefins which may initiate secondary chain growth and thereby increases the C5+ selectivity. This suggests that a variation in the reaction-diffusion path length that changes residence time of α -olefins within the pellet would result in an increase in C5+ selectivity. However severe internal mass transport limitation would increase intra-pellet H_2/CO , which will increase methane formation. Thus, a maximum C5+ selectivity or a minimum in methane selectivity can be expected with a variation of reaction-diffusion path length. However, no maximum C5+

selectivity with various diffusion-reaction path lengths was observed in any type of structural catalyst pellet. The effectiveness factor of egg-shell type of catalysts is close to 1, this means that they were exposed to a moderate internal mass transport limitation. This excludes the possibility that the experimental sample range was in the severe internal mass transport limitation. The product selectivity towards paraffins increases with increasing reaction-diffusion path length. Thus, it may be concluded that hydrogenation of re-adsorbed α -olefins is favoured and re-incorporation of α -olefins is not encouraged under conditions of internal mass transport limitation. This agrees with the findings of Schulz and Claeys (1999b), who reported that upon co-feeding 1-octene, ca. 75% of the re-adsorbed 1-octene is hydrogenated, 15% is isomerised and only 10% is re-incorporated.

University of Cape Town

5.3.4 C3-C8 Chain Growth Probability

The experimental chain growth probability was extracted from the slope of the straight line obtained in semi-logarithmic plots of the molar product distribution of products (Anderson-Schulz-Flory plot) containing 3 to 8 carbons (excluding oxygenates). The chain growth probabilities with respect to reaction-diffusion path length show similar trend as the methane selectivity at the tested reaction temperatures (see Figure 5.61, Figure 5.62 and Figure 5.63). This can be explained by the increased methane selectivity due to the increasing intra-pellet H_2/CO ratio with increasing reaction-diffusion path length.

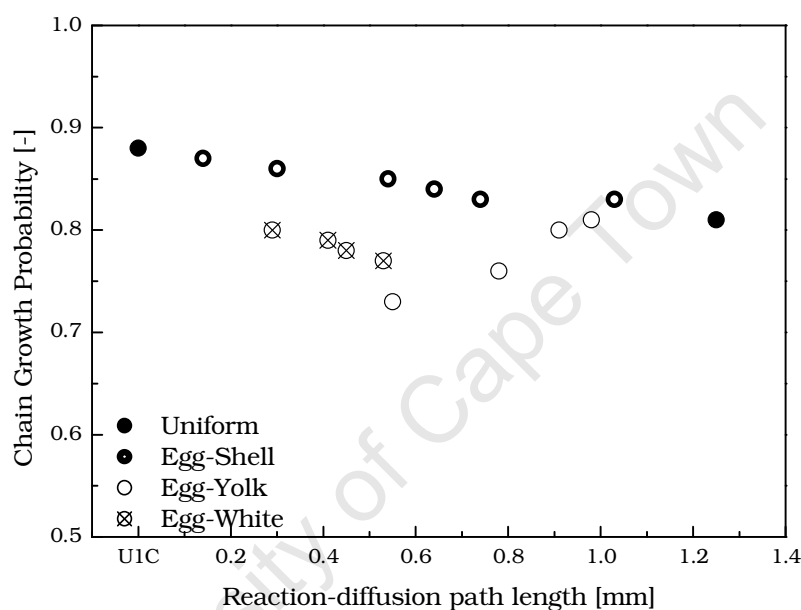


Figure 5.61: C3-C8 chain growth probability of structured catalyst at reaction temperature of 220°C

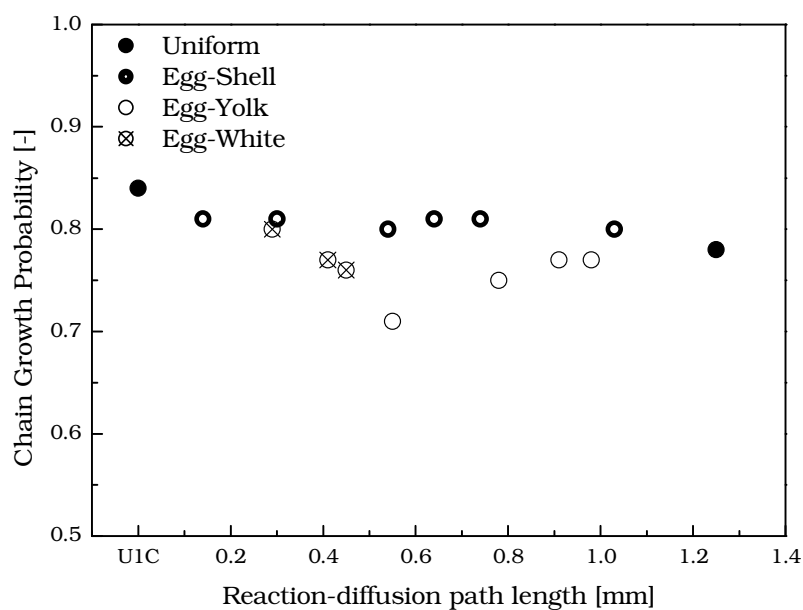


Figure 5.62: C3-C8 chain growth probability of structured catalyst at reaction temperature of 230°C

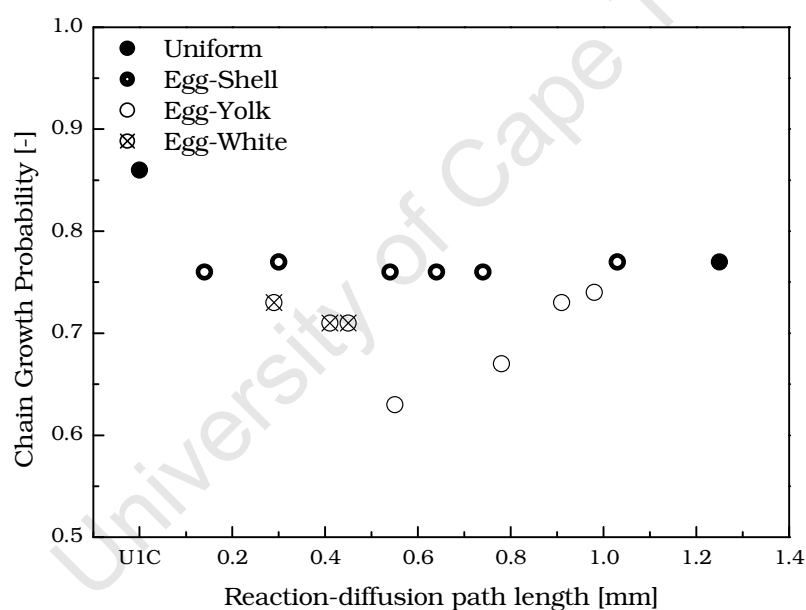


Figure 5.63: C3-C8 chain growth probability of structured catalyst at reaction temperature of 240°C

5.3.5 C5 Oxygenate Content

Oxygenates content with respect to linear hydrocarbons in C5 fraction is below 5% for all structured catalyst pellets and uniform powder. No obvious trend for oxygenate with structural parameter were observed, this suggests that oxygenate formation is not directly affected by internal mass transport limitation (see Table 5-9).

Table 5-9: C5 Oxygenates in C5 linear hydrocarbons at various reaction temperatures

Catalyst Code	220°C [%]	230°C [%]	240°C [%]	Catalyst Code	220°C [%]	230°C [%]	240°C [%]
U1C	3	5	4	Y1	5	1	-
U1	1	1	1	Y2	2	1	-
U2	1	1	2	Y3	1	1	1
S1	1	1	1	Y4	1	1	1
S2	2	1	1	Y5	1	1	1
S3	1	1	1	Y6	1	1	1
S4	1	1	1	Y7	1	2	1
S5	3	2	1	W1	1	1	1
S6	2	1	1	W2	3	1	1
				W3	1	1	1
				W4	5	-	-

University of Cape Town

6 SUMMARY AND CONCLUSIONS

Uniform, egg-shell, egg-yolk and egg-white type of structured cobalt catalyst pellets were successfully synthesised. The structured catalysts synthesis method was based on hydrophobic properties of the silica support. Thermodynamic calculation on the surface wetting scenarios inside the pores of the pellet showed a sharp boundary between the organics and aqueous solution will always be somewhat perpendicular to wards the walls of the pellet pores, irrespective of the amount of organics in the pore and the geometry of the pore. Thus, a sharp boundary between the cobalt-enriched region and cobalt-free silica can be expected. The egg-shell type of catalysts were synthesised by covering the core of the silica support with organics to inhibit contact from aqueous impregnation solution. The shell thickness can be varied by changing the amount of organic solution inside the silica support. The egg-yolk type of catalysts were synthesised by covering the inner core of an uniform pellet with organics to inhibit the core from contacting with diluted acid during leaching of the reduced cobalt. The synthesis of egg-white type of catalyst is similar to the synthesis of egg-yolk type of catalyst synthesis method, except an egg-shell type of catalyst is used as the starting precursor. The sometimes observed irregular boundary between cobalt-enriched silica and cobalt-free silica is due to the cracks in the surface of silica support prior to impregnation. According to N₂ physisorption the average pore size in the pellet was not changed by the synthesis method. This confirms that the use of diluted acid and a slow cobalt leaching rate did not affect the structural integrity of the silica pellet. Thus, this structural catalyst synthesis method provides a plausible route for synthesizing non-uniform transition metal catalysts with a sharp boundary between the metal enriched region and metal free support. The weakness of the synthesis method is that the leaching of the metal in egg-yolk and egg-white type synthesis can only be achieved after reduction of cobalt oxide in the calcined catalyst to cobalt metal, therefore additional reduction and calcination steps are required.

In all synthesized structured catalyst, the average cobalt particle size is greater than 6nm. Therefore, the results are unlikely to be clouded by particle size effect. The reduction of the structured pellets appears not been affected by the exposure to organics and diluted acids during synthesis method. The TPR-TPO experiments showed that under the influence of internal mass transport limitation, formation of cobalt (hydro-) silicate is enhanced. The increased amount of cobalt silicate in egg-yolk and egg-white type of catalyst leads to the conclusion that the acid leaching step in the catalyst synthesis may result in formation of cobalt silicate.

The performance of the catalyst pellets was tested in a modified slurry reactor. The catalyst pellets were kept in a mesh-wire basket to minimise structural damage due to attrition in the slurry reactor, while immersed in wax. The stirring speed was adjusted to ensure the absence of external mass transport limitation at operation conditions. The activation energy of the uniform powder catalyst was in good agreement with literature; therefore it was used as a basis for this study.

A reaction-diffusion pellet inside a CSTR model was derived for infinite cylindrical geometry with Yates and Satterfield intrinsic rate expression for cobalt catalyst. The model can only adequately predict the activity when the ratio of the H_2 diffusivity to CO diffusivity in wax ratio is around 1.3. This diffusivity ratio is in agreement with the Wilke-Chang (1955) diffusivity correlation, but not in accordance with the experimental data presented by Erkey *et al.* (1990).

The intra-pellet metal distribution affects the extent of internal mass transport limitation, thus affecting intra-pellet H_2/CO ratio. Egg-shell type of catalyst showed a slight increase in activity compared to the rest of the structured types. The egg-yolk type of catalyst showed a decrease in activity with a decrease in its cobalt enriched core size. The cobalt-free shell of the egg-yolk type of catalyst lengthens the diffusion path length for the reactant, therefore limits the concentration of reactant in the core. This results in a decrease in the Fischer-Tropsch activity. In the case of egg-white type of catalyst, the thickness and the position of the cobalt-enriched region affect its activity.

An increase in methane selectivity and a decrease in $C5+$ selectivity with an increase in internal mass transport limitation were observed in all types of structured catalysts. Neither a minimum in methane selectivity nor a maximum in $C5+$ selectivity with increasing internal mass transport limitation was observed in this study. The reaction-diffusion path length appears to be a good correlation parameter. The methane selectivity increases and $C5+$ selectivity decreases with increasing reaction-diffusion path length of uniform, egg-shell and egg-white type of catalyst. The methane selectivity decreases and $C5+$ selectivity increases with an increase in reaction-diffusion path length in the egg-yolk type of catalyst. This observation can be attribute to the increase in the intra-pellet H_2/CO ratio with increasing reaction-diffusion path length for the uniform, egg-shell and egg-white type of catalyst, while the intra-pellet H_2/CO ratio increases with a decrease in reaction-diffusion path length in the egg-yolk type of catalyst.

The olefin content in the C2 and C5 fraction of the structured catalyst decreases with an increase in reaction-diffusion path length. While the α -olefin in olefin content of the C5 fraction decreases with increasing reaction-diffusion path length. Thus, it can be concluded that the α -olefin re-adsorption is enhanced by an increase in the reaction-diffusion path length. However, the fact that neither minimum in methane selectivity nor a maximum in C5+ selectivity with increasing reaction-diffusion path length suggests the simultaneous increase in the intra-pellet H_2/CO ratio and enhancement of α -olefin re-adsorption due to internal mass transport limitation is not beneficial to secondary chain growth. The increased paraffin product selectivity with increasing reaction-diffusion path length shows that hydrogenation of the re-adsorbed α -olefin is favoured. The ratio of the branched hydrocarbons to linear hydrocarbons in the C5 fraction of structured catalyst increases with an increase in reaction-diffusion path length, further indicating the enhancement of α -olefin re-adsorption.

These observations lead to the conclusion that enhancement of α -olefin re-adsorption in the presence of reactant arrival limitation that increased intra-pellet H_2/CO ratio, does not promote the probability of secondary chain growth. Hydrogenation, isomerisation and re-incorporation (branching) of α -olefin are more likely to take place.

7 RECOMMENDATIONS FOR FUTURE WORK

Base on the conclusions drawn from this study, the follow recommendations are made

- Catalyst synthesis: Modify the leaching step in the synthesis of egg-yolk type of catalyst. This synthesis method would be very attractive as a commercial process, if reduction step is not required as part of egg-yolk type of catalyst synthesis. An alternative synthesis route is to inhibit the inner core of the vacuum dried uniform catalyst precursor with organics. The cobalt nitrate in the outer shell of the uniform catalyst precursor can be removed by re-dissolving in de-ionised water (washing). The analogy can be applied on vacuum dried egg-shell type catalyst precursor in the synthesis of egg-white type of catalyst.
- Kinetic modelling: The diffusivity of hydrogen, alkanes and alkenes in wax needs to be determined for the development of a complete diffusion-reaction model with product selectivity for slurry phase Fischer-Tropsch synthesis.
- Further investigation: The combined effect of reaction-diffusion path length and the inter-particle distance may be decoupled by synthesis of a series of structured catalysts with identical reaction-diffusion path length and different metal loading. The Fischer-Tropsch performance of these catalysts can be tested at constant CO conversion.
- Further investigation: The effect of conversion on product selectivity could not be separated from catalyst structure effect due to instrumentation limitation. Flow control valves with wider flow range needs to be considered for future work. A conversion target is recommend for catalyst performance test, therefore a longer period of initial catalyst condition (initial deactivation and conversion adjustment) can be considered.
- Further investigation: The experimentally determined reaction rate constant by assuming a literature value (Yates and Satterfield, 1991) for CO adsorption rate constant decreased with increase in temperature. This indicates the inadequacy of using literature CO adsorption rate constant values. Further work can be co-currently advanced with a project of which the kinetic parameters are been experimentally determined.
- Further investigation: This study can be repeated on iron catalyst, the use of egg-shell type of catalyst maybe beneficial to iron catalyst as it is more sensitive to oxidation in the presence of water. The product removal (water) may be improved by shorten the reaction-diffusion path length.

8 REFERENCES

- ADESINA, A.A. (1996) Hydrocarbon synthesis via Fischer-Tropsch reaction: travails and triumphs. *Journal of Catalysis*, 138, 345-367.
- ANDERSON, R.B. (1956a) In *Catalysis Vol. IV*. New York, Reinhold.
- ANDERSON, R.B. (1956b) Catalysis for the Fischer-Tropsch Synthesis. *Catalysis*, 4, 29-255.
- ANDERSON, R.B. (1984) *The Fischer-Tropsch Synthesis*, Orlando, Academic Press, INC.
- ANDERSON, R.B. & KARN, F.S. (1960) A rate equation for the Fischer-Tropsch synthesis on iron catalysts. *Journal of Physical Chemistry*, 64, 805-808.
- ANFRAY, J., BREMAUD, M., FONGARLAND, P., KHODAKOV, A., JALLAIS, S. & SCHWEICH, D. (2007) Kinetic study and modeling of Fischer-Tropsch reaction over a Co/Al₂O₃ catalyst in a slurry reactor. *Chemical Engineering Science*, 62, 5353-5356.
- BARRETT, E.P., JOYNER, L.G. & HALENDA, P.P. (1951) The Determination of Pore Volume and Area Distributions in Porous Substances. I. Computations from Nitrogen Isotherms. *J. Am. Chem. Soc.*, 73, 373-380.
- BARTHOLOMEW, C.H. (1987) Mechanisms of Ni Catalyst Poisoning, In *Catalyst Deactivation*. 81 Amsterdam, Elsevier.
- BARTHOLOMEW, C.H. (2001) Mechanisms of catalyst deactivation. *Applied Catalysis A: General*, 212, 17-60.
- BECKER, E.R. & WEI, J. (1977a) Nonuniform distribution of catalysts on supports : I. Bimolecular Langmuir reactions. *Journal of Catalysis*, 46, 372-381.
- BECKER, E.R. & WEI, J. (1977b) Nonuniform distribution of catalysts on supports : II. First order reactions with poisoning. *Journal of Catalysis*, 46, 372-381.
- BENENATI, R.F. & BROSILOW, C.B. (1962) Void fraction distribution in beds of spheres. *AIChE Journal*, 8, 359-361.
- BERGERET, G. & GALLEZOT, P. (2008) Particle Size and Dispersion Measurements, In *Handbook of Heterogeneous Catalysis*. 2nd ed. Weinheim, Wiley-VCH.
- BERGIUS, F. (1932) Chemical reactions under high pressure, http://nobelprice.org/nobel_prizes/chemistry/laureates/1931/bergius-lecture.pdf
- BEZEMER, G.L., BITTER, J.H., KUIPERS, H.P.C.E., OOSTERBEEK, H., HOLEWIJN, J.E., XU, X., KAPTEIJN, F., JOS VAN DILLEN, A. & DE JONG, K.P. (2006) Cobalt Particle Size Effects in the Fischer-Tropsch Reaction Studied with Carbon Nanofiber Supported Catalysts. *Journal of the American Chemical Society*, 128, 3956-3964.

- BIRD, R.B., STEWART, W.E. & LIGHTFOOT, E.N. (1962) *Transport Phenomena*, John Wiley & Sons.
- BLEKKAN, E.A., HOLMEN, A. & VADA, S. (1993) Alkali promotion of alumina supported cobalt Fischer-Tropsch catalysts studied by TPR, TPD and pulse chemisorption. *Acta Chem. Scand*, 47, 275.
- BORG, Ø., RØNNING, M., STORSTER, S., VAN BEEK, W., HOLMEN, A. & OCCELLI, B.H.D.A.M.L. (2007) Identification of cobalt species during temperature programmed reduction of Fischer-Tropsch catalysts, In *Studies in Surface Science and Catalysis*. 255-272, Elsevier.
- BP (2007) BP Statistical Review of World Energy June 2007.
- BRADY, R.C. & PETTIT, R. (1980) Reactions of diazomethane on transition-metal surfaces and their relationship to the mechanism of the Fischer-Tropsch reaction. *Journal of the American Chemical Society*, 102, 6181-6182.
- BRADY, R.C. & PETTIT, R. (1981) Mechanism of the Fischer-Tropsch reaction. The chain propagation step. *Journal of American Chemical Society*, 103, 1287-1289.
- BROMFIELD, T.C. & COVILLE, N.J. (1999) The effect of sulfide ions on a precipitated iron Fischer-Tropsch catalyst. *Applied Catalysis A: General*, 186, 297.
- BROTZ, W. (1949) Systematics of the Fischer-Tropsch catalysis. *Zeitschrift fuer Elektrochemie und Angewandte Physikalische Chemie*, 53, 301-306.
- BROWN, R., COOPER, M.E. & WHAN, D.A. (1982) Temperature programmed reduction of alumina-supported iron, cobalt and nickel bimetallic catalysts. *Applied Catalysis*, 3, 177-186.
- CARMAN, P.C. (1937) Fluid flow through granular beds. *Transactions of the Institution of Chemical Engineers (London)*, 15, 150-166.
- CHANG, P. & WILKE, C.R. (1955) Some Measurements of Diffusion in Liquids. *Journal of Physical Chemistry*, 59, 592-596.
- CHAO, K.C.L., H. M. (1988) Synthesis gas solubility in Fischer-Tropsch slurry: final report., DOE.
- CHAPMAN, S. & COWLING, T.G. (1951) *Mathematical Theory of Non-Uniform Gases*, Cambridge University Press.
- CHE, M., CLAUSE, O. & MARCILLY, C.H. (1997) Impregnation and ion exchange, In *Handbook of Heterogeneous Catalysis*. 191-207 Weinheim, Wiley-VCH.
- CHOU, J.S. & CHAO, K.C. (1992) Solubility of synthesis and product gases in a Fischer-Tropsch SASOL wax. *Ind. Eng. Chem. Res.*, 31, 621-623.
- CIA (2008) CIA World Fact Book.

- CIOBÎCĂ, I.M., KRAMER, G.J., GE, Q., NEUROCK, M. & VAN SANTEN, R.A. (2002) Mechanisms for Chain Growth in Fischer-Tropsch Synthesis over Ru(0001). *Journal of Catalysis*, 212, 136-144.
- CLAEYS, M. & VAN STEEN, E. (2002) On the effect of water during Fischer-Tropsch synthesis with a ruthenium catalyst. *Catalysis Today*, 71, 419 - 427.
- CLAEYS, M. & VAN STEEN, E. (2005) *Die Fischer-Tropsch Synthese*, Weinheim, Wiley-VCH.
- CLAEYS, M., VAN STEEN, E. & ANDRÉ STEYNBERG AND MARK, D. (2004) Chapter 8 Basic studies, In *Studies in Surface Science and Catalysis*. 601-680, Elsevier.
- COOK, L. (2005) The role of LNG in a global gas market. *Oil & Money*. London.
- CORBETT, W.E. & LUSS, D. (1974) Influence of nonuniform catalytic activity on the performance of a single spherical pellet. *Chemical Engineering Science*, 29, 1473-1483.
- CROZIER, T.E. & YAMAMOTO, S. (1974) Solubility of Hydrogen in Water, Seawater, and NaCl Solutions. *Journal of Chemical Engineering Data*, 19, 242-244.
- DAVIS, B. (2005) Fischer-Tropsch synthesis: Overview of reactor development and future potentialities. *Topics in Catalysis*, 32, 143-168.
- DAVIS, B.H. (2002) Overview of reactors for liquid phase Fischer-Tropsch synthesis. *Catalysis Today*, 71, 249-300.
- DE DEUGD, R.M., KAPTEIJN, F. & MOULIJN, J.B. (2003) Using monolithic catalysts for highly selective Fischer-Tropsch synthesis. *Catalysis Today*, 79-80, 495-501.
- DE JONG, K.P. (1991) Deposition precipitation onto pre-shaped carrier bodies. Possibilities and limitations., In *Preparation of Catalysts*. 19-36 Amsterdam, Elsevier.
- DE KOSTER, A. & VAN SANTEN, R.A. (1991) Molecular orbital studies of the adsorption of CH₃, CH₂, and CH on Rh(111) and Ni(111) surfaces. *Journal of Catalysis*, 127, 141-166.
- DELANCEY, G.B. (1973) Optimal catalyst activation policy for poisoning problems. *Chemical Engineering Science*, 28, 105-118.
- DRY, M.E. (1976) Advances in Fischer-Tropsch chemistry. *Industrial & Engineering Chemical Production Research and Development*, 15, 282-286.
- DRY, M.E. (1981) *Catalysis Science and Technology*, New York, Springer Verlag.
- DRY, M.E. (1990) The Fischer-Tropsch process - Commercial Aspects. *Catalysis Today*, 6, 183-206.
- DRY, M.E. (1996) Practical and theoretical aspects of the catalytic Fischer-Tropsch process. *Applied Catalysis A: General*, 138, 319-344.

- DRY, M.E. (2002) The Fischer-Tropsch process: 1950-2000. *Catalysis Today*, 71, 227-241.
- DRY, M.E. (2004a) Chemical concepts used for engineering purposes, In *Fischer-Tropsch Technology*. Amsterdam, Elsevier.
- DRY, M.E. (2004b) Present and future applications of the Fischer-Tropsch process. *Applied Catalysis A: General*, 276, 1-3.
- DUVENHAGE, D.J., COVILLE, N.J. & ESPINOZA, R.L. (1994) Fischer-Tropsch precipitated iron catalysts: Deactivation studies. *Studies in Surface Science and Catalysis*, 88, 3501.
- EIA (2009) Approximate Heat Content of Natural Gas (1949-2007), http://www.eia.doe.gov/emeu/aer/append_a.html
- EILERS, J., POSTHUMA, S.A. & SIE, S.T. (1990) The Shell Middle Distillate synthesis Process (SMDS). *Catalysis Letters*, 7, 253.
- EISFELD, B. & SCHNITZLEIN, K. (2001) The influence of confining walls on the pressure drop in packed beds. *Chemical Engineering Science*, 56, 4321-4329.
- ERKEY, C., RODDEN, J.B. & AKGERMAN, A. (1990) Diffusivities of synthesis gas and n-alkanes in Fischer-Tropsch wax. *Energy Fuels*, 4, 275-276.
- ERNST, B., LIBS, S., CHAUMETTE, P. & KIENNEMANN, A. (1999) Preparation and characterization of Fischer-Tropsch active Co/SiO₂ catalysts. *Applied Catalysis A: General*, 186, 145-168.
- ESPINOZA, R.L., RAJE, A.P. & JACK, D. (2004) Recycling light olefins in multiphase Fischer-Tropsch process, US 2004/0092609
- ESPINOZA, R.L., STEYNBERG, A.P., JAGER, B. & VOSLOO, A.C. (1999) Low temperature Fischer-Tropsch synthesis from a Sasol perspective. *Applied Catalysis A: General*, 186, 13-26.
- ESPINOZA, R.L., VISAGIE, J.L., VAN BERGE, P.J. & BOLDER, F.H. (1998) Cobalt based catalyst, US 5733839
- FELLER, A., CLAEYS, M. & VAN STEEN, E. (1999) Cobalt Cluster Effects in Zirconium Promoted Co/SiO₂ Fischer-Tropsch Catalysts. *Journal of Catalysis*, 185, 120-130.
- FISCHER, F. & TROPSCH, H. (1926) Direct synthesis of petroleum hydrocarbons at ordinary pressure I. *Ber.*, 59, 830-831.
- FLORY, P. (1936) Molecular size distribution in linear condensation products. *Journal of American Chemical Society*, 58, 1877-1885.
- FOGLER, H.S. (1999) *Elements of Chemical Reaction Engineering*, New Jersey, Prentice Hall.
- FORZATTI, P. & LIETTI, L. (1999) Catalyst deactivation. *Catalysis Today*, 52, 165.

- FRÖSSLING, N. (1938) *Gerlands Beitr. Geophys.*, 52, 170.
- GE, Q. & NEUROCK, M. (2006) Adsorption and Activation of CO over Flat and Stepped Co Surfaces: A First Principles Analysis. *Journal of Physical Chemistry B.*, 110, 15368-15380.
- GIRARDON, J.-S., LERMONTOV, A.S., GENGEMBRE, L., CHERNAVSKII, P.A., GRIBOVAL-CONSTANT, A. & KHODAKOV, A.Y. (2005) Effect of cobalt precursor and pretreatment conditions on the structure and catalytic performance of cobalt silica-supported Fischer-Tropsch catalysts. *Journal of Catalysis*, 230, 339-352.
- GOULA, M.A., KORDULIS, C. & LYCOURGHOTIS, A. (1992) Influence of Impregnation Parameters on the Axial Mo/ γ -Alumina Profiles Studied Using a Novel Simple Technique. *Journal of Catalysis*, 133, 486-497.
- GOVENDER, N.S., JANSEVANVUUREN, M., CLAEYS, M. & VAN STEEN, E. (2006) Importance of the Usage Ratio in Iron-Based Fischer-Tropsch Synthesis with Recycle. *Ind. Eng. Chem. Res.*, 45, 8629-8633.
- HAGGIN, J. (1991) Several issues drive research for new catalysts for methane conversion. *Chemical Engineering News*, 22.
- HARKINS, W.D. & JURA, G. (1944) Surfaces of Solids. XII. An Absolute Method for the Determination of the Area of a Finely Divided Crystalline Solid. *Journal of the American Chemical Society*, 66, 1362-1366.
- HEGEDUS, L.L. & MCCABE, R.W. (1984) Catalyst Poisoning, In *Chemical Industries Series*. New York, Dekker.
- HEPBURN, J.S., STENGER, H.G. & LYMAN, C.E. (1991) Co-impregnation of rhodium chloride with hydrofluoric acid into dry and pre-wet alumina. *Applied Catalysis*, 71, 205-218.
- HERINGTON, E.F.G. (1946) The Fischer-Tropsch synthesis considered as a polymerisation reaction. *Chemistry and Industry*, 346-347.
- HINDERMAN, J., HUTCHINGS, G.J. & KIENNEMANN, A. (1993) Mechanistic aspects of the formation of hydrocarbons and alcohols from CO hydrogenation. *Catalysis Review Science and Engineering*, 35, 1-127.
- HUBER, G.W., IBORRA, S. & CORMA, A. (2006) Synthesis of transportation fuels from biomass: Chemistry, Catalysts, and Engineering. *Chemical Reviews*, 106, 4044-4098.
- HUFF, G.A. & SATTERFIELD, C.N. (1984) Intrinsic kinetics of the Fischer-Tropsch synthesis on a reduced fused-magnetite catalyst. *Industrial & Engineering Chemical Process Design and Development*, 23, 696-705.

- IGLESIA, E. (1997a) Design, synthesis, and use of cobalt-based Fischer-Tropsch synthesis catalysts. *Applied Catalysis A: General*, 161, 59-78.
- IGLESIA, E. (1997b) Fischer-Tropsch Synthesis on Cobalt Catalysts: Structural Requirements and Reaction Pathways, In *Studies in Surface Science Catalysis*. 153-162 Amsterdam, Elsevier.
- IGLESIA, E. & MADON, R.J. (1987) Process for reducing methane formation and increasing liquid yields in a Fischer-Tropsch process, EP 0522666B1
- IGLESIA, E., REYES, S.C., MADON, R.J., SOLED, S.L. & D.D. ELEY, H.P.A.P.B.W. (1993) Selectivity Control and Catalyst Design in the Fischer-Tropsch Synthesis: Sites, Pellets, and Reactors, In *Advances in Catalysis*. 221-302, Academic Press.
- IGLESIA, E., SOLED, S.L., BAUMGARTNER, J.E. & REYES, S.C. (1995) Synthesis and Catalytic Properties of Eggshell Cobalt Catalysts for the Fischer-Tropsch Synthesis. *Journal of Catalysis*, 153, 108-122.
- IGLESIA, E., SOLED, S.L. & FIATO, R.A. (1992) Fischer-Tropsch Synthesis on Cobalt and Ruthenium. Metal Dispersion and Support Effects on Reaction Rate and Selectivity. *Journal of Catalysis*, 137, 212.
- IMF (2008) IMF Primary Commodity Prices,
<http://www.imf.org/external/np/res/commod/index.asp>
- IOANNIDES, T. & VERYKIOS, X.E. (1993) Influence of the carrier on the interaction of H₂ and CO with supported Rh. *Journal of Catalysis*, 140, 353.
- JAGER, B. (1998) *5th Natural Gas Conversion Symposium*. Taormina, Italy.
- JAGER, B. & ESPINOZA, R.L. (1995) Advances in low temperature Fischer-Tropsch synthesis. *Catalysis Today*, 23, 17.
- JANSSEN, D., DE PALMA, R., VERLAAK, S., HEREMANS, P. & DEHAEN, W. (2006) Static solvent contact angle measurements, surface free energy and wettability determination of various self-assembled monolayers on silicon dioxide. *Thin Solid Films*, 515, 1433-1438.
- JOHNSON, B., BARTHOLOMEW, C.H. & GOODMAN, D. (1991) The role of surface structure and dispersion in CO hydrogenation on cobalt. *Journal of Catalysis*, 128, 231-247.
- JORDAN, D.S. & BELL, A.T. (1987) The influence of butene on CO hydrogenation over ruthenium. *Journal of Catalysis*, 108.
- KAISER, R. (1969) *Chromatographie in der Gasphase*, Mannheim, Bibliographisches Institut.
- KARRICK, L.C. (1942) Improved fuel from Utah type coal, US 2268989

- KAPTEIJN, F., DE DEUGD, R.M. & MOULIJN, J.A. (2005) Fischer-Tropsch synthesis using monolithic catalysts. *Catalysis Today*, 105, 350-356.
- KASAOKA, S. & SAKATA, Y. (1968) Effectiveness Factors for Non-uniform Catalyst Pellets. *Journal of Chemical Engineering of Japan*, 2, 138-142.
- KAZANSKY, V.B., ZAITSEV, A.V., BOROVKOV, V.Y. & LAPIDUS, A.L. (1988) Infrared diffuse reflectance study of alkali promoted iron/alumina and cobalt/alumina Fischer-Tropsch catalysts prepared by decomposition of carbonyls. *Applied Catalysis*, 40, 17.
- KIM, C.J. (1989) Process for hydrocarbon synthesis catalyzed by cobalt on titania, enhanced by water addition, EP 0339923A1
- KIM, C.J. & HILLS, S.N.J. (1985) Reducing methane production in Fischer-Tropsch reactions, US 4547525
- KNUDSEN, J.G., HOTTEL, H.C., SAROFIM, A.F., WANKAT, P.C. & KNAEBEL, K.S. (2001) Heat and Mass Transfer, In *Perry's Chemical Engineers' Handbook*. 7th ed. 5-54 New York, McGraw-Hill.
- KOGELBAUER, A., GOODWIN, J.J.G. & OUKACI, R. (1996) Ruthenium Promotion of Co/Al₂O₃ Fischer-Tropsch Catalysts. *Journal of Catalysis*, 160, 125-133.
- KOMIYAMA, M. & MURAKI, H. (1990) Design of intrapellet activity profiles in supported catalysts, In *Handbook of Heat and Mass Transfer*. 447-500 Houston, Gulf.
- KOVÁTS, E. (1958) Gas-chromatographische Charakterisierung organischer Verbindungen. Teil 1: Retentionsindices aliphatischer Halogenide, Alkohole, Aldehyde und Ketone. *Helvetica Chimica Acta*, 41, 1915-1932.
- KRAUM, M. & BAERNS, M. (1999) Fischer-Tropsch synthesis: the influence of various cobalt compounds applied in the preparation of supported cobalt catalysts on their performance. *Applied Catalysis A: General*, 186, 189-200.
- KRISHNAMOORTHY, S., TU, M., OJEDA, M.P., PINNA, D. & IGLESIA, E. (2002) An Investigation of the Effects of Water on Rate and Selectivity for the Fischer-Tropsch Synthesis on Cobalt-Based Catalysts. *Journal of Catalysis*, 211, 422-433.
- LEDAKOWICZ, S., NETTELHOFF, H., KOKUUN, R. & DECKWER, W.D. (1985) Kinetics of the Fischer-Tropsch synthesis in the slurry phase on a potassium promoted iron catalyst. *Industrial & Engineering Chemical Process Design and Development*, 24, 1043-1049.
- LEE, S.-Y. & ARIS, R. (1985) The Distribution of Active Ingredients in Supported Catalysts Prepared by Impregnation. *Catalysis Review Science and Engineering*, 27, 207-340.

- LEVICH, V.G. (1962) *Physicochemical Hydrodynamics*, New Jersey, Prentice-Hall.
- LI, J., DING, Y., LI, X., JIAO, G., WANG, T., CHEN, W. & LUO, H. (2008) New method for the preparation of nonuniform distributed Co/SiO₂ catalysts. *The Royal Society of Chemistry*, 5954-5956.
- LI, S., KRISHNAMOORTHY, S., LI, A., MEITZNER, G.D. & IGLESIA, E. (2002) Promoted Iron-based catalyst for the Fischer-Tropsch synthesis: Design, synthesis, site densities, and catalytic properties. *Journal of Catalysis*, 206, 202-217.
- LILEY, P.E., THOMSON, G.H., FRIEND, D.G., DOUBERT, T.E. & BUCK, E. (2001) Physical and Chemical Data, In *Perry's Chemical Engineers' Handbook*. 7th ed. 2-337 New York, McGraw-Hill.
- LIU, Y. (1992) Untersuchungen zur Selektivität der Fischer-Tropsch-Synthese an Kobalt und Eisenkatalysatoren, *Ph.D. Thesis*, Technische Hochschule Darmstadt
- MAATMAN, R.W. & PRATER, C.D. (1957) Adsorption and Exclusion in Impregnation of Porous Catalytic Supports. *Industrial and Engineering Chemistry*, 49, 253-257.
- MABASO, I. (2005) Nanosized Iron Crystallites for Fischer-Tropsch Synthesis, *Ph.D. Thesis*, University of Cape Town
- MAITLIS, P.M., QUYOUN, R., LONG, H.C. & TURNER, M.L. (1999) Towards a chemical understanding of the Fischer-Tropsch reaction: Alkene formation. *Applied Catalysis A: General*, 186, 363.
- MALHERBE, J.A. (2006) The Effect of Catalyst Pre-Treatment on The Mechanical Integrity and Synthesis Performance of an Iron based Fischer-Tropsch Catalyst, *M.Sc. Thesis*, University of Cape Town
- MARANO, J.J. & HOLDER, G.D. (1997) Prediction of Bulk Properties of Fischer-Tropsch Derived Liquids. *Ind. Eng. Chem. Res.*, 36, 2409-2420.
- MARS, P. & GORGELS, M.J. (1964) Hydrogenation of acetylene - a theory of selectivity, In *Chemical Reaction Engineering: Proceedings of the Third European Symposium*. 55-65 Oxford, Pergamon.
- MARURI, A.E.C. (2003) Influence of Preparation Techniques on the Fischer-Tropsch Performance of Supported Cobalt Catalysts, *Ph.D. Thesis*, University of Cape Town
- MENON, P.G. (1990) Coke on catalysts-harmful, harmless, invisible and beneficial types. *Journal of Molecular Catalysis*, 59, 207.
- MICHALKO, E. (1966) Oxidizing gaseous combustible waste products, US 3259454

- MOODLEY, D.J., VAN DE LOOSDRECHT, J., SAIB, A.M., OVERETT, M.J., DATYE, A.K. & NIEMANTSVERDRIET, J.W. (2009) Carbon deposition as a deactivation mechanism of cobalt-based Fischer-Tropsch synthesis catalysts under realistic conditions. *Applied Catalysis A: General*, 354, 102-110.
- MOULIJN, J., VAN DIEPEN, A.E. & KAPTEIJN, F. (2001) Catalyst deactivation: is it predictable? What to do? *Applied Catalysis A: General*, 212, 3.
- NIELD, D.A. (1983) Alternative model for wall effect in laminar flow of a fluid through a packed column. *AIChE Journal*, 29, 688-689.
- OVERBURY, S.H., BERTRAND, P.A. & SOMORJAI, G.A. (1975) Surface composition of binary systems. Prediction of surface phase diagrams of solid solutions. *Chemical Reviews*, 75, 547-560.
- PAPAGEORGIOU, P., PRICE, D.M., GAVRIILIDIS, A. & VARMA, A. (1996) Preparation of Pt/ γ -Al₂O₃ Pellets with Internal Step-Distribution of Catalyst: Experiments and Theory. *Journal of Catalysis*, 158, 439-451.
- PICHLER, H. & SCHULZ, H. (1970) Neuere Erkennttnisse auf dem Gebiet der Synthese von Kohlenwasserstoffen aus CO und H₂. *Chem. -Ing. Techn.*, 42, 1162.
- PONEC, V. & VAN BARNEVELD, W.A. (1979) The Role of Chemisorption of Fischer-Tropsch Synthesis. *Industrial & Engineering Chemical Process Desing and Development*, 18, 268-271.
- PRAUSNITZ, J.M. & SHAIR, F.H. (1961) A Thermodynamic Correlation of Gas Solubilities. *AIChE Journal*, 7.
- PUSKAS, I., FLEISCH, T.H., FULL, P.R., KADUK, J.A., MARSHALL, C.L. & MEYERS, B.L. (2006) Novel aspects of the physical chemistry of Co/SiO₂ Fischer-Tropsch catalyst preparations: The chemistry of cobalt silicate formation during catalyst preparation or hydrogenation. *Applied Catalysis A: General*, 311, 146-154.
- PUSKAS, I. & HURLBUT, R.S. (2003) Comments about the causes of deviations from the Anderson-Schulz-Flory distribution of the Fischer-Tropsch reaction products. *Catalysis Today*, 84, 99-109.
- REYNHARDT (1985) NMR investigation of Fischer-Tropsch waxes: II. Hard wax. *J. Phys. D: Appl. Phys.*, 18, 1185-1197.
- ROBLEE, L.H.S., BAIRD, R.M. & TIERNEY, J.W. (1958) Radial porosity variations in packed beds. *AIChE Journal*, 4.
- ROSTRUP-NIELSEN, J.R. (1974) Coking on nickel catalysts for steam reforming of hydrocarbons. *Journal of Catalysis*, 33, 184.

- ROSTRUP-NIELSEN, J.R. (1991) Catalyst Deactivation. *Studies in Surface Science and Catalysis*, 68, 85.
- ROSTRUP-NIELSEN, J.R. (1994) Catalysis and large-scale conversion of natural gas. *Catalysis Today*, 21, 257-267.
- RUCKENSTEIN, E. & DADYBURJOR, D.B. (1983) Sintering and redispersion in supported metal catalysts. *Reviews in Chemical Engineering*, 1, 251.
- SAIB, A.M., BORGNA, A., VAN DE LOOSDRECHT, J., VAN BERGE, P.J., GEUS, J.W. & NIEMANTSVERDIET, J.W. (2006) Preparation and characterisation of spherical Co/SiO₂ model catalysts with well-defined nano-sized cobalt crystallites and a comparison of their stability against oxidation with water. *Journal of Catalysis*, 239, 326-339.
- SAIB, A.M., CLAEYS, M. & VAN STEEN, E. (2002) Silica supported cobalt Fischer-Tropsch catalysts: effect of pore diameter of support. *Catalysis Today*, 71, 395-402.
- SARUP, B. & WOJCIECHOWSKI, B.W. (1989) Studies of the Fischer-Tropsch Synthesis on a Cobalt Catalyst II. Kinetics of Carbon Monoxide Conversion to Methane and to Higher Hydrocarbons. *The Canadian Journal of Chemical Engineering*, 67, 62-74.
- SCHEUCH, S., KAMPHUIS, A.J., MCKAY, I.R. & WALLS, J.R. (1996) A two stage fluidized/spouted bed for the granulation of catalyst powder, In *Proceedings of the 1996 IChemE Reserch Event*. 997-999.
- SCHULZ, G. (1930) Highly polymerized compounds. CXXII The relation between reaction rate and composition of the reaction product in macropolymerization processes. *Zeitschrift fuer Elektrochemie und Angewandte Physikalische Chemie*, B30, 379-398.
- SCHULZ, H. (1999) Short history and present trends of Fischer-Tropsch synthesis. *Applied Catalysis A: General*, 186, 3 - 12.
- SCHULZ, H., BÖHRINGER, W., KOHL, C., RAHMAN, N. & WILL, A. (1984) Entwicklung und Anwendung der Kapillar-GC-Gesamtprobentechnik für Gas/Dampf-Vielstoffgemische, In *DGMK Forschungsbericht*. 320-329.
- SCHULZ, H. & CLAEYS, M. (1999a) Kinetic modelling of Fischer-Tropsch product distributions. *Applied Catalysis A: General*, 186, 91-107.
- SCHULZ, H. & CLAEYS, M. (1999b) Reactions of α -olefins of different chain length added during Fischer-Tropsch synthesis on a cobalt catalyst in a slurry reactor. *Applied Catalysis A: General*, 186, 71-90.
- SCHULZ, H., CLAEYS, M. & HARMS, S. (1997) *Studies in Surface Science and Catalysis*, 107, 193.

- SCHULZ, H. & CRONJÉ, J. (1977) Kohle, Fischer-Tropsch Synthese, In *Ullmanns Enzyklopädie der technischen Chemie*. 329-350 Weinheim, Verlag Chemie.
- SCHULZ, H., SCHAUB, G., CLAEYS, M. & RIEDEL, T. (1999) Transient initial kinetic regimes of Fischer-Tropsch synthesis. *Applied Catalysis A: General*, 186, 215-227.
- SCHULZ, H., VAN STEEN, E. & CLAEYS, M. (1994) Selectivity and Mechanism of Fischer-Tropsch Synthesis with Iron and Cobalt Catalysts. *Studies in Surface Science and Catalysis*, 81, 455-460.
- SCHULZ, H., VAN STEEN, E. & CLAEYS, M. (1995) Specific inhibition as the kinetic principle of Fischer-Tropsch synthesis. *Topics in Catalysis*, 2, 223.
- SEWELL, G. (1996) The reductive animation of ethanol using supported metal catalysts, *Ph.D. Thesis*, University of Cape Town
- SEXTON, B.A., HUGHES, A.E. & TURNEY, T.W. (1986) An XPS and TPR study of the reduction of promoted cobalt-kieselguhr Fischer-Tropsch catalysts. *Journal of Catalysis*, 97, 390-406.
- SHADMAN-YAZDI, F. & PETERSEN, E.E. (1972) Changing catalyst performance by varying the distribution of active catalyst within porous supports. *Chemical Engineering Science*, 27, 227-237.
- SHULTZ, J., HOFER, L., KARN, F. & ANDERSON, R.B. (1962) Studies of the Fischer-Tropsch Synthesis. *Journal of Physical Chemistry*, 66, 501-506.
- SHYR, Y.-S. & ERNST, W.R. (1980) Preparation of Nonuniformly Active Catalysts. *Journal of Catalysis*, 63, 425-432.
- SIE, S.T. & KRISHNA, R. (1999) Fundamentals and selection of advanced Fischer-Tropsch reactors. *Applied Catalysis A: General*, 186, 55-70.
- SIE, S.T., SENDEN, M.M.G. & VAN WEICHEM, H.M.H. (1991) Conversion of natural gas to transportation fuels via the shell middle distillate synthesis process (SMDS). *Catalysis Today*, 8, 371.
- SNEL, R. (1987) Olefins from syngas. *Catalysis Review Science and Engineering*, 29, 361-445.
- SPURR, A.R. (1969) A low-viscosity epoxy resin embedding medium for electron microscopy. *Journal of Ultrastructure Research*, 26, 31-43.
- STERNBERG, A. & WENDER, J. (1959) *Proceedings of International Conference of Coordinated Chemistry*. London, The Chemical Society.
- STEYNBERG, A.P., ESPINOZA, R.L., JAGER, B. & VOSLOO, A.C. (1999) High temperature Fischer-Tropsch synthesis in commercial practice. *Applied Catalysis A: General*, 186, 41-54.

- STORCH, H.H., GOLUMBIC, N. & ANDERSON, R.B. (1951) *The Fischer-Tropsch and related synthesis*, New York, John Wiley & Sons.
- TAUSTER, S.L., FUNG, S.C. & GARTEN, R.L. (1978) Strong metal-support interaction: Group VIII noble metals support on TiO₂. *Journal of American Chemical Society*, 100, 170.
- TOYOSHIMA, I. & SOMORJAI, G.A. (1979) Heats of chemisorption of O₂, H₂, CO, CO₂, and N₂ on polycrystalline and single transition metal surfaces. *Catalysis Review Science and Engineering*, 19, 105-159.
- TRIMM, D.L. (1983) Catalyst design for reduced coking. *Applied Catalysis*, 5, 263.
- VAN'T BLIK, H.F.J. & PRINS, R. (1986) Characterization of supported cobalt and cobalt-rhodium catalysts : I. Temperature-programmed reduction (TPR) and oxidation (TPO) of Co-Rh/Al₂O₃. *Journal of Catalysis*, 97, 188-199.
- VAN BARNEVELD, W.A. & PONEC, V. (1984) Reactions of CH_xCl_{4-x} with hydrogen: Relation to the Fischer-Tropsch synthesis of hydrocarbons. *Journal of Catalysis*, 88, 382-387.
- VAN BERGE, P.J. (1997) Cobalt as an alternative Fischer-Tropsch catalyst to iron for the production of middle distillates. *Studies in Surface Science and Catalysis*, 107, 207-212.
- VAN DER LAAN, G.P. & BEENACKERS, A.A.C.M. (1999) Kinetics and Selectivity of the Fischer-Tropsch Synthesis: A Literature Review. *Catalysis Reviews*, 41, 255 - 318.
- VAN HARDEVELD, R. & HARTOG, F. (1969) The statistics of surface atoms and surface sites on metal crystals. *Surface Science*, 15, 189-230.
- VAN HARDEVELD, R.M., MESTERS, C.M.A.M. & NIESEN, G.P.L. (2002) A shell metal catalyst and a precursor thereof, a process for their preparation and the use of the catalyst,
- VAN STEEN, E., CLAEYS, M., DRY, M.E., VAN DE LOOSDRECHT, J., VILJOEN, E.L. & VISAGIE, J.L. (2005) Stability of Nanocrystals: Thermodynamic Analysis of Oxidation and Re-reduction of Cobalt in Water/Hydrogen Mixtures. *Journal of Physical Chemistry B.*, 109, 3575-3577.
- VAN STEEN, E. & SCHULZ, H. (1999) Polymerisation kinetics of the Fischer-Tropsch CO hydrogenation using iron and cobalt based catalysts. *Applied Catalysis A: General*, 186, 309-320.
- VAN STEEN, E., SEWELL, G.S., MAKHOTHE, R.A., MICKLETHWAITE, C., MANSTEIN, H., DE LANGE, M. & O'CONNOR, C.T. (1996) TPR Study on the Preparation of Impregnated Co/SiO₂ Catalysts. *Journal of Catalysis*, 162, 220-229.

- VANNICE, M.A. (1975a) The Catalytic Synthesis of Hydrocarbons from H_2/CO Mixtures over the Group VIII Metals I. The Specific Activities and Product Distributions of Supported Metals. *Journal of Catalysis*, 37, 449-461.
- VANNICE, M.A. (1975b) The Catalytic Synthesis of Hydrocarbons from H_2/CO Mixtures over the Group VIII Metals II. The Kinetics of the Methanation Reaction over Supported Metals. *Journal of Catalysis*, 37, 462-473.
- VILLADSEN, J. (1976) The effectiveness factor for an isothermal pellet with decreasing activity towards the pellet surface. *Chemical Engineering Science*, 31, 1212-1213.
- VISWANATHAN, B. & GOPALAKRISHNAN, R. (1986) Effect of support and promoter in Fischer-Tropsch cobalt catalysts. *Journal of Catalysis*, 99, 342-348.
- VOSLOO, A.C. (2001) Fischer-Tropsch: a futuristic view. *Fuel Processing Technology*, 71, 149-155.
- WANKE, S.E. & FLYNN, P.C. (1975) A model of supported metal catalysts sintering. I. Development of model. *Catalysis Review Science and Engineering*, 12, 93.
- WEAST, R.C. (1983) *CRC Handbook of Chemistry Physics*, CRC Press.
- WELKER, C. (2007) Ruthenium based Fischer-Tropsch Synthesis on Crystallites and Clusters of Different Sizes, *Ph.D. Thesis*, University of Cape Town
- WERGY (2005) LNG Centre,
<http://gmaiso.free.fr/lng/index.php3?suj=gtl&page=gtlsearch>
- WERTHER, J. (2008) Fluidised-bed reactors, In *Handbook of Heterogeneous Catalysis*. 2nd ed. 2106-2132 Weinheim, Wiley-VCH.
- WU, Z. (2006) China bets big on coal-to-oil projects. *Asia Times*.
- YATES, I.C. & SATTERFIELD, C.N. (1991) Intrinsic Kinetics of the Fischer-Tropsch Synthesis on a Cobalt Catalyst. *Energy & Fuels*, 5, 168-173.
- ZHENG, C., APELOIG, Y. & HOFFMANN, R. (1988) Bonding and coupling of C1 fragments on metal surfaces. *Journal of American Chemical Society*, 110, 749-774.
- ZHUANG, Y.Q., CLAEYS, M. & VAN STEEN, E. (2006) Novel synthesis route for egg-shell, egg-white and egg-yolk type of cobalt on silica catalysts. *Applied Catalysis A: General*, 301, 138 - 142.

APPENDIX A

1. GTL & CTL Potential Index

A reserve of coal or natural gas is needed for a country to consider CTL or GTL. Proven coal and natural gas reserve as at 1 January 2008 according to CIA (2008) was classified into 6 levels and illustrated on thematic maps.

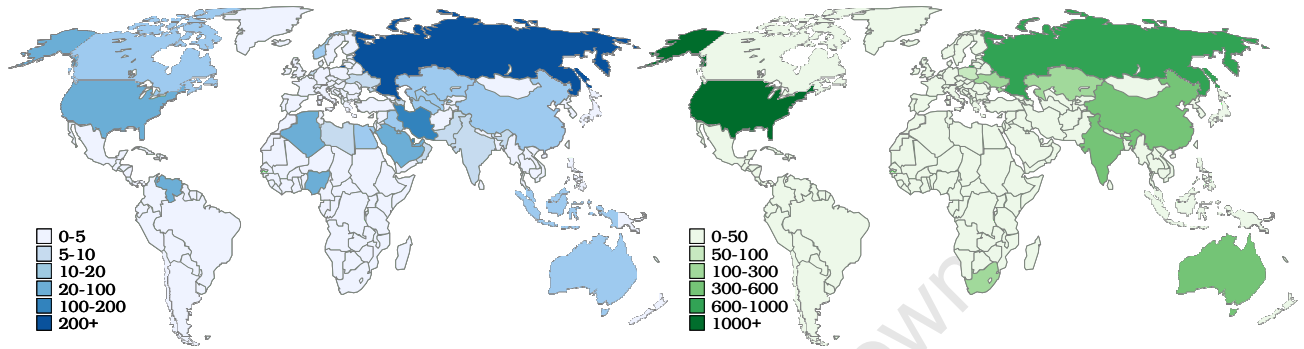


Figure A.1: Thematic maps of proven natural gas (left) and coal (right) reserves [10⁹ boe]

Defining FTS necessity index as percentage of oil imports to oil consumption, GTL index is then defined as the product of FTS necessity index and natural gas reserve, while CTL index is the product of FTS necessity index and coal gas reserve. The scale of the indices were made from 0 to 36.

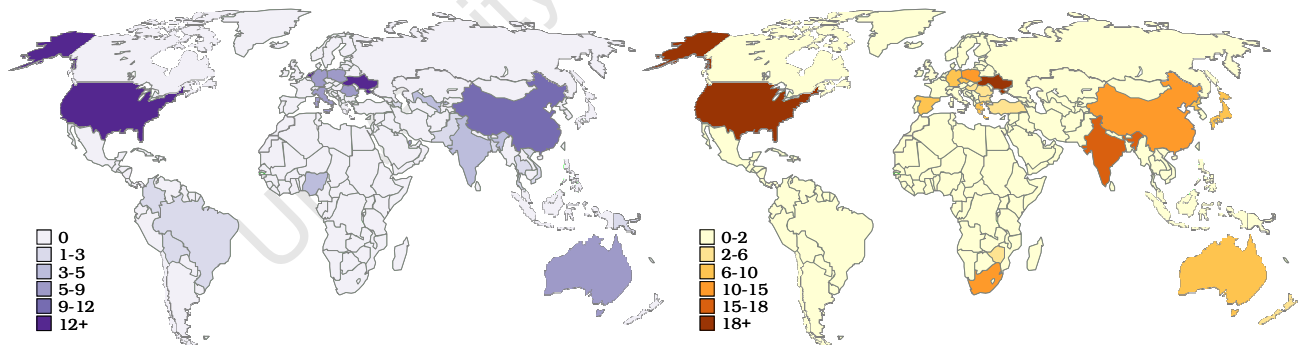


Figure A.2: Thematic maps of GTL index (left) and CTL index (right)

APPENDIX B

1. AAS Acid Digestion Procedure

Approximately 0.1g of each dried; calcined catalyst were crushed ($-200\mu\text{m}$) and weighed into 250ml wide mouthed Erlenmeyer flasks. Ten millilitres of HCl/HF mixture, which is made of 4 parts hydrochloric acid ($\sim 40\%$) and 1 part hydrofluoric acid ($\sim 30\%$), was added to each sample and heated to boil. Once the mixture is boiled, 10ml of nitric acid ($\sim 60\%$) was added and heated further. When sample volume was approximately 2ml, 5ml of perchloric acid was added and heated further. Samples were cooled down when the volume in the flask was approximately 2ml.

The aqueous sample was transferred quantitatively into a 100ml plastic volumetric flask and made up to 100ml with distilled water. This solution is then filtered through filter paper (Whatman No1) into sample bottles. The filtrate is then read on Atomic Absorption Spectrophotometer Varian 3.0, which is calibrated with a standard cobalt solution.

The cobalt concentration of the aqueous sample is measured in milligrams per litre. Hence the cobalt loading of calcined catalyst is calculated as follows

$$\text{Co Content}[\%] = \frac{\text{Co Concentration}[\text{mg}/\ell] \times 0.1[\ell]}{\text{Sample Mass}[\text{g}] \times 10}$$

Assuming all cobalt oxide is in the form Co_3O_4 , cobalt loading of a fully reduced catalyst is then

$$\text{Co Loading}[\%] = \frac{100}{\left(1 + \frac{100}{\text{Co Content}[\%]} - \frac{M(\text{Co}_3\text{O}_4)}{3 \times M(\text{Co})}\right)}$$

2. SEM Sample Preparation

A low viscosity embedding resin developed by Spurr (1969) for electron microscopy was used to anchor catalyst pellet. Composition of this resin is shown in Table B-1. Catalysts were placed in resin such that its cross-sectional area is perpendicular to the electron beam.

Catalysts embedded in resin were hardened in oven at 60°C for 24 hours, subsequently cut in half. The surface of the cross-sectional area was then polished using a Metaserv Polisher with 0.05µm γ -alumina powder.

Table B-1: Composition of Spurr's resin used in electron microscopy

Composition	[wt%]
ERL 4206	24.8
DER 736	14.9
NSA	59.4
S-1	1.0

3. TEM Image Analysis Procedure

IMAGE J is image software coded in Java. It converts picture in any format to 8-bit greyscale image, in which contrast of the image can be isolated and outlined. Contrast image of cobalt metal particles within a local cluster were combined and outlined. Feret's diameter, which defined as the largest distance possible between any two points along the boundary of a region of interest, were determined from outlined image of clusters as shown in Figure B.1.

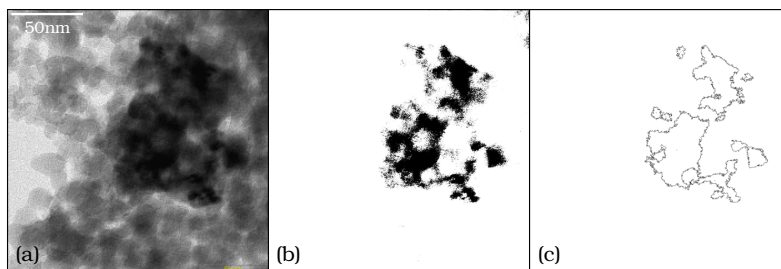


Figure B.1: Raw TEM image of catalyst S1 (a) Contrast isolated image showing metal cluster (b) Contrast outlined defining boundary of metal cluster (c)

Metal particles were isolated by segmenting contrast isolated images using Euclidian distance map algorithm. Raw TEM images are converted to binary images, local maxima on the binary image were determined. Segmentation was performed by assuming each maximum belongs to one metal particle.

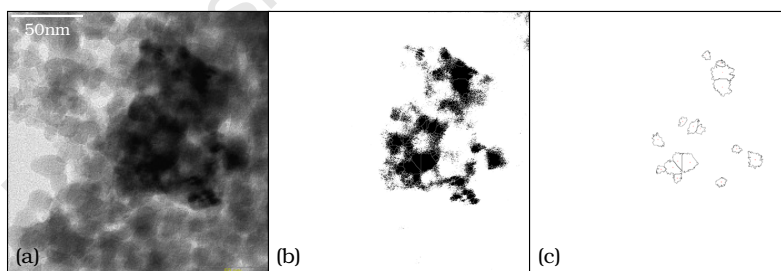


Figure B.2: Segmented TEM image of catalyst S1 (a) Contrast isolated image showing segmented metal particles (b) Contrast outlined defining boundary of metal particles (c)

The average volume based metal particle sizes were calculated by the following equation.

$$d_{\text{volume}} = \frac{1}{6} \times \frac{\sum d^3}{\sum d^2}$$

4. XRD Procedure and Calculations

The baseline noise of the X-ray diffraction intensity data was minimised by averaging measured data using the 5 point average method before estimating particle size using the Debye-Scherrer equation. Peak heights were estimated from averaged baseline data and peak maximum. Peak width at half peak height was recorded; particle size are estimated according to Debye-Scherrer equation at Miller indices of (3 1 1); (5 1 1) and (4 4 0). Particle sizes of these planes were in close agreement. These values are averaged to represent the Co_3O_4 particle size of calcined catalysts.

Table B-2: Co_3O_4 particle size in [nm] calculated from XRD pattern using Debye-Scherrer equation at various Miller indices

Catalyst	(3 1 1)	(5 1 1)	(4 4 0)
U1	11.8	10.9	11.7
U2	17.0	14.2	13.5
S1	10.8	12.1	11.2
S2	11.4	12.8	10.5
S3	10.8	9.6	10.5
S4	10.3	10.3	11.9
S5	10.2	10.2	11.5
S6	13.3	9.1	10.9
Y1	6.6	6.6	7.9
Y2	6.5	8.1	6.9
Y3	5.5	6.3	10.7
Y4	6.9	15.2	7.3
Y5	9.3	11.0	8.2
Y6	5.9	5.9	6.1
Y7	5.8	-	-
W1	7.3	9.9	8.0
W2	7.1	7.8	10.2
W3	7.4	7.8	-
W4	7.7	10.1	6.5

5. BET and BJH Model Calculations

The fundamental assumption of this theory is that the forces active in the condensation of gases are also responsible for the binding energy in multi-molecular adsorption. By equating the rate of condensation of gas molecules onto an already adsorbed layer to the rate of evaporation from that layer and summing for an infinite number of layers, Brunauer-Emmet-Teller (BET) isotherm can be written as

$$\frac{V_{\text{ads}}}{V_{\text{mono}}} = \frac{C_{\text{ads}} \times \frac{P}{P_{\text{sat}}}}{\left(1 + (C_{\text{ads}} - 1) \frac{P}{P_{\text{sat}}}\right) \left(1 - \frac{P}{P_{\text{sat}}}\right)}$$

and can be linearised into

$$\frac{1}{V_{\text{ads}} \left(\frac{P_{\text{sat}}}{P} - 1 \right)} = \frac{(C_{\text{ads}} - 1)}{C_{\text{ads}} \times V_{\text{mono}}} \times \frac{P}{P_{\text{sat}}} + \frac{1}{C_{\text{ads}} \times V_{\text{mono}}}$$

Thus the isotherm is plotted in this form and yielded a straight line. Data obtained from nitrogen gas adsorption and desorption were used to fit the BET isotherm, from which the volume of gas absorbed to form a monolayer is estimated (Figure B.3).

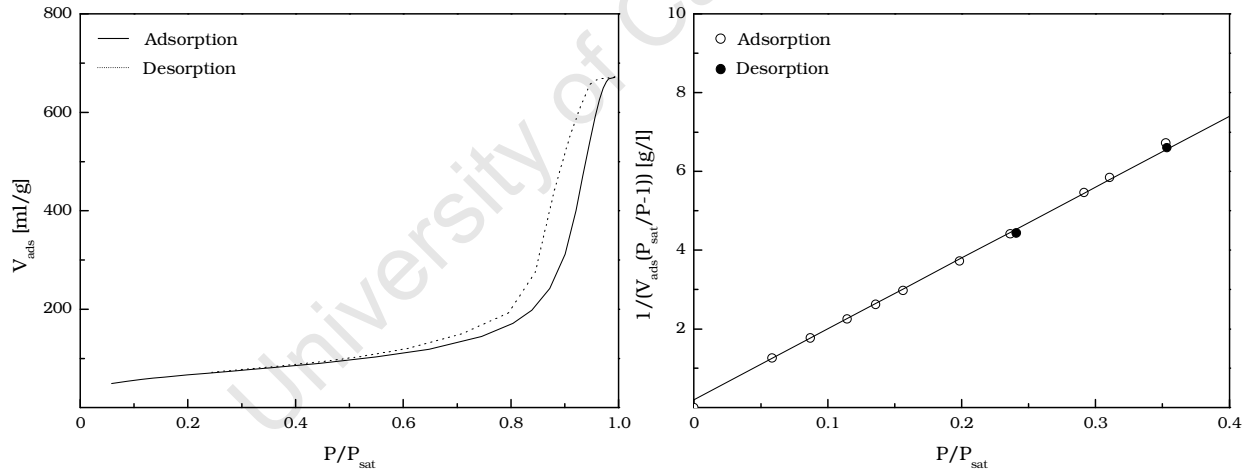


Figure B.3: Nitrogen physisorption isotherms (left) and BET isotherms (right) of pure silica support

Pore size distribution was determined using the Barrett-Joyner-Halenda (BJH) method described by Barrett *et al.* (1951), which imagine the isotherm as a series of steps downward of equal relative pressure, the amount of adsorptive lost in each step represents the core volumes of pores emptied in that step. Desorption isotherms were followed for the mathematics of the technique. The condition of which all pores are to be considered filled was taken to be at about 99.5% relative pressure ($P/P_{\text{sat}} = 0.995$).

The thickness of the adsorbed layer remaining on the pore walls is calculated from a thickness relationship described by Harkins and Jura (1994). The quantity adsorbed can be related to the statistical thickness of the adsorbed film by the relationship

$$t = \sqrt{\frac{13.99}{0.34 - \log\left(\frac{P_{\text{sat}}}{P}\right)}}$$

A sample of pore size distribution determined by this method is demonstrated in Figure B.4.

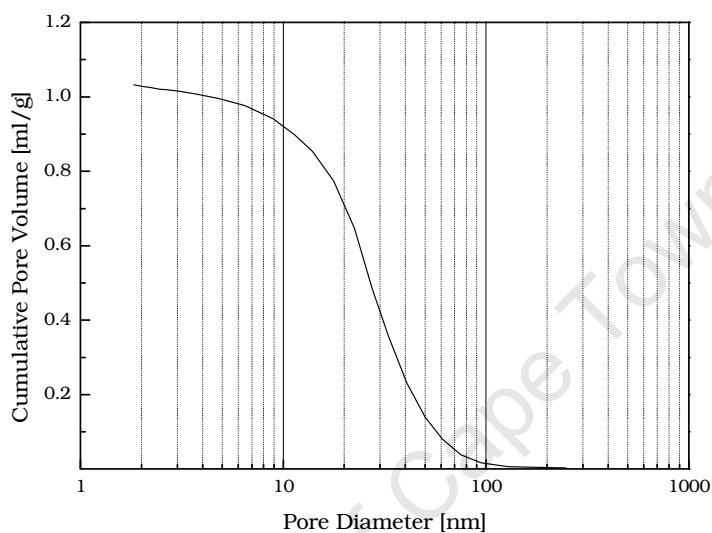


Figure B.4: BJH pore size distribution of pure silica support

6. Chemisorption Particle Diameter Derivation

Average particle diameter of the cobalt metal was calculated using the following relation

$$\frac{A_m[\text{m}^2/\text{g}_{\text{catalyst}}]}{M_{\text{Co}}[\text{g}]} = \frac{A_m[\text{m}^2/\text{g}_{\text{catalyst}}]}{V_{\text{Co}}[\text{m}^3] \times \rho_{\text{Co}}[\text{g}/\text{m}^3]}$$

Assuming particles are spherical in shape, the above equation can be rewritten as

$$\frac{A_m}{M_{\text{Co}}} = \frac{\pi d^2}{(\pi d^3/6) \rho_{\text{Co}}} = \frac{6}{d \rho_{\text{Co}}}$$

Therefore average particle diameter is then

$$d[\text{nm}] = \frac{6}{A_m[\text{m}^2/\text{g}_{\text{active}}] \rho_{\text{Co}}[\text{g}/\text{m}^3]} \times \frac{L_{\text{Co}}^{\circ}[\text{g}/\text{g}_{\text{catalyst}}] M_{\text{catalyst}}[\text{g}_{\text{catalyst}}]}{R^{\circ}[\text{g}_{\text{active}}/\text{g}]} \times 1000$$

where A_m is active metal surface area according to chemisorption, L_{Co}° is cobalt loading of the catalyst, M_{catalyst} is the mass of catalyst used in chemisorption, R° is degree of reduction and ρ_{Co} is density of cobalt metal which is 8.9g/ml. Cobalt loading of the catalyst used in this equation was taken from AAS results and degree of reduction from TPR-TPO results.

7. TPR-TPO Calibrations and Calculations

Micromeritics AutoChem 2910 was calibrated using five standards of NiO samples with various mass. Hydrogen and oxygen consumption of these samples during TPO-TPR analysis were recorded.

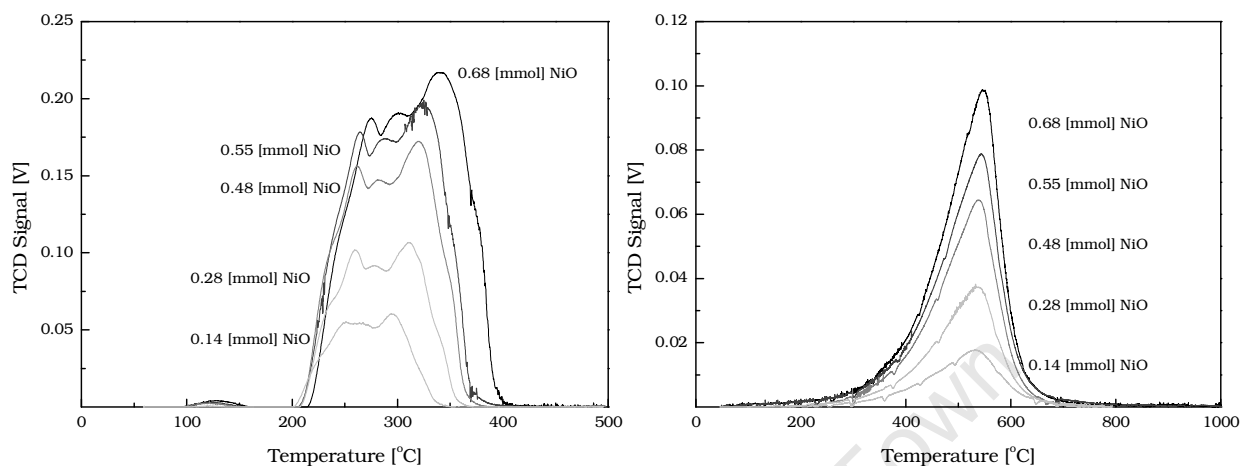


Figure B.5: TPR H₂ calibration (left) and TPO O₂ calibration (right) using NiO

Hydrogen and oxygen consumption rate were correlated using TCD integration area and amount of NiO used by assuming 1 mol of H₂ per NiO during reduction and 0.5 mol of O₂ per NiO during oxidation.

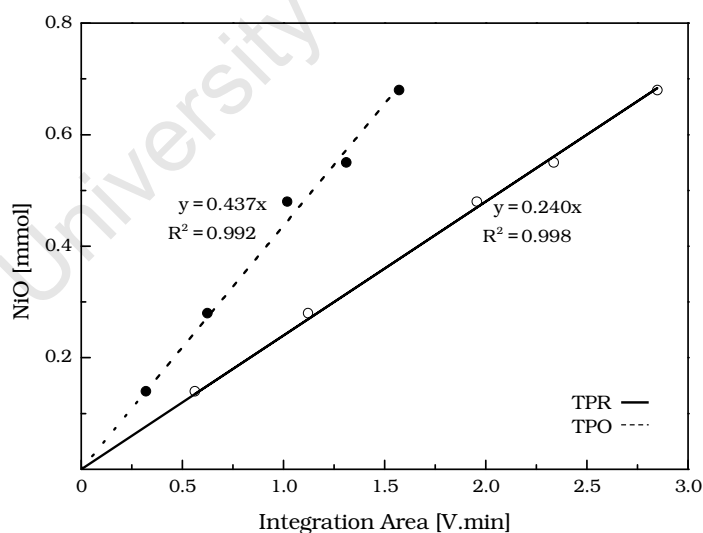


Figure B.6: H₂ and O₂ calibration curves

The degree of reduction and the cobalt loading were calculated as follows:

The mass of catalyst U1C loaded into the TPR-TPO machine is 0.2131g. The amount of H₂ consumed during the TPR of the reduced U1C is 0.148mmol (0.58mmol/g). The amount of O₂ consumption and O₂ released during TPO were 0.237mmol (1.11mmol/g)

and 0.068mmol (0.32mmol/g) respectively. If cobalt is completely reduced to metal after the post-reduction-TPR, and the oxygen released during TPO can be described as:

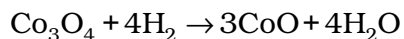


The amount of cobalt metal on the catalyst is thus: $6 \times 0.068\text{mmol} = 0.41\text{mmol}$.

The cobalt metal loading of the calcined catalyst (if cobalt exists as Co_3O_4) is then:

$$\frac{58.94(0.41)}{\left(\frac{0.2131}{1000} - \left(\frac{4}{3} \times 15.99\right)0.41\right)} = 11.8\%$$

If the hydrogen consumed during the post-reduction-TPR can be described as:



The amount of unreduced cobalt is $\frac{3}{4} \times 0.148\text{mmol} = 0.111\text{mmol}$.

Thus, the degree of reduction is $0.111/0.41 = 73\%$

University of Cape Town

8. TCD Trace

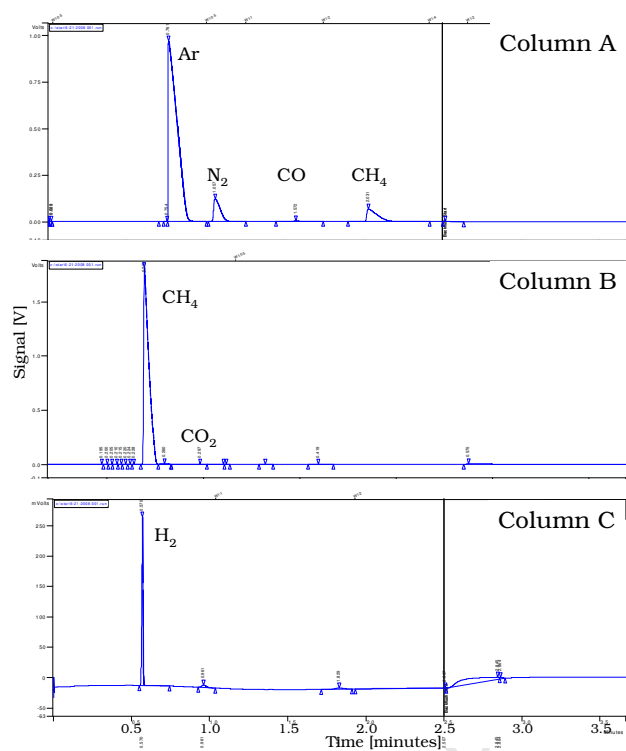


Figure B.7: Example of a TCD spectrum

9. FID Operating Conditions and Peak Identification

Temperature and pressure program used in FID analysis is summarised in Figure B.8. Example of product distribution determined from FID analysis is illustrated in Figure B.9.

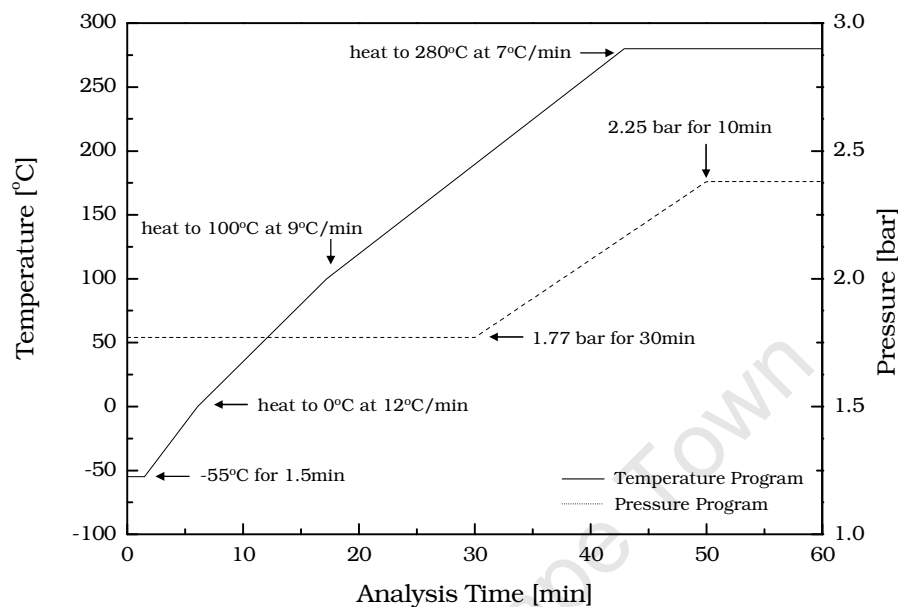


Figure B.8: Temperature and pressure programs used for the separation of VOC in FID analysis

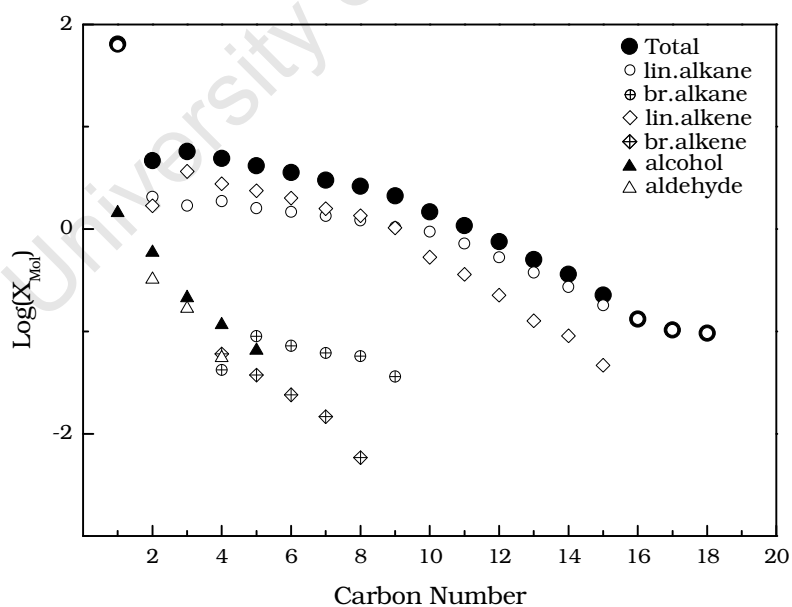


Figure B.9: Example of product distribution (U1C) obtained from FID analysis

Peaks were assigned using the retention indexes suggested by Kováts, 1958.

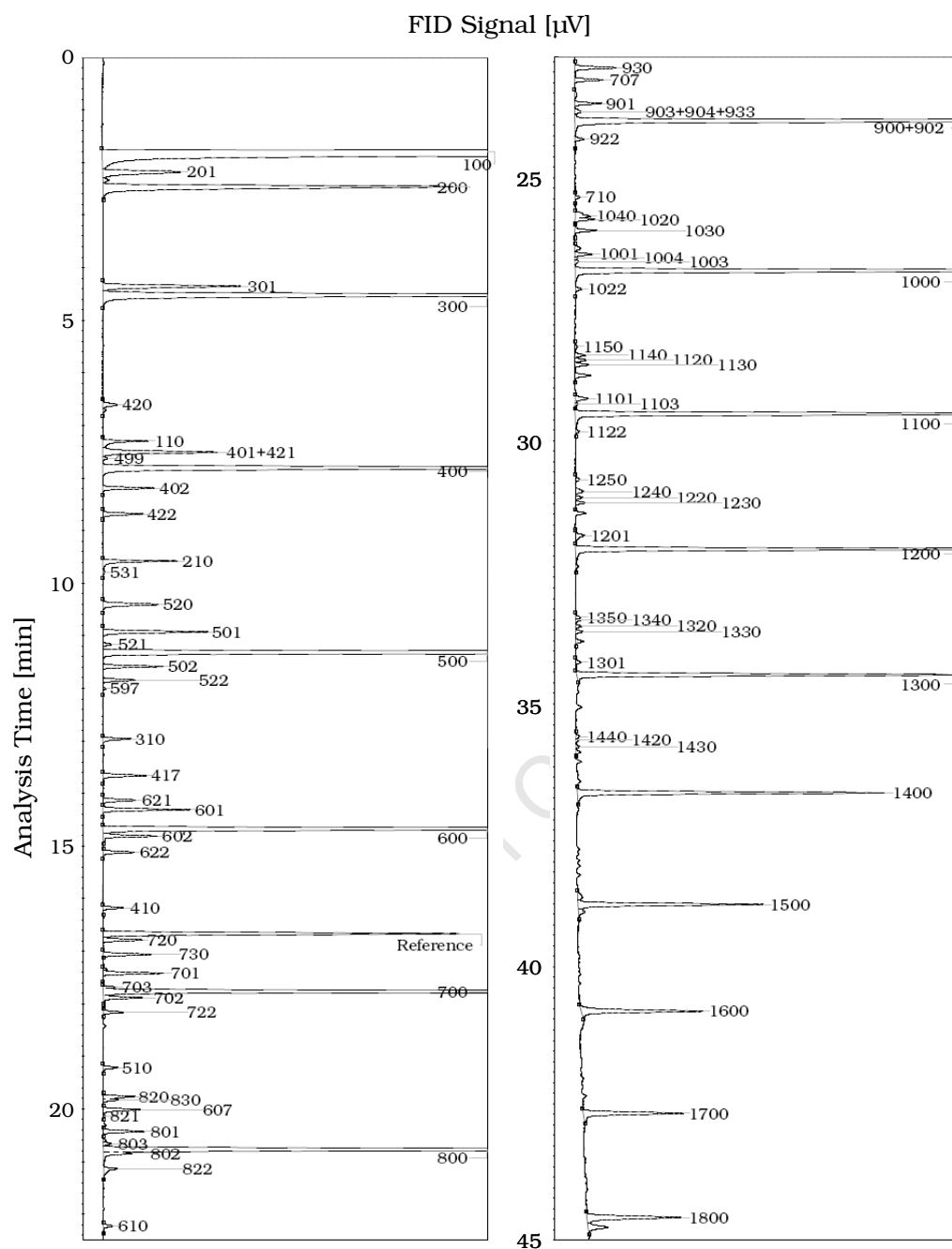


Figure B.10: Example of a FID spectrum (U1, 120h07m30s)

Table B-2: Compound codes used for FID peak identification

Compound	Code	Compound	Code	Compound	Code
Methane	100	2-Me-Pentene (1)	621	5-Me-Heptene (1)	851
Methanol	110	3-Me-Pentene (1)	631	z-Octene (2)	802
Ethane	200	4-Me-Pentene (1)	641	c-Octene (2)	822
Ethene	201	2,3 Di-Me-Butene (1)	664	z-Octene (3)	803
Ethanal	207	z-Hexene (2)	602	c-Octene (3)	833
Ethanol	210	c-Hexene (2)	622	z-Octene (4)	804
Propane	300	z-Hexene (3)	603	Me-C8-Olefin	891
Propene	301	c-Hexene (3)	633	Octanal	807
Propanal	307	Hexanal	607	Octanol (1)	810
Propanol (1)	310	Hexanol (1)	610	Octanone (2)	817
Propanol (2)	315	Hexanone (2)	617	Rest C8	899
Propanone	317	Cyclo-Hexane	REF	n-Nonane	900
n-Butane	400	n-Heptane	700	2-Me-Octane	920
2-Me-Propane	420	2-Me-Hexane	720	2,4 Di-Me-Heptane	924
Butene (1)	401	2,3 Di-Me-Pentane	723	2,5 Di-Me-Heptane	925
2-Me-Propene (1)	421	3-Me-Hexane	730	3-Me-Octane	930
z-Butene (2)	402	3-Et-Pentane	780	4-Me-Octane	940
c-Butene (2)	422	Heptene (1)	701	3-Et-Octane	980
Butadiene (1,3)	499	2-Me-Hexene (1)	721	Nonene (1)	901
Butanal	407	3-Me-Hexene (1)	731	2-Me-Octene (1)	921
Butanol (1)	410	4-Me-Hexene (1)	741	z-Nonene (2)	902
Butanol (2)	415	5-Me-Hexene (1)	751	c-Nonene (2)	922
Butanone (2)	417	z-Heptene (2)	702	z-Nonene (3)	903
n-Pentane	500	c-Heptene (2)	722	c-Nonene (3)	933
2-Me-Butane	520	z-Heptene (3)	703	Nonene (4)	904
Pentene (1)	501	c-Heptene (3)	733	Nonanal	907
2-Me-Butene (1)	521	2-Me-Hexene (2)	797	Nonanol (1)	910
3-Me-Butene (1)	531	3-Me-Hexene (2)	732	Nonanone (2)	917
z-Pentene (2)	502	Heptanal	707	Rest C9	999
c-Pentene (2)	522	Heptanol (1)	710	n-Decane	1000
2-Me-Butene (2)	597	Heptanone (2)	717	2-Me-Nonane	1020
Pentanal	507	Rest C7	799	3-Me-Nonane	1030
Pentanol (1)	510	n-Octane	800	4-Me-Nonane	1040
Pentanone (2)	517	2-Me-Heptane	820	5-Me-Nonane	1050
n-Hexane	600	3-Me-Heptane	830	Decene (1)	1001
2-Me-Pentane	620	4-Me-Heptane	840	z-Decene (2)	1002
3-Me-Pentane	630	Octene (1)	801	c-Decene (2)	1022
2,3 Di-Me-Butane	623	2-Me-Heptene (1)	821	z-Decene (3)	1003
2,4 Di-Me-Butane	624	3-Me-Heptene (1)	831	c-Decene (3)	1033
Hexene (1)	601	4-Me-Heptene (1)	841	z-Decene (4)	1004

Compound	Code	Compound	Code	Compound	Code
c-Decene (4)	1044	4-Me-Undecane	1240	Rest C13-Olefin	1304
Decene (5)	1005	5-Me-Undecane	1250	Tridecanal	1307
Decanol (1)	1010	6-Me-Undecane	1260	Tridecanol (1)	1310
Decanal	1007	Dodecene (1)	1201	Tridecanone (2)	1317
Decanone (2)	1017	z-Dodecene (2)	1202	Rest C13	1399
Rest C10	1099	c-Dodecene (2)	1222	n-Tetradecane	1400
n-Undecane	1100	z-Dodecene (3)	1203	2-Me-Tridecane	1420
2-Me-Decane	1120	c-Dodecene (3)	1233	3-Me-Tridecane	1430
3-Me-Decane	1130	Rest-C-12-Olefin	1204	4-Me-Tridecane	1440
4-Me-Decane	1140	Dodecanal	1207	5-Me-Tridecane	1450
5-Me-Decane	1150	Dodecanol (1)	1210	6-Me-Tridecane	1460
Undecene (1)	1101	Dodecanone (2)	1217	7-Me-Tridecane	1470
z-Undecene (2)	1102	Rest C12	1299	Tetradecene (1)	1401
c-Undecene (2)	1122	n-Tridecane	1300	z-Tetradecene (2)	1402
z-Undecene (3)	1103	2-Me-Dodecane	1320	c-Tetradecene (2)	1422
c-Undecene (3)	1133	3-Me-Dodecane	1330	Rest-C-14-Olefin	1404
Rest-C-11-Olefin	1104	4-Me-Dodecane	1340	Tetradecanal	1407
Undecanal	1107	5-Me-Dodecane	1350	Tetradecanol (1)	1410
Undecanol (1)	1110	6-Me-Dodecane	1360	Tetradecanone (2)	1417
Undecanone (2)	1117	Tridecene (1)	1301	Rest C14	1499
Rest C11	1199	z-Tridecene (2)	1302	n-Pentadecane	1500
n-Dodecane	1200	c-Tridecene (2)	1322	n-Hexadecane	1600
2-Me-Undecane	1220	z-Tridecene (3)	1303	n-Heptadecane	1700
3-Me-Undecane	1230	c-Tridecene (3)	1333	n-Octadecane	1800

APPENDIX C

1. Scilab Code for Surface Wetting

```

clear;clc;format(20);
//*****Wetting Phase of Organic and Water*****
//-----Assumptions
//1) Cylindrical pores with diameter D, average pore length L
//2) Filling with water, fraction of pore volume filled with organic
//3) The interfacial profile is flat
//-----Solution Properties
//Handbook of Chemistry$Physics 63rd Edition
//Tension air/water, [dyn/cm2], 25oC, (F-35)
gvw=71.97;
//Tension air/n-Hexane, [dyn/cm2], 20oC, (F-37)
gvo=18.43;
//Tension water/n-Hexane, [dyn/cm2], 20oC, (F-35)
gwo=51.1;
//Chemical Reviews, Volume 75, Number 5, October 1975
//Tension solid/air, [dyn/cm2], 25oC, (Table V)
gsv=605;
//Measured contact angle of solid/water is 150 degrees
cangsw=150/180*pi;
//Tension solid/water, Young's equation
gsw=gsv+gvw*cos(cangsw);
//Measured contact angle of organic/water is 150 degrees
cangso=6/180*pi;
//Tension organic/water, Young's equation
gso=gsv+gvo*cos(cangso);
//-----Pore Properties
//Diameter of the pore [cm], 13 nm
D=13*1e-7;
//Length of the pore [cm]
L=1*D;
//-----Gibb's Free Energy of System
for i=1:50;
    d(i)=i*D/100;
    //Water fraction as function of d
    Xw(i)=((D-2*d(i))^2)*(L-d(i))/D^2/L;
    //Case 1: Water close to pore mouth-----
    //Area between water and organic
    Awo1(i)=(pi*D^2)/4;
    //Area between solid and water
    Asw1(i)=pi*D*L*Xw(i);
    //Area between solid and organic
    Aso1(i)=pi*D*L*(1-Xw(i));
    //Free energy of Case 1
    G1(i)=Awo1(i)*gwo+Asw1(i)*gsw+Aso1(i)*gso;
    //Case 2: Water on top of organic-----
    //Area between water and organic
    Awo2(i)=pi*(D-2*d(i))*(L-d(i))+pi*((D)^2)/4;
    //Area between solid and organic
    Aso2(i)=pi*D*L+pi*(D^2)/4;
    //Free energy of Case 2
    G2(i)=Awo2(i)*gwo+Aso2(i)*gso;
    //Free energy of occurrence of Case 2
    Gd(i)=G1(i)-G2(i);
end
//-----Export Data to File
print('phase.txt',Gd,Xw);

```

2. Wetting Calculations

N-undecane soaked silica pellet has greater transparency compared to soaked pellets with n-undecane on the pellet surface evaporated as shown in Figure C.1. This can be explained by the different refraction index of silica and n-undecane.

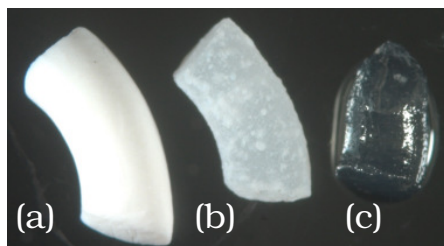


Figure C.1: Optical image of dry silica pellet (a) n-undecane soaked pellets with surface free of n-undecane (b) Pellet completely soaked in n-undecane (c)

The volume of n-undecane and water filling the pores without wetting the pellet surface was determined gravimetrically by observing the transparency change during evaporation.

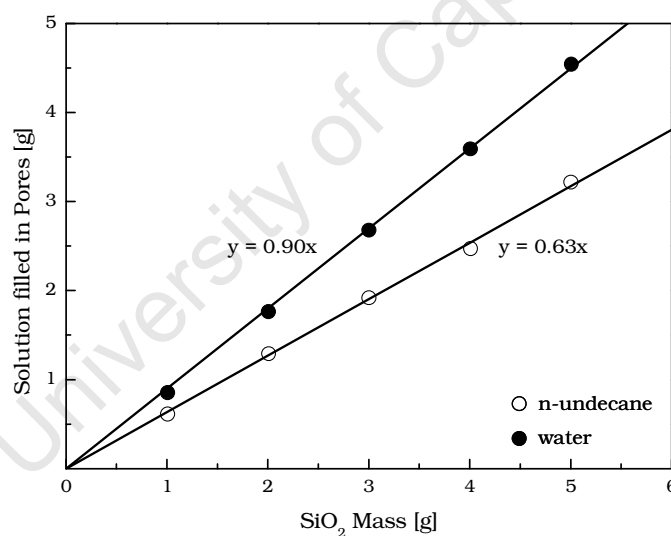


Figure C.2: Experimentally determined amount of solution required to fill pore volume

3. Synthesis Gas Properties at Reaction Conditions

3.1. Density

Using the ideal gas law, gas density at 220°C and total pressure of 20bar is

$$\rho_{\text{CO}} = \frac{M_{\text{CO}} P_{\text{CO}}}{RT} = \frac{(28)^{\frac{1}{3}} (20 \times 10^5)}{(8.314)(493)} = 4554 \frac{\text{g}}{\text{m}^3} = 4.554 \times 10^{-3} \frac{\text{g}}{\text{cm}^3}$$

$$\rho_{\text{H}_2} = \frac{M_{\text{H}_2} P_{\text{H}_2}}{RT} = \frac{(2)^{\frac{2}{3}} (20 \times 10^5)}{(8.314)(493)} = 650 \frac{\text{g}}{\text{m}^3} = 6.5 \times 10^{-4} \frac{\text{g}}{\text{cm}^3}$$

$$\rho_{\text{sg}} = \frac{M_{\text{sg}} P_{\text{sg}}}{RT} = \frac{(\frac{2}{3}(2) + \frac{1}{3}(28))(20 \times 10^5)}{(8.314)(493)} = 5204 \frac{\text{g}}{\text{m}^3} = 5.204 \times 10^{-3} \frac{\text{g}}{\text{cm}^3}$$

3.2. Viscosity

Gas viscosity according to Chapman and Cowling (1951) is

$$\mu = 2.6693 \times 10^{-5} \frac{\sqrt{M_{\text{CO}} T}}{\sigma^2 \Omega_{\mu}}$$

where σ is the characteristic diameter of the gas molecule, and Ω_{μ} is the coefficient of viscosity which is correlated with the characteristic energy of interaction between the molecules (ϵ) over Boltzmann constant (κ). Correlation of viscosity coefficient was done using tables provided in Bird *et al.*, 1962. Step-wise calculation is shown in the following table.

Table C-1: Values used for the estimation of gas viscosity at 220°C

Gas	M [g mol ⁻¹]	σ [Å]	ϵ/κ [°K]	$\kappa T/\epsilon$ [-]	Ω_{μ}	μ [g cm ⁻¹ s ⁻¹]
CO	28	3.59	110	4.48	0.9464	2.57×10^{-4}
H ₂	2	2.915	38	12.97	0.8242	1.19×10^{-4}

3.3. Diffusivity

The Chapman-Enskog formula for gas diffusivity at low density is

$$D_{AB} = 0.0018583 \frac{\sqrt{T^3 (\frac{1}{M_A} + \frac{1}{M_B})}}{P \sigma_{AB}^2 \Omega_{D_{AB}}}$$

Lennard-Jones parameters of species A and B can be estimated empirically

$$\sigma_{AB} = \frac{1}{2}(\sigma_A + \sigma_B)$$

$$\epsilon_{AB} = \sqrt{\epsilon_A \epsilon_B}$$

In the synthesis gas mixture only CO and H₂ are present, therefore

$$\sigma_{\text{H}_2, \text{CO}} = \frac{1}{2}(2.915 + 3.59) = 3.253$$

$$\frac{\epsilon_{\text{H}_2, \text{CO}}}{\text{K}} = \sqrt{38(110)} = 65$$

The correlated diffusivity coefficient of synthesis gas species is then 0.7712

$$\left(\frac{\text{K}}{\epsilon_{\text{H}_2, \text{CO}}} = 8.0 \right).$$

Diffusivity for mixture of CO and H₂ at 220°C and 20bar total pressure is then

$$D_{\text{CO}, \text{H}_2} = 0.0018583 \frac{\sqrt{(493)^3 \left(\frac{1}{28} + \frac{1}{2} \right)}}{(20)(3.253)^2(0.7712)} = 0.0912 \frac{\text{cm}^2}{\text{s}}$$

University of Cape Town

4. External Mass Transport Limitation Polymath Code

4.1. Gas-phase mass transport in Fixed-bed reactor

```
f(CCOs) = kcCO * ac * (CCObulk - CCOs) - rateCO
f(CH2s) = kcH2 * ac * (CH2bulk - CH2s) - rateH2
rateCO = (a * CCOs * CH2s) / (1 + b * CCOs) ^ 2
rateH2 = 2 * rateCO
CCObulk = 0.162 # [mmol/cm3]
CH2bulk = 0.324 # [mmol/cm3]
a = 15 # [mmol/s/g(cm6/mmol2)]
b = 91 # [cm3/mmol]
ac = 28 # [cm2/g]
U = 1 # [cm/s]
kcCO = 0.486 + 0.384 * U ^ (1 / 2) # [cm/s]
kcH2 = 0.486 + 0.262 * U ^ (1 / 2) # [cm/s]
COdiff = (CCObulk - CCOs) / CCObulk * 100
Flow = U * 3.1416 * 0.5 ^ 2
CCOs(0) = 0
CH2s(0) = 0
```

4.2. Liquid-phase mass transport in Fixed-bed reactor

```
f(d) = Rate - a * (COsat - Rate * d / DCO) * (H2sat - (2 * Rate) * d / DH2) / ((1 + kads * (COsat - Rate * d / DCO)) ^ 2) #
[cm]
k = 15 # [mmol/s/gcat/(mmol2/cm6)]
a = k / ac # [mmol/s/cm2/(mmol2/cm6)]
kads = 91 # [cm3/mmol]
rate = 58 # observed [mmol/min/gcat] (57,78)
ac = 28 # measured [cm2/gcat]
Rate = rate / ac / 60 # observed [mmol/s/cm2]
U = 1.36 # [cm/s] (0.68, 1.36)
DCO = 0.000174/10 # [cm2/s] (effective diffusivity)
DH2 = 0.000473/10 # [cm2/s] (effective diffusivity)
COsat = 0.0356 # [mmol/cm3]
H2sat = 0.0537 # [mmol/cm3]
wax = 0.78 # [g/cm3]
d(max) = 0.162
d(min) = 0
d(0) = 0
```

5. Dimensionless Reaction-Diffusion Model Derivation

Mass balance on CO in an open ended cylinder with a vertical orientation (Figure C.3) at steady-state condition is

$$\overbrace{W_{\text{CO}} \times l_{\text{pellet}} \times 2\pi r \Big|_r}^{\text{Mass In}} - \overbrace{W_{\text{CO}} \times l_{\text{pellet}} \times 2\pi r \Big|_{r+\Delta r}}^{\text{Mass Out}} + \overbrace{R_{\text{volume}} \times l_{\text{pellet}} \times 2\pi r \times \Delta r}^{\text{Mass Generation}} = 0$$

Divide the above equation by $2\pi l_{\text{pellet}} \Delta r$

$$\frac{W_{\text{CO}} \times r \Big|_r - W_{\text{CO}} \times r \Big|_{r+\Delta r}}{\Delta r} + R_{\text{volume}} \times r = 0$$

$$\lim_{\Delta r \rightarrow 0} \frac{d(W_{\text{CO}} \times r)}{dr} = R_{\text{volume}} \times r$$

substituting mass flux with

$$W_{\text{CO}} = -D_{\text{CO}} \frac{dC_{\text{CO}}}{dr}$$

and taking intrinsic reaction rate expression suggested by Yates and Satterfield (1991) in a active metal based form, the mass balance is then

$$\frac{d^2 C_{\text{CO}}}{dr^2} = -\frac{1}{r} \frac{dC_{\text{CO}}}{dr} + \frac{k C_{\text{CO}} C_{\text{H}_2}}{(1 + k_{\text{ads}} C_{\text{CO}})^2} \frac{\rho_{\text{structured}}}{D_{\text{CO}}}$$

where $\rho_{\text{structured}}$ is the metal density within the active region of structured catalyst in $[\text{m}^2/\text{m}^3_{\text{catalyst}}]$.

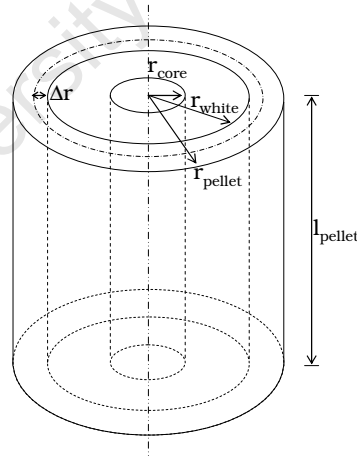


Figure C.3: DVE of reaction-diffusion model

Using egg-shell catalyst as an example, $\rho_{\text{egg-shell}}$ can be derived for constant metal loading

$$\begin{aligned}\rho_{\text{total}} \pi r_{\text{pellet}}^2 l_{\text{pellet}} &= \rho_{\text{egg-shell}} \pi (r_{\text{pellet}}^2 - r_{\text{core}}^2) \\ \rho_{\text{egg-shell}} &= \rho_{\text{total}} \frac{r_{\text{pellet}}^2}{(r_{\text{pellet}}^2 - r_{\text{core}}^2)} \\ \rho_{\text{egg-shell}} &= \rho_{\text{total}} \sigma_{\text{egg-shell}}\end{aligned}$$

similarly, $\sigma_{\text{structured}}$ of other structured types are

$$\sigma_{\text{uniform}} = 1; \sigma_{\text{egg-yolk}} = \left(\frac{r_{\text{pellet}}}{r_{\text{core}}} \right)^2; \sigma_{\text{egg-white}} = \frac{r_{\text{pellet}}^2}{r_{\text{white}}^2 - r_{\text{core}}^2}$$

CO mass balance can then be written as

$$\begin{aligned}\frac{d^2 C_{\text{CO}}}{dr^2} &= -\frac{1}{r} \frac{dC_{\text{CO}}}{dr} + \frac{k C_{\text{CO}} C_{\text{H}_2}}{(1 + k_{\text{ads}} C_{\text{CO}})^2} \frac{\rho_{\text{total}} \sigma_{\text{structured}}}{D_{\text{CO}}} \quad \text{BC:} \\ C_{\text{CO}} \Big|_{r=r_{\text{pellet}}} &= C_{\text{CO,S}}; \frac{dC_{\text{CO}}}{dr} \Big|_{r=0} = 0\end{aligned}$$

Similarly, H_2 mass balance is

$$\begin{aligned}\frac{d^2 C_{\text{H}_2}}{dr^2} &= -\frac{1}{r} \frac{dC_{\text{H}_2}}{dr} + 2 \frac{k C_{\text{CO}} C_{\text{H}_2}}{(1 + k_{\text{ads}} C_{\text{CO}})^2} \frac{\rho_{\text{total}} \sigma_{\text{structured}}}{D_{\text{H}_2}} \quad \text{BC: } C_{\text{H}_2} \Big|_{r=r_{\text{pellet}}} = C_{\text{H}_2,\text{S}}; \frac{dC_{\text{H}_2}}{dr} \Big|_{r=0} = 0\end{aligned}$$

Define dimensionless parameters as

$$\begin{aligned}\psi_{\text{CO}} &= \frac{C_{\text{CO}}}{C_{\text{CO,S}}}; \psi_{\text{H}_2} = \frac{C_{\text{H}_2}}{C_{\text{H}_2,\text{S}}}; \lambda = \frac{r}{r_{\text{pellet}}} \\ \frac{dC_{\text{CO}}}{d\psi_{\text{CO}}} &= C_{\text{CO,S}}; \frac{dC_{\text{H}_2}}{d\psi_{\text{H}_2}} = C_{\text{H}_2,\text{S}}; \frac{d\lambda}{dr} = \frac{1}{r_{\text{pellet}}}\end{aligned}$$

substituting into CO mass balance becomes

$$\frac{d^2 \psi_{\text{CO}}}{d\lambda^2} \left(\frac{C_{\text{CO,S}}}{r_{\text{pellet}}^2} \right) = -\frac{1}{\lambda r_{\text{pellet}}} \left(\frac{C_{\text{CO,S}}}{r_{\text{pellet}}} \right) \frac{d\psi_{\text{CO}}}{d\lambda} + \frac{k C_{\text{CO,S}} C_{\text{H}_2,\text{S}} \psi_{\text{CO}} \psi_{\text{H}_2}}{(1 + k_{\text{ads}} C_{\text{CO,S}} \psi_{\text{CO}})^2} \frac{\rho_{\text{total}} \sigma_{\text{structured}}}{D_{\text{CO}}}$$

multiply both sides by $r_{\text{pellet}}^2 / C_{\text{CO,S}}$

$$\begin{aligned}\frac{d^2 \psi_{\text{CO}}}{d\lambda^2} &= -\frac{1}{\lambda r_{\text{pellet}}} \frac{d\psi_{\text{CO}}}{d\lambda} + \frac{r_{\text{pellet}}^2 k C_{\text{H}_2,\text{S}} \psi_{\text{CO}} \psi_{\text{H}_2}}{(1 + k_{\text{ads}} C_{\text{CO,S}} \psi_{\text{CO}})^2} \frac{\rho_{\text{total}} \sigma_{\text{structured}}}{D_{\text{CO}}} \\ \text{BC: } \psi_{\text{CO}} \Big|_{\lambda=1} &= 1; \frac{d\psi_{\text{CO}}}{d\lambda} \Big|_{\lambda=0} = 0\end{aligned}$$

Similarly, H_2 mass balance becomes

$$\begin{aligned}\frac{d^2 \psi_{\text{CO}}}{d\lambda^2} &= -\frac{1}{\lambda r_{\text{pellet}}} \frac{d\psi_{\text{CO}}}{d\lambda} + 2 \frac{r_{\text{pellet}}^2 k C_{\text{H}_2,\text{S}} \psi_{\text{CO}} \psi_{\text{H}_2}}{(1 + k_{\text{ads}} C_{\text{CO,S}} \psi_{\text{CO}})^2} \frac{\rho_{\text{total}} \sigma_{\text{structured}}}{D_{\text{H}_2}} \quad \text{BC: } \psi_{\text{H}_2} \Big|_{\lambda=1} = 1; \frac{d\psi_{\text{H}_2}}{d\lambda} \Big|_{\lambda=0} = 0\end{aligned}$$

Define Thiele modulus as $\Phi = r_{\text{pellet}} \sqrt{\frac{k C_{\text{H}_2, \text{S}} \rho_{\text{total}} \sigma_{\text{structured}}}{D_{\text{CO}}}}$

and adsorption constant $K_{\text{ads}} = k_{\text{ads}} C_{\text{CO, S}}$

Substituting above defined parameters into dimensionless mass balance gives

$$\frac{d^2 \psi_{\text{CO}}}{d\lambda^2} = -\frac{1}{\lambda} \frac{d\psi_{\text{CO}}}{d\lambda} + \Phi^2 \frac{\psi_{\text{CO}} \psi_{\text{H}_2}}{(1 + K_{\text{ads}} \psi_{\text{CO}})^2}$$

$$\frac{d^2 \psi_{\text{H}_2}}{d\lambda^2} = -\frac{1}{\lambda} \frac{d\psi_{\text{H}_2}}{d\lambda} + 2\Phi^2 \frac{D_{\text{CO}}}{D_{\text{H}_2}} \frac{\psi_{\text{CO}} \psi_{\text{H}_2}}{(1 + K_{\text{ads}} \psi_{\text{CO}})^2}$$

Effectiveness factor is defined as

$$\eta = \frac{\text{overall rate within structured catalyst}}{\text{rate of reaction at catalyst surface (absence of IMTL)}}$$

therefore

$$\eta = \frac{(2\pi r_{\text{pellet}} l_{\text{pellet}}) D_{\text{CO}} \left. \frac{d\psi_{\text{CO}}}{d\lambda} \right|_{\lambda=1}}{(\pi r_{\text{pellet}}^2 l_{\text{pellet}} \rho_{\text{total}} \sigma_{\text{structured}}) (k C_{\text{CO, S}} C_{\text{H}_2, \text{S}} / (1 + k_{\text{ads}} C_{\text{CO, S}})^2)}$$

$$= \frac{2r_{\text{pellet}}}{x} \frac{(1 + K_{\text{ads}})^2}{C_{\text{CO, S}}} \left. \frac{d\psi_{\text{CO}}}{d\lambda} \right|_{\lambda=1}$$

Energy balance for the differential volume at steady-state is

$$\overbrace{Q \times l_{\text{pellet}} \times 2\pi r}^{\text{Heat In}} \Big|_r - \overbrace{Q \times l_{\text{pellet}} \times 2\pi r}^{\text{Heat Out}} \Big|_{r+\Delta r} + \overbrace{R_{\text{volume}} \times l_{\text{pellet}} \times 2\pi r \times \Delta r \times \Delta H_{\text{rxn}}}^{\text{Heat Generation}} = 0$$

Divide the above equation by $2\pi l_{\text{pellet}} \Delta r$

$$\frac{Q \times r \Big|_r - Q \times r \Big|_{r+\Delta r}}{\Delta r} + R_{\text{volume}} \times \Delta H_{\text{rxn}} \times r = 0$$

$$\lim_{\Delta r \rightarrow 0} \frac{d(Q \times r)}{dr} = R_{\text{volume}} \times \Delta H_{\text{rxn}} \times r$$

Assuming energy flux is only due to the conductivity of species

$$Q = -\kappa_t \frac{dT}{dr}$$

Substitute energy flux into energy balance, and rewrite reaction constant k as a function of temperature

$$\frac{d^2 T}{dr^2} = -\frac{1}{r} \frac{dT}{dr} + \frac{C_{\text{CO}} C_{\text{H}_2}}{(1 + k_{\text{ads}} C_{\text{CO}})^2} \frac{\rho_{\text{total}} \sigma_{\text{structured}} \Delta H_{\text{rxn}}}{\kappa_t} \bar{A} \exp\left(\frac{-E_a}{RT}\right)$$

The ratio of rate constant at surface temperature versus local temperature in the catalyst is

$$\frac{k}{k_s} = \frac{\bar{A} \exp\left(\frac{-E_a}{RT}\right)}{\bar{A} \exp\left(\frac{-E_a}{RT_s}\right)} = \exp\left(\frac{-E_a}{R} \left(\frac{1}{T} - \frac{1}{T_s}\right)\right)$$

Hence, energy balance can be rewritten as

$$\frac{d^2T}{dr^2} = -\frac{1}{r} \frac{dT}{dr} + \frac{C_{CO} C_{H_2}}{(1 + k_{ads} C_{CO})^2} \frac{k_s \rho_{total} \sigma_{structured} \Delta H_{rxn}}{\kappa_t} \exp\left(\frac{-E_a}{R} \left(\frac{1}{T} - \frac{1}{T_s}\right)\right)$$

$$\text{BC: } T|_{r=r_{pellet}} = T_s ; \left. \frac{dT}{dr} \right|_{r=0} = 0$$

Define dimensionless temperature as

$$\Gamma = \frac{T}{T_s}$$

Arrhenius number (measure of activation energy versus potential energy) as

$$\gamma_a = \frac{E_a}{RT_s}$$

Prater number as

$$\beta = \frac{(-\Delta H_{rxn}) D_{CO} C_{CO,s}}{\kappa_t T_s}$$

The dimensionless energy balance is then

$$\frac{d^2\Gamma}{d\lambda^2} = -\frac{1}{\lambda} \frac{d\Gamma}{d\lambda} + \Phi^2 \beta \exp\left(-\gamma_a \left(\frac{1}{\Gamma} - 1\right)\right) \frac{\psi_{CO} \psi_{H_2}}{(1 + K_{ads} \psi_{CO})^2} \quad \text{BC: } \Gamma|_{\lambda=1} = 1 ; \left. \frac{d\Gamma}{d\lambda} \right|_{\lambda=0} = 0$$

Thiele Modulus of uniform catalyst pellet (U1) is estimated using kinetic parameter suggested by Anfray *et al.* (2007),

$$\begin{aligned} \Phi^2 &= \frac{r_{pellet}^2 k \rho_{total}}{D_{CO}} \\ &= \frac{(0.00123^2)(5.392 \times 10^{-7})(65437)}{(17.4 \times 10^{-9})} \\ &= 3.07 \end{aligned}$$

6. Scilab Code for Derived Reaction Model

6.1. Uniform Pellets

```

clear;clc;format(20);
//*****Yates&Satterfield Cylinder bvodeS in CSTR*****
//Infinite Cylinder
//CO Mass DE: CO''=-(1/x)*CO'+density/DCO*(k*CO*H2/(1+kads*CO)^2)
//CO Mass BC: CO'(0)=0 ; CO(1)=COsat
//H2 Mass DE: H2''=-(1/x)*H2'+2*density/DH2*(k*CO*H2/(1+kads*CO)^2)
//H2 Mass BC: H2'(0)=0 ; H2(1)=H2sat
//z=[CO CO' H2 H2']
//pellet model in CSTR model loop
//-----Physical Parameters
mcat=1.85;//Mass of catalyst loaded [gcat]
smet=2.1;//[m2co*/gcat]
SCo=mcat*smet;//area of active cobalt [m2co*]
Sil=1;//Average silica density [g/cm3]
AAS=0.29;//Metal loading [g/gcat]
rou=smet/(Sil/(1-AAS));//Active cobalt density [m2co*/cm3]
Flow=103.1/3/60/22.414;//flow of CO [mmol/s]
Rp=0.125;//Pellet radius [cm]
//-----Chemical Parameters
Ktemp(1)=167;//at 220C [mmol/s/m2co*/(mmol2/cm6)]
Ktemp(2)=199;//at 230C [mmol/s/m2co*/(mmol2/cm6)]
Ktemp(3)=232;//at 240C [mmol/s/m2co*/(mmol2/cm6)]
kadstemp(1)=423;//at 220C [cm3/mmol]
kadstemp(2)=423;//at 220C [cm3/mmol]
kadstemp(3)=423;//at 220C [cm3/mmol]
DCOtemp(1)=1.5e-4;//[cm2/s](Erkey)
DCOtemp(2)=1.74e-4;//[cm2/s](Erkey)
DCOtemp(3)=1.8e-4;//[cm2/s](Erkey)
Temp(1)=493;//220C
Temp(2)=503;//230C
Temp(3)=513;//240C
//-----Experimental Data
UR_exp(1)=2.2;//H2/CO usage ratio [H2/CO]
UR_exp(2)=2.2;//H2/CO usage ratio [H2/CO]
UR_exp(3)=2.2;//H2/CO usage ratio [H2/CO]
X_exp(1)=0.14;
X_exp(2)=0.17;
X_exp(3)=0.22;
//-----Rate Expression
function rf=Rate(z)
    if z(1)>0 then
        if z(3)>0 then
            rf=K*z(1)*z(3)/((1+kads*z(1))^2);
        else rf=0;
        end
    else rf=0;
    end
endfunction
//-----Differential Equations
function RhS=fsub(x,z)
    RhS=[-z(2)/x+Rate(z)*rou/DCO;-z(4)/x+UR*Rate(z)*rou/DH2]
endfunction
//-----Initial Guess
function [z,lhS]=ystart(x)
    z=zeros(4,1);z(1)=CObulk;z(3)=H2bulk
    lhS=[0;0];
endfunction
//-----Boundary Conditions
function g=gsub(i,z)
    g=[z(2) z(4) z(1)-CObulk z(3)-H2bulk]
    g=g(i)
endfunction
//-----Solve as function of Temperature
for i=1:3
    Xexp=X_exp(i);
    ERROR_exp=1;
    K=Ktemp(i);//[mmol/s/m2co/(mmol2/cm6)]
    kads=kadstemp(i);//[cm3/mmol]
    UR=UR_exp(i);
    ds=0.5;//initial guess for H2/CO diffusivity loop
    while ERROR_exp>1e-2
        DCO=DCOtemp(i);//[cm2/s]

```

```

DH2=ds*DCO; //[cm2/s]
XCO_Old=1; //initiating guess for CSTR loop
XCO_New=0; //initiating guess for CSTR loop
ERROR_XCO=1; //initiating CSTR loop error
while ERROR_XCO>1e-3
    pCO=(1-XCO_New)/(3-(UR-1/3)*XCO_New)*20; //CO Partial pressure
    pH2=(2-UR*XCO_New)/(3-(UR-1/3)*XCO_New)*20; //H2 Partial pressure
    CObulk=(1.169e-5*Temp(i)-4.281e-4)*pCO; //[mmol/cm3] (Chou&Chao)
    H2bulk=(1.507e-5*Temp(i)-3.399e-3)*pH2; //[mmol/cm3] (Chou&Chao)
    H2COb=H2bulk/CObulk;
    //bvoidS Parameters-----
    n=2; //Number of DE's
    m=[2 2]; //Maximum order of DE's
    N=100; //Number of step points
    a=0; b=Rp; //End points of BC's
    zeta=[a b b]; //BC position of defined BC function
    tol=[1e-2 1e-2 1e-2 1e-2];
    //Distributing Distance of Integration-----
    x=linspace(a,b,N);
    Tp(i)=Rp*sqrt(K*H2bulk*rou/DCO); //Thiele
    //ODE solver-----
    z=bvoidS(x,m,n,a,b,fsub,gsub,zeta,ystart=ystart,tol=tol);
    //Average H2/CO ratio-----
    H2sum=0;
    COsum=0;
    for j=2:N
        H2sum=H2sum+(z(3,j-1)*(x(j)-x(j-1))*x(j));
        COsum=COsum+(z(1,j-1)*(x(j)-x(j-1))*x(j));
    end
    H2CO(i)=H2sum/COsum;
    //Effectiveness Factor-----
    Eff(i)=2*DCO*z(2,N)/(Rp*rou*K*CObulk*H2bulk/((1+kads*CObulk)^2));
    //Closing the CSTR loop-----
    Ratebulk=SCo*(K*CObulk*H2bulk/((1+kads*CObulk)^2)); //[mmol/s]
    XCO_cal=Ratebulk*Eff(i)/Flow; //Calculated conversion
    XCO_OLD=XCO_New; //Update old conversion
    XCO_New=XCO_cal; //Update new conversion
    ERROR_XCO=abs(XCO_New-XCO_OLD)/XCO_New; //Update CSTR error
end
ERROR_exp=abs(Xexp-XCO_cal)/Xexp; //Update Conversion error
if Xexp>XCO_cal
    ds=ds+0.1; //Increase H2/CO diffusivity ratio if too low
else ds=ds-0.01; //decrease H2/CO diffusivity ratio if too high
end
end
XCO(i)=XCO_cal; //Record conversion
DF(i)=ds; //Record H2/CO diffusivity ratio
end
//-----Export Data to File
print ('Uniform.txt',H2CO,XCO,DF)
//*****End*****

```

6.2. Egg-shell Type Pellets

```

clear;clc;format(20);
//*****Yates&Satterfield Cylinder bvodeS in CSTR*****
//Infinite Cylinder
//CO Mass DE: CO'=- (1/x)*CO'+density*sig/DCO*(k*CO*H2/(1+kads*CO)^2)
//CO Mass BC: CO'(0)=0 ; CO(1)=COsat
//H2 Mass DE: H2'=- (1/x)*H2'+2*density*sig/DH2*(k*CO*H2/(1+kads*CO)^2)
//H2 Mass BC: H2'(0)=0 ; H2(1)=H2sat
//z=[CO CO' H2 H2']
//pellet model in CSTR model loop
//-----Physical Parameters
mcat=5.59;//Mass of catalyst loaded [gcat]
smet=1.69;//[m2co*/gcat]
SCo=mcat*smet;//area of active cobalt [m2co*]
Sil=1;//Average silica density [g/cm3]
AAS=0.082;//Metal loading [g/gcat]
rou=smet/(Sil/(1-AAS));//Active cobalt density [m2co*/cm3]
Flow=77.1/3/60/22.414;//flow of CO [mmol/s]
Rp=0.125;//Pellet radius [cm]
Rc=0.18*Rp;//Cobalt Free core [cm]
//-----Chemical Parameters
Ktemp(1)=167;//at 220C [mmol/s/m2co*/(mmol2/cm6)]
Ktemp(2)=199;//at 230C [mmol/s/m2co*/(mmol2/cm6)]
Ktemp(3)=232;//at 240C [mmol/s/m2co*/(mmol2/cm6)]
kadstemp(1)=423;//at 220C [cm3/mmol]
kadstemp(2)=423;//at 230C [cm3/mmol]
kadstemp(3)=423;//at 240C [cm3/mmol]
DCOtemp(1)=1.5e-4;//[cm2/s](Erkey)
DCOtemp(2)=1.74e-4;//[cm2/s](Erkey)
DCOtemp(3)=1.8e-4;//[cm2/s](Erkey)
Temp(1)=493;//220C
Temp(2)=503;//230C
Temp(3)=513;//240C
//-----Experimental Data
UR_exp(1)=2.2;//H2/CO usage ratio [H2/CO]
UR_exp(2)=2.2//H2/CO usage ratio [H2/CO]
UR_exp(3)=2.2;//H2/CO usage ratio [H2/CO]
X_exp(1)=0.48;
X_exp(2)=0.65;
X_exp(3)=0.74;
//-----Differential Equations
function RhS=fsub(x,z)
RhS=[-z(2)/x+Rate(z)*rou*sig/DCO;-z(4)/x+UR*Rate(z)*rou*sig/DH2]
endfunction
//-----Initial Guess
function [z,lhS]=ystart(x)
z=zeros(4,1);z(1)=CObulk;z(3)=H2bulk
lhS=[0;0];
endfunction
//-----Boundary Conditions
function g=gsub(i,z)
g=[z(2) z(4) z(1)-CObulk z(3)-H2bulk]
g=g(i)
endfunction
//-----Rate Expression
function rf=Rate(z)
if z(1)>0 then
if z(3)>0 then
if x>=Rc then
rf=K*z(1)*z(3)/((1+kads*z(1))^2);
else rf=0;
end
else rf=0;
end
else rf=0;
end
endfunction
//-----Solve as function of Pellet Size
for i=1:3
Xexp=X_exp(i);
ERROR_exp=1;
K=Ktemp(i);//[mmol/s/m2co/(mmol2/cm6)]
kads=kadstemp(i);//[cm3/mmol]
UR=UR_exp(i);
ds=0.5;//initial guess for H2/CO diffusivity loop
while ERROR_exp>1e-2

```

```

DCO=DCOtemp(i);//[cm2/s]
DH2=ds*DCO;//[cm2/s]
XCO_Old=1; //initiating guess for CSTR loop
XCO_New=0; //initiating guess for CSTR loop
ERROR_XCO=1; //initiating CSTR loop error
while ERROR_XCO>1e-3
    pCO=(1-XCO_New)/(3-(UR-1/3)*XCO_New)*20; //CO Partial pressure
    pH2=(2-UR*XCO_New)/(3-(UR-1/3)*XCO_New)*20; //H2 Partial pressure
    CObulk=(1.169e-5*Temp(i)-4.281e-4)*20/3; //[mmol/cm3] (Chou&Chao)
    H2bulk=(1.507e-5*Temp(i)-3.399e-3)*20/3*2; //[mmol/cm3] (Chou&Chao)
    H2COb=H2bulk/CObulk;
    //bvoidS Parameters-----
    n=2; //Number of DE's
    m=[2 2]; //Maximum order of DE's
    N=100; //Number of step points
    a=0; b=Rp; //End points of BC's
    zeta=[a b]; //BC position of defined BC function
    tol=[1e-2 1e-2 1e-2 1e-2];
    //Distributing Distance of Integration-----
    x=zeros(1,N);
    N1=N/10+1; //Number of points inside the cobalt free core
    N2=N-N/10; //Number of points inside the cobalt enriched shell
    x1=zeros(1,N1);
    for p=2:N1
        x1(p)=(Rc-x1(p-1))*0.25+x1(p-1);
    end
    for q=2:N1
        x(q-1)=x1(q-1);
    end
    x2=linspace(Rc,b,N2);
    for o=1:N2
        x(N1-1+o)=x2(o);
    end
    fixpnt=Rc; //Fix mesh point at boundary
    //Density redistribution function-----
    sig=Rp^2/(Rp^2-Rc^2); //Egg-shell catalysts
    Tp(i)=Rp*sqrt(K*H2bulk*rou*sig/DCO); //Thiele
    //ODE Solver-----
    z=bvoidS(x,m,n,a,b,fsub,gsub,zeta,fixpnt=fixpnt,...
    ystart=ystart,tol=tol);
    //Average H2/CO ratio-----
    H2sum=0;
    COsum=0;
    for j=N1:N
        H2sum=H2sum+(z(3,j-1)*(x(j)-x(j-1))*x(j));
        COsum=COsum+(z(1,j-1)*(x(j)-x(j-1))*x(j));
    end
    H2CO(i)=H2sum/COsum;
    //Effectiveness Factor-----
    Eff(i)=2*DCO*z(2,N)/(Rp*rou*K*CObulk*H2bulk/((1+kads*CObulk)^2));
    //Closing the CSTR loop-----
    Ratebulk=SCo*(K*CObulk*H2bulk/((1+kads*CObulk)^2)); //[mmol/s]
    XCO_cal=Ratebulk*Eff(i)/Flow; //Calculated conversion
    XCO_OLD=XCO_New; //Update old conversion
    XCO_New=XCO_cal; //Update new conversion
    ERROR_XCO=abs(XCO_New-XCO_OLD)/XCO_New; //Update CSTR error
end
ERROR_exp=abs(Xexp-XCO_cal)/Xexp; //Update conversion error
if Xexp>XCO_cal
    ds=ds+0.1; //Increase H2/CO diffusivity ratio if too low
else ds=ds-0.01; //decrease H2/CO diffusivity ratio if too high
end
end
XCO(i)=XCO_cal; //Record conversion
DF(i)=ds; //Record H2/CO diffusivity ratio
end
//Export Data to File-----
print('Shell.txt',H2CO,XCO,DF)
//*****End*****

```

6.3. Egg-yolk Type Pellets

```

clear;clc;format(20);
//*****Yates&Satterfield Cylinder bvodeS in CSTR*****
//Infinite Cylinder
//CO Mass DE: CO'=- (1/x)*CO'+density*sig/DCO*(k*CO*H2/(1+kads*CO)^2)
//CO Mass BC: CO'(0)=0 ; CO(1)=COsat
//H2 Mass DE: H2'=- (1/x)*H2'+2*density*sig/DH2*(k*CO*H2/(1+kads*CO)^2)
//H2 Mass BC: H2'(0)=0 ; H2(1)=H2sat
//z=[CO CO' H2 H2']
//pellet model in CSTR model loop
//-----Physical Parameters
mcat=5.02; //Mass of catalyst loaded [gcat]
smet=0.86; // [m2co*/gcat]
SCo=mcat*smet; //area of active cobalt [m2co*]
Sil=1; //Average silica density [g/cm3]
AAS=0.087; //Metal loading [g/gcat]
rou=smet/(Sil/(1-AAS)); //Active cobalt density [m2co*/cm3]
Flow=75.6/3/60/22.414; //flow of CO [mmol/s]
Rp=0.125; //Pellet radius [cm]
Rc=0.78*Rp; //Cobalt Free core [cm]
//-----Chemical Parameters
Ktemp(1)=167; //at 220C [mmol/s/m2co*/(mmol2/cm6)]
Ktemp(2)=199; //at 230C [mmol/s/m2co*/(mmol2/cm6)]
Ktemp(3)=232; //at 240C [mmol/s/m2co*/(mmol2/cm6)]
kadstemp(1)=423.6; //at 220C [cm3/mmol]
kadstemp(2)=423.6; //at 230C [cm3/mmol]
kadstemp(3)=423.6; //at 240C [cm3/mmol]
DCOtemp(1)=1.5e-4; // [cm2/s](Erkey)
DCOtemp(2)=1.74e-4; // [cm2/s](Erkey)
DCOtemp(3)=1.8e-4; // [cm2/s](Erkey)
Temp(1)=493; //220C
Temp(2)=503; //230C
Temp(3)=513; //240C
//-----Experimental Data
UR_exp(1)=2.2; //H2/CO usage ratio [H2/CO]
UR_exp(2)=2.2; //H2/CO usage ratio [H2/CO]
UR_exp(3)=2.2; //H2/CO usage ratio [H2/CO]
X_exp(1)=0.21;
X_exp(2)=0.26;
X_exp(3)=0.31;
//-----Differential Equations
function RhS=fsub(x,z)
RhS=[-z(2)/x+Rate(z)*rou*sig/DCO;-z(4)/x+UR*Rate(z)*rou*sig/DH2]
endfunction
//-----Initial Guess
function [z,lhS]=ystart(x)
z=zeros(4,1);z(1)=CObulk;z(3)=H2bulk
lhS=[0;0];
endfunction
//-----Boundary Conditions
function g=gsub(i,z)
g=[z(2) z(4) z(1)-CObulk z(3)-H2bulk]
g=g(i)
endfunction
//-----Rate Expression
function rf=Rate(z)
if z(1)>0 then
if z(3)>0 then
if x<=Rc then
rf=K*z(1)*z(3)/((1+kads*z(1))^2);
else rf=0;
end
else rf=0;
end
else rf=0;
end
endfunction
//-----Solve as function of Pellet Size
for i=1:3
Xexp=X_exp(i);
ERROR_exp=1;
K=Ktemp(i); // [mmol/s/m2co/(mmol2/cm6)]
kads=kadstemp(i); // [cm3/mmol]
UR=UR_exp(i);
ds=0.5; //initial guess for H2/CO diffusivity loop
while ERROR_exp>1e-2

```

```

DCO=DCOtemp(i);//[cm2/s]
DH2=ds*DCO;//[cm2/s]
XCO_Old=1; //initiating guess for CSTR loop
XCO_New=0; //initiating guess for CSTR loop
ERROR_XCO=1; //initiating CSTR loop error
while ERROR_XCO>1e-3
    pCO=(1-XCO_New)/(3-(UR-1/3)*XCO_New)*20; //Co Partial pressure
    pH2=(2-UR*XCO_New)/(3-(UR-1/3)*XCO_New)*20; //H2 Partial pressure
    CObulk=(1.169e-5*Temp(i)-4.281e-4)*pCO; //[mmol/cm3] (Chou&Chao)
    H2bulk=(1.507e-5*Temp(i)-3.399e-3)*pH2; //[mmol/cm3] (Chou&Chao)
    H2COb=H2bulk/CObulk;
    //bvodeS Parameters-----
    n=2; //Number of DE's
    m=[2 2]; //Maximum order of DE's
    N=100; //Number of step points
    a=0; b=Rp; //End points of BC's
    zeta=[a a b b]; //BC position of defined BC function
    tol=[1e-2 1e-2 1e-2 1e-2];
    //Distributing Distance of Integration-----
    x=zeros(1,N);
    N1=N-2*N/10; //Number of points inside the cobalt enriched core
    N2=2*N/10; //Number of points inside the cobalt free shell
    x1=linspace(a,Rc,N1);
    x2=zeros(1,N2);
    x2(N2)=Rc;
    x2(1)=Rp;
    for o=2:N2
        x2(o)=x2(o-1)-((x2(o-1)-x2(N2))*0.4);
    end
    for p=1:N1
        x(p)=x1(p);
    end
    for q=1:N2
        x(N1+q)=x2(N2-q+1);
    end
    fixpnt=Rc; //Fix mesh point at boundary
    //Density redistribution function-----
    sig=Rp^2/(Rc^2); //Egg-yolk catalysts
    Tp(i)=Rp*sqrt(K*H2bulk*rou*sig/DCO); //Thiele
    //ODE Solver-----
    z=bvodeS(x,m,n,a,b,fsub,gsub,zeta,fixpnt=fixpnt,...
    ystart=ystart,tol=tol);
    //Average H2/CO ratio-----
    H2sum=0;
    COsum=0;
    for j=2:N1
        H2sum=H2sum+(z(3,j-1)*(x(j)-x(j-1))*x(j));
        COsum=COsum+(z(1,j-1)*(x(j)-x(j-1))*x(j));
    end
    H2CO(i)=H2sum/COsum;
    //Effectiveness Factor-----
    Eff(i)=2*DCO*z(2,N)/(Rp*rou*K*CObulk*H2bulk/((1+kads*CObulk)^2));
    //Closing the CSTR loop-----
    Ratebulk=SCo*(K*CObulk*H2bulk/((1+kads*CObulk)^2)); //[mmol/s]
    XCO_cal=Ratebulk*Eff(i)/Flow; //Calculated conversion
    XCO_OLD=XCO_New; //Update old conversion
    XCO_New=XCO_cal; //Update new conversion
    ERROR_XCO=abs(XCO_New-XCO_OLD)/XCO_New; //Update CSTR error
end
ERROR_exp=abs(Xexp-XCO_cal)/Xexp; //Update conversion error
if Xexp>XCO_cal
    ds=ds+0.1; //Increase H2/CO diffusivity ratio if too low
    else ds=ds-0.01; //decrease H2/CO diffusivity ratio if too high
end
end
XCO(i)=XCO_cal; //Record conversion
DF(i)=ds; //Record H2/CO diffusivity ratio
end
//Export Data to File-----
print('Yolk.txt',H2CO,XCO,DF)
//*****End*****

```


6.4. Egg-white Type Pellets

```

clear;clc;format(20);
//*****Yates&Satterfield Cylinder bvodeS in CSTR*****
//Infinite Cylinder
//CO Mass DE: CO'=- (1/x)*CO'+density*sig/DCO*(k*CO*H2/(1+kads*CO)^2)
//CO Mass BC: CO'(0)=0 ; CO(1)=COsat
//H2 Mass DE: H2'=- (1/x)*H2'+2*density*sig/DH2*(k*CO*H2/(1+kads*CO)^2)
//H2 Mass BC: H2'(0)=0 ; H2(1)=H2sat
//z=[CO CO' H2 H2']
//pellet model in CSTR model loop
//-----Physical Parameters
mcat=5.21; //Mass of catalyst loaded [gcat]
smet=0.81; // [m2co*/gcat]
SCo=mcat*smet; //area of active cobalt [m2co*]
Sil=1; //Average silica density [g/cm3]
AAS=0.066; //Metal loading [g/gcat]
rou=smet/(Sil/(1-AAS)); //Active cobalt density [m2co*/cm3]
//-----Chemical Parameters
Ktemp(1)=167; //at 220C [mmol/s/m2co*/(mmol2/cm6)]
Ktemp(2)=199; //at 230C [mmol/s/m2co*/(mmol2/cm6)]
Ktemp(3)=232; //at 240C [mmol/s/m2co*/(mmol2/cm6)]
kadstemp(1)=423.6; //at 220C [cm3/mmol]
kadstemp(2)=423.6; //at 230C [cm3/mmol]
kadstemp(3)=423.6; //at 240C [cm3/mmol]
DCOtemp(1)=1.5e-4; // [cm2/s](Erkey)
DCOtemp(2)=1.74e-4; // [cm2/s](Erkey)
DCOtemp(3)=1.8e-4; // [cm2/s](Erkey)
Temp(1)=493; //220C
Temp(2)=503; //230C
Temp(3)=513; //240C
//-----Experimental Data
UR_exp(1)=2.2; //H2/CO usage ratio [H2/CO]
UR_exp(2)=2.2; //H2/CO usage ratio [H2/CO]
UR_exp(3)=2.2; //H2/CO usage ratio [H2/CO]
X_exp(1)=0.21;
X_exp(2)=0.32;
X_exp(3)=0.40;
Flow=60.6/3/60/22.414; //flow of CO [mmol/s]
Rp=0.125; //Pellet radius [cm]
Rc=0.63*Rp; //Cobalt Free core [cm]
Rw=0.86*Rp; //Boundary of shell and white [cm]
mid=(Rw-Rc)/2+Rc;
//-----Differential Equations
function RhS=fsub(x,z)
RhS=[-z(2)/x+Rate(z)*rou*sig*SIG(x)/DCO;...
-z(4)/x+UR*Rate(z)*rou*sig*SIG(x)/DH2]
endfunction
//-----Initial Guess
function [z,lhS]=ystart(x)
z=zeros(4,1);z(1)=CObulk;z(3)=H2bulk
lhS=[0;0];
endfunction
//-----Boundary Conditions
function g=gsub(i,z)
g=[z(2) z(4) z(1)-CObulk z(3)-H2bulk]
g=g(i)
endfunction
//-----Rate Expression
function rf=Rate(z)
if z(1)>0 then
if z(3)>0 then
rf=K*z(1)*z(3)/((1+kads*z(1))^2);
else rf=0;
end
else rf=0;
end
endfunction
//-----Density Function
function sa=SIG(x)
if x<mid then
sa=(-atan((Rc-x)/Rp*1000)+%pi/2)/%pi;
else sa=(atan((Rw-x)/Rp*1000)+%pi/2)/%pi;
end
endfunction
//-----Solve as function of Pellet Size
for i=1:3

```

```

Xexp=X_exp(i);
ERROR_exp=1;
K=Ktemp(i);/[mmol/s/gcat/(mmol2/cm6)]
kads=kadstemp(i);/[cm3/mmol]
UR=UR_exp(i);
ds=0.5; //initial guess for H2/CO diffusivity loop
while ERROR_exp>1e-2
    DCO=DCOtemp(i);/[cm2/s]
    DH2=ds*DCO;/[cm2/s]
    XCO_Old=1; //initiating guess for CSTR loop
    XCO_New=0; //initiating guess for CSTR loop
    ERROR_XCO=1; //initiating CSTR loop error
    while ERROR_XCO>1e-3
        pCO=(1-XCO_New)/(3-(UR-1/3)*XCO_New)*20; //CO Partial pressure
        pH2=(2-UR*XCO_New)/(3-(UR-1/3)*XCO_New)*20; //H2 Partial pressure
        CObulk=(1.169e-5*Temp(i)-4.281e-4)*pCO;/[mmol/cm3] (Chou&Chao)
        H2bulk=(1.507e-5*Temp(i)-3.399e-3)*pH2;/[mmol/cm3] (Chou&Chao)
        H2COb=H2bulk/CObulk;
        //bnodeS Parameters-----
        n=2; //Number of DE's
        m=[2 2]; //Maximum order of DE's
        N=100; //Number of step points
        a=0; b=Rp; //End points of BC's
        zeta=[a b b]; //BC position of defined BC function
        tol=[1e-2 1e-2 1e-2 1e-2];
        //Distributing Distance of Integration-----
        x=zeros(1,N);
        N1=1.5*N/10; //Number of points form 0 to Rc
        N2=N-3*N/10; //Number of points form Rc to Rw
        N3=1.5*N/10; //Number of points from Rw to Rp
        x1=zeros(1,N1);
        for p=2:N1
            x1(p)=(Rc-x1(p-1))*0.25+x1(p-1);
        end
        for q=1:N1
            x(q)=x1(q);
        end
        x2=linspace(Rc,Rw,N2);
        for p=1:N2
            x(p+N1)=x2(p);
        end
        x3=zeros(1,N3);
        x3(N3)=Rw;
        x3(1)=Rp;
        for o=2:N3
            x3(o)=x3(o-1)-((x3(o-1)-x3(N3))*0.4);
        end
        for q=1:N3
            x(N2+N1+q)=x3(N3-q);
        end
        fixpnt=[Rw,Rc]; //Fix mesh point at boundary
        //Density redistribution function-----
        sig=Rp^2/(Rw^2-Rc^2); //Egg-white catalysts
        Tp(i)=Rp*sqrt(K*H2bulk*rou*sig/DCO); //Thiele
        //ODE Solver-----
        z=bvodeS(x,m,n,a,b,fsub,gsub,zeta,fixpnt=fixpnt,...
            ystart=ystart,tol=tol);
        //Average H2/CO ratio-----
        H2sum=0;
        COsum=0;
        for j=N1+1:N1+N2
            H2sum=H2sum+(z(3,j-1)*(x(j)-x(j-1))*x(j));
            COsum=COsum+(z(1,j-1)*(x(j)-x(j-1))*x(j));
        end
        H2CO(i)=H2sum/COsum;
        //Effectiveness Factor-----
        Eff(i)=2*DCO*z(2,N)/(Rp*rou*K*CObulk*H2bulk/((1+kads*CObulk)^2));
        //Closing the CSTR loop-----
        Ratebulk=SCo*(K*CObulk*H2bulk/((1+kads*CObulk)^2));/[mmol/s]
        XCO_cal=Ratebulk*Eff(i)/Flow; //Calculated conversion
        XCO_OLD=XCO_New; //Update old conversion
        XCO_New=XCO_cal; //Update new conversion
        ERROR_XCO=abs(XCO_New-XCO_OLD)/XCO_New; //Update CSTR error
    end
    ERROR_exp=abs(Xexp-XCO_cal)/Xexp; //Update conversion error
    if Xexp>XCO_cal
        ds=ds+0.1; //Increase H2/CO diffusivity ratio if too low
    end
end

```

```
        else ds=ds-0.009;//decrease H2/CO diffusivity if too high
    end
end
XCO(i)=XCO_cal;//Record conversion
DF(i)=ds;//Record H2/CO diffusivity ratio
end
//Export Data to File-----
print ('White.txt',H2CO,XCO,DF)
//*****End*****
```

APPENDIX D

1. Fixed-bed Reactor Set-up

Two sets of experiments were performed in a fixed-bed reactor set-up (see Figure D.1). CO (Afrox, 99.97%) and H₂ (Air Liquide, 99.999%) were fed to the reactor at a head pressure of 40bar. The mass flow of each stream was controlled individually and mixed before entering the reactor. The composition of the feed gas was determined by leading the gas mixture over the reactor-by-pass through a 4-way valve to the online gas chromatograph equipped with a thermal conductivity detector. A H₂/CO ratio of 2 was ensured before the start of each experiment. At the start of the reaction, the 4-way valve was switched to allow the feed gas to flow through the reactor. The flow of argon to the reactor effluent was pressure controlled, in order to maintain a reaction pressure of 20bar. A known amount of cyclohexane (0.15%) premixed with N₂ was added to the product effluent stream as an internal standard for quantitative data analysis.

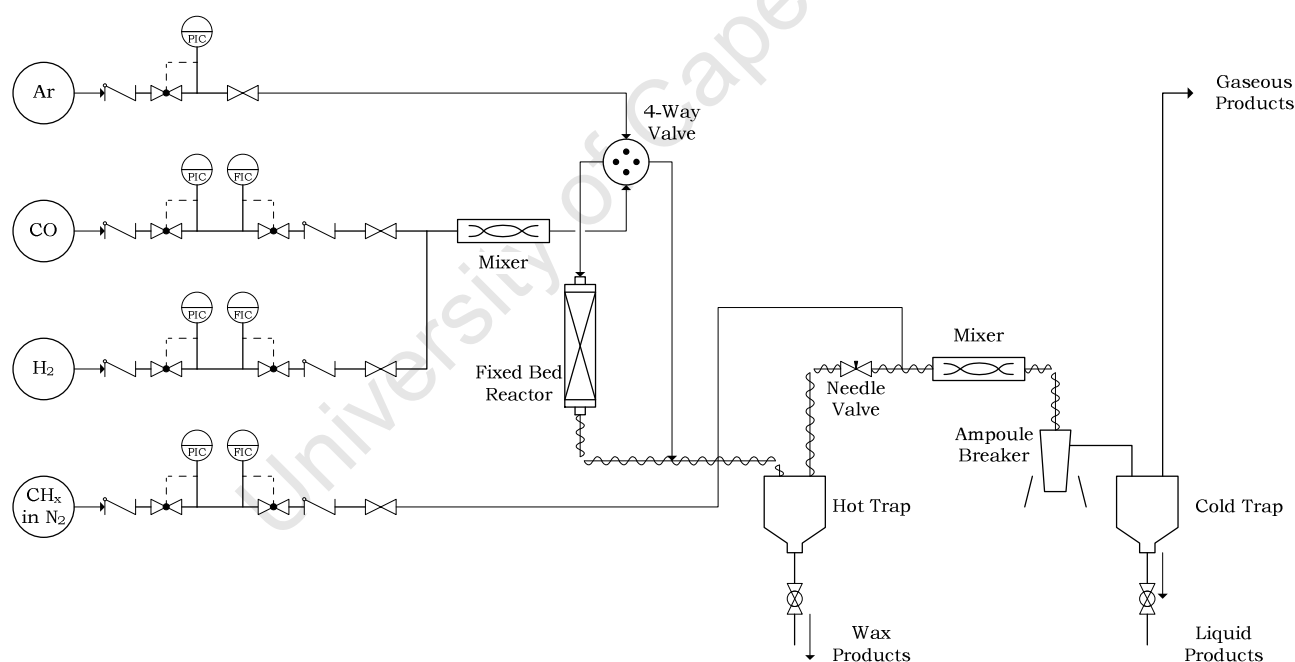


Figure D.1: Flow diagram of Fixed-Bed reactor set-up

The fixed-bed reactor consisted of a stainless steel tube with an internal diameter of 10mm and an isothermal zone of 40mm, which was heated electrically by using a metal jacket with 6 heating elements. The reaction temperature was measured in the centre of the catalyst bed with a thermocouple. Uniform catalyst pellets (U1) (0.4g for the first test; 0.8g for the second) was loaded into the centre of isothermal zone in the reactor. Silicon carbide (d_p : 400 μ m, ca. 3g) was added to fill up the isothermal zone to minimise the axial and radial temperature gradient. The catalyst was kept in place by

plugs of glass wool at the top and bottom of the catalyst bed. Coarse silicon carbide (d: 3-4mm, ca. 10g) was packed on top of the catalyst bed to serve as a pre-heating zone of 10cm in length.

The liquid products were separated from the gas stream in a wax trap operating at 180°C. The product water was separated from the gas stream in the cold trap operating at room temperature. The line from the reactor effluent to the ampoule breaker, in which volatile organic gas samples were taken, was heated to 180°C to prevent condensation. The sampling method will be described in section 4.4.

Catalyst pellets were reduced in-situ using the standard reduction condition of this study (hydrogen flow rate of 90ml(STP)/min/g_{silica} at 350°C for 16 hours with heating rate of 5°C/min). After reduction, the system was cooled to 220°C and pressurised with argon to 20bar. The synthesis gas mixture at flow rate of 32ml(STP)/min for the first test and 64ml(STP)/min for the second was introduced. CO conversion and methane selectivity were recorded at steady-state condition (TOS>24hrs).

2. Wall Effect in Fixed-bed Set-up

In a fixed bed reactor, catalyst pellets are packed closely to each other introducing a resistance to the flow of reactant gas. This resistance to gas flow results a pressure drop along the catalyst bed. Pressure drop of the catalyst bed is also be influenced by the reactor wall, and therefore wall effects may affect the catalysts performance in the reactor. It has been suggests that the reactor wall has counter influence on pressure drop (Carman, 1937; Nield, 1983). The presence of catalyst near the reactor wall results in a large void surrounding these catalyst pellets, which can be as large as half of the pellet diameter (Roblee *et al.*, 1958; Benenati and Brosilow, 1962). At high Reynolds numbers, when the mass transfer boundary layer is thin, the increased local porosity increases the local gas velocity and hence decreases pressure drop over the catalyst bed. However at low Reynolds number, the additional friction introduced by the reactor wall may reduce the local velocity and thereby increasing the pressure drop across the catalyst bed. Since Reynolds number is a function of pellet diameter, the extent of the reactor wall effect is expected to be a function of the ratio of reactor to particle diameter ($D_{\text{tube}}/d_{\text{pellet}}$). A correlation containing over 2300 experimental point shows that the reactor wall effect on pressure drop across the catalyst bed becomes negligible when $D_{\text{tube}}/d_{\text{pellet}}$ is greater than 15 for cylindrical pellets (Eisfeld and Schnitzlein, 2001).

Silicon carbide (d_p : 400 μm) was used as diluents to minimise the wall effect. The reactor bed was packed in such a way that the catalyst pellets were separated from the reactor wall with a layer of silicon carbide to avoid immediate contact between reactor wall and catalyst pellet (see Figure D.2). The ratio of reactor diameter (10mm) to silicon carbide is 25. Thus, the reactor wall effect on pressure drop across the catalysts bed should be minimal.

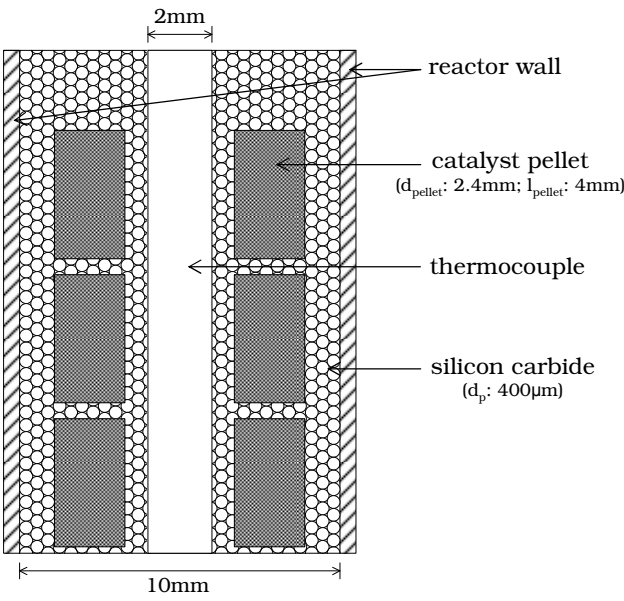


Figure D.2: Schematic representation of pellet packing inside the fixed-bed reactor

3. External Mass Transport Limitations in Fixed-bed Set-up

External mass transport limitation decreases reactant concentration from bulk phase towards the surface of the catalyst. This may falsify the performance of catalyst pellets. The existence of external mass transport limitation was tested based on the idea that when reaction is mass transfer limited, the mass transport coefficient (k_c) is much smaller than the pseudo first order rate constant for the Fischer-Tropsch synthesis (k_r). Mass transport coefficient can be correlated with gas flow around a single spherical pellet through the Frössling correlation (Frössling, 1938). Levich (1962) suggested that the flow pattern around an isolated sphere is not much different from that around a sphere surrounded by other spheres, particularly near the sphere surface where most of the mass transport takes place. Therefore the Frössling correlation is applied in this study.

$$Sh = 2 + 0.6Re^{1/2}Sc^{1/3}$$

where Sherwood number (Sh) is defined as

$$Sh = \frac{k_c d_{\text{pellet}}}{D_{AB}}$$

with k_c , the mass transport coefficient [m/s], d_{pellet} is the pellet diameter [m], and D_{AB} is diffusivity of species A in fluid B [m^2/s]

Schmidt number (Sc) is defined as

$$Sc = \frac{\nu}{D_{AB}}$$

with kinematic viscosity (ν), defined as fluid viscosity over density (μ/ρ) [m^2/s]

Reynolds number (Re) is

$$Re = \frac{\rho d_{\text{pellet}} U}{\mu} = \frac{d_{\text{pellet}} U}{\nu}$$

with linear gas velocity represented as U .

In the case of gas-phase reaction, Schmidt number is sufficiently large enough that the constant 2 in the Frössling correlation is negligible with respect to the second term (Fogler, 1999). The Frössling correlation can then be written as

$$\begin{aligned} \frac{k_c d_{\text{pellet}}}{D_{AB}} &= 0.6 \left(\frac{d_{\text{pellet}} U}{\nu} \right)^{1/2} \left(\frac{\nu}{D_{AB}} \right)^{1/3} \\ k_c &= 0.6 \frac{D_{AB}^{2/3}}{\nu^{1/6}} \frac{U^{1/2}}{d_{\text{pellet}}^{1/2}} \end{aligned}$$

To increase the observed reaction rate for a fast reaction, or otherwise stated $k_r \gg k_c$, the limiting factor i.e. the mass transfer coefficient (k_c), must be increased. If linear

velocity of the reactant gas is doubled while keeping D_{AB} , v and d_{pellet} constant, then mass transfer coefficient would increase by a factor of

$$\frac{k_{c,2}}{k_{c,1}} = \left(\frac{U_2}{U_1} \right)^{\frac{1}{2}} = (2)^{\frac{1}{2}} = 1.41$$

Two sets of extreme catalyst packing scenario were tested in the fixed-bed reactor set-up at 220°C and 20bar. In the first scenario (Run F1), 0.4g of U1 pellets (ca. 10 pellets) was packed into the reactor, which is considered as the minimum amount of pellets to represent a catalyst sample. In the second scenario (Run F2), 0.8g of U1 pellets (ca. 20 pellets) was packed into the reactor, which is the maximum amount of catalyst that could be loaded into the isothermal zone of the reactor. The space velocity of the synthesis gas was kept at 80ml(STP)/min/g_{catalyst}. Thus, the linear gas velocity in the reactor was doubled in the second packing scenario. The CO conversion was increased by a factor of 1.38 by doubling the linear gas velocity (Figure D.3). This clearly implies the existence of severe external mass transport limitation for testing the performance of these catalyst pellets in this fixed-bed reactor set-up.

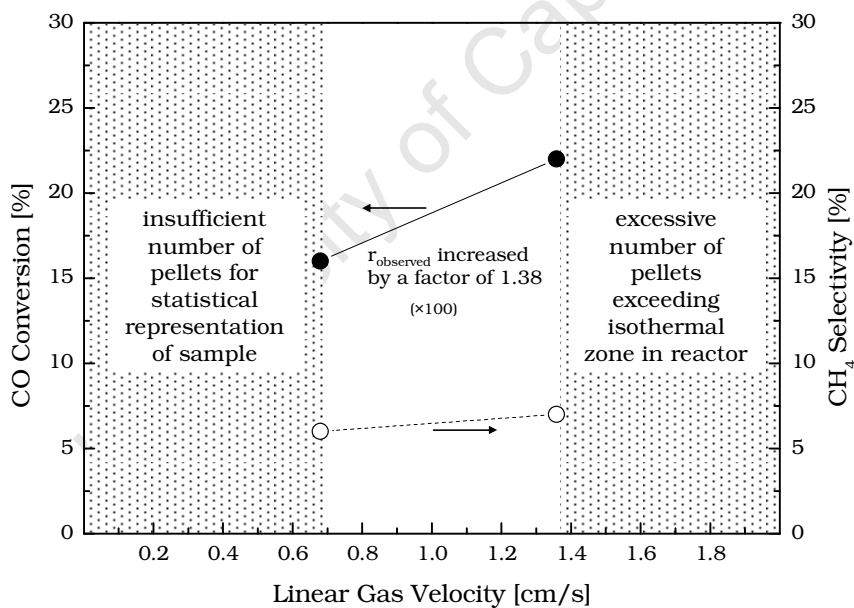


Figure D.3: Fischer-Tropsch performance of catalyst pellet U1 as a function of the linear gas velocity in a fixed-bed reactor at 220°C, 20bar and 80ml(STP)/min/g_{catalyst} with H₂/CO ratio of 2.

The strong external mass transport limitation observed under these conditions is surprising. The concentration difference between the reactant on catalyst surface and reactant in the bulk can be estimated by equating the rate of mass transport and reaction rate (see Figure D.4).

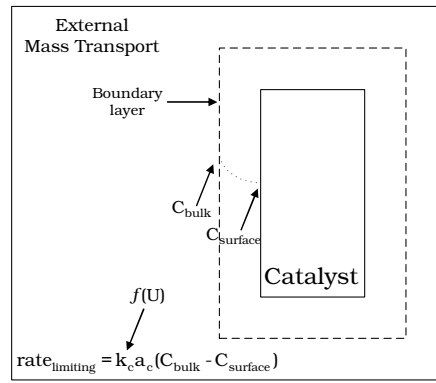


Figure D.4: Concentration profile of a reacting species in the vicinity of a gas-catalyst interface

Using the Fischer-Tropsch rate expression by Yates and Satterfield (1991), the mass transfer rate for CO and H₂ is

$$k_{c,CO} a_c (C_{CO,b} - C_{CO,s}) = \frac{k C_{CO,s} C_{H_2,s}}{(1 + k_{ads} C_{CO,s})^2}$$

$$k_{c,H_2} a_c (C_{H_2,b} - C_{H_2,s}) = \frac{2k C_{CO,s} C_{H_2,s}}{(1 + k_{ads} C_{CO,s})^2}$$

were $k_{c,i}$ is the mass transfer coefficient of species i , a_c is the interface surface area for mass transport, $C_{i,b}$ is the concentration of species i in the bulk phase, $C_{i,s}$ is the concentration of species i on the catalyst surface, k is the rate constant and k_{ads} is the adsorption constant. The Fischer-Tropsch rate constant and adsorption constant at 220°C according to Yates and Satterfield (1991) are 0.55 mmol/min/g_{cat}/MPa² (or 15 mmol/s/g_{cat}/(mmol/cm³)²) and 2.66 MPa⁻¹ (or 91 cm³/mmol) respectively. The interface surface area for mass transport was assumed to be the external surface area of the catalyst pellet (28 cm²/g_{catalyst}). The mass transfer coefficient ($k_{c,i}$) can be written as a function of linear gas velocity using the Frössling correlation

$$k_{c,i} = \frac{D_i}{d_{pellet}} \left(2 + 0.6 \left(\frac{\rho_i d_{pellet} U}{\mu_i} \right)^{1/2} \left(\frac{\mu_i}{\rho_i D_i} \right)^{1/3} \right)$$

with the equivalent diameter of the pellet (d_{pellet}) is 0.375 cm. The density of gases at reaction condition was estimated using ideal gas law, while diffusivity and viscosity of CO and H₂ in synthesis gas were estimated according to Chapman and Cowling (1951) (see Appendix C.3).

Table D-1: Estimated synthesis gas properties at reaction condition

Gas	ρ_i [g cm ⁻³]	μ_i [g cm ⁻¹ s ⁻¹]	D_{CO,H_2} [cm ² s]
CO	1.37×10^{-2}	2.57×10^{-4}	0.0912
H ₂	6.5×10^{-4}	1.19×10^{-4}	

The mass transfer coefficient of carbon monoxide and hydrogen as function of linear gas velocity [cm/s] is then given by

$$k_{c,\text{CO}} = 0.486 + 0.384U^{1/2}$$

$$k_{c,\text{H}_2} = 0.486 + 0.262U^{1/2}$$

The difference between the CO concentration in the bulk phase and at the catalyst surface (ΔC_{CO}) was even at low linear gas velocity (less than 1 cm/s) is less than 0.2% (see Figure D.5, Appendix C.4 for Polymath code). This means that the Fischer-Tropsch kinetics is slower than the rate of mass transport in the gas phase at the reaction condition. Even a significant increase in the rate constant does not yield a significant change in the concentration gradient across the boundary layer. Hence, the observed increase in the rate upon changing the linear velocity is unlikely to be caused by the mass transport limitation in the gas phase.

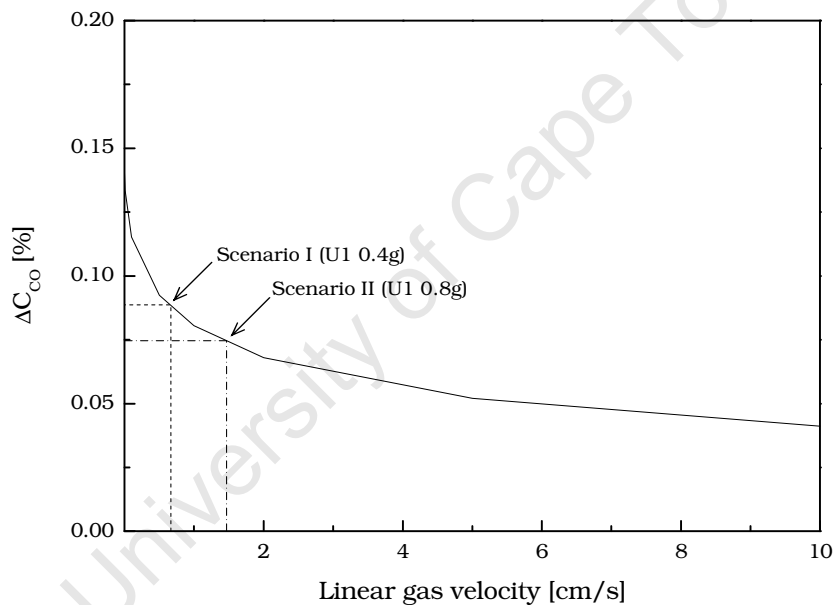


Figure D.5: CO concentration difference between bulk and catalyst surface as a function of linear gas velocity

The surface of the spent catalyst from the fixed-bed tests was coated with a layer of wax after the reactor test. This led to the suspicion that the observed mass transfer limitation was due to the diffusion of reactant species through the layer of wax produced during Fischer-Tropsch synthesis (see Figure D.6).

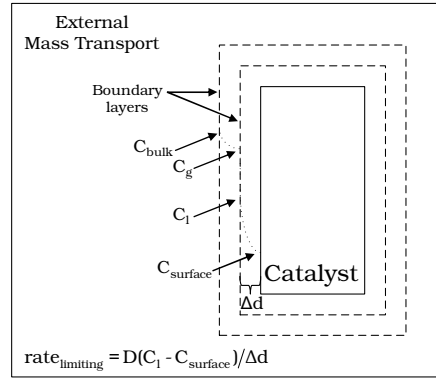


Figure D.6: Concentration profile of a reacting species in the vicinity of a gas-wax-catalyst interface

Since the rate of the Fischer-Tropsch synthesis is less than the gas-phase mass transport rate (as established earlier in this section), the reactant concentration in liquid phase at the gas-liquid interface can be considered to be the saturation concentration of the reactant at its partial pressure in the bulk phase. Therefore the observed rate is then

$$\begin{aligned} -\text{rate}_{\text{CO}} &= D_{\text{CO}} \frac{(C_{\text{CO,sat}} - C_{\text{CO,s}})}{\Delta d} \\ -\text{rate}_{\text{H}_2} &= -2 \times \text{rate}_{\text{CO}} \end{aligned}$$

where D_i is the diffusivity of species i in the liquid layer, Δd is the thickness of the liquid layer, and $C_{i,\text{sat}}$ is the liquid concentration of i species at the gas-wax interface. The typical tortuosity range for silica gel is $2 \leq \tau \leq 6$ (Knudsen *et al.*, 2001). Thus, the effective diffusivity of CO and H₂ in the calculation was assumed to be an order of magnitude less than the bulk phase diffusivity. The CO and H₂ saturation concentration at the inlet partial pressure (CO: 6.67atm; H₂: 13.33atm; 220°C) in the gas phase were estimated to be 0.0356mmol/cm³ and 0.0537mmol/cm³ respectively according to solubility study done by Chou and Chao (1992).

The surface concentration of CO and H₂ can then be written as a function of liquid thickness (Δd), which substituted into the rate expression

$$-\text{rate}_{\text{CO}} = \frac{k(C_{\text{CO,sat}} - \frac{(-\text{rate}_{\text{CO}})\Delta d}{D_{\text{CO}}})(C_{\text{H}_2,\text{sat}} - \frac{(-2\text{rate}_{\text{CO}})\Delta d}{D_{\text{H}_2}})}{(1 + k_{\text{ads}}(C_{\text{CO,sat}} - \frac{(-\text{rate}_{\text{CO}})\Delta d}{D_{\text{CO}}}))^2}$$

Using the experimentally observed CO consumption rates, the thickness of the wax layer is determined to be 0.456μm for run F1 and 0.335μm for run F2 (see Table D-2). Thus even a very thin wax layers surrounding the catalyst pellet would result in severe mass transport limitation. The amount of the liquid phase present on the catalyst surface (thickness of liquid layer) would be a function of the catalyst performance

(liquid product formation rate) and linear gas velocity (liquid product removal by sweeping effect). Therefore adequate control over the reactant concentration at the catalyst surface in the fixed-bed reactor set-up could not be achieved. Hence testing of the activity of the structured cobalt catalyst pellets were performed in a slurry type reactor.

Table D-2: Summary of results of uniform pellets (U1) tests in fixed-bed reactor set-up

Run	Catalysts [g]	Syngas [mℓ(STP)/min]	X _{CO} [%]	d _{wax} [†] [μm]
F1	0.4	32	22	0.456
F2	0.8	64	16	0.335

[†] calculated film thickness